Fundamental Limits of Optical Frequency Comb Interferometry and Spectroscopy with Coherent, Thermal, and Quantum Light

by

Eugene J. Tsao

B.A., Washington University in St. Louis, 2017

M.S., University of Colorado Boulder, 2022

A thesis submitted to the
Faculty of the Graduate School of the
University of Colorado in partial fulfillment
of the requirements for the degree of
Doctor of Philosophy
Department of Electrical, Computer, and Energy Engineering
2024

Committee Members:
Scott A. Diddams, Chair
Joshua Combes
Franklyn Quinlan
Jun Ye
Laura Sinclair

Tsao, Eugene J. (Ph.D., Electrical Engineering)

Fundamental Limits of

Optical Frequency Comb Interferometry and Spectroscopy

with Coherent, Thermal, and Quantum Light

Thesis directed by Prof. Scott A. Diddams

The measurement and manipulation of coherent optical fields have been transformed by the optical frequency comb. Today, the optical frequency comb grants measurements precise enough to count individual cycles of light as well as the generation of nearly any coherent electromagnetic field from the ultraviolet through the infrared. These capabilities have enabled the most precise realizations and comparisons of time, precision spectroscopy over broad bandwidths, and the ability to convert stable signals between optical and microwave fields–seamlessly connecting the entire electromagnetic spectrum from hertz (10^0) to petahertz (10^{15}). These applications involve the interference of a frequency comb with another coherent light source, such as another frequency comb or a single-frequency continuous-wave laser. However, coherent light represents only one type of light. The vast majority of light emanates from "black bodies" such as stars, which is in a thermal state as opposed to a coherent state, and carries profound information about the universe and humanity's place within it. Other types of light defy classical electromagnetism and are known as non-classical or quantum light. Such quantum light may play central roles in quantum communication, quantum computation, and quantum-enhanced metrology. In this thesis, the use of the optical frequency comb in the interferometric measurement of thermal and quantum light is investigated, with a focus on assessing fundamental limits to the sensitivity of such measurements.

In order to measure thermal light, a technique called dual-comb correlation spectroscopy is explored. This technique entails heterodyne measurement of the field of thermal light and subsequent correlation of the field in time. This process reveals the spectrum of thermal light at high resolution and across broad bandwidths. New theoretical work uncovers previously unknown fundamental limits on sensitivity when measuring realistically weak thermal light. Experimental investigation verifies this scaling and is accompanied by a demonstration of spectroscopy at the equivalent power spectral density of our Sun, realizing a greater than 1000-fold sensitivity increase over past demonstrations of this technique. These insights pave the way for expansion of this technique to comb-based spatial correlation of thermal fields. This advancement would allow for extended baseline synthetic aperture hyperspectral imaging throughout the optical spectrum, facilitating novel and profound observations of the universe.

The use of frequency combs for the measurement of quantum light is also investigated. This scenario breaks typical quantum optics assumptions, such as large, mode-matched local oscillators, and necessitates new quantum measurement operators. Such measurement operators are derived, which not only describe homodyne measurements on any quantum state of light with a frequency comb local oscillator, but also indicate that the shot noise limit generally reached in comb-based measurements of coherent light (such as in continuous-wave laser heterodyne and dual-comb spectroscopy) does not correspond to the quadrature or coherent state-overlap description standard in quantum optics. Efforts to experimentally reach this “standard” quantum limit demonstrate a significant improvement in the signal-to-noise ratio over the conventional comb-based shot noise limit, paving the way for lower-power portable optical clocks and quantum-enhanced frequency-comb metrology.

Acknowledgements

Research is both rewarding and difficult, not only intellectually but also emotionally. I am fortunate to have an incredible support system on which I have relied throughout my doctoral work.

I want to thank my advisor, Scott Diddams, for his steady support and enthusiasm for my efforts over the past five years. As Alex Lind once mentioned, despite the inevitable challenges and setbacks in research, with Scott, you never feel that those setbacks are your fault—you are working together on a shared and exciting problem. I certainly needed that support at key moments.

Speaking of Alex, I am lucky to have had his mentorship and friendship throughout my Ph.D. Beyond technical knowledge, I have learned much from his calm thinking, patient confidence, and compassionate outlook.

This thesis work would not have been possible without many others. Josh Combes introduced me to the powerful world of quantum measurement and statistics. Frank Quinlan provided valuable guidance that encouraged me to think critically about my measurements. I have also greatly benefited from my interactions and friendships with Noah Lordi, Connor Fredrick, Kristina Chang, Emily Caldwell, and Ryan Cole.

On a personal note, I want to thank my parents and brother Emil for their support and encouragement in all areas of my life. I also want to acknowledge my grandparents—Grammy and Grandy, and Popo and Gonggong—their predecessors, and the countless others whose support has given me the opportunity to create and explore.

Lastly, I am grateful to my partner Allison. Her unwavering support, encouragement, and passion for life always lift my spirits.

Contents

Chapter

Appendix

List of Tables

Table

List of Figures

Figure

It is human nature to be curious and seek new experiences to better understand our world. One natural avenue for this curiosity is through measurement, which is the quantification of some thing. Although we may merely seek, initially, to satisfy our curiosity, these measurements often reveal deeper mysteries about the universe beyond our imagination. Such mysteries provoke new questions for which we seek new and more advanced measurements. This continued advancement in measurement has driven our current technological and scientific revolution, profoundly changing the way humans interact with each other and within nature.

Chapter 1

Introduction

In the more than 200,000 years that humans have been a species, it is only in the past 10,000 years that large-scale civilization has grown. As these societal networks grew, new measurements were needed to sustain these complex organizations [1]. Such measurements include counting large numbers of objects (perhaps leading to early writing), delimiting and distributing agricultural land (such as after the annual flood of the Nile valley), and ensuring fair trade standards (such that a bushel of wheat meant the same for everyone).[1] The proliferation of measurements for the organization of society also laid the groundwork for scientific and technological advance. One notable example is timekeeping, whose primary purpose 500 years ago was to synchronize lives and labor in cities [2]; today, the most advanced timekeeping measures if fundamental constants are truly constant [3, 4]. The reciprocal relationship also exists–measurements that advance science also impact society. For example, networks of rubidium atomic clocks form the Global Positioning System (GPS), which provides the positioning and timing infrastructure on which our society so heavily relies today.

Advancement in measurement arises when one can measure something that was not measurable before. Very often, this occurs when *sensitivity* increases. For example, the Laser Interferometer Gravitational Wave Observatory (LIGO) is built around a large optical interferometer, the basic design of which has been understood since the 19th century [5]. Through advancements in laser and materials science, coupled with moving to larger physical scales, instrument sensitivity has

---

[1] It was during the first French revolution that the Système International D'Unités (SI) was created to promote fairness and equality.

increased such that one can detect gravitational waves emitted by colossal celestial events. LIGO now provides an entirely new view of the universe, granting the measurement of fundamentally different phenomena than ever before [6].

However, before new and more advanced measurement instruments can enable these discoveries, their sensitivity must be understood and quantified. In this thesis, I seek to understand the fundamental limits on uncertainty and sensitivity[2] for new measurements of light. Specifically, I investigate the use of a revolutionary tool called an optical frequency comb to measure coherent, thermal, and quantum light. This investigation reveals new bounds on uncertainty and sensitivity for important applications such as astronomical spectroscopy and imaging, timekeeping, and precision sensing in general. To understand the context of this work, I first offer a brief history for the general reader before providing an outline of this thesis. I begin with an overview of measuring frequency and time, upon which my research builds.

1.1 Measuring Time and Frequency

The measurement of frequency and its conjugate quantity time has seen dramatic advancement over the past millennium. Humans naturally follow a circadian clock set by the cycles of night and day, as well as by the passing seasons that dictate planting, harvesting, and access to food sources. Through the development of new technologies, we have divided time into increasingly fine increments, far beyond that dictated by Earth's rotation and relationship to the Sun.

One of the first uses for finer timekeeping was the tracking of celestial bodies in the night sky, both for astronomy and astrology. Astronomers were interested in predicting the night sky and building a map of the galaxy. In measuring the positions and velocities of stars and planets overhead, they required a stable timekeeper independent of the Sun. By the late 17th century, the most stable clocks were built on pendula, an invention credited to Christiaan Huygens (1629-1695) that was based on earlier work by Galileo Galilei (1564-1642), who noted the isochronism of

---

[2] Sensitivity is concerned with how small a quantity one can detect or how small a change in a quantity one can detect. Sensitivity is closely related to uncertainty, which quantifies the consistency of a measurement.

pendula. Such clocks indicated time to the minute, yet in a pattern that would continue to occur, a finer demarcation was desired, and astronomers would track the individual teeth on the gears of the clocks to measure celestial trajectories at second-level uncertainties [2].

During the expansion of maritime trade and European colonization the question arose: how could one know where on Earth one was–or, more pertinently, how close to land? A clock that operated independently of the sun and stars allowed sailors to establish longitude. Sunrise and sunset could be compared with the time read on the marine chronometer, thereby computing a "time zone." John Harrison (1693-1776), after several failed attempts, successfully brought a sufficiently stable timekeeper to sea by miniaturizing the mechanical clock, using a higher frequency 5 Hz balance spring instead of traditional pendula-based clocks.[3]

The advance of timekeeping has largely followed the dual discovery and development of new *oscillators* and *methods of tracking or "counting"* such oscillations at ever higher frequencies. Using higher frequencies, one can divide time into finer and more regular increments. This is analogous to a meter stick with finer millimeter markings, as opposed to courser centimeter markings, enabling length measurement at a finer scale. By counting these fast oscillations, we are able to translate this precision to the timescales of interest such as seconds, hours, and days.[4]

By the mid-20th century, the piezoelectric quartz crystal (10s kHz to 100s MHz) had succeeded the balance spring mechanical oscillator (few Hz), and this technology is used today in every electronic device to clock and coordinate intricate chip-level computations (and to tell the time). Shortly thereafter, atoms surpassed quartz crystals. Each atom (of the same isotope) is exactly the same as the next one, promoting consistency between different clocks. Furthermore, electronic oscillations in atoms like cesium were found at frequencies higher than those of quartz. Cesium clocks were much more regular than the Earth's orbit (solar year), on which the existing "ephemeris second" was defined, and these clocks are now used to define the modern-day second; the oscilla-

---

[3] The balance spring was a breakthrough stable source of frequency and time and is still used today in fine mechanical watchmaking.

[4] Another related benefit is that the uncertainty of high frequency oscillators is divided down when the oscillator's frequency itself is divided down, such as to the human scale of single Hz (one oscillation per second).

tion frequency corresponding to the transition between the hyperfine ground states of cesium 133 is defined at 9,192,631,770 Hz (9 GHz).[5] Such cesium clocks require not just the cesium atom, but a stable microwave oscillator[6] to lock to the atom. In a way, the equivalent of the mechanical pendulum oscillator is now the joint system of coherent electromagnetic waves (at 9 GHz) and the atoms they drive. Indeed, the atomic clock revolution was enabled by breakthroughs in the control of radio-frequency electromagnetic radiation, owing to many developments throughout the 19th and early 20th centuries, such as the discovery of Maxwell's equations [8], progress in radar, and invention of the maser [9].

Even as the cesium standard was adopted, it was understood that more accurate definitions of time and frequency could yet be realized through atomic spectroscopy at higher frequencies, such as in the optical range or beyond (100s+ THz). However, while the microwave oscillations could be counted by existing electronics (much as the individual oscillations of a pendulum could be counted in the mechanical clock) no means to measure and track the cycles of light existed. No "gear" could connect the optical transition to the ticking second hand. It was not until the invention of a broadband laser light source called the optical frequency comb [10] that this connection was made. Shortly thereafter, this discovery enabled the current generation of optical clocks, which are the most accurate keepers of time today [4]. At the time of writing this thesis, laser excitation and spectroscopy of a low-lying nuclear transition of thorium-229 have been demonstrated at 2 PHz [11, 12, 13], heralding a new era of nuclear atomic clocks operating at frequencies in and beyond the vacuum ultraviolet, measuring time and frequency with even greater precision.

1.2 Optical Frequency Combs: Their Applications and Capabilities

Out of the pursuit of enhanced timekeeping, the optical frequency comb arose as a means to connect the world of microwaves (0 Hz to 1 THz) and the world of light (1 THz-10 PHz+), granting

---

[5] Today, cesium clocks from all over the world coordinate to form International Atomic Time (TAI), which is the basis for Coordinated Universal Time (UTC). Another network of atomic clocks underpins the Global Positioning System (GPS), a crucial timing and positioning network formed from atomic clocks on each satellite and a primary reference at the United States Naval Observatory [7].

[6] A maser (microwave amplification by stimulated emission of radiation) is used to generate this stable microwave radiation.

the ability to establish and compare new optical clocks. However, the impact of the frequency comb goes beyond timekeeping. Often referred to as a ruler or meter for light, the frequency comb enables counting and control of every cycle of the electromagnetic field of light, which occurs at the femtosecond and subfemtosecond levels, or faster than a millionth of a billionth of a second. Today, the frequency comb is used to generate highly stable microwaves [14], transfer time across vast distances [15, 16], and perform ultrahigh-resolution and broadband direct spectroscopy [17]. Not only does the optical frequency comb grant absolute measurement of electromagnetic fields of light, it also allows for the generation and arbitrary control of nearly any coherent optical field [18]. These established and emerging capabilities now extend a level of mastery over coherent optical fields that has long been exercised at much slower frequencies, i.e., radio waves. Just as technological command of radio waves has revolutionized communication, computation, ranging, medicine, astronomy, and a host of other fields and parts of our lives, it is likely that this relatively newfound mastery of coherent light will further enable profound technologies and scientific discoveries.

1.3 Electromagnetic Fields Beyond Coherent States

Coherence[7] is a property that describes the regularity of electromagnetic radiation and is a hallmark of laser light; the electromagnetic field of laser light is highly regular in its oscillation. The frequency comb can be understood as a coherent state of light. And its use has largely been applied toward interferometry with other coherent states of light, such as other frequency combs or continuous-wave (single-frequency) lasers. Yet, there are other states of light of great interest. For example, thermal light constitutes the vast majority of light in our universe, and quantum (nonclassical) light–which defies classical electromagnetism–could increase measurement sensitivity beyond what is possible with classical (coherent) light. However, the application of the optical frequency comb for the interferometry with and measurement of thermal and quantum light is largely unexplored. In this dissertation, I investigate the application of the frequency comb toward not only coherent states of light, but also thermal and quantum states of light. I do so by providing

---

[7] Coherence is explored extensively in chapter 3.

new frameworks and experiments that quantify the fundamental sensitivity of such measurements, which has so far been unknown (see Fig. 1.1).

1.4 Thesis Outline

In chapter 2, I give a general technical background essential for understanding metrology with optical frequency combs, including a review of statistical distributions, noise, signal-to-noise ratio, and standard optical interferometry techniques such as homodyne and heterodyne.

In chapter 3, I detail the investigation of a new technique to measure the field of thermal light, such as starlight, and the subsequent temporal correlation and spectral measurement of this light. I demonstrate this technique, called dual-comb correlation spectroscopy, on thermal light having the equivalent power spectral density of a 5770 K black body such as our Sun at a wavelength of 1550 nm. The sensitivity reached in this measurement is a factor of 1000 to 10,000 better than in previous demonstrations of this technique [19, 20]. I also provide new theoretical work that reveals the previously unknown fundamental shot noise (quantum noise) limited sensitivity of this technique. This provides crucial information for how this technique could realistically be used for measuring distant stellar objects. I also experimentally verify this sensitivity scaling across three orders of magnitude of thermal light strength. In addition, I provide comparison with more traditional ways of measuring the field of thermal light (such as through laser heterodyne radiometry), analyzing the complex trade space of sensitivity and technical complexity. Lastly, I show how this work also lays a foundation for long-baseline synthetic aperture hyperspectral imaging at optical frequencies–which could grant the imaging of stellar objects thus far indiscernible in our universe, yielding essential information on planetary formation, molecular composition, and Earth's place in the universe.

In chapter 4, I show new theoretical work that provides a quantum description of homodyne measurements with optical frequency combs in the form of quantum measurement operators. This quantum optical framework is necessary to describe frequency comb-based measurements of quantum light, thereby providing a road map for quantum-enhanced frequency-comb metrology.[8] This

---

[8] The measurement operators derived describe the full statistics of these measurements, which is essential for

work also reveals a lower quantum limit than previously recognized for the heterodyne measurement of coherent light. This discovery has important implications for optical timekeeping, since it is through a heterodyne measurement with an optical frequency comb that the timing stability of an optical atomic transition is translated to electronically countable frequencies. Although it has been known that the previously accepted "quantum limit" could be surpassed through purely classical processing [21, 22], there was no defined limit for this improvement. I provide this bound and detail a series of experiments aiming to reach this bound. Although this limit is not reached, I detail critical information on the technical challenges involved in reaching this limit. I then provide calculations and planning to continue seeking this lower frequency comb "standard quantum limit." This approach could result in more efficient portable optical clocks and is a necessary step before experimentally realizing a true quantum advantage in frequency comb metrology.

In chapter 5, I conclude by presenting a broader view of where I believe this work is headed.

---

describing the uncertainty and sensitivity afforded through such measurements.

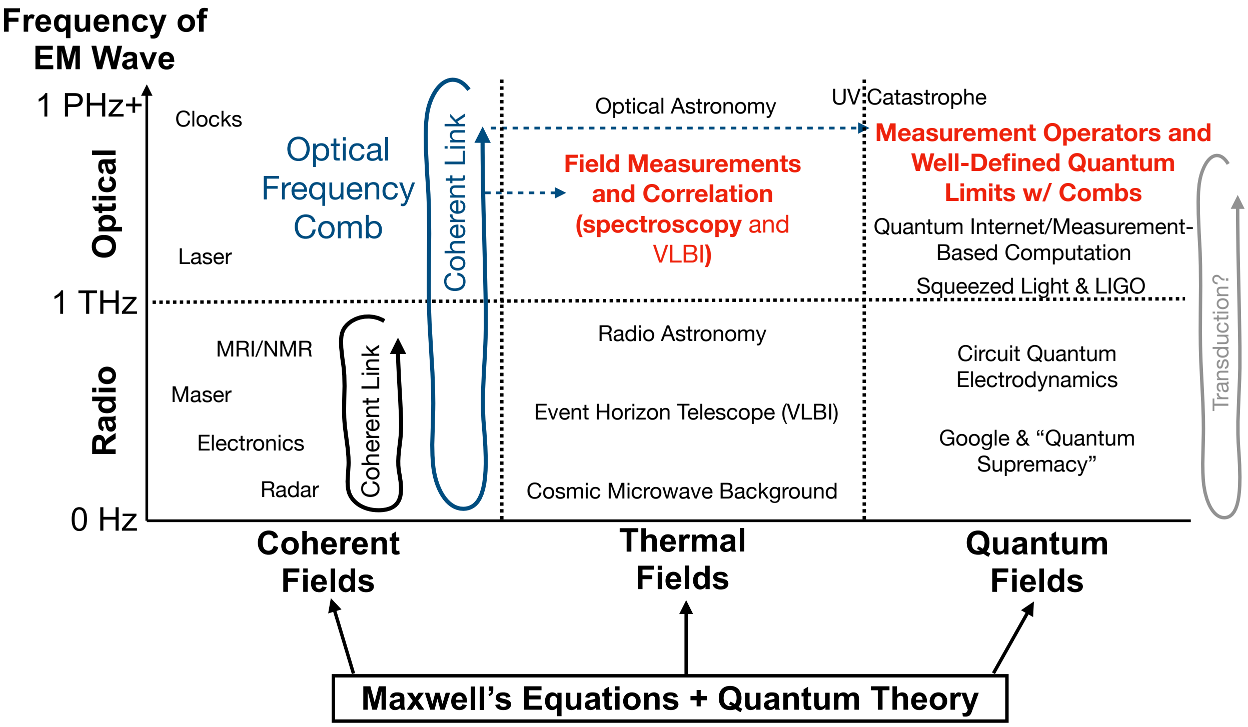

Figure 1.1: The unification of electricity, magnetism, and their dynamics, with notable contributions from James Clerk Maxwell and Michael Faraday [8], combined with the establishment of quantum theory by Albert Einstein, Max Planck, and many others, such as Roy Glauber [23], have led to foundational understanding of coherent, thermal, and quantum electromagnetic fields. Technological progress over the 20th century granted unparalleled control over radio fields, establishing a coherent link between frequencies from 0 Hz to 1 THz. The optical frequency comb at the turn of the 21st century provided a coherent link across vastly increased bandwidths, today beyond PHz frequencies. Just as mastery of coherent radio fields has yielded powerful measurements and exquisite control of thermal fields in radio astronomy and quantum fields in circuit quantum electrodynamics, it is likely that newfound facility with coherent optical fields–provided through the optical frequency comb–will enable diverse and impactful capabilities. This thesis describes efforts to define the fundamental limits for the application of the optical frequency comb toward the measurement of coherent, thermal, and quantum light, with applications in astronomical spectroscopy and imaging, and quantum-enhanced sensing.

Chapter 2

General Technical Background

Here, I survey general background information essential for understanding this thesis work. Perhaps the most common figure of merit that assesses sensitivity is the signal-to-noise ratio (SNR), but in order to fully understand SNR, one must first understand what is signal and what is noise. Ultimately, these are properties of a probability distribution, so I review the basic nature and properties of probability distributions. Next, I provide context on a class of statistical distributions called Gaussian distributions and why they are so ubiquitous and important. I also cover white noise. Two examples of approximately white Gaussian noise we often see are thermal noise and shot noise, and I describe their origins.

Lastly, I describe the basics of optical interferometry and homodyne and heterodyne with continuous-wave local oscillators. I describe how these measurements are made with coherent signals and their classical shot noise-limited SNR, which prepares the reader for new work in this thesis establishing the limits of frequency-comb interferometry of coherent, thermal and quantum light.

Additional technical background specific to Chapter 3 and Chapter 4 is included in those chapters.

2.1 Signal and Noise

A typical measurement involves reading a number or value, whether on a counter, an oscilloscope, or graphed on the computer. This value corresponds to some measurement, but it is only in the comparison of this value with other values on subsequent measurements that notions of signal and noise can be defined. Ideally, we would make many measurements that form a statistical ensemble, thus yielding (or approximating) a statistical distribution. Most of the time, we simply assume the structure of the distribution.

2.1.1 Statistical Distributions

Statistical distributions are described by probability densities, e.g., $P(x)$ where x is a possible value that could be measured and X the unknown quantity that is measured. $P(x)$ must sum to 1, i.e.,

$$\int_{-\infty}^{\infty} P(x)dx = 1 \tag{2.1}$$

2.1.2 Mean, Variance, and SNR

The average, mean, or expectation value of X is:[1]

$$\langle X\rangle \equiv \int_{-\infty}^{\infty} P(x)x dx \tag{2.2}$$

and the variance of X is:

$$V_X \equiv \langle X^2\rangle - \langle X\rangle^2 \tag{2.3}$$

In many instances we encounter in the laboratory, the distributions we deal with are (approximately) Gaussian and are defined solely by these two values. And usually, we are concerned with assessing the mean of this distribution, but we are constrained in assessing this mean because we are sampling across the whole distribution, the width of which is described by the variance. Thus we define the signal as the mean and the square root of the variance[2] as the noise, and the signal-to-noise ratio (SNR) as their ratio:

---

[1] Here we are assuming the ergodic hypothesis–that temporal averages and ensemble averages are equivalent. This may not always be the case, and one should carefully define the periods over which one averages or the quantities one is characterizing in order to satisfy ergodicity. For example, the statistics of pulsed frequency comb measurements are not stationary in time, and one must measure far beyond the timescale of each repetition period to equate temporal and ensemble averages.

[2] I.e., the standard deviation, thus maintaining a unit-less SNR.

$$\mathrm{SNR} = \frac{\langle X\rangle}{\sqrt{\langle X^2\rangle - \langle X\rangle^2}} = \frac{\langle X\rangle}{\sqrt{V_X}} \tag{2.4}$$

Note that in general non-Gaussian distributions require more than mean and variance to be fully characterized. Mean and variance fall into a class of terms called moments and cumulants, where the first moment is the mean and the second cumulant is the variance. Higher order moments (and cumulants) are essential to describe more complex probability densities, though here we concern ourselves with the simple (beautiful) and ubiquitous Gaussian distribution for which mean and variance are sufficient.

2.1.3 Averaging

As taught in introductory STEM classes, averaging the results of independent but methodologically identical measurements produces a more accurate result. Why and how does this happen?

Averaging is a two-step process. First random variables must be added then divided by the number of measurements. If independent random variables X and Y are added, such that $Z = X + Y$, the probability density of Z is

$$P_Z(z) = \int_{-\infty}^{\infty} P_X(z-s)P_Y(s)ds = P_X * P_Y, \tag{2.5}$$

which is the convolution of the two probability densities P_X and P_Y. This has the consequence that both the means and the variances add, i.e.,

$$\langle Z\rangle = \langle X\rangle + \langle Y\rangle \tag{2.6}$$

and

$$V_Z = V_X + V_Y. \tag{2.7}$$

Since averaging is not only a summation but also a division, we write the mean of the average as:

$$\mu_{\mathrm{avg}} = \left\langle \sum_{n=1}^{N} \frac{X_n}{N} \right\rangle = \frac{1}{N}\sum_{n=1}^{N} \mu = \mu, \tag{2.8}$$

where μ is the expectation value for a single measurement, N is the number of measurements, and μ_{avg} is the expectation value for the averaged measurement. So the mean or expectation value does not change with the number of averages.

But the variance does! Note that $V[aX] = a^2V[X] = a^2V_X$, where subscript and bracketed notation refer to the same functional relationship. This equality can be derived from the definition of the variance above. Using this equality alongside the property that variances add, we derive the variance of the average:

$$V_{\text{avg}} = V\left[\sum_{n=1}^{N} \frac{X_n}{N}\right] = \sum_{n=1}^{N} \frac{V_X}{N^2} = \frac{V_X}{N} \tag{2.9}$$

So the variance of the average decreases by the number of averages. As a consequence, the SNR increases by the square root of the number of averages:

$$\text{SNR}[N] = \frac{\langle X \rangle}{\sqrt{V_X}} \times \sqrt{N} \tag{2.10}$$

Note that often times we also specify the SNR in terms of power ratios, so our power ratio SNR is:

$$\text{SNR}_{\text{PR}}[N] = \frac{\langle X \rangle^2}{V_X} \times N \tag{2.11}$$

2.1.4 Gaussian Distributions

Gaussian, or normal, distributions are spectacularly ubiquitous in physics and statistics and have a long history in which Carl Friedrich Gauss (1777-1855) is one contributor (and Abraham de Moivre (1667-1754) and Pierre-Simon Laplace (1749-1827) are other notable contributors). An enjoyable and technical account of the history can be found in E.T. Jayne's book *Probability Theory* [24]. The Gaussian distribution can be written as,

$$P(x) = \frac{1}{\sqrt{2\pi\sigma^2}} e^{-\dfrac{(x-\mu)^2}{2\sigma^2}} = \mathcal{N}(\mu, \sigma^2) \tag{2.12}$$

where the mean of the probability density is $\langle X \rangle = \mu$ and the variance is $V[x] = \sigma^2$ (see Fig. 2.1). Since Gaussian distributions are entirely defined by mean and variance, the SNR detailed above is a very sensible figure of merit for assessing how well we know the distribution and its mean!

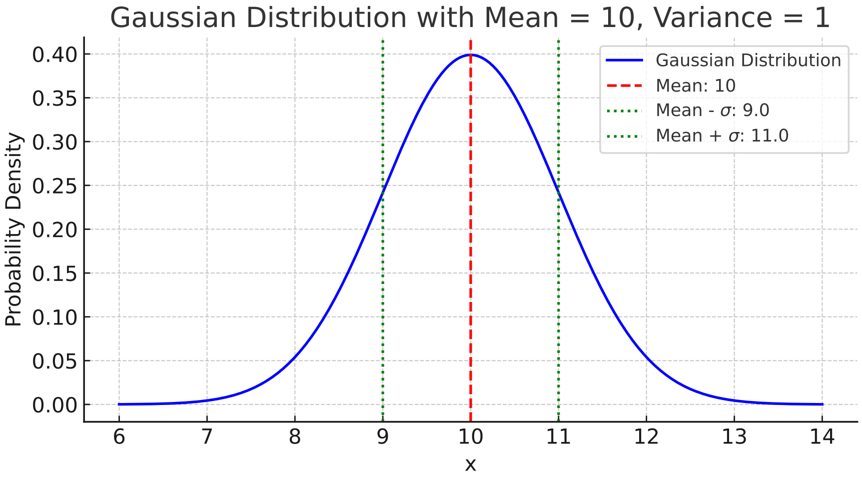

Figure 2.1: Example Gaussian distribution with $\sigma^2 = 1$ and $\mu = 10$.

2.1.5 The Central Limit Theorem

Why are Gaussian distributions so common, and why are so many of the physical quantities we want to measure defined by a Gaussian distribution? While not entirely inclusive of all processes that result in Gaussian distributions, most Gaussian processes we encounter can be understood through the central limit theorem, which states that when many (independent) distributions with finite mean and variance are convolved, the result is a Gaussian distribution. In other words, when we add many independent variables, the resulting probability distribution is Gaussian. This can be stated softly for the case of independent processes with the same expectation values[3] as:

$$\lim_{n \to -\infty} \sqrt{n}(\bar{X}_n - \mu) = \mathcal{N}(0, \sigma^2), \tag{2.13}$$

where

$$\bar{X}_n = \frac{X_1 + X_2 + X_3 + ... + X_n}{n} \tag{2.14}$$

and

$$\mathcal{N}(0, \sigma^2) = \frac{1}{\sqrt{2\pi\sigma^2}} e^{\frac{-x^2}{2\sigma^2}}. \tag{2.15}$$

Already we can see why measurements (and noise) we encounter in the laboratory are defined by Gaussian distributions–we are often viewing the result of many uncorrelated events. A proof of the above can be found in [25], extensive discussion can be found in [24], and excellent intuition can be gleaned from Grant Sanderson's Youtube channel 3Blue1Brown [26]. Before we discuss the connection to thermal noise and shot noise, we note two other common distributions that limit to the Gaussian distribution.

2.1.6 Binomial Distributions

The binomial distribution describes the probability of one of two outcomes in a sequence of n independent measurements. A typical example is a sequence of coin flips, but in a laser metrology laboratory, a very common setting for a binomial distribution is in balanced detection with a single

---

[3] Though this result holds for *any* independent processes with finite mean and variance.

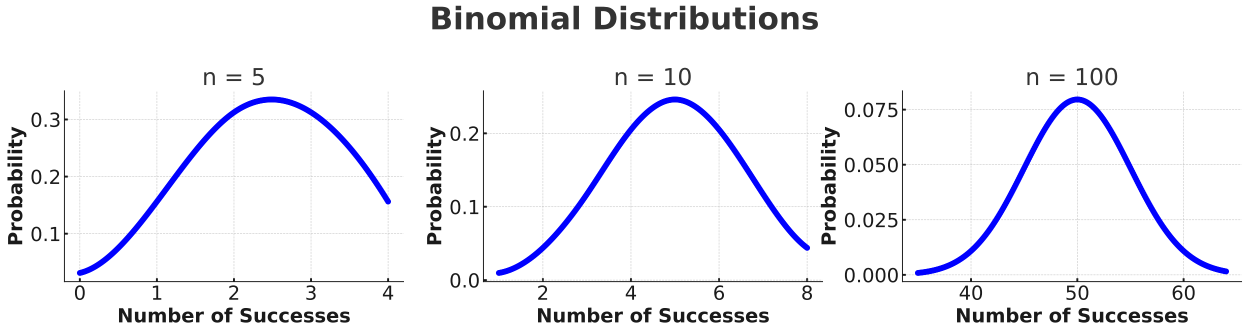

Figure 2.2: Example binomial distributions with spline interpolation as n increases and $k = 0.5$. As n increases the binomial distribution approaches a Gaussian distribution.

coherent input (which will be discussed later) where the photon must "choose" between being detected on one detector or the other in the balanced pair. The binomial distribution can be stated as

$$\Pr(X = k) = \frac{n!}{k!(n-k)!} p^k (1-p)^{n-k} \tag{2.16}$$

where $k = 0, 1, 2, ..., n$ and p is the probability of one of two outcomes for a single measurement. Importantly, as n and np approach infinity (i.e., satisfying the central limit theorem), the binomial distribution approaches the Gaussian distribution of $\mathcal{N}(np, np(1-p))$, which is again solely described by a mean and a variance!

2.1.7 Poisson Distributions

The Poisson distribution is also a very common distribution, occurring notably in the direct detection of photons from a laser (approximately a coherent state where photons are uncorrelated–see discussion of photon statistics in following sections). In fact, it is another limiting case of the binomial distribution where n goes to infinity, but np remains finite. Physically, the Poisson distribution defines the probability of a given number of events given some fixed time interval under the conditions that these events have a mean rate and are independent of each other:

$$\Pr(X = k) = \frac{\lambda^k e^{-\lambda}}{k!}. \tag{2.17}$$

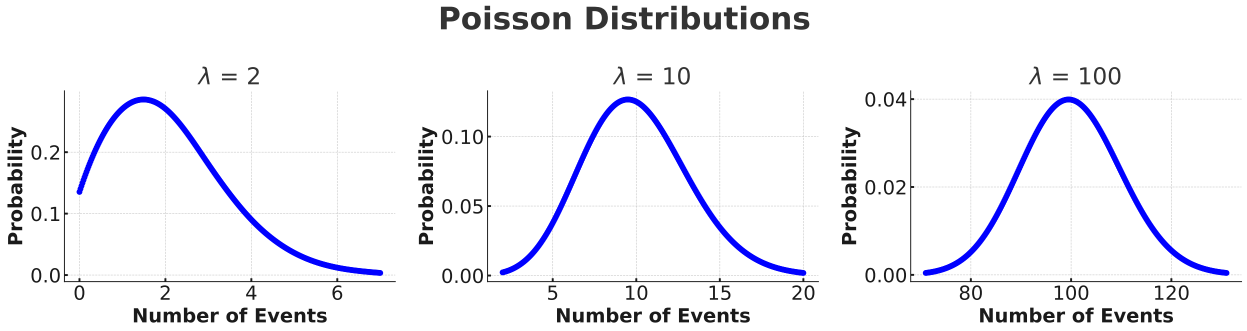

Figure 2.3: Example Poisson distributions with spline interpolation as λ increases. As λ increases the Poisson distribution also approaches a Gaussian distribution.

Here, k is the number of events in the fixed interval, and λ is the expectation value for the number of events in the fixed interval. The Poisson distribution also has the property that $\lambda = \langle X \rangle = V[X]$; in other words, the mean is equal to the variance, which is parameterized by λ. In addition, as λ grows large, the Poisson distribution *also* approaches the Gaussian distribution $\mathcal{N}(\lambda, \lambda)$.

So it seems that many distributions end up becoming Gaussian–especially when there is an element of summation over uncorrelated random variables. But I would like to emphasize that many important distributions are non-Gaussian, too. One particularly relevant non-Gaussian distribution is the Bose-Einstein distribution, which will be important in discussions on black-body radiation and thermal light.

2.2 Noise Basics

Now that the basics of distributions have been covered, I review a couple other aspects of noise: the power spectral density and the shape of this spectrum, specifically the case where the shape is flat, i.e., "white noise."

2.2.1 Power Spectral Density

Up to now, I have considered the statistics of events up to a certain time and have not considered distinguishing these events in time and characterizing their relationships. One way to describe the temporal properties of a random process is through the conjugate variable, i.e., through the spectrum (Fourier transform), but random processes are not as simply related through a Fourier transform as are deterministic processes. In order to define the spectrum of a random process, one must define the power spectral density (PSD). Consider the random process $x(t)$. The average power of this process is:

$$P[x(t)] = \lim_{T\to\infty} \frac{1}{T} \int_{-T/2}^{T/2} \langle x^2(t) \rangle dt. \tag{2.18}$$

One is interested in the average power in some band of frequencies, so one may imagine bandpass filtering $x(t)$ to form a filtered signal $Y(t)$ that has been averaged over all sample trajectories:

$$P[Y(t)] = \int_{\nu_1}^{\nu_2} S(\nu) d\nu, \tag{2.19}$$

where ν_1 and ν_2 define the edges of the bandpass filter, and $S(\nu)$ is the function over which the filtering would have occurred. $S(\nu)$ is the PSD and can be defined as:

$$S(\nu) = \int_{-\infty}^{\infty} R(\tau) e^{-i2\pi\nu\tau} d\tau, \tag{2.20}$$

where

$$R(\tau) = \langle x(t) x(t+\tau) \rangle. \tag{2.21}$$

This definition of PSD is called the Wiener-Khintchine theorem, and I will return to this in Chapter 3 to understand dual-comb correlation spectroscopy.

2.2.2 White Noise

A special case for the power spectral density of a random process is where the power is evenly distributed across all frequencies. This is called white noise (and it is not physically realizable because of the infinite energy carried by infinite-bandwidth white noise). However, approximately white noise is very common. In the time domain, the PSD of a random process is white if the random process has the following autocorrelation:

$$R(\tau) = \sigma^2 \delta(\tau), \tag{2.22}$$

and the PSD is

$$S(\nu) = \sigma^2. \tag{2.23}$$

In reality, $R(\tau)$ is not composed of a delta function but an impulse response of non-zero temporal width, and thus a spectrum that is approximately white up to a finite bandwidth.[4] It is important to emphasize that an underlying Gaussian distribution is not equivalent to a white noise process, but often they come together, as in subsequent examples of thermal noise and shot noise. This is a particularly convenient simplification because the noise of the random process can (ideally) be entirely characterized by the PSD or variance at any point in the PSD (up until some cut-off point).

2.3 Examples of White Noise

Echoing the earlier discussion, noise is a property of our probability distribution that makes it difficult to characterize the center, or expectation, of that distribution. For a Gaussian distribution, this can easily be parameterized by the variance σ^2 or equivalently the standard deviation σ. Now we discuss two of the principal noise types encountered in the detection of photons, thermal (Johnson-Nyquist) noise and shot noise. Other sources of noise, such as excessive relative intensity noise and digitization noise, will be discussed in later chapters.

2.3.1 Thermal Noise

Thermal noise in electronic circuits, as quantified and measured by John Bertrand Johnson (1887-1970) and explained by Harry Nyquist (1889-1976)[5] [27, 28], is a manifestation of the fluctuation-dissipation theorem, which states that any system at thermodynamic equilibrium will exhibit fluctuations that correspond to its dissipative processes [29][6] . In the case of an electrical

---

[4] Note here it is convenient to specify the variance in units of spectral density, but for any measurement there is a specified bandwidth, so there would be a total integrated variance that aligns with subsequent definitions of noise.

[5] In 1928 and both at AT&T's Department of Development and Research–what would become Bell Telephone Laboratories.

[6] Later we will see another example of the fluctuation dissipation theorem in the generation of light from a black body.

conductor, the dissipative process is its resistance, and the corresponding fluctuation is the voltage or current noise caused by the thermal motion of the electrons. As is perhaps intuitive from the physical basis of thermal noise, the probability distribution for a thermal noise across a finite bandwidth is Gaussian, and the PSD is white corresponding to a temporally uncorrelated process.

The mean square[7] of the current through a (source) resistor is:

$$\overline{i^2_{\mathrm{TN,s}}} = \frac{4k_B T \Delta f}{R}, \tag{2.24}$$

where $k_B = 1.380649 \times 10^{-23}$ J/K is the Boltzmann constant (defined exactly), T is the temperature in K, R is the resistance in Ω, and Δf is some finite bandwidth in Hz over which the noise is filtered.

If this is the current power dissipated by a source resistor, the power measured across the load of a measurement resistor is a factor of 4 less than this, since the voltage is divided equally (by two) across the two resistors. Thus, the current power measured is:

$$\overline{i^2_{\mathrm{TN,l}}} = \frac{k_B T \Delta f}{R}. \tag{2.25}$$

Putting some typical numbers here, if I measured thermal noise from a 50 Ohm resistor at 300 K (room temperature) on my RF spectrum analyzer with 50 Ohm termination, I would measure a power spectral density of -174 dBm/Hz, which is quite low.

2.3.2 Shot Noise

In a classical picture, shot noise arises from uncorrelated and distinct events. In Chapter 4 I will show that shot noise has other interpretations from a quantum optics metrology view, but here I derive the photon shot noise PSD of a laser from the classical perspective following the abbreviated treatments of Hermann Haus [30] and Robert Kingston [31].

The current i measured in a time interval τ is

$$i = nq/\tau, \tag{2.26}$$

---

[7] Which is equivalent to the variance due to a zero mean.

where n is the number of photo-electrons excited in this time interval and q is the elementary charge of (defined exactly) $1.602176634 \times 10^{-19}$ C. The average current is

$$\bar{i} = \bar{n}q/\tau, \tag{2.27}$$

where $\bar{n}$ is the average number of excited photo-electrons. The mean-square noise current over independent measurements all of time τ is

$$\overline{i^2_{\mathrm{SN}}} = \overline{(i-\bar{i})^2} = \frac{q^2}{\tau^2}\overline{(n-\bar{n})^2} = \frac{q^2}{\tau^2}\bar{n} = \frac{qI}{\tau}, \tag{2.28}$$

where we have used the Poissonian condition that the variance is equal to the mean.[8] Note that the mean current $I = \frac{q\bar{n}}{\tau}$. In defining τ, I assumed an impulse response function $h(t)$ that integrates electrons over some time τ. For simplicity, assuming that $h(t)$ is a rectangular or box car function of length τ, and thus a sinc-shaped spectrum, the equivalent rectangular spectrum of the same peak height and equal area has a width of $\Delta f = \frac{1}{2\tau}$. Therefore, we can rewrite the shot noise as

$$\overline{i^2_{\mathrm{SN}}} = \frac{2q^2}{\tau}\bar{n}\Delta f = 2qI\Delta f. \tag{2.29}$$

A useful number to keep in mind is the power at which shot noise equals thermal noise. Here I will make the (realistic) assumption that the quantum efficiency from photons to electrons is 2/3. We can include this efficiency by rewriting shot noise as

$$\overline{i^2_{\mathrm{SN}}} = 2\eta q^2\frac{P\Delta f}{h\nu} = 2q \times Re \times P\Delta f, \tag{2.30}$$

where $\eta = 2/3$, P is the optical power incident on the detector, h is the (exactly defined) Planck constant of $6.62607015 \times 10^{-34}$ J/Hz, ν is the frequency of the laser, and $Re = \eta q/h\nu$ is the responsivity of the detector in A/W. For a laser around 1550 nm in wavelength, the power needed to equal 50 Ohm thermal noise at room temperature is approximately 320 µW.

---

[8] This though begs the question, *why*, when a laser is photo-detected, are the photon arrival times uncorrelated. It turns out that *must* be this way for a field that radiates from a classical dipole antenna, i.e. for a coherent state. More about this can be found in the work of Roy Glauber, e.g., [23]

2.4 Optical and Laser Interferometry

The interferometry of light is a powerful technique with a wide array of variations and applications. Various interferometers of historical and practical importance include Young's double slit interferometer (highlighting the complementarity of the wave and particle nature of light), the Sagnac interferometer (used to detect rotation), the Fabry-Pérot interferometer (laser stabilization), the Michelson stellar interferometer (astronomical imaging), and the Michelson interferometer (Fourier transform spectroscopy and gravitational wave detection).

At the core of optical interferometry is the superposition of light followed by photodetection. Consider two light fields $A(t)$ and $B(t)$. Combined on a, for example, 50:50 beam splitter, one of the output ports now contains the field $\frac{A(t)+B(t)}{\sqrt{2}}$. Photodetection measures the intensity of the light, resulting in:

$$i_{\mathrm{PD}}(t) \propto \left|\frac{A(t)+B(t)}{\sqrt{2}}\right|^2 = \frac{1}{2}\Big[|A(t)|^2 + |B(t)|^2 + A(t)B^*(t) + A^*(t)B(t)\Big]. \tag{2.31}$$

Most often, the interference terms $A(t)B(t)$ are of interest.

2.4.1 Classical Homodyne and Heterodyne

Very often, one of the fields (e.g. $B(t)$) is known, and the other field (e.g. $A(t)$) is unknown. Through interferometry, the unknown field can be reconstructed or some parameter of the unknown field can be estimated. For optical fields, $B(t) = \mathscr{B}(t)e^{i\omega_0 t}$,[9] where there is a high frequency THz+ carrier ω_0 riding on the complex envelope $\mathscr{B}(t)$. These oscillations cannot be measured by electronics, and interferometry between light fields of close carrier frequencies enables a down-mixing to DC or RF frequencies that enable reconstruction or estimation of the unknown field through conventional electronics.

Homodyne and heterodyne interferometry address this use case of a known local oscillator $B(t)$ and an unknown signal $A(t)$. There are a number of variations, but here I address standard homodyne and heterodyne with a standard balanced detection setup in the large local oscillator

---

[9] Excluding the spatial dependence for simplicity.

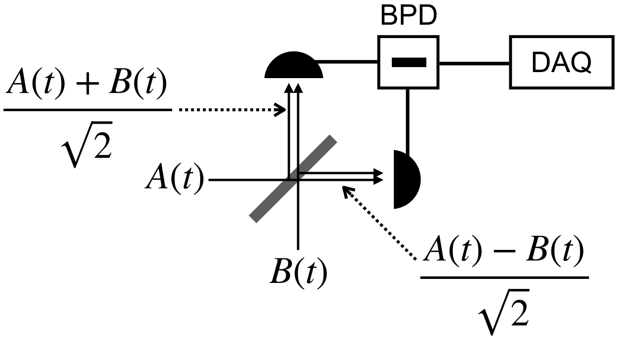

Figure 2.4: Layout for a balanced homodyne or heterodyne ('Dyne) measurement with a 50:50 beamsplitter. BPD is a balanced photodetector, and DAQ is data acquisition.

limit. The difference between homodyne and heterodyne conventionally lies in whether the carrier frequencies are degenerate or not, and I will (classically) show how this leads to a factor of 2 difference in the SNRs of the two otherwise identical techniques. I will come back to this distinction in Chapter 4 and show that there is another measurement interpretation that results in a distinction between homodyne and heterodyne.

Consider now the other term for the other photodetector aside from that described in Equation 2.4:[10]

$$i_{\mathrm{PD2}}(t) \propto \left|\frac{A(t)-B(t)}{\sqrt{2}}\right|^2 = \frac{1}{2}\Big[|A(t)|^2+|B(t)|^2-A(t)B^*(t)-A^*(t)B(t)\Big]. \tag{2.32}$$

Balancing (subtraction of the currents) yields:

$$\begin{aligned} i_{\mathrm{BPD}}(t) = i_{\mathrm{PD1}}(t) - i_{\mathrm{PD2}}(t) \propto \frac{1}{2}\Big[A(t)B^*(t)+A^*(t)B(t)\Big] - \frac{1}{2}\Big[-A(t)B^*(t)-A^*(t)B(t)\Big] \\ = A(t)B^*(t)+A^*(t)B(t). \end{aligned} \tag{2.33}$$

One observes two advantages for balancing–one, the mean-field components of $|A(t)|^2$ and $|B(t)|^2$ are removed[11] , and two, we used all the photons available to us.

---

[10] Note that there are different beam splitter transfer matrices. Here I use the non-imaginary transfer matrix.

[11] And in so doing, laser technical noise, or excess relative intensity noise (RIN) is also canceled in the large local oscillator case. However, if both fields are of nearly equal strength, the so-called cross-RIN terms do not cancel. One can derive this by noting that the excess RIN is purely classical, so it can be written as an additive noise term on top of the field. For example, $A_{\mathrm{RIN}}(t) = A(t) + N(t)$. Recalculating the work above shows that only in the large LO limit is excess RIN canceled, and other cross-RIN terms are assumed to be lower than the noise of the shot

2.4.1.1 Homodyne

In the homodyne case the carriers cancel and the current is:

$$i_{\text{BPD}}(t) \propto \mathcal{A}(t)\mathcal{B}^*(t) + \mathcal{A}^*(t)\mathcal{B}(t). \tag{2.34}$$

For a real envelope (such as the case of no chirp), this is

$$i_{\text{BPD}}(t) \propto 2\mathcal{A}(t)\mathcal{B}(t). \tag{2.35}$$

and in the case of two CW lasers with average field stengths $\mathcal{A}_0$ and $\mathcal{B}_0$, our electrical signal is

$$i_{\text{BPD}} = 2\frac{\eta q}{hv}\mathcal{A}_0\mathcal{B}_0, \tag{2.36}$$

where we have now included the detector responsivity. Recall that the shot noise is not correlated, so we may add the variances. The total shot noise is then $\overline{i^2_{\text{SN, tot}}} = \overline{i^2_{\text{SN, A}}} + \overline{i^2_{\text{SN, B}}}$, which is

$$\overline{i^2_{\text{SN, tot}}} = 2\eta q^2\frac{|\mathcal{A}|^2\Delta f}{hv} + 2\eta q^2\frac{|\mathcal{B}|^2\Delta f}{hv} = \frac{2\eta q^2\Delta f}{hv}(|\mathcal{A}|^2 + |\mathcal{B}|^2).^{12} \tag{2.37}$$

The homodyne power SNR is then:

$$\text{SNR} = \frac{\overline{i^2_{\text{BPD}}}}{\overline{i^2_{\text{SN, tot}}}} = \frac{4\frac{\eta^2 q^2}{h^2 v^2}|\mathcal{A}|^2|\mathcal{B}|^2}{\frac{2\eta q^2\Delta f}{hv}(|\mathcal{A}|^2 + |\mathcal{B}|^2)} = \frac{2\eta|\mathcal{A}|^2|\mathcal{B}|^2}{hv\Delta f(|\mathcal{A}|^2 + |\mathcal{B}|^2)}. \tag{2.38}$$

For the large local oscillator limit, we assume that $|\mathcal{B}|^2 \gg |\mathcal{A}|^2$:[13]

$$\text{SNR} = \frac{2\eta|\mathcal{A}|^2}{hv\Delta f} = \frac{2\eta P_A}{hv\Delta f} \approx 2\eta N, \tag{2.39}$$

where $P_A = |A|^2$, which is the power of the signal A, and N is the number of signal photons. This is the typical expression for the homodyne SNR. In this limit, it is notable that the SNR no longer scales with the size of the local oscillator; no increase in the LO strength will aid in enhanced SNR. However, there may be technical reasons to increase the LO strength if one is limited by classical noise, such as thermal noise or other electronic noise. One also may notice that in a 1 Hz bandwidth (approximately 1 s measurement time), the SNR is nearly twice the number of photons

---

[12] Note that we use the convention that field units are in square root power, or square root Watts.

[13] It is interesting to explore how much larger the LO must be than the signal to maintain the typical properties of homodyne. I discuss this in Chapter 4.

detected–usually a very large number. This gives a sense of how sensitive homodyne in the large LO limit can be.

One can also already see that the SNR equation may not be constant with respect to time when dealing with non-CW states of light (i.e., $\mathcal{A}(t) \neq \mathcal{A}_0$), and perhaps sometimes the large LO limit is satisfied and sometimes it is not. In fact, this temporal dependence results in important differences in the optimal signal processing of homodyne and heterodyne for optical frequency combs that I address in Chapter 4.

2.4.1.2 Heterodyne

In the heterodyne case the carriers do not cancel and the current is:

$$i_{\text{BPD}}(t) \propto \mathcal{A}(t)\mathcal{B}^*(t)e^{-i\Delta\omega t} + \mathcal{A}^*(t)\mathcal{B}(t)e^{i\Delta\omega t}. \tag{2.40}$$

We make the same assumption as in homodyne, that for a real envelope (such as the case of no chirp), the current is

$$i_{\text{BPD}}(t) \propto \mathcal{A}(t)\mathcal{B}(t)e^{-i\Delta\omega t} + \mathcal{A}(t)\mathcal{B}(t)e^{i\Delta\omega t}. \tag{2.41}$$

and in the case of two CW lasers with average field stengths $\mathcal{A}_0$ and $\mathcal{B}_0$, this is

$$i_{\text{BPD}}(t) \propto \mathcal{A}\mathcal{B}e^{-i\Delta\omega t} + \mathcal{A}\mathcal{B}e^{i\Delta\omega t} = 2\mathcal{A}\mathcal{B}\cos{(\Delta\omega t)}. \tag{2.42}$$

We are interested in the average power of this signal:

$$\overline{i_{\text{BPD}}(t)} = 4\frac{\eta^2 q^2}{h^2 v^2}|\mathcal{A}|^2|\mathcal{B}|^2\overline{\cos{(\Delta\omega t)}^2} = 2\frac{\eta^2 q^2}{h^2 v^2}|\mathcal{A}|^2|\mathcal{B}|^2 \tag{2.43}$$

The power SNR for heterodyne is then:

$$\text{SNR} = \frac{\overline{i^2_{\text{BPD}}}}{i^2_{\text{SN, tot}}} = \frac{2\frac{\eta^2 q^2}{h^2 v^2}|\mathcal{A}|^2|\mathcal{B}|^2}{\frac{2\eta q^2 \Delta f}{hv}(|\mathcal{A}|^2 + |\mathcal{B}|^2)} = \frac{\eta|\mathcal{A}|^2|\mathcal{B}|^2}{hv\Delta f(|\mathcal{A}|^2 + |\mathcal{B}|^2)}. \tag{2.44}$$

Again assuming the large local oscillator limit:

$$\text{SNR} = \frac{\eta|\mathcal{A}|^2}{hv\Delta f} = \frac{\eta P_A}{hv\Delta f} \approx \eta N. \tag{2.45}$$

One can observe that the SNR of heterodyne is the same as that of homodyne, but worse by a factor of 2. This arose in the classical derivation above from averaging over a time-varying cosine. In Chapter 4 I will discuss a couple additional ways to understand this, including measurement on a different measurement basis or as additional vacuum states involved in the measurement.

I also note that there are a number of technical reasons to prefer heterodyne over homodyne. First, one does not need to exactly match the carrier frequency of the LO with the signal, which is technically demanding when the LO and the signal are generated by separate laser cavities. Second, the electronic noise of the measurement equipment typically falls off beyond a MHz, meaning that much quieter measurement can be made at higher RF frequencies. The impacts of shot noise-limited heterodyne on fractional instability, i.e., Allan variance, are shown in App. C.

Chapter 3

Dual-Comb Correlation Spectroscopy of Thermal Light

Throughout history, the detection of thermal light across the electromagnetic (EM) spectrum has been the principle means by which humans gather information about not only our world but also the cosmos. Up until the laser [32], sunlight was often the only means to obtain a “bright enough” light source. Early experiments by Isaac Newton (1643-1727) uncovering the ray optics of light used sunlight as light source [33]. The beginnings of spectroscopy also began with sunlight, as Joseph Fraunhofer (1787-1826) discovered spectral features on sunlight that he dispersed on optical prisms, motivating future work developing higher power optical gratings [34].

3.1 Astronomical Spectroscopy and Synthetic Aperture Imaging

In astronomy, the direct detection of photons coupled with the resolution of their spectra has been key to discoveries of the broadest scope and impact. Such measurements have led to breakthroughs such as the discovery of the galactic redshift and the expanding universe [35], the identification of quasars [36, 37], and the detection of Earth-like exoplanets and an abundance of solar systems very different than our own [38]. However, such direct detection measurements do not take advantage of the information held in the phase of the electromagnetic field of light.

In the past half century, radio astronomy instrumentation has provided a means to address this shortcoming and take advantage of this phase [39, 40]. Most significantly, the heterodyne detection of thermal EM fields relative to a common phase reference enables the reconstruction of images with improved angular resolution from arrays of telescopes arranged over long baselines. Such synthetic aperture telescopes have yielded astonishing results such as the resolution of radiation emanating around the event horizon of a black hole [41].

In similar fashion, direct interferometry with light collected at distributed apertures, as originally demonstrated by Michelson [42], yields benefits in imaging resolution, with coverage extending into the visible region of the EM spectrum. Today, baselines may cover hundreds of meters, including Michelson stellar interferometer-based telescopes such as the Center for High Angular Resolution Astronomy (CHARA) array on Mt. Wilson [43] and the Navy Precision Optical Interferometer (NPOI) at Lowell Observatory's Anderson Mesa site [44].

3.1.1 Frequency Combs in Phase-Coherent Thermal Sensing

However, these powerful phase-coherent imaging techniques have largely been disconnected from tremendous advances in the generation of, and measurement with, coherent laser light. For example, the most stable optical oscillators and clocks now have sub-cycle attosecond coherence over extended timescales [45]. Furthermore, this level of coherence and timing precision can be distributed over hundreds of kilometers in free space and thousands of kilometers in fiber [15, 46, 16]. And optical frequency combs allow one to coherently synthesize and broadcast this coherence from the radio to the optical domain, encompassing hundreds of terahertz of the EM spectrum [47]. Critically, phase-coherent optical imaging requires reconstruction at the sub-optical wavelength level, and these advancements could be foundational for phase-coherent optical imaging and spectroscopy over baselines of kilometers or more and across many sites.

Stellar imaging based on optical-heterodyne (i.e., optical antennas) may enable high resolution imaging that existing telescopes cannot reach. For example, standard telescopes must increase in size to resolve smaller objects in the sky; but as telescopes grow, mirrors must be kept at submicron tolerances across many meters–which quickly increases costs to unmanageable levels. In fact, estimates show that costs scale as the diameter to the 2.5 power [48]. Currently under construction is the Extremely Large Telescope with a diameter of 39.3 meters, estimated to cost over 1 billion USD.

As mentioned, Michelson stellar interferometer-based telescopes can reach longer baselines up to hundreds, or perhaps thousands of meters. However, maintaining path lengths at this scale becomes increasingly challenging. In addition, stellar interferometers must physically split the light, imposing a penalty on the number of sites that compose the array [49, 50].

At optical wavelengths, phase sensitive measurement must occur through a laser heterodyne process–analogous to a super-heterodyne radio receiver. In optical astronomy, this has occurred through a technique called laser heterodyne radiometry (LHR), referring to a continuous-wave (CW) laser that heterodynes with thermal light. However, since optical frequencies and bandwidths are so much larger than their radio counterparts, the fraction of thermal light measured through conventional LHR is very small compared to the bandwidths of interest. For example, a high speed balanced detector may have a bandwidth of 5 GHz. This leads to a total measurement bandwidth of 10 GHz of thermal light (Fig. 3.1a). In units of wavelength, this is less than 0.1 nm at 1550 nm. But there are many features of interest that may span hundreds of nanometers. For example the Sun exhibits thousands of iron lines arising from the energetic transitions of differing iron ions and angular momenta across its spectrum. Between 1 and 2 µm, neutral and single ionized iron exhibit hundreds of lines [51, 52], with different susceptibilities to the complex magneto-hydrodynamics around the surface of the sun that may prove crucial to disentangling solar dynamics from exoplanet-induced red shifts.

Here, we aim to harness the aforementioned revolutionary attributes of laser light and understand their optimal application to the phase-coherent heterodyne detection of broad bandwidth EM fields of thermal origin. Specifically, we demonstrate and analyze the implementation of a frequency-comb local oscillator in the coherent detection of thermal light. Instead of a single local oscillator, the frequency comb provides thousands of local oscillators for heterodyne detection (Fig. 3.1a). This provides the opportunity for a significant expansion of the detection bandwidth, $\Delta\nu$, and the associated improvement in quantum-limited signal-to-noise ratio constrained by $\sqrt{\Delta\nu}$ [53].

There are several ways to use a frequency comb as an LO, which I discuss in later sections. In this work, I explore dual-comb correlation spectroscopy (DCCS-Fig. 3.1b), which allows for the capture of thermal light across optical bandwidths on the order of 100 GHz with balanced photodetection having only 50 MHz of electrical bandwidth. This significant simplification is enabled by the spectral compression and correlation of thermal heterodyne signals with two frequency combs that have slightly different mode spacing.

3.2 Overview

In this chapter, I theoretically define the sensitivity scaling and experimentally verify our model of DCCS on thermal light having power spectral density equivalent to a 5770 K black body ("Solar Planck limit"). I then provide a first-of-its-kind synthesis and comparative analysis of frequency comb-based spectroscopy of thermal light, and thereby evaluate the complex trade-space of SNR, instrument complexity, and technological maturity between DCCS and more conventional laser heterodyne radiometry (LHR) methods.

In providing the sensitivity limits and technical context for optical-frequency-comb-based thermal spectroscopy with a single aperture, this work forms a crucial foundation for future work analyzing long-baseline hyperspectral imaging at frequencies in the range of ∼20 to 300 THz. This work may most directly impact astronomical imaging [50], but it could also impact more general scenarios in the coherent detection of thermal radiation. These scenarios include remote sensing, trace gas detection, and atmospheric science [54] (Fig. 3.1c), particularly leveraging the low size, weight, power, and cost (SWaP-C) offered by emerging photonics and electronics platforms [55] (Fig. 3.1d). In addition DCCS may be particularly useful for applications requiring high spectral resolution but a compact footprint (e.g., low SWaP-C), since other techniques such as Michelson interferometer-based Fourier transform spectrometers and grating monochromators must grow in size and complexity in order to reach higher resolutions such as 100 MHz resolution.[1]

---

[1] In contrast, increased resolution in DCCS relies solely on increasing the cavity length of the frequency comb oscillator, which is straightforward for current fiber-based mode-locked (frequency comb) laser oscillators. This is the same advantage as conventional dual-comb spectroscopy [17], but DCCS is passive instead of direct, meaning that this technique senses ambient thermal light instead of requiring laser light to pass through the sample of interest.

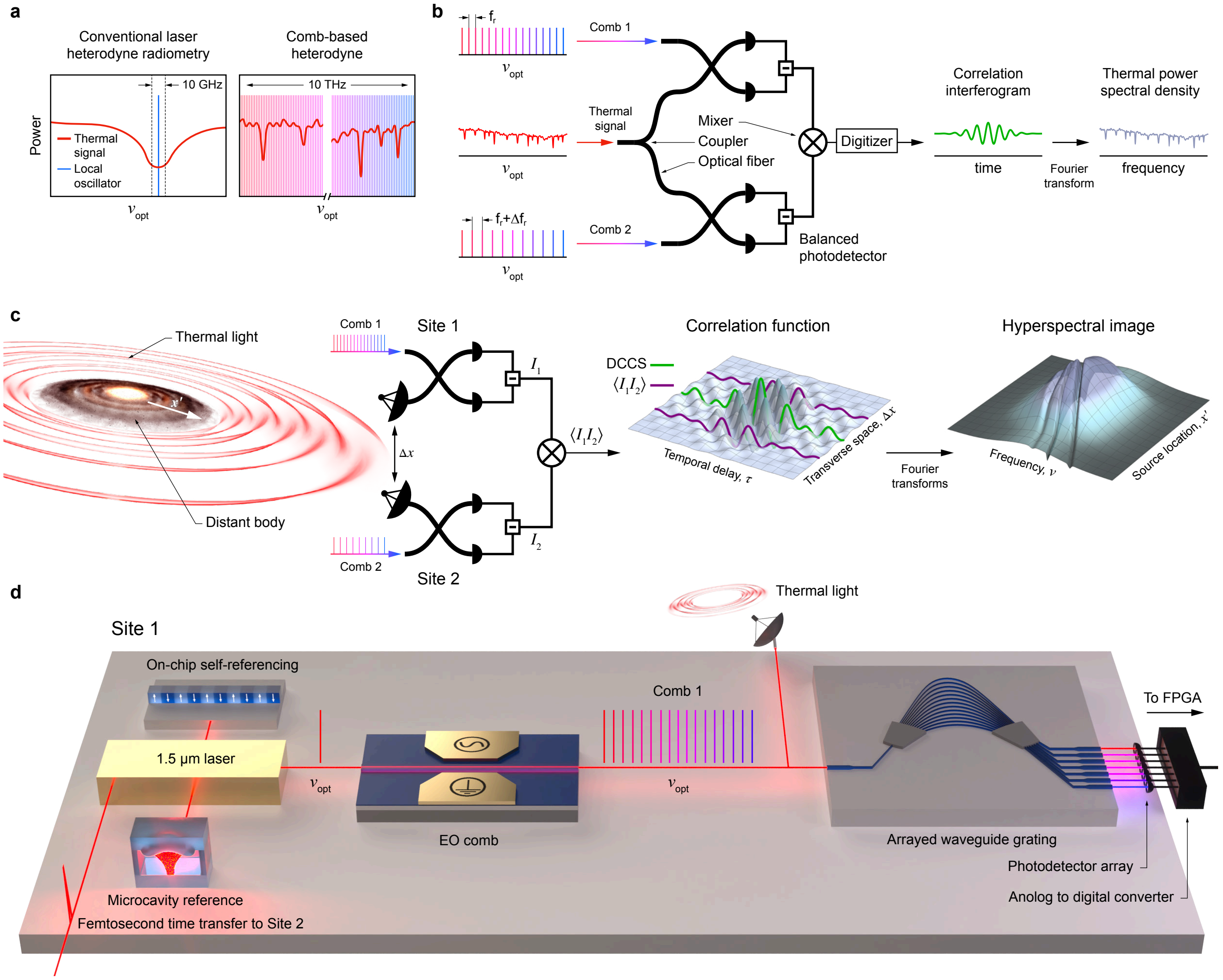

Figure 3.1: Dual-comb correlation spectroscopy and its applications and enabling technologies. **a**, Compared to conventional laser heterodyne radiometry (LHR) with a continuous-wave local oscillator (LO), a frequency comb LO provides 1000× greater bandwidth–e.g., 10+ THz versus 10 GHz, capturing many features and photons across broad optical bandwidths **b**, In DCCS, thermal light is split then separately interfered with two mutually coherent frequency combs with offset repetition rates. The resulting photocurrents are mixed, and averaging the mixer output reveals a correlation interferogram. A Fourier transform then reveals the spectrum of the thermal light. **c**, Dual-comb correlation is fundamentally a means to measure correlations between broadband optical fields. For example, it can measure spatial-temporal correlation functions and enable high angular resolution hyperspectral synthesis imaging. **d**, Advances in integrated photonics may enable robust and portable comb-based high-resolution spectroscopy and optical synthesis imaging. Key technologies include low SWaP-C chip-integrated combs, compact optical cavities, integrated nonlinear photonics, telecom arrayed waveguide gratings, fast photodetector arrays, heterogenous integration, high speed data processing, and femtosecond time transfer.

3.3 Prior Work

Earlier work by teams at the University of Laval (Boudreau and Genest) [20], and NIST (Giorgetta et al.) [19] first showed the feasibility of DCCS, showing that combs with offset repetition rates could auto-correlate thermal light and produce a first order correlation interferogram, $g^{(1)}$, and the corresponding power spectrum. These works found that at high thermal powers[2] , the single-shot time domain signal-to-noise ratio (SNR) approached 1. Boudreau and Genest examined the necessary conditions for this high power, unity SNR regime, showing when the signal strength would be much greater than shot and technical noise [20]. However, the fundamental scaling of DCCS at realistically weak thermal powers (corresponding to realistic astrophysical black bodies) remained unexplored.

3.4 Fundamentals of Thermal Light

What is thermal light? Although its name refers to a typical source of thermal light: a black body at some finite temperature, thermal light as a term is often used to describe the more general state of light called chaotic light, which arises in many additional scenarios from other kinds of sources. In a sense, thermal or chaotic light is defined by its first- and second-order coherence, which I will cover in the following sections.

However, in our case, we really are interested in light emitted by black bodies (thermal light of thermal origin), and in order to understand the strength and wavelength dependence of this thermal light, a brief review of the Planck distribution (governing relationship between temperature, brightness, and wavelength) is required.

Heterodyne detection of thermal light also imposes limits on the amount of thermal light available from any black body. This is described by the optical antenna theorem. The optical antenna theorem coupled with the Planck distribution dictate the maximum power spectral density

---

[2] Since these papers were initial demonstrations, they did not explicitly list the actual power spectral density of the thermal light they used. However, in the case of [19], the SNR achieved corresponds to largely un-physical blackbody temperatures of tens to hundreds of thousands of Kelvin and a PSD approximately 1000x higher than we measure here. In the case of [20], the authors claim that the thermal light used was increased beyond a few uW, which is also approximately 1000x higher than the demonstration here.

available for heterodyne measurements with a laser, which I derive here.

Lastly, I highlight the defining photon statistics of thermal light and discuss how the statistics are also influenced by the interval over which the state is defined. In doing so, I seek to answer the following question: What is the boundary between coherent and thermal light?

3.4.1 Origins of Thermal and Chaotic Light

Chaotic light[3] arises from the uncorrelated addition of many electromagnetic fields. Such a process, as I have mentioned, leads to Gaussian statistics through the Central Limit Theorem, which we will see shortly. One way to illustrate this is by modeling an ensemble of of n emitters of equal strength, emitting the summed field:

$$\begin{aligned} E(t) &= E_1(t) + E_2(t) + E_3(t) + ... + E_n(t) \\ &= E_0 e^{-i\omega_0 t}[e^{-i\phi_1(t)} + e^{-i\phi_2(t)} + ... + e^{-i\phi_n(t)}] = E_0 e^{-i\omega_0 t} a(t) e^{-i\phi(t)} \end{aligned} \tag{3.1}$$

where $a(t)$ and $\phi(t)$ are random amplitudes and phases. Each individual phase ϕ_j is random and uncorrelated with the next. This process is illustrated in phase space in Figure 3.2, representing 100 examples (to give a sense for the statistical distribution) of fields or trajectories formed from 2000 emitters or randomly phased steps.

For $n \gg 1$, the probability of the strength of the field within a region of unit area at $a(t)$ and $\phi(t)$ turns out, through the central limit theorem, to be Gaussian distributed about zero:

$$p[a(t)] = \frac{1}{\pi n} e^{\frac{-a(t)^2}{n}}, \tag{3.2}$$

and is independent of the phase $\phi(t)$. In fact, there is no defined phase for chaotic light. If we were to continue adding more example trajectories to Figure 3.2, we would see the distribution of the red Xs' distances from the origin approach this Gaussian distribution. Note that the specific line broadening mechanism (Gaussian or Lorentzian), or arbitrary shape of the spectrum, does not influence the eventual Gaussian distribution of the field amplitude around zero that is characteristic

---

[3] Discussion here of chaotic light borrows heavily from Rodney Loudon's book, *The Quantum Theory of Light* [56], chapter 3. This is an excellent reference.

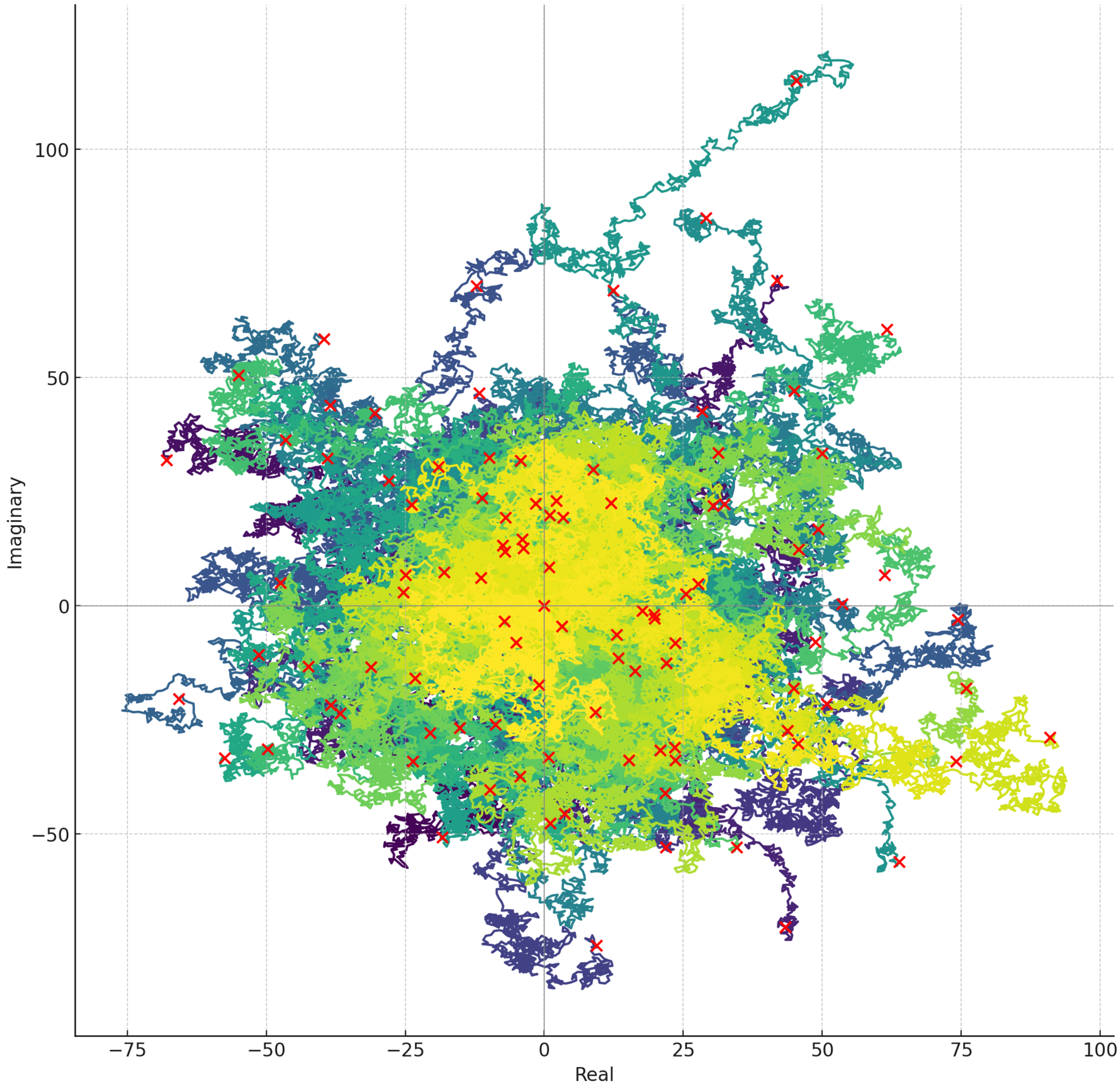

Figure 3.2: 100 example random walks/trajectories through complex phase space, where unit vectors with random phases are added. Red Xs mark the end points of the walk after 2000 steps, equivalent to 2000 emitters.

of chaotic and thermal light. The spectral width does, however, define the temporal window over which the light is chaotic–the light field must be defined at a scale longer than its coherence time, as I discuss in the next section.

Note also that the amplitude distribution of a thermal state is *not* Gaussian distributed, but Rayleigh distributed with a finite mean and higher order moments. This can be shown by integrating over the Gaussian distribution in the complex plane over all angles.

3.4.2 Statistics of Chaotic Light and Coherence Functions

The bandwidth and coherence time of chaotic light with a Gaussian frequency distribution (which again arises from the central limit theorem through the summation of random processes like Doppler broadening) are related by:

$$\tau_c = \frac{\sqrt{\pi}}{\Delta}, \tag{3.3}$$

where τ_c is the coherence time and Δ is the full-width half maximum of the Gaussian spectral line. Note that the coherence time is a measure of the first order coherence of light and is defined as the time delay at which $\frac{1}{e}g^{(1)}(\tau_c) = g^{(1)}(0)$, which we define now.

The first-order coherence function is

$$g^{(1)}(\tau) = \frac{\langle E^*(t)E(t+\tau)\rangle}{\langle E^*(t)E(t)\rangle} \tag{3.4}$$

Note that in practice we assume the ergodic hypothesis–that averages in time are equivalent to ensemble averages. In this case, the expectation value symbols $\langle\ \rangle$ can refer to either an ensemble average, or, for example in dual-comb spectroscopy [17] or Fourier transform spectroscopy[57], the average as delays are swept in a periodic fashion. For coherent light,

$$g^{(1)}(\tau)_{\text{coh}} = e^{i\omega_0 t}. \tag{3.5}$$

For Gaussian broadened chaotic light,

$$g^{(1)}(\tau)_{\text{cha}} = e^{i\omega_0 t - \frac{\pi}{2}(\frac{\tau}{\tau_c})^2}. \tag{3.6}$$

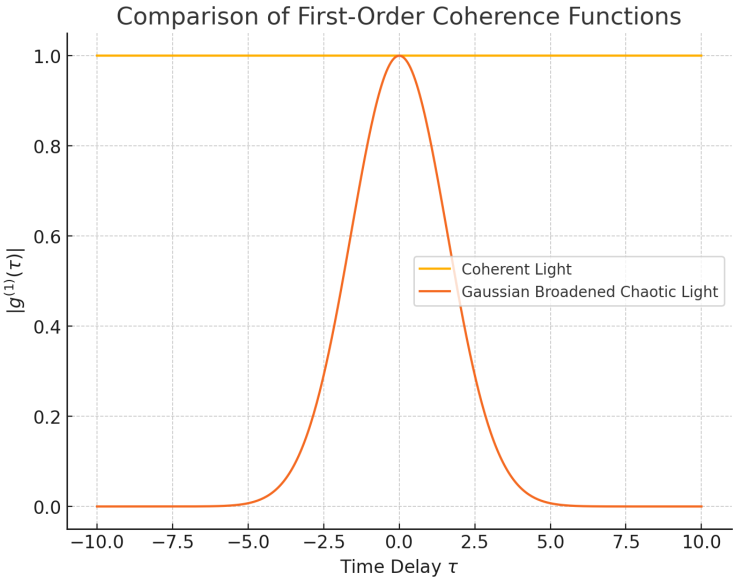

Figure 3.3: Examples of $|g^{(1)}(\tau)|$ for coherent light and Gaussian broadened chaotic light.

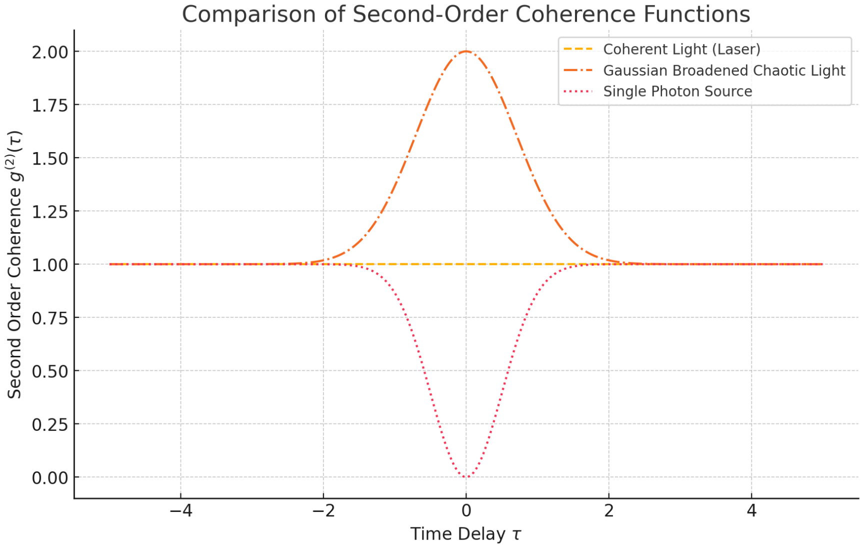

Figure 3.4: Examples of $g^{(2)}(\tau)$ for coherent light, Gaussian broadened chaotic light, and sub-Poissonian light from, for example, a single photon emitter.

Examples are shown in Figure 3.3.

The second order coherence function of light is defined as:

$$g^{(2)}(\tau) = \frac{\langle I(t)I(t+\tau)\rangle}{\langle I\rangle^2} = \frac{\langle I(t)I(t+\tau)\rangle}{\langle I\rangle^2} = \frac{\langle E^*(t)E(t)E^*(t+\tau)E(t+\tau)\rangle}{\langle E^*(t)E(t)\rangle}^2, \tag{3.7}$$

where $I(t) = |E(t)|^2$. For chaotic light,

$$g^{(2)}(\tau) = 1 + |g^{(1)}(\tau)|^2. \tag{3.8}$$

Later, I will show the consequences of this for the estimation of the first-order coherence function of thermal light. Since $g^{(2)}(0) = 2$, this is often called photon bunching or super-Poissonian. $g^{(2)}(0)$ for coherent light is one, thus indicating uncorrelated intensities and Poissonian statistics. And $g^{(2)}(0)$ for light from single quantum emitters can be zero, indicating anticorrelated intensities and sub-Poissonian statistics (see Figure 3.4).

3.4.2.1 Coherent Light vs. Chaotic Light

A question I have often wondered about is this: What is the difference between a laser and thermal or chaotic light. Brightness of light notwithstanding[4] , can I make "synthetic laser light" simply by spectrally filtering chaotic or thermal light? Illustrated in Figure 3.3, the transition between the first-order coherence properties of coherent and chaotic light appears to make this case–as the spectrum of chaotic light is narrowed and the coherence time increased, the chaotic light will continue to approach the behavior of coherent light. However, the second-order coherence seen in Fig. 3.4 exhibits a clear discontinuity between coherent and thermal light that does not seem to be rectified simply by increasing the coherence time. No amount of spectral narrowing will make the second-order coherence of chaotic light move to 1 at $\tau = 0$.

However, this kind of thinking is misleading. A major definition that has been swept under the rug here–but comes to the forefront in the definition of quantum states of light–is the time over which the state is defined. In our definitions here, a coherent state is "defined" to be coherent within the temporal window of interest. For a chaotic or thermal state, we have "defined" it to be incoherent, and thus the temporal window over which it exists must extend much longer than its coherence time. This essentially sets the samples over which the expectation values are assessed–and indeed, these samples show bunching behavior because we are sampling over a long enough time period for the bunching behavior to be exhibited. Another way of thinking about this is the following: the canonical thermal state has no defined phase. Yet we know that all classical light has a phase and that the phase can be defined within a coherence time. Thus, the thermal state *must* be defined over a temporal window much longer than its coherence time to be phase-less.

3.4.3 Planck's Law

The radiance of black body radiation is governed by the Planck distribution. The familiar form derived in coursework is the spectral radiance in units of Watts per steradian per square meter

---

[4] Laser light, in a single spatial and polarization mode, and in some narrow spectral bandwidth, is incredibly bright compared to black body radiation.

per Hertz:

$$B(\nu,T) = \frac{2h\nu^3}{c^2}\frac{1}{e^{\frac{h\nu}{kT}}-1}. \tag{3.9}$$

Ultimately we are interested in how much of this black body radiation we can heterodyne with our laser local oscillator, so we need to manipulate this formula. The total *power* emitted into a hemisphere across a bandwidth $\Delta\nu$ and from a small section of area ΔA on the black body is:

$$\Delta P(\nu,T) = \pi B(\nu,T)\Delta\nu\Delta A = \frac{2\pi}{\lambda^2}\frac{h\nu\Delta\nu}{e^{h\nu/kT}-1}\Delta A, \tag{3.10}$$

where π is the projected solid angle onto a hemisphere. Given a receiving aperture of A_R at a distance R from the black body, the solid angle subtended by this aperture is A_R/R^2. The power per steradian emitted normal to the surface is a factor $1/\pi$ lower, and we consider only half of this light for a single polarization. Incoherent addition means that the powers from different parts of the black body add, and the section of the black body in the field of view of the receiver is $R^2\Omega_R$, where Ω_R is the angular field of view. The power from the black body imaged by the optical system is then:

$$P_{\text{sig}} = \frac{1}{2}\frac{A_R}{\pi R^2}\frac{2\pi}{\lambda^2}\frac{h\nu\Delta\nu}{e^{h\nu/kT}-1}R^2\Omega_R = \frac{A_R\Omega_R}{\lambda^2}\frac{h\nu\Delta\nu}{e^{h\nu/kT}-1} \tag{3.11}$$

3.4.4 Optical Antenna Theorem and Planck Law-limited Power Spectral Density

The optical antenna theorem, or more generally, the antenna aperture theorem for microwave antennas, states that the angular field of view and the effective aperture are constrained by the wavelength of the captured or transmitted radiation. This can be written as:

$$A_R\Omega_R = \lambda^2. \tag{3.12}$$

Substituting this into Equation 3.4.3, the power of the signal is:

$$P_{\text{sig}} = \frac{h\nu\Delta\nu}{e^{h\nu/kT}-1}. \tag{3.13}$$

We can rewrite this expression in terms of the photon occupancy $\langle n \rangle$, or equivalently the number spectral density in a single spatial and polarization mode from a resolved black body. This results in:

$$\langle n \rangle = (\exp[h\nu/kT] - 1)^{-1}, \tag{3.14}$$

where the power spectral density in W/Hz is $h\nu\langle n \rangle = P_{\text{sig}}/\Delta\nu$. One sees that this expression is merely a function of the frequency of light ν in Hz and the temperature of the black body T in K. One might think that the size of the black body should matter, since more photons should be emitted by more atoms, or that if one had an infinite diameter lens one could always retrieve more light. While these are both true in a sense, this derivation shows that there is a fundamental limit on capturing light of a single mode from a black body, such that once the distant black body is resolved, the power spectral density is solely constrained by the Bose-Einstein distribution factor dependent on wavelength and temperature.

3.5 Fundamental Sensitivity Limits of Dual-Comb Correlation Spectroscopy

3.5.1 Principle of Operation: First-Order Correlation and Wiener-Khintchine Theorem

DCCS, (as well as Fourier transform spectroscopy, and dual-comb spectroscopy) all rely on the Wiener-Khintchine theorem described in the technical introduction. There, we observed that:

$$S(\nu) = \int_{-\infty}^{\infty} R(\tau) e^{-i2\pi\nu\tau} d\tau, \tag{3.15}$$

where

$$R(\tau) = \langle x(t)x(t+\tau) \rangle. \tag{3.16}$$

These techniques seek to measure the first-order correlation function $R(\tau)$, then take the Fourier transform to reach the power spectral density $S(\nu)$.

3.5.2 Statistical Limit of Single-Shot Time Domain Signal-to-Noise Ratio

The time domain signal is the mean of the auto-correlation function of the electric field:

$$A(\tau_d) = \frac{1}{t_{\text{tot}}} \int_t dt E^*(t) E(t - \tau_d), \tag{3.17}$$

and the time domain noise is the variance of the auto-correlation function of the electric field:

$$N(\tau) = \frac{1}{t_{\text{tot}}} \int_t dt [E^*(t) E(t - \tau_d) - A(\tau_d)]^2. \tag{3.18}$$

Ultimately, we care about the power spectral density determined by the time-domain interferogram, which can be expressed through the Wiener-Khinchin theorem:

$$S(f) = \int_{-\infty}^{\infty} d\tau e^{-2\pi i f \tau_d} R(\tau_d), \tag{3.19}$$

where

$$R(\tau_d) = A(\tau_d) \pm \sqrt{\frac{N(\tau_d)}{\mathcal{N}}}. \tag{3.20}$$

$R(\tau_d)$ is the captured interferogram, $\sqrt{N(\tau_d)}$ is the standard deviation, and $\mathcal{N}$ is the number of trials. However, here we simply compute the time domain SNR. The frequency domain SNR is computed in a following section. As $\mathcal{N} \to \infty$, $R(\tau) \to A(\tau)$. We now analyze the case of SNR for one trial. The single shot SNR is:

$$\text{SNR}_s(\tau_d) = \frac{A(\tau_d)}{\sqrt{N(\tau_d)}} \tag{3.21}$$

Note that:

$$A(\tau_d) = g^{(1)}(\tau_d) \times \langle |E(t)|^2 \rangle = g^{(1)}(\tau_d) \times \langle I \rangle. \tag{3.22}$$

Here we define $g^{(1)}(\tau_d) = \frac{\langle E^*(t) E(t+\tau_d) \rangle}{\langle |E(t)|^2 \rangle}$, $g^{(2)}(\tau_d) = \frac{\langle I^*(t) I(t+\tau_d) \rangle}{\langle |I(t)| \rangle^2}$, and $I \propto |E|^2$. The variance is the expected value of the squared deviation from the mean:

$$N(\tau_d) = \langle (E^*(t) E(t - \tau_d) - A(\tau_d))^2 \rangle = \langle (E^*(t) E(t - \tau_d))^2 \rangle - \langle 2(E^*(t) E(t - \tau_d) A(\tau_d) \rangle + \langle A(\tau_d)^2 \rangle, \tag{3.23}$$

simplifying:

$$N(\tau_d) = \langle (I^*(t) I(t - \tau_d) \rangle - \langle A(\tau_d))^2 \rangle = \langle I \rangle^2 (g^{(2)}(\tau_d) - g^{(1)}(\tau_d)^2). \tag{3.24}$$

Thus,

$$\mathrm{SNR}_s(\tau_d) = \frac{g^{(1)}(\tau_d)}{\sqrt{g^{(2)}(\tau_d) - g^{(1)}(\tau_d)^2}} \tag{3.25}$$

For thermal light, we know that:

$$g^{(2)}(\tau_d) = 1 + g^{(1)}(\tau_d)^2 \tag{3.26}$$

Thus,

$$\mathrm{SNR}_{s,th}(\tau_d) = \frac{g^{(1)}(\tau_d)}{\sqrt{1 + g^{(1)}(\tau_d)^2 - g^{(1)}(\tau_d)^2}} = g^{(1)}(\tau_d). \tag{3.27}$$

At the zero delay point ($\tau_d = 0$), the single-shot SNR is 1 and falls off to 0 as a function of $g^{(1)}$ or the spectral lineshape and width.

3.5.3 Derivation of Dual-Comb Correlation SNR vs. PSD

In order to derive the SNR of DCC on thermal light we first find the heterodyne powers between a coherent LO (CW or comb) and thermal light. Note that we interchangeably use the terms ASE, thermal light, and chaotic light.

3.5.3.1 CW Laser and Thermal Light Heterodyne

Before deriving the heterodyne power between a comb LO and thermal light, we first re-derive the heterodyne power between a CW LO and thermal light. To our knowledge, this equation was first derived by N.A. Olsson in 1989 [58] and A. Yariv in 1990 [59]. Both authors were motivated by the presence of amplified spontaneous emission in optical communications.

Following Olsson, we first rederive the heterodyne level of a CW laser with ASE in our own notation. We will maintain this notation as we derive the comb and ASE case as well as the dual-comb correlation measurement of ASE. P_t is the power of the CW laser or a single comb tooth. S is the power spectral density of the ASE or quasi-thermal light source. B_o is the total optical bandwidth over which the comb tooth heterodynes with the ASE light, equivalent to twice the detector bandwidth (see Fig. 3.5).

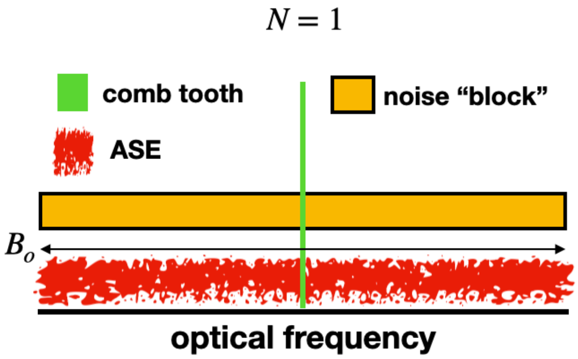

Figure 3.5: Frequency domain picture of ASE and single comb tooth (CW).

We represent the electric field (expressed in root power) of the ASE light as:

$$E_{\text{ASE}}(t) = \sum_{k=-B_o/2\delta\nu}^{B_o/2\delta\nu} \sqrt{2S\delta\nu} \times \cos((\omega_o + 2\pi k \delta\nu)t + \Phi_k), \tag{3.28}$$

where the average power in a chunk of ASE is $S\delta\nu$, and $\delta\nu$ is a small frequency slice. ω_o is the optical frequency of one comb tooth. Φ_k is a random phase. t is time. Note that the mean square of the electric field of the ASE is the average power: $SB_o = P_{\text{avg, ASE}}$. The electric field of the CW laser or one tooth of the comb light is:

$$E_t(t) = \sqrt{2P_t} \cos(\omega_o t + \Theta). \tag{3.29}$$

Θ is the phase of this comb tooth. Note that the mean square of the comb tooth/CW field is also the average power: $P_t = P_{\text{avg, CW}}$. The optical power incident on the detector is then the square of the sum of the two fields:

$$P(t) = (\sum_{k=-B_o/2\delta\nu}^{B_o/2\delta\nu} \sqrt{2S\delta\nu} \times \cos((\omega_o + 2\pi k \delta\nu)t + \Phi_k) + \sqrt{2P_t} \cos(\omega_o t + \Theta))^2. \tag{3.30}$$

We ignore the products between the laser with itself and the ASE with itself. Note the laser self-heterodyne will result in a DC component and a very high optical frequency component, both of which can be ignored. We will assume a large LO limit for the laser, so the self heterodyne of the ASE will be negligible compared to the laser-ASE heterodyne. We then ignore the sum components of the heterodyne oscillating at frequencies around 2ω far beyond our detector bandwidth. The resulting optical power for the difference components is:

$$2\sqrt{2S\delta\nu 2P_t}\sum_{k=-B_o/2\delta\nu}^{B_o/2\delta\nu}\frac{1}{2}\cos(2\pi k\delta\nu t+\Phi_k-\Theta). \tag{3.31}$$

The photocurrent is then:

$$i(t)=\frac{\eta e}{h\nu}\sqrt{2S\delta\nu 2P_t}\sum_{k=-B_o/2\delta\nu}^{B_o/2\delta\nu}\cos(2\pi k\delta\nu t+\Phi_k-\Theta), \tag{3.32}$$

where η is the quantum efficiency of the detector, e is the elementary charge, and $h\nu$ is the energy per photon. We're interested in the noise power of the photocurrent, and when multiplying the cosine terms of the sum, we add each product in quadrature due to the random phases of Φ_k.

$$\langle i(t)^2\rangle=\left(\frac{\eta e}{h\nu}\sqrt{2S\delta\nu 2P_t}\right)^2\times\left(\sqrt{2\times\frac{B_o}{2\delta\nu}}\right)^2\times\frac{1}{2}. \tag{3.33}$$

The second product term is the square root (due to quadrature addition) of the number of products between the different cosine functions. The third product term, $\frac{1}{2}$, is the average of the square of cosine. We simplify further:

$$\langle i(t)^2\rangle=\frac{\eta^2e^2}{(h\nu)^2}\times 4S\delta\nu P_t\times 2\times\frac{B_o}{2\delta\nu}\times\frac{1}{2}. \tag{3.34}$$

We then cancel terms terms:

$$\langle i(t)^2\rangle=2\frac{\eta^2e^2}{(h\nu)^2}SP_t\times B_o. \tag{3.35}$$

This current folds uniformly into a bandwidth of $B_o/2$, hence we divide by this bandwidth to extract the power spectral density:

$$\langle i(t)^2\rangle_{\text{PSD,CW}}=4\frac{\eta^2e^2}{(h\nu)^2}SP_t. \tag{3.36}$$

3.5.3.2 Comb and Chaotic Light Heterodyne

For the case of the frequency comb heterodyning with ASE, we can simply multiply the single tooth PSD by the number of comb teeth N. The power spectral density is:

$$\langle i(t)^2\rangle_{\text{PSD,Comb}}=4\frac{\eta^2e^2}{(h\nu)^2}SP_tN=4\frac{\eta^2e^2}{(h\nu)^2}SP_c. \tag{3.37}$$

Here P_c is the total comb power. While this may make intuitive sense, we supply the following step-by-step derivation.

To move to the power spectral density of the comb heterodyne, we define the field of the comb as a sum over the N comb teeth:

$$E_c(t) = \sum_{n=1}^{N} \sqrt{2P_t} \cos(\omega_n t + \Theta_n), \tag{3.38}$$

where Θ_n is an arbitrary phase. Each tooth is spaced $B_o/2$ away from the adjacent teeth, i.e., $\omega_1 - \omega_0 = f_r = B_o/2$ and follows the comb equation $\omega_n = n_c \times \omega_r + \omega_0$. Across this bandwidth, the ASE can be represented as:

$$E_{\text{ASE, tot}}(t) = \sum_{m=1}^{N} \sum_{k=-B_o/4\delta\nu}^{B_o/4\delta\nu} \sqrt{2S\delta\nu} \times \cos((\omega_m + 2\pi k\delta\nu)t + \Phi_{k,m}), \tag{3.39}$$

where $\Phi_{k,m}$ is a random phase. Note that our ASE bins are defined from $-B_o/4$ to $B_o/4$, or $-f_r/2$ to $f_r/2$. This choice of bin size counts the ASE exactly once. The photodetected power is then:

$$P_{\text{comb, ASE}}(t) = \left(\sum_{n=1}^{N} \sqrt{2P_t} \cos(\omega_n t + \Theta_n) + \sum_{m=1}^{N} \sum_{k=-B_o/4\delta\nu}^{B_o/4\delta\nu} \sqrt{2S\delta\nu} \times \cos((\omega_m + 2\pi k\delta\nu)t + \Phi_{k,m}) \right)^2 \tag{3.40}$$

We expand this to:

$$\begin{aligned} P_{\text{comb, ASE}}(t) = &\left(\sum_{n=1}^{N} \sqrt{2P_t} \cos(\omega_n t + \Theta_n) \right)^2 \\ &+ 2 \sum_{n=1}^{N} \sqrt{2P_t} \cos(\omega_n t + \Theta_n) \times \sum_{m=1}^{N} \sum_{k=-B_o/4\delta\nu}^{B_o/4\delta\nu} \sqrt{2S\delta\nu} \times \cos((\omega_m + 2\pi k\delta\nu)t + \Phi_{k,m}) \\ &+ \left(\sum_{m=1}^{N} \sum_{k=-B_o/4\delta\nu}^{B_o/4\delta\nu} \sqrt{2S\delta\nu} \times \cos((\omega_m + 2\pi k\delta\nu)t + \Phi_{k,m} \right)^2. \end{aligned} \tag{3.41}$$

As before, only the heterodyne difference frequency terms remain after squaring:

$$P_{\text{comb, ASE, dif}}(t) = 2\sqrt{2P_t 2S\delta\nu} \sum_{n=1}^{N} \sum_{m=1}^{N} \sum_{k=-B_o/4\delta\nu}^{B_o/4\delta\nu} \frac{1}{2} \cos((\omega_n - \omega_m)t - 2\pi k\delta\nu t + \Theta_n - \Phi_{k,m}). \tag{3.42}$$

Given a detector RF bandwidth of $B_o/2 = f_r$, we note that a single f_r-sized bin of ASE does not heterodyne with all the comb teeth; instead, it heterodynes with the comb tooth that splits it and also the comb tooth at its upper edge and its lower edge. We can thus split the above power into three components:

$$P_{\text{comb, ASE, dif, three}}(t) = \sqrt{2P_t 2S\delta\nu}\Bigg(\sum_{n=1,m=n}^{N} \sum_{k=-B_o/4\delta\nu}^{B_o/4\delta\nu} \cos((\omega_n - \omega_m)t - 2\pi k\delta\nu t + \Theta_n - \Phi_{k,m}) + \sum_{n=1,m=n+1}^{N-1} \sum_{k=-B_o/4\delta\nu}^{0} \cos((\omega_n - \omega_m)t - 2\pi k\delta\nu t + \Theta_n - \Phi_{k,m}) + \sum_{n=2,m=n-1}^{N} \sum_{k=0}^{B_o/4\delta\nu} \cos((\omega_n - \omega_m)t - 2\pi k\delta\nu t + \Theta_n - \Phi_{k,m})\Bigg). \tag{3.43}$$

Next, we turn the power into a photocurrent:

$$i_{\text{comb,ASE}}(t) = \frac{\eta e}{h\nu}\sqrt{2P_t 2S\delta\nu}\Bigg(\sum_{n=1,m=n}^{N} \sum_{k=-B_o/4\delta\nu}^{B_o/4\delta\nu} \cos((\omega_n - \omega_m)t - 2\pi k\delta\nu t + \Theta_n - \Phi_{k,m}) + \sum_{n=1,m=n+1}^{N-1} \sum_{k=-B_o/4\delta\nu}^{0} \cos((\omega_n - \omega_m)t - 2\pi k\delta\nu t + \Theta_n - \Phi_{k,m}) + \sum_{n=2,m=n-1}^{N} \sum_{k=0}^{B_o/4\delta\nu} \cos((\omega_n - \omega_m)t - 2\pi k\delta\nu t + \Theta_n - \Phi_{k,m})\Bigg). \tag{3.44}$$

Because there are no correlated phases here[5] , we take the root mean square of cosine and sum in quadrature:

$$\sqrt{\langle i_{\text{comb, ASE}}(t)^2\rangle} = \frac{\eta e}{h\nu}\sqrt{2P_t 2S\delta\nu}\frac{1}{\sqrt{2}}\left(\sqrt{N\frac{B_o}{2\delta\nu}}^2 + \sqrt{(N-1)\frac{B_o}{4\delta\nu}}^2 + \sqrt{(N-1)\frac{B_o}{4\delta\nu}}^2\right)^{\frac{1}{2}}. \tag{3.45}$$

Note that the first term comes from the central tooth heterodyne and is distributed as white noise from DC to $B_o/4$. The next two terms are from the outer tooth heterodynes and are distributed from $B_o/4$ to $B_o/2$. In fact, these terms add to form a white noise floor from DC to $B_o/2$. Simplifying the equation:

$$\sqrt{\langle i_{\text{comb, ASE}}(t)^2\rangle} = \frac{\eta e}{h\nu}\sqrt{2P_t 2S\delta\nu}\frac{1}{\sqrt{2}}\left(N\frac{B_o}{2\delta\nu} + (N-1)\frac{B_o}{2\delta\nu}\right)^{\frac{1}{2}}. \tag{3.46}$$

Simplifying further:

$$\sqrt{\langle i_{\text{comb, ASE}}(t)^2\rangle} = \frac{\eta e}{h\nu}\sqrt{2P_t 2S\delta\nu}\frac{1}{\sqrt{2}}\sqrt{\frac{B_o}{2\delta\nu}}\left(2N-1\right)^{\frac{1}{2}}. \tag{3.47}$$

---

[5] The phase contributions from the comb teeth are correlated, but the phase contributions from the thermal light are uncorrelated, thus the total phases are uncorrelated.

Further simplifying:

$$\sqrt{\langle i_{\text{comb, ASE}}(t)^2\rangle} = \frac{\eta e}{h\nu}\sqrt{2P_t 2S\delta\nu}\frac{1}{\sqrt{2}}\sqrt{\frac{B_o}{2\delta\nu}}\sqrt{2N-1}. \tag{3.48}$$

Canceling terms and simplifying:

$$\sqrt{\langle i_{\text{comb, ASE}}(t)^2\rangle} = \frac{\eta e}{h\nu}\sqrt{P_t S B_o}\sqrt{2N-1}. \tag{3.49}$$

The power is then:

$$\langle i_{\text{comb, ASE}}(t)^2\rangle = \left(\frac{\eta e}{h\nu}\right)^2 P_t S B_o (2N-1). \tag{3.50}$$

We recover the PSD by dividing by the RF bandwidth $B_o/2$:

$$\langle i_{\text{comb, ASE}}(t)^2\rangle_{\text{PSD}} = 2\left(\frac{\eta e}{h\nu}\right)^2 P_t S(2N-1). \tag{3.51}$$

Now we make the assumption for large N, i.e., that $2N-1 \to 2N$:

$$\langle i_{\text{comb, ASE}}(t)^2\rangle_{\text{PSD}} = 4\left(\frac{\eta e}{h\nu}\right)^2 P_t S N = 4\left(\frac{\eta e}{h\nu}\right)^2 S P_c. \tag{3.52}$$

This expression holds for both a single detector and balanced detector, assuming that the thermal power and comb power are the same in total. Consider the case of balanced detection:

$$\langle i_{\text{D1}}(t)^2\rangle_{\text{PSD}} = \langle i_{\text{D2}}(t)^2\rangle_{\text{PSD}} = 4\left(\frac{\eta e}{h\nu}\right)^2 \frac{S}{2}\frac{P_c}{2} = \left(\frac{\eta e}{h\nu}\right)^2 S P_c, \tag{3.53}$$

where these are the PSDs of the current outputs of the two detectors. Note that the thermal power and comb power to each detector is one half the total. Also note that this "noise" is correlated (identical), so the signal amplitudes add linearly, not in quadrature. I.e.:

$$\langle i_{\text{BPD}}(t)^2\rangle_{\text{PSD}} = \left(\sqrt{\left(\frac{\eta e}{h\nu}\right)^2 S P_c} + \sqrt{\left(\frac{\eta e}{h\nu}\right)^2 S P_c}\right)^2 = 4\left(\frac{\eta e}{h\nu}\right)^2 S P_c, \tag{3.54}$$

3.5.4 Simplified SNR Derivation

We just derived that the electrical power spectral density of the heterodyne between thermal light and a frequency comb LO is the following, now rewritten with a subscript denoting thermal heterodyne and omitting the PSD subscript:

$$\langle i_T^2 \rangle = 4\left(\frac{\eta e}{h\nu}\right)^2 S P_{LO}, \tag{3.55}$$

where $P_{LO} = P_c$. The shot noise PSD is:

$$\langle i_{SN}^2 \rangle = 2\frac{\eta e^2}{h\nu} P_{LO}. \tag{3.56}$$

The total root-mean-square current from the first balanced detector is $\sqrt{\langle i_{BD_1}^2 \rangle} = \sqrt{\langle i_{SN_1}^2 \rangle + \langle i_{T_1}^2 \rangle}$, and the total root-mean-square current from the other balanced detector is defined in the same way. The mixer multiplies these two photocurrents, such that the RMS output of the mixer is:

$$\sqrt{\langle i_{SN_1}^2 \rangle + \langle i_{T_1}^2 \rangle} \times \sqrt{\langle i_{SN_2}^2 \rangle + \langle i_{T_2}^2 \rangle}. \tag{3.57}$$

The resulting terms are:

$\sqrt{\langle i_{SN_1}^2 \rangle \langle i_{SN_2}^2 \rangle}$, $\sqrt{\langle i_{SN_1}^2 \rangle \langle i_{T_2}^2 \rangle}$, $\sqrt{\langle i_{T_1}^2 \rangle \langle i_{SN_2}^2 \rangle}$, and $\sqrt{\langle i_{T_1}^2 \rangle \langle i_{T_2}^2 \rangle}$.

The last term defines the signal, and all terms, including the last, comprise the noise. Assuming the same levels of S and P_{LO} at each detector, the signal-to-noise ratio (SNR) is:

$$\mathrm{SNR} = \frac{\langle i_T^2 \rangle}{\sqrt{\langle i_T^2 \rangle^2 + \langle i_T^2 \rangle \langle i_{SN}^2 \rangle + \langle i_T^2 \rangle \langle i_{SN}^2 \rangle + \langle i_{SN}^2 \rangle^2}}, \tag{3.58}$$

where the mixer output terms are all added in quadrature since they are uncorrelated. Simplifying:

$$\mathrm{SNR} = \frac{\langle i_T^2 \rangle}{\sqrt{\langle i_T^2 \rangle^2 + 2\langle i_T^2 \rangle \langle i_{SN}^2 \rangle + \langle i_{SN}^2 \rangle^2}} = \frac{\langle i_T^2 \rangle}{\sqrt{[\langle i_T^2 \rangle + \langle i_{SN}^2 \rangle]^2}}. \tag{3.59}$$

Further simplifying:

$$\mathrm{SNR} = \frac{\langle i_T^2 \rangle}{\langle i_T^2 \rangle + \langle i_{SN}^2 \rangle}, \tag{3.60}$$

Plugging in the terms, where $S_{tot} = 2S$, i.e., now looking at the total amount of thermal light on both balanced detectors:

$$\mathrm{SNR} = \frac{2\left(\frac{\eta e}{h\nu}\right)^2 P_{LO} S_{tot}}{2\left(\frac{\eta e}{h\nu}\right)^2 P_{LO} S_{tot} + 2\frac{\eta e^2}{h\nu} P_{LO}} = \frac{\frac{\eta}{h\nu} S_{tot}}{\frac{\eta}{h\nu} S_{tot} + 1} = \frac{\eta \langle n \rangle}{\eta \langle n \rangle + 1}, \tag{3.61}$$

where $S_{tot} = h\nu\langle n\rangle$.

While this is the shot noise limit, additional measurement noise can be considered as

$$\mathrm{SNR}_{\mathrm{tech}} = \frac{\eta\langle n\rangle}{\eta\langle n\rangle + \chi}, \tag{3.62}$$

where χ is a factor greater than 1 describing additional noise such as electronic noise, excess relative intensity noise (RIN), or degradation of the signal strength.

Note that a full accounting for signal and noise is most rigorously done by tracking phasors and bandwidths in the frequency domain. For the readability of the thesis, I have placed this lengthy derivation in App. A.

3.6 Sensitivity Comparison With Other Modalities of Thermal Light Spectroscopy

To evaluate the utility of DCCS, we compare the frequency domain SNR of DCCS alongside existing methods for thermal light spectroscopy. These methods include channelized direct detection (echelle spectrographs–Fig. 3.6a), where all resolved frequency bins are channelized onto as many photodetectors [53]; swept direct detection (grating monochromators–Fig. 3.6b), where thermal light is separated on a grating and scanned across a single detector; shot noise-limited Fourier transform spectroscopy (FTS–Fig. 3.6c) [20]; channelized laser heterodyne radiometry (Fig. 3.6d), where all resolved frequency bins are channelized onto as many photodetectors [53]; swept laser heterodyne radiometry (Fig. 3.6d), where laser local oscillator light is scanned in frequency using a single detector; and DCCS (Fig. 3.6e). Note that we consider the detection of a single mode of thermal light and thus do not treat the multiplex advantage possible in direct detection techniques. However, the most precise spectral measurements in direct detection also image a single mode due to dispersion-related uncertainty [60]. Thus we believe that a single spatial mode-based comparison is fair and illustrative.

The SNR of all methods share the well-known square root scaling with averaging time and frequency resolution, but differ in scaling with respect to photon occupation $\langle n\rangle$ and number of resolved frequency bins N (Fig. 3.6 Table). For swept techniques, FTS, and DCCS, N is the number of resolved frequency bins per detector. Channelized techniques, however, host one resolved frequency bin per detector and thus do not scale with N.

We graphically compare the SNR as a function of wavelength (λ), resolution ($\Delta\nu$), number of resolved spectral bins (N), and black body temperature (T) in Fig. 3.6. In each of the separate plots, we scan one variable from standard conditions of $N = 30$, $\Delta\nu = 1$ GHz, T = 5770 K, $\tau = 1$ s, $\lambda = 1550$ nm. Note the total bandwidth measured is $N\Delta\nu = 30$ GHz. In Fig. 3.6f, we see that all techniques suffer SNR degradation at shorter wavelengths, but direct detection techniques fare better in the regime where $\langle n \rangle < 1$. This is due to direct detection techniques scaling as $\sqrt{\langle n \rangle}$ vs heterodyne techniques scaling as $\langle n \rangle$. At longer wavelengths, all techniques exhibit SNR of greater than 10^2, sufficient for many applications. Square root scaling with spectral resolution $\Delta\nu$ is shown in Fig. 3.6g. In Fig. 3.6h we plot the SNR scaling with number of resolved spectral bins N, showing that all techniques are roughly equivalent when $N = 1$, but DCCS shows a disadvantage at high N due to $1/N$ scaling. One can think of this scaling as a temporal mode-mismatch penalty between the two comb LOs and the thermal light, or as an optical to RF spectral compression penalty. Fig. 3.6i shows scaling with temperature, illustrating that cooler objects are better measured with direct detection methods due to $\sqrt{\langle n \rangle}$ scaling.

3.7 Comparison With Other Phase-Sensitive Techniques, i.e., Laser Heterodyne Radiometry Methods

Heterodyne techniques such as LHR and DCCS, while not as sensitive as direct detection, are essential for applications requiring phase sensitivity such as synthetic aperture imaging.

Here we compare implementations of LHR and DCCS to understand the complex trade-space of sensitivity (SNR), technological maturity, and realistic technical practicalities. First, we compare the quantum-limited frequency domain SNR for these techniques, listed in Table 3.1, where $\Delta\nu$ is the spectral resolution in hertz, τ is the total averaging time in seconds, and N is the number of resolved frequency bins per detector. Note that N is a measure of optical to electronic spectral

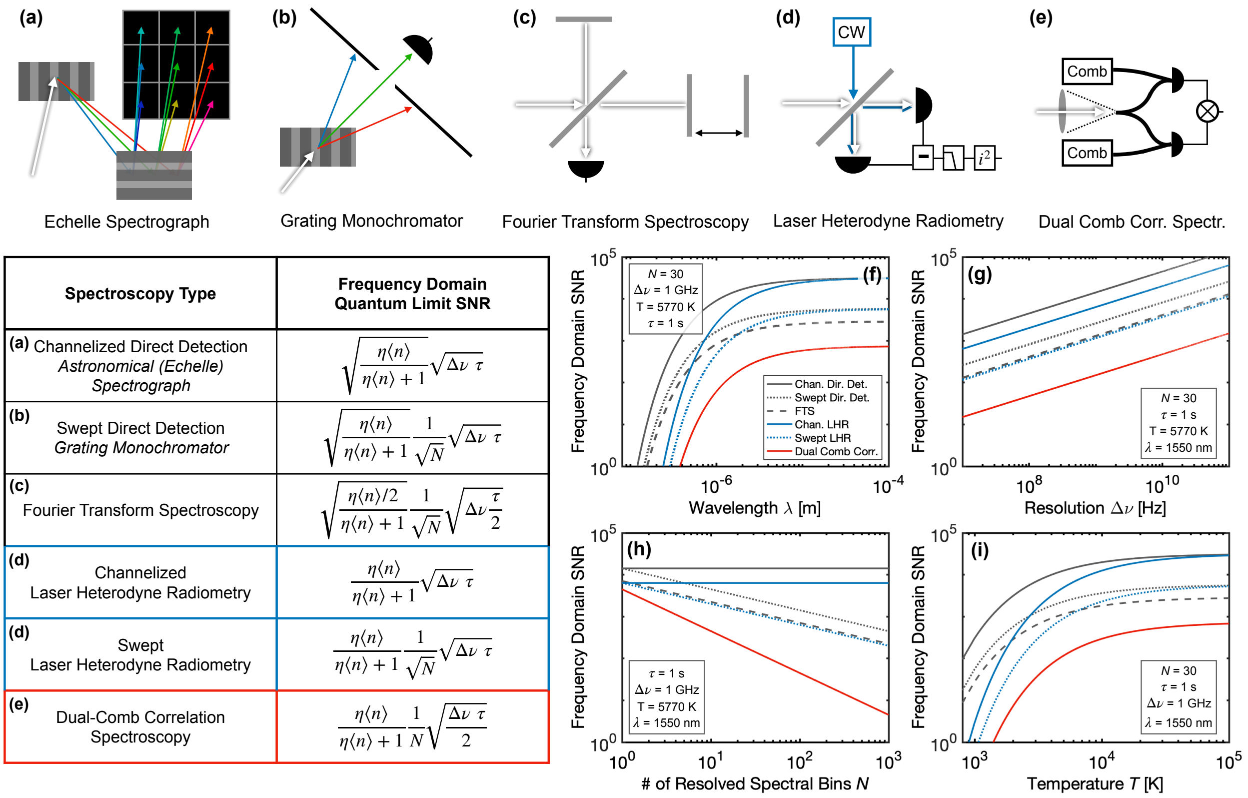

Spectroscopy Type	**Frequency Domain Quantum Limit SNR**
(a) Channelized Direct Detection *Astronomical (Echelle) Spectrograph*	$\sqrt{\frac{\eta\langle n\rangle}{\eta\langle n\rangle+1}}\sqrt{\Delta\nu\ \tau}$
(b) Swept Direct Detection *Grating Monochromator*	$\sqrt{\frac{\eta\langle n\rangle}{\eta\langle n\rangle+1}\frac{1}{\sqrt{N}}}\sqrt{\Delta\nu\ \tau}$
(c) Fourier Transform Spectroscopy	$\sqrt{\frac{\eta\langle n\rangle/2}{\eta\langle n\rangle+1}\frac{1}{\sqrt{N}}}\sqrt{\Delta\nu\frac{\tau}{2}}$
(d) Channelized Laser Heterodyne Radiometry	$\frac{\eta\langle n\rangle}{\eta\langle n\rangle+1}\sqrt{\Delta\nu\ \tau}$
(d) Swept Laser Heterodyne Radiometry	$\frac{\eta\langle n\rangle}{\eta\langle n\rangle+1}\frac{1}{\sqrt{N}}\sqrt{\Delta\nu\ \tau}$
(e) Dual-Comb Correlation Spectroscopy	$\frac{\eta\langle n\rangle}{\eta\langle n\rangle+1}\frac{1}{N}\sqrt{\frac{\Delta\nu\ \tau}{2}}$

Figure 3.6: Comparing SNR of thermal spectroscopy techniques **(a)** Echelle spectrograph diagram. **(b)** Grating monochromator diagram. **(c)** Fourier transform spectrometer diagram. **(d)** Laser heterodyne radiometry diagram. Channelized LHR would host many CW LOs and detectors. Swept LHR would sweep the frequency of the CW LO using one detector. **(e)** Dual comb correlation diagram. **(f)** Frequency domain SNR vs. wavelength **(g)** Frequency domain SNR vs. resolution **(h)** Frequency domain SNR vs. N, the number of resolved spectral bins **(i)** Frequency domain SNR vs black-body temperature. Note, $\langle n\rangle = (\exp[h\nu/kT]-1)^{-1}$.

compression, which is crucial when measuring 10s of THz wide optical spectra.

In channelized LHR (Table 3.1 and Fig. 3.7a), each $\Delta\nu$-sized spectral section of thermal light is dispersed onto a single detector; thus N is always 1, and the SNR does not scale with N by definition (Eqn. 3.62). In swept LHR (Fig. 3.7b), a single detector captures a wide band of thermal spectra as the CW local oscillator is swept in frequency, but the SNR is lowered by $1\sqrt{N}$ versus channelized LHR due to spectral dead time (Eqn. 3.63). DCCS (Fig. 3.7c) captures the full broadband thermal spectrum simultaneously on a single detection channel, coming at a cost of $1/\sqrt{2}N$ over channelized LHR (Eqn. 3.64).

In practice, due to the aforementioned $1/\sqrt{N}$ or $1/N$ penalty of spectral multiplexing on a single detection channel, some degree of channelization is necessary for measurement across broad optical bandwidths. For a realistic comparison of implementations, we compare the following three cases: channelized LHR, hybrid swept and channelized LHR, and channelized DCCS.

Channelized LHR (Fig. 3.7a) is a compelling candidate for the most sensitive measurements due to its high SNR [50]. As mentioned earlier, there is no SNR penalty for increasing the number of resolved spectral bins (increasing optical bandwidth measured). However, this can only be accomplished by matching one photodetection chain to each spectral bin. For high resolution detection over broad optical bandwidths, this requirement presents significant technical challenges. For example, consider a 10 THz (80 nm at 1550 nm) section of optical bandwidth over which one desires 1 GHz resolution. A $f_r = 1$ GHz frequency comb may span this bandwidth; however, this measurement would also require a complex, low loss system for de-multiplexing 10,000 channels built on a high resolving power (R = 200,000) spectrometer. In addition, this would require 10,000 balanced detectors, rectification circuits, and digitization channels.

Hybrid Swept and Channelized LHR is an attractive alternative both to pure channelization (above) or sweeping a single CW laser across 10 THz of optical bandwidth and introducing large amounts of dead time. As pictured in Fig. 3.7b, a hybrid LHR approach alleviates the number of detectors and decreases the required resolving power of the spectrometer and de-multiplexing complexity as compared to channelized LHR. For example, addressing the same measurement sit-

Spectroscopy Type	**Frequency Domain SNR**	
Channelized Laser Heterodyne Radiometry	$\frac{\eta\langle n\rangle}{\eta\langle n\rangle+1}\sqrt{\Delta\nu\tau}$	(3.63)
Swept Laser Heterodyne Radiometry	$\frac{\eta\langle n\rangle}{\eta\langle n\rangle+1}\frac{1}{\sqrt{N}}\sqrt{\Delta\nu\tau}$	(3.64)
Dual-Comb Correlation Spectroscopy	$\frac{\eta\langle n\rangle}{\eta\langle n\rangle+1}\frac{1}{N}\sqrt{\frac{\Delta\nu\tau}{2}}$	(3.65)

Table 3.1: Quantum-limited frequency domain SNR of channelized LHR, swept LHR, and channelized DCCS. $\Delta\nu$ is the optical resolution in Hz, τ is the averaging time in s, and N is the number of resolved frequency bins per detector. Other variables defined in text.

uation as before, this approach would consist of a 10 GHz resolution spectrometer separating 10 THz total bandwidth of light onto 1000 (vs. 10,000) photodetection and digitization channels, coming at a cost of $1/\sqrt{10}$ in SNR over the channelized approach. To match this grid, one might utilize 1000 CW lasers or a $f_r = 10$ GHz comb with 10 GHz tunability of the offset frequency. Presently the operation and active calibration of 1000 simultaneously swept CW lasers appears unrealistic. However, a frequency comb would reduce the number of lasers from 1000 to 1 and ease instrument complexity. Such tunable, high f_r frequency combs are in development in the context of astronomical spectrograph calibration [61, 62].

Channelized DCCS (Fig. 3.7c) increases instrumental simplicity compared with the LHR methods above. Channelized DCCS with 10 GHz channels measuring 10 THz of optical bandwidth with 1 GHz resolution would offer a significant simplification over pure channelized LHR–requiring, for example, 1000 instead of 10,000 digitization and detection channels. Moreover, compared to hybrid swept and channelized LHR, a channelized DCCS approach could utilize more mature frequency comb platforms with 1 GHz repetition rates, allow for static calibration (such as through a conventional dual-comb measurement [17]), and host no dead time. See Fig. 3.7d for a comparison of channelized LHR, hybrid LHR, and channelized DCCS across channel resolution, number of detectors, dead time, frequency calibration, and SNR. Note that the SNR is calculated with parameters $\eta = 1$, $T = 5770$ K, $\lambda = 1550$ nm, $\Delta\nu = 1$ GHz, $t = 1$ s, and $N = 10$.

We highlight that in broad spectrum measurements of black-body radiation, much of the spectrum does not convey desired information, i.e., much of the spectrum consists of a smooth Planck law profile or absorption features not of interest. A spectrally tailored DCCS approach, where the combs contain power solely in spectral regions matching the absorption lines of interest, would grant even broader bandwidth measurements on a single detection channel while maintaining high SNR, which would otherwise be degraded by high spectral multiplexing, N, if continuously measuring broad optical spectra.

Digitization requirements for LHR are low due to the analog rectification that converts the broadband noise to a measure of DC power [63]. We note that the digitization requirements of

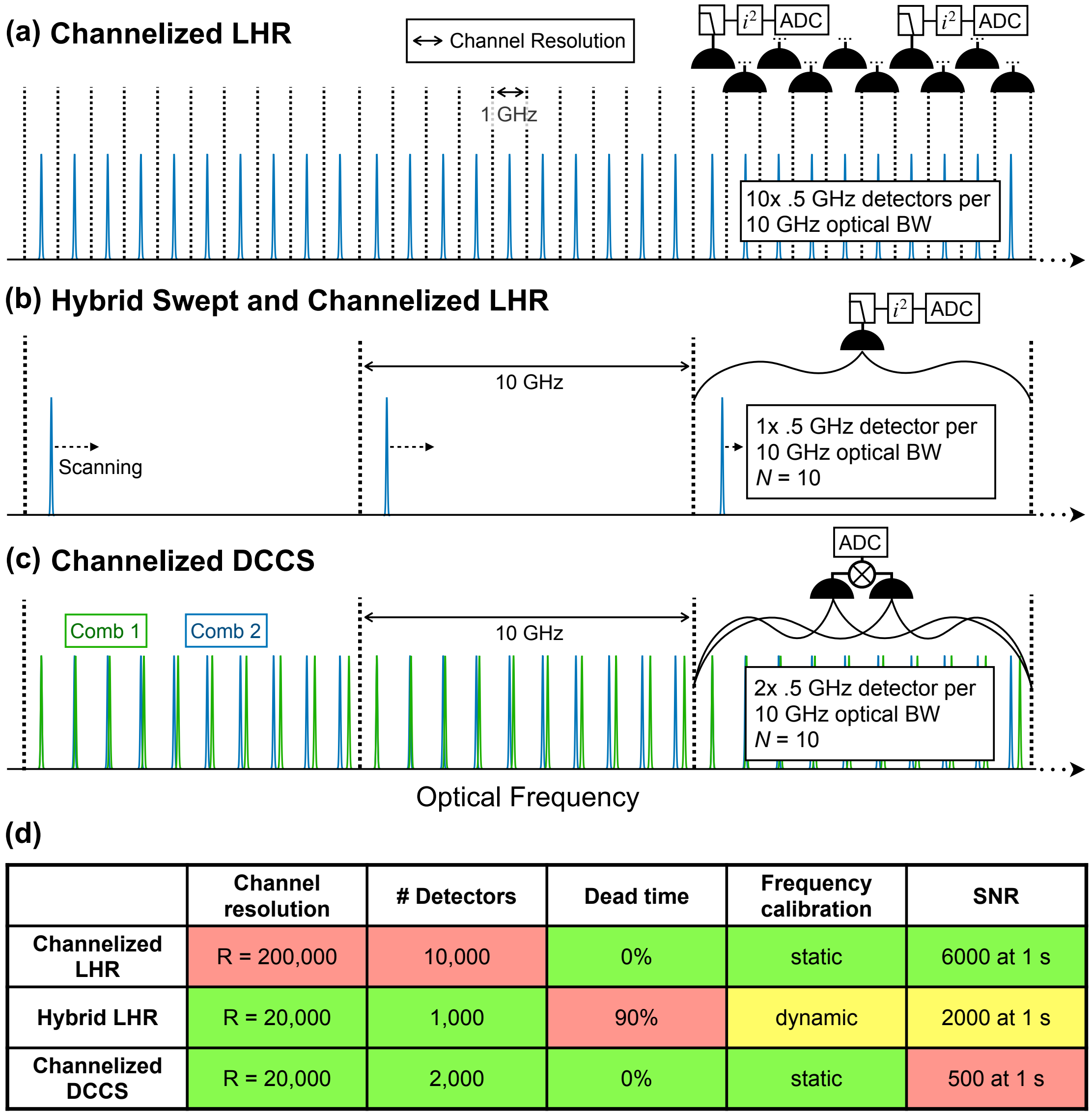

	Channel resolution	# Detectors	Dead time	Frequency calibration	SNR
Channelized LHR	R = 200,000	10,000	0%	static	6000 at 1 s
Hybrid LHR	R = 20,000	1,000	90%	dynamic	2000 at 1 s
Channelized DCCS	R = 20,000	2,000	0%	static	500 at 1 s

Figure 3.7: **(a)** Channelized LHR. **(b)** Hybrid swept and channelized LHR. **(c)** Channelized DCCS. Note that **(a)**, **(b)**, and **(c)** depict only 0.3% of the total example optical bandwidth. **(d)** Comparison of techniques across channel resolution, number of detectors, dead time, frequency calibration, and SNR–see main text for parameters used. Green, yellow, and red highlighting indicates best, intermediate, and worst performance, respectively.

hybrid DCCS are also relatively easy. As a dual-comb method that maps an optical spectrum to an RF spectrum, the two combs can be tuned to map the optical spectrum to a low frequency and narrowband RF spectrum. Ultimately, this compression is limited by the mutual stability of the two combs which dictate the lowest possible Δf_r and thus the timescale over which phase correction is necessary. Note that spectral compression is set by the ratio $\frac{\Delta f_r}{f_r}$ [17]. In practice, we have found the two combs used in the present demonstration generate phase-stable interferograms for several seconds (without requiring phase correction). With conservative parameters of 1 kHz Δf_r (each interferogram is 1 ms in duration), 10 GHz of optical bandwidth per channel, and $f_r = 1$ GHz, the size of the compressed RF spectrum is 10 kHz. Multiplexed across 1000 channels with 10 THz total optical bandwidth, only a modest data collection rate of 10 MB/s is required at 4 bit digitization, or 824 GB per day.

We note that an alternative heterodyne spectroscopy method would be to directly digitize the heterodyne of a demultiplexed comb and thermal radiation, then to post-process this data (e.g., through auto-correlation or FFT such as in radio spectroscopy [64]) to achieve finer resolutions. A sensitivity analysis of such a technique that also addresses image-band ambiguity would be very valuable; however, the digitization requirements would likely pose significant technical challenges at broad bandwidths. For example, digitization across 10 THz would require a sampling rate of 10+ TS/s. At a bit depth of 4, this translates to a technically challenging data acquisition rate of 5+ TB/s or 86.4+ PB per day.

3.8 How Does This SNR Constrain Line Center Estimation?

DCCS offers advantages in terms of instrumental simplicity versus both channelized and hybrid LHR, but does not offer as high SNR as these methods (Fig. 3.7d). Despite lower SNR, DCCS may still provide the needed sensitivity for precise astronomical spectroscopy. Consider an example Gaussian absorption line with a width of 3 GHz and depth of 0.5 imparted on light from a 5770 K black body, and a measurement efficiency of $\eta = 0.5$. A channelized DCCS scenario such as the one above, where $N = 10$ and $\Delta\nu = 1$ GHz, would reach a frequency domain SNR of 22,000 after 40 minutes. This SNR and resolution limits the line-center measurement to an uncertainty of 8.9 cm/s, equalling the Doppler shift that the Earth imparts on Sunlight.

3.8.1 Calculating SNR-Limited Line Center Uncertainty

The uncertainty in the position of a spectral absorption line (σ_ν) is related to the uncertainty in the amplitude by the following relationship:

$$\sigma_\nu = \sigma_f / |df/d\nu|, \tag{3.66}$$

where ν is the optical frequency and $f(\nu)$ is the spectral line function. One can rewrite this in terms of SNR and the line depth (D) of the absorption line as:

$$\sigma_\nu = \frac{1}{\mathrm{SNR} \times D \times \frac{ds}{d\nu}}, \tag{3.67}$$

where $s(\nu)$ is the normalized spectral line function. Consider the Gaussian function $s(\nu) = e^{-\frac{1}{2}(\frac{\nu}{\mathcal{D}\nu})^2}$, where $\mathcal{D}\nu$ is the line width. The derivative is:

$$\frac{ds}{d\nu} = \frac{-\nu}{\mathcal{D}\nu^2} e^{-\frac{1}{2}(\frac{\nu}{\mathcal{D}\nu})^2}, \tag{3.68}$$

and the uncertainty is then:

$$\sigma_\nu = \frac{1}{\mathrm{SNR} \times D \times \frac{-\nu}{\mathcal{D}\nu^2} e^{-\frac{1}{2}(\frac{\nu}{\mathcal{D}\nu})^2}}. \tag{3.69}$$

We are interested in the total uncertainty over a measurement resolving the whole line. The uncertainty of multiple measurements is:

$$\sigma_{tot} = \frac{1}{\sqrt{\sum_i \sigma_{\nu,i}^{-2}}} = \frac{1}{\sqrt{\sum_i (\mathrm{SNR} \times D \times \frac{-\nu_i}{\mathcal{D}\nu^2} e^{-\frac{1}{2}(\frac{\nu_i}{\mathcal{D}\nu})^2})^2}}, \tag{3.70}$$

Simplifying,

$$\sigma_{tot} = \frac{1}{\frac{\mathrm{SNR} \times D}{\mathcal{D}\nu^2} \sqrt{\sum_i (-\nu_i e^{-\frac{1}{2}(\frac{\nu_i}{\mathcal{D}\nu})^2})^2}} = \frac{1}{\frac{\mathrm{SNR} \times D}{\mathcal{D}\nu^2} \sqrt{\sum_{n=1}^{N\rangle 3\mathcal{D}\nu/\Delta\nu} (-2n\Delta\nu e^{-\frac{1}{2}(\frac{n\Delta\nu}{\mathcal{D}\nu})^2})^2}}, \tag{3.71}$$

where one is assuming the capture of the line at greater than 3 standard deviations. The Doppler shift that can be resolved is $\delta V = \sigma_{tot} \times c/\nu_0$, where c is the speed of light and ν_0 is the center optical frequency.

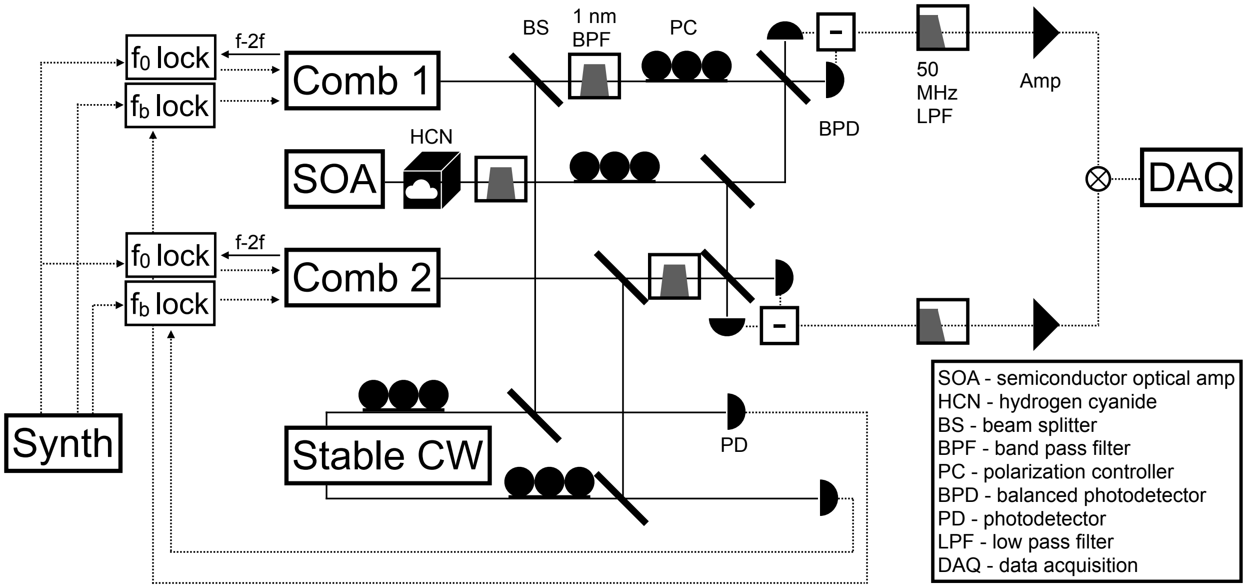

Figure 3.8: Experimental diagram

We consider an efficiency of 0.5, a line depth D of 0.5, a line width $\mathcal{D}\nu$ of 3 GHz, a spectral resolution $\Delta\nu$ of 1 GHz, and a center optical frequency ν_0 of 200 THz (near 1550 nm). A 8.9 cm/s uncertainty occurs at approximately SNR = 22,000, which occurs at around 2 hours.

A similar analysis is carried out in [65]. Note that if one only cares about the line center, there is no benefit to over-resolving the line with higher resolution. However, other phenomena may be of interest, such as complex magnetohydrodynamics that reshape the line itself. In such cases, over resolving the line may provide crucial information that disentangles line center shifts from other phenomena.

3.9 Experimental Considerations for Dual-Comb Correlation Spectroscopy

In this section, I provide information on the experimental set-up (see Fig. 3.8) used in the present demonstration as well as practical and technical suggestions for dual-comb correlation spectroscopy in general.

3.9.1 Local Oscillators

The frequency comb oscillators used are two figure-9 Menlo systems Er:fiber-based frequency combs that are fully self-referenced (offset frequency and optical beat frequency locked). The two combs have a repetition rate around 100 MHz, an output bandwidth around 10 nm at approximately 1550 nm, and a power of approximately 10 mW. For the experiment, the two combs were filtered down to 1 nm and approximately 50 µW before mixing with the thermal light.

As mentioned in previous sections, the repetition rate sets the resolution of the measurement, and coarser resolutions results in higher SNRs. In fact, if one is only interested in line center information, over-resolving the line does not help, and one should choose a resolution close to the linewidth of the line itself. Typical solar linewidths in the near infrared are in the single to few GHz range.

As will be shown in Section 3.10, technical noise of the frequency combs should be minimized, as this imposes additional penalties on top of the unavoidable shot noise. Care should be taken to not amplify the LO light any more than necessary, as excess relative intensity noise from amplified spontaneous emission can degrade SNR further.

3.9.1.1 Detector Saturation

Detector saturation is also a critical issue for DCCS, since the light is coming from a mode-locked laser. To put some numbers to this, an estimate on the peak power per pulse for a 100 MHz comb with 100 GHz bandwidth (a little less than 1 nm at 1550 nm) and 60 µW average power is 60 mW–and the CW saturation power listed for the Thorlabs PDB410C (the detector used) is listed at 72 µW. So we should expect to see saturation, which may arise from charge carrier shielding and also in the saturation of the transimpedance amplifier built into the detector [66]. As mentioned in Section 3.10, I believe this plays a role in the lower than expected signal strength. In the experiment, variable attenuators were used on the comb local oscillators to not over saturate the detectors. Increasing the power of the LO light increased the deviation of the expected signal strength from that actually measured, indicating saturation. In practice, however, if the power of the LO was too low, electronic noise would dominate and overall SNR would be lower. So there was a “happy medium” of some saturation on the signal and some technical contributions to the noise that offered the highest SNR.

One might imagine that chirping the optical pulses would assist in the saturation issue. Yet fiber lengths for such chirping to widen pulses of only 1 nm in bandwidth are unrealistically long, and free space optics add an additional layer of complexity. Naturally highly chirped frequency combs such as electro-optic combs may be very helpful in reaching quantum limited performance– allowing enough light to reach the shot noise limit while lowering peak power that saturates the photodetector.

3.9.2 Experimental Thermal Light

The thermal light used in the above demonstration is amplified spontaneous emission from a semiconductor optical amplifier. This light was then passed through a hydrogen cyanide (HCN) gas cell (NIST Standard Reference Material 2519a) to impart absorption features. Although not strictly from a black-body source, ASE exhibits the statistical and coherence properties of thermal light that define the SNR limit.

Ultimately, solar and stellar light is desired, and techniques of telescope-to-fiber coupling that are already in use can be used for DCCS [63, 60].

To calibrate the power of the thermal light, I tapped the thermal light and measured this with an optical power meter while also reading the monitor ports of the balanced detectors. At higher powers, the balanced detector monitors were used to calibrate the thermal tap, and at lower powers, where the uncertainty on the balanced detector monitors was higher than the contribution of the thermal light, the optical power meter on the thermal tap was used.

3.9.3 Mutual Coherence, Locking, and Phase Correction

Mutual coherence of the two combs is a vital part of DCCS. Challenges and solutions are similar to that in conventional dual-comb spectroscopy, with the additional requirement that the two combs must scan over the same section of thermal light–so after the thermal light is split, both paths of the thermal light must be stable (or at least mutually stable). In the experiment, comb and thermal light passed through several meters of single mode fiber, and fiber sections after splitting thermal light were kept to under half a meter. Of particular help was taping and weighting down of optical fibers so that air currents and acoustic vibrations were damped.

Optimal locking and phase correction are also essentially the same as for conventional dual-comb spectroscopy. There is some debate in the field as to what degree of locking one requires for dual-comb spectroscopy, such as whether the combs need to be fully self-referenced, what degree of mutual coherence must exist, and what can be fixed in real-time or post phase correction. This is a subject that deserves greater treatment in another document. In the experiment, locking conditions were set in the most "conservative" fashion. Both frequency combs were locked and fully-self referenced, clocked by the the NIST hydrogen maser. Since the spectrum being measured occurred around 1547 nm, setting both optical beat frequencies between the two combs and the CW laser to the same RF frequency effectively set $\Delta f_0 = 0$. In other words, we defined the Δf_0 of the measured Nyquist zone with Δf_b because the CW frequency $f\nu_{\mathrm{CW}}$ defined the beginning of this Nyquist zone. This choice ensured that there would be no walking from interferogram to interferogram. Repetition rates were set such that the maser-referenced counter read 100.000000 MHz and 100.000000 MHz + 2.083333 kHz up to the µHz level. This fulfills the repetitive sampling condition that $f_r/\Delta f_r$ is an integer, meaning that the same point of the interferogram is being sampled each cycle of the interferogram. While this gave a good starting point, there was still some interferogram to interferogram drift at longer timescales–slightly tuning f_0 based on the interferogram drift shown on the oscilloscope enabled even longer periods where no phase correction was required. Note that the oscilloscope used was also clocked by the maser reference.

Of course, interferogram-by-interferogram phase correction can adjust for any settings of f_0 and f_b, but because each interferogram displayed an SNR much less than one, I required enough phase-identical interferograms such that the average exhibited high enough SNR to phase correct. This effectively set the sensitivity of the measurement, since the same SNR could be acquired for weaker thermal light at longer averaging times.

Note that mutual stability conditions between the two frequency combs may be relaxed if one is also monitoring a conventional dual-comb interferogram that has been tapped out from the two combs. So long as this interferogram is effectively "in-loop" of the thermal heterodyne, the thermal interferogram should require the same phase correction as the dual-comb interferogram.

3.9.4 Mode-Matching

Mode matching plays a critical role for optimal measurement, as any degree of mode mismatch attenuates the signal but does not affect the shot or technical noise. Mode matching parameters include transverse spatial modes, which were automatically matched in the experiment due to the use of single mode fiber, as well as polarization and spectral modes. The ASE used in the experiment was well polarized up to 99%; however, thermal light from a black body is unpolarized, and it is essential that both frequency combs heterodyne with the same polarization mode.

3.9.5 Technical Noise

Because this experiment operates in the strong local oscillator limit, technical noise on the comb LOs can be canceled by balanced detection, which relies on well balanced photodetectors as well as even couplers. However, it is usually best to use the lowest noise LOs possible, since the common mode rejection ratio of the photodetector is finite and there may be deviation from even splitting in the 50:50 couplers used.

Another source of noise is the electronics. While many unamplified detectors are nearly thermal noise-limited by their 50 ohm impedance, built-in transimpedance amplifiers may add a few dB higher noise (i.e., have a noise figure of a few dB). Low noise amplifiers with 1-2 dB noise figures may be used to lower the threshold at which shot noise limits the measurement (i.e., lower the required laser power to reach the strong LO limit).

The use of analog mixers with white noise-like signals also requires attention. In the experiment, electronic amplifiers were added after the photodetectors to raise the input powers into the mixer. At low electronic powers, mixer leakage current plays a larger role in the mixed output. After testing several mixers from Mini-circuits, it appeared as though 50 MHz of white noise required an integrated RMS power level approximately 5 dB higher than the mixer optimal input power specification to achieve optimal mixing.

3.10 Spectroscopy at the Solar Planck Limit and Experimental Verification of SNR Scaling

We seek to validate the achievable SNR with two frequency combs (f_r = 100 MHz) that are heterodyned with thermal light generated by amplified spontaneous emission (ASE) from an unseeded optical amplifier. The overall spectral bandwidth is set by 1 nm bandpass filters, and a hydrogen cyanide (HCN) cell is placed in the path of the thermal light to impart a sharp absorption feature.

The power spectral density (PSD) of the Sun sets a benchmark for realistic sensitivity, shown as a line labeled Solar Planck Limit (Fig. 3.9c), referring to the equivalent PSD of a 5770 K blackbody at 1547 nm. We experimentally demonstrate spectroscopy at this PSD over the course of 1 hour, showing both zoomed-in interferograms and the PSD at the full 100 MHz comb resolution obtained through a fast Fourier transform (Fig. 3.9a and 3.9b). At 1 hour, we clearly observe the hydrogen cyanide (HCN) absorption line (Fig. 3.9b) with a measured and predicted SNR of approximately 10. We emphasize that Fig. 3.9b displays the highest sensitivity measurement with DCCS and the first at a PSD corresponding to a realistic astronomical source.

Our measurement exhibits a $\chi = 6.25$ (see Sec. 3.5.4) that we attribute to an electronic noise floor that is $\sim$ 3 dB greater than shot noise and a heterodyne power level that is 5 dB lower than ideal. This second factor is likely due to a combination of spectral mode-matching and detector saturation. We show close agreement between measured SNR (circles) and the theoretical technical limit (red curve) across three orders of magnitude of thermal PSD at 1547 nm (Fig. 3.9c). Note that the theoretical technical limit does not rely on parameters fitted to the measured SNR. The experimental SNR is estimated by dividing the peak value of the averaged interferogram envelope by the root-mean-square value at time delays well beyond the center burst. Hence, at lower SNR, the estimate on SNR has greater uncertainty as shown by the $\pm\sigma$ standard deviation at 16,000 averages. Clearly, reaching the shot noise (quantum) limit would yield a substantive improvement over the current technical limit (Fig. 3.9c), and we address reaching that regime in the discussion.

Note that given our technical noise and saturation issues, the frequency domain SNR at the Solar Planck limit would be around 10. The SNR in the frequency domain is estimated at around 6 by taking the average value within the 1 nm spectral section (around 15 MHz Fourier frequency) and dividing it by the average value in a nearby noise floor (around 20 MHz). Note that the noise floor is not perfectly white, and that at higher Fourier frequencies the noise floor is slightly reduced. Perhaps this is due to mixer or filter responses, or the presence of correlated noise at lower Fourier frequencies.

3.10.1 Analysis of Signal and Noise Contributions to PSD

The PSDs of the signals and noise were measured on the Agilent MXA Signal Analyzer N9020A, with an estimated absolute uncertainty of ±0.5 dBm/Hz, that was cross-calibrated with a standard NIST noise source with Archita Hati's help. I plot the measured levels alongside the theoretically estimated levels of the PSD in dBm/Hz out of the Thorlabs PDB415C photodetectors in Fig. 3.10.

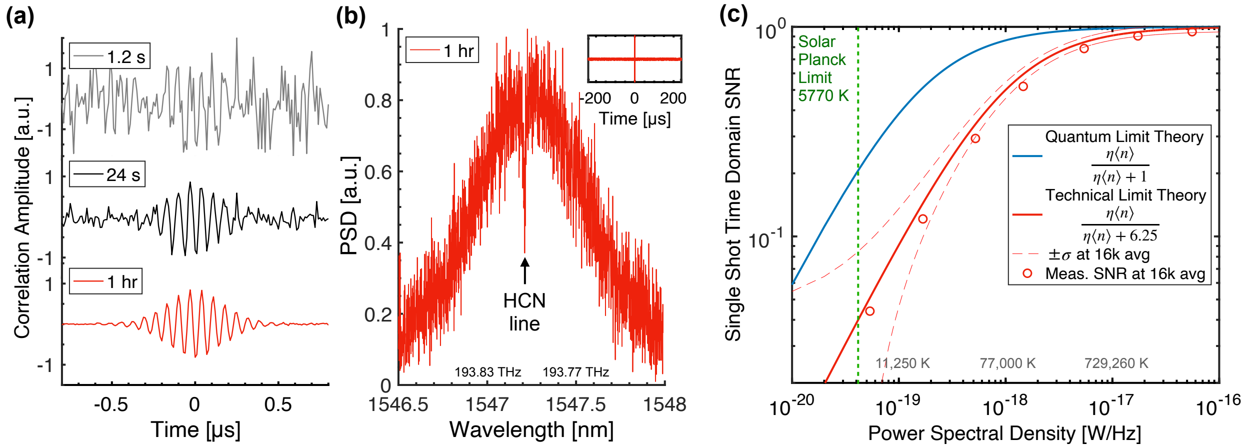

Figure 3.9: **(a)** DCCS interferograms recorded with thermal light at the PSD of 4×10^{-20} W/Hz, which is equivalent to a 5770 K black body. The interferograms are displayed at increasing averaging times. **(b)** The Fourier transform of the interferogram with 1 hr averaging yields the thermal PSD at 100 MHz resolution. The inset shows the full interferogram window over $1/\Delta f_r \approx 500$ μs, and the molecular absorption of a HCN line is clearly imprinted on the thermal light. **(c)** Theoretical and experimental scaling of the *single-shot* SNR (see Fundamental SNR Scaling). The SNR of DCCS is measured (red circles) across three orders of magnitude of PSD. The trend shows close agreement with the theoretically predicted SNR (red line) based on measurements of technical noise and detector saturation. Note, this equation is not fitted to the measured SNR. The shot noise limit (blue line) is also shown.

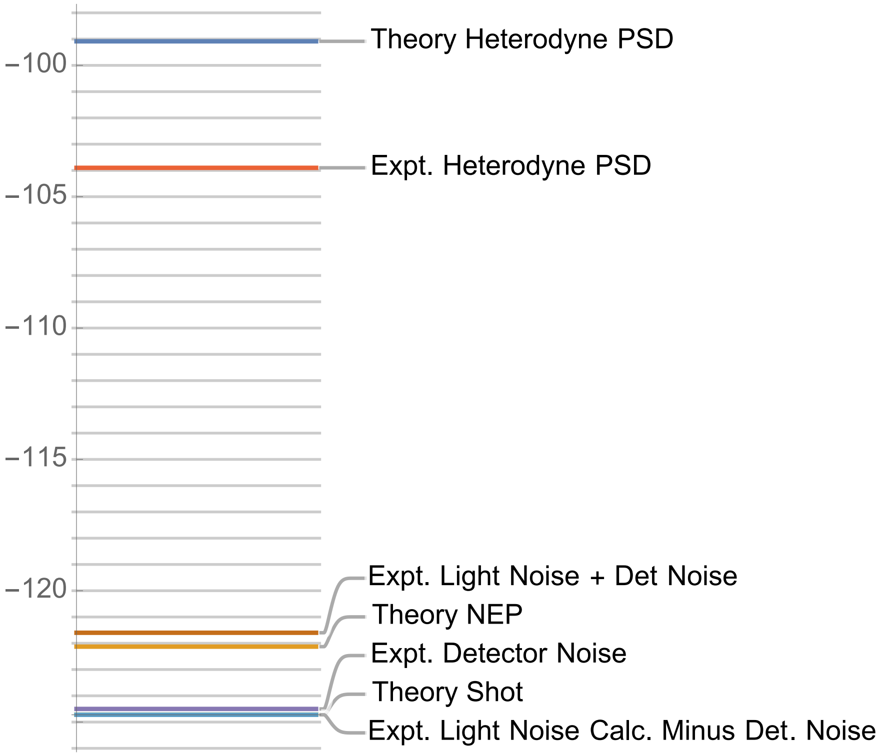

Figure 3.10: A comparison of the different PSD levels and experimental measurements vs theoretical predictions. Note that the Y axis is in units of dBm/Hz, where the Agilent Signal Analyzer divides out its estimated resolution bandwidth for the experimental data.

3.11 Future Outlook

3.11.1 Reaching Quantum-Limited Performance

Looking to the future, it is important to reach and thus unambiguously verify the shot noise limit and reach the quantum-limited sensitivity. This entails not just raising the shot noise above other sources of noise, but also not reaching the saturation regime through too much peak pulse power. One possible solution is the use of electro-optic combs, whose outputs when purely phase modulated are constant in power, or when both intensity and phase modulated, exhibit highly chirped pulses on the order of half the pulse-to-pulse round trip time. This contrasts with the experimental situation with the Menlo combs, where there was an approximate duty cycle of 1/1000th the round trip time.

3.11.2 Increasing Sensitivity and Bandwidth

As is evident by the $1/N$ scaling of the SNR, there is a trade-off in terms of optical to RF spectral compression and sensitivity. The optimal balance between experimental simplicity and sensitivity likely depends on the application. A sensible pathway is to make use of inexpensive and low loss telecommunications components, such as dense wavelength division multiplexers (DWDMs). Such components separate telecom wavelength light into 100 GHz bins, and, given a 5 GHz repetition rate, this amounts to a $N = 20$. Alongside reaching the quantum noise limit, compared to the SNR achieved in the demonstrated experiment, this would yield an increase in SNR of $6.25 \times 50 \times \sqrt{50} \approx 2000$ due to χ decreasing from 6.25 to 1, N decreasing from 1000 to 20, and $\Delta\nu$ increasing by 50–see Table 3.1. The DWDM is not only a spectral filter, but also grants broader band channelization as shown in hybrid DCCS (Figure 3.7c), and one could increase the number of detectors to reach broader and broader bandwidths.

3.11.3 Mid and Far-Infrared Thermal Light Spectroscopy

Our experimental work operated near 1550 nm due to the availability of inexpensive, high-quality, telecommunications-compatible components such as high quantum efficiency balanced photodetectors and low-loss fiber optics. However, many other regions of the optical spectrum are of great interest, particularly further into the infrared. At longer wavelengths, the mean photon occupancy $\langle n \rangle$ increases, granting the ability to measure cooler objects.[6] However, shot noise-limited DCCS is challenging in the mid- and far IR due to a lack of high-power, low-excess RIN combs and a lack of high-speed, low-noise, high-quantum-efficiency balanced detectors. A compelling alternative is through electro-optic sampling [67, 68, 69], where MIR/FIR light is up-converted to the NIR for higher efficiency, low noise detection. Further analysis of the nonlinear conversion efficiency is required to fairly assess the merits of nonlinear DCCS.

3.11.4 Broadband Optical Synthesis Imaging with Dual-Comb Correlation

Dual-comb correlation spectroscopy measures the coherence of thermal light as a function of the temporal delay across the same spatial mode. This results in a $g^{(1)}$-type measurement of thermal light, and a Fourier transform yields the spectrum of this light. The thermal field can also be sampled and correlated at different spatial "delays," then Fourier transformed to produce an image of the source. Such techniques are used for synthesis imaging in radio astronomy [70, 71], and hyperspectral images are formed as image "cubes,", which are generated through Fourier transforms of complex visibility (coherence) as a function of the two spatial delays and the temporal delay.

Most generally, dual-comb correlation consists of the broadband phase-sensitive measurement of thermal fields with two combs followed by correlation of these signals. It is a means to measure the similarity of broadband optical fields at different points in time and space. This similarity is described as coherence or as complex visibility, and the combination of many pairwise comparisons fills out the complex visibility, which can be Fourier transformed in time and space to generate a

---

[6] However, this also requires a larger aperture to capture the larger coherence radius of a single mode of thermal light.

hyperspectral image of a distant source. Here, we provide a brief description of how dual-comb correlation synthesis imaging might be deployed and how the sensitivity bounds provided in this work provide the fundamental limits for such a system.

First, we review the Fourier relationships between the complex visibility,

$$V(u,\tau) = \langle E(v,t)E(v+u,t+\tau)\rangle \tag{3.72}$$

and a hyperspectral image (modified intensity)

$$I(l,\omega). \tag{3.73}$$

For simplicity, only one spatial (transverse) dimension (u and l) and a temporal (longitudinal) dimension (τ and ω) are specified. The complex visibility can first be Fourier transformed to reveal the spectrum at each spatial frequency u:

$$V(u,\omega) = \int V(u,\tau)e^{2\pi i\tau\omega}d\tau, \tag{3.74}$$

and the hyperspectral image can be recovered by taking the visibility at each spatial frequency and performing another Fourier transform:

$$I(l,\omega) = \int V(u,\omega)e^{2\pi iul}du, \tag{3.75}$$

where $u = \frac{\omega}{2\pi c}\Delta x$ is the distance between sites in terms of the number of wavelengths. These transform pairs are described by the Wiener-Khinchin theorem and the van Cittert-Zernike theorem.

Dual-comb correlation can sample this complex visibility (and thus generate a high-resolution hyperspectral image), and here we describe one possible implementation. The standard setup for dual-comb correlation spectroscopy is arranged at many sites, in Figure 3.11 showing three sites. The photocurrents between the thermal light and the frequency combs are recorded, and timing synchronization is maintained by optical time transfer [16]. These photocurrents are then pairwise correlated with others, noted as $\langle I_x I_y\rangle$, resulting in a plane-by-plane recording of the complex visibility. Such a complex visibility can be transformed as described above to form a hyperspectral image.

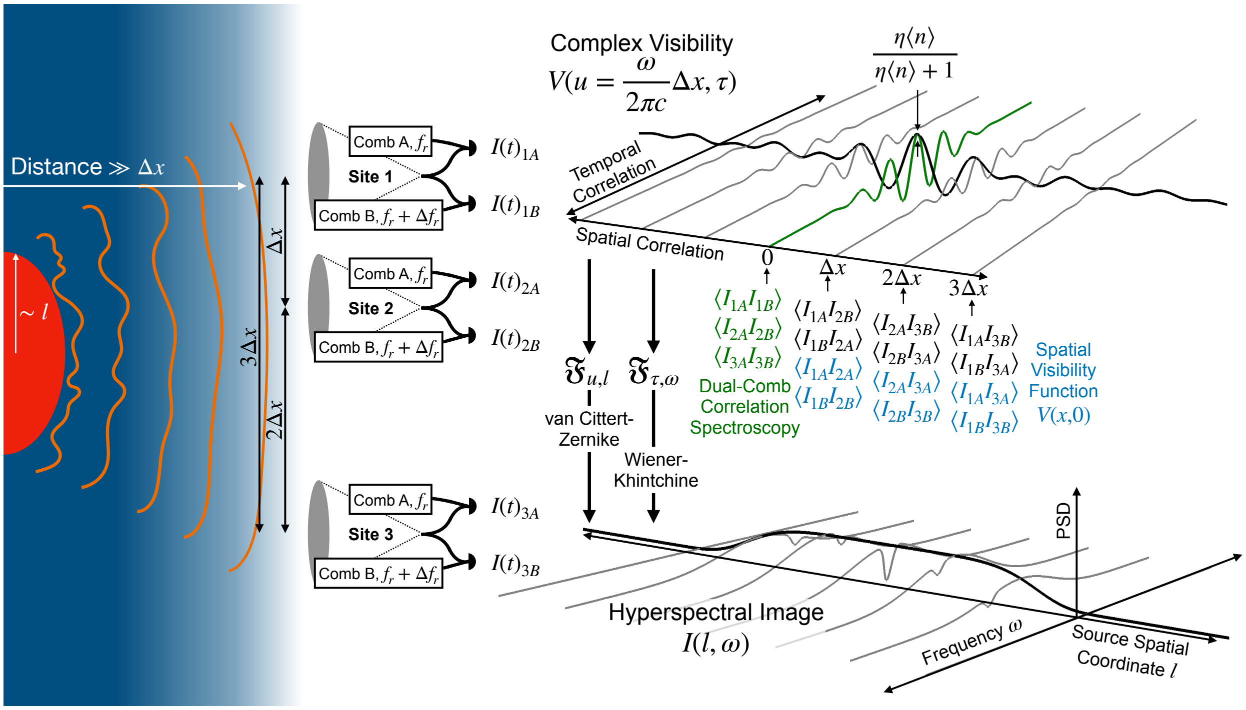

Figure 3.11: Reconstructing the complex (spatial-temporal) visibility function with dual-comb correlation. Here a minimal three sites are represented to correlate the thermal field across three locations. Each pairwise correlation of photo-currents fills in a plane of the complex visibility. The double Fourier transform over frequency and space results in a hyperspectral image of the source.

We note that dual-comb correlation spectroscopy records the complex visibility in the zero transverse spatial delay plane. The maximum single shot signal-to-noise ratio for dual-comb correlation of $\frac{\langle n\rangle}{\langle n\rangle+1}$ derived and verified in this work in fact sets the upper limit for sampling the complex visibility in general. In this work, we showed how this sensitivity translates to the frequency domain for different thermal light powers given our spectral resolution; but this limit can also be used to bound the spatial domain sensitivity limit, though this depends on the specific parameters of the measurement apparatus (aperture size, filling factor, etc.) and source (brightness, distance, wavelength, etc.) [71].

As with radio astronomy arrays, image synthesis of broadband light could provide much higher angular resolution than is available with today's large telescopes and Michelson stellar interferometers. One important area this would address is planetary formation [72], as imaging the Hill sphere in the closest star-forming regions would require baselines/diameters on the order of kilometers, far larger than current optical telescopes. The cost of large-scale telescopes is estimated to scale with a power greater than the square of the diameter [48] quickly reaching infeasible levels, and prohibitive technical challenges occur when scaling up Michelson stellar interferometers to longer distances and especially between many sites [43]. An array of smaller optical telescopes connected and calibrated through optical time transfer may circumvent the need for larger optically aligned single telescopes and provide more advantageous cost scaling as well as a larger area to collect more photons.

3.11.4.1 Ultra-broadband Gray-scale Imaging

I note that higher SNR in the image can be achieved by throwing out the spectral information at each point. This amounts to gray-scale imaging and could simply be achieved by adding all the images at different optical frequencies to construct a brightness map. This can be thought of as equivalent to post-apodization of a dual-comb interferogram to coarsen the spectral resolution. This would grant an SNR improvement of $\sqrt{N_t}$, that is, the square root of the total number of resolved frequencies across all detectors.

Chapter 4

Quantum Optics of Frequency Comb Interferometry

Frequency comb interferometry has supported the most precise realizations and comparisons of time and frequency [73, 74, 46]–and frequency comb interferometry is increasingly used for broadband spectroscopy [17, 75] and broad bandwidth frequency synthesis generation[76, 77, 78]. The fundamental quantum limits of frequency comb measurements have not yet been the limiting factor in measurement precision for these applications, as noise and uncertainty related to other parts of the measurement outweigh the noise of frequency comb measurement.

Yet we may be approaching an era where the noise from the interferometry itself limits measurement precision. In the scenarios highlighted above, often an excess of laser and frequency comb power exists, and higher SNRs can be achieved simply by increasing signal power. Yet there are applications in portable clocks and perhaps also future nuclear clocks in the vacuum ultraviolet and beyond, where coherent laser and frequency comb light are not easy to come by, or there are power limits in terms of photodetection. In these scenarios, one should optimally use the photons available–and in this limit, it is usually the noise set by quantum mechanics that sets the fundamental limit.[1]

In these scenarios, a quantum optical understanding of homodyne and heterodyne with optical frequency combs (or any arbitrary coherent field) is extremely helpful in understanding where the so-called "standard quantum limit" (SQL) lies, and necessary for moving beyond such an SQL with

---

[1] Moreover, it is likely that future experiments utilizing light-matter interaction will rely on coherent and arbitrary optical waveforms (based on optical frequency combs). These might be used, for example, to optimally drive natural quantum systems [18], such as molecules in complex chemical reactions, or synthetic quantum systems such as physical qubits [79].

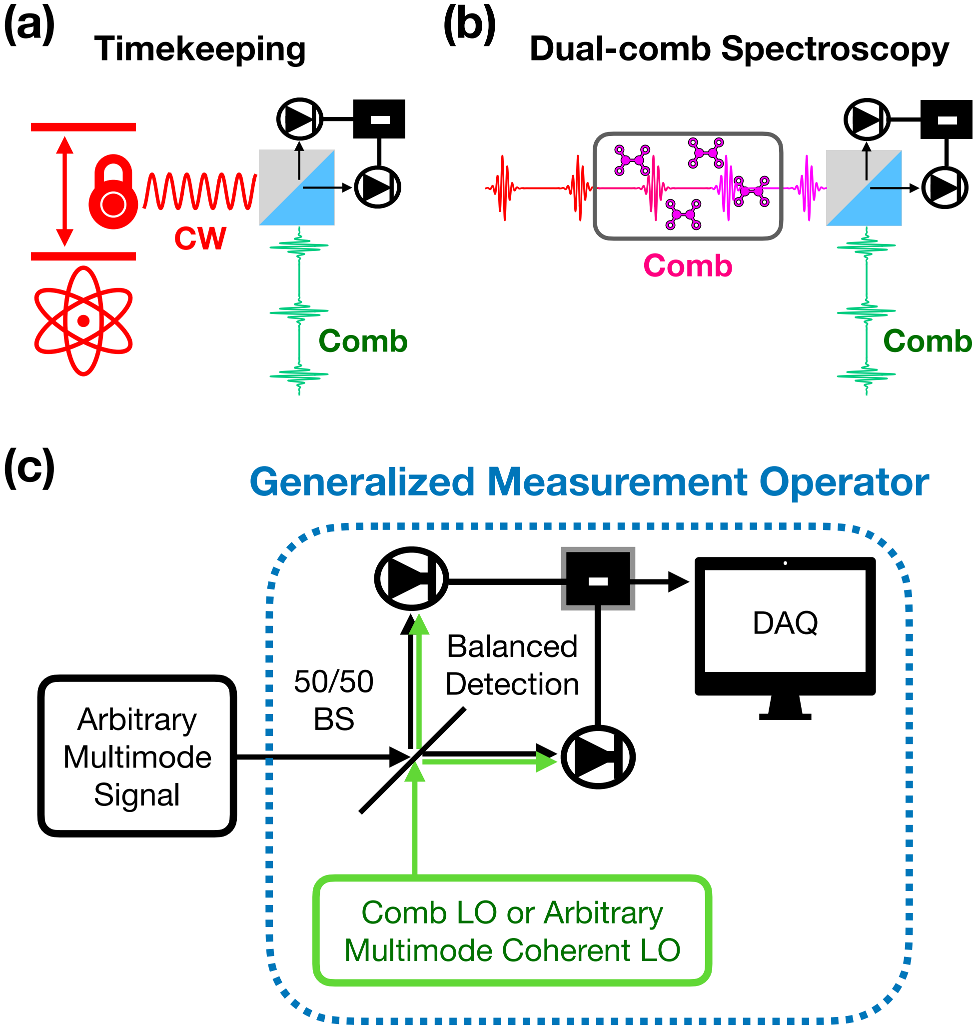

Figure 4.1: How a generalized measurement operator (POVM) applies to frequency comb interferometry.

non-classical states of light.

In this chapter, I present work developed jointly with Noah Lordi and Josh Combes-deriving the measurement operators for homodyne with an optical frequency comb–a scenario which (as explained in the next section) was not describable through existing methods in quantum optics. In general, the homodyne operators describe a scenario that relaxes the large local oscillator limit and treats arbitrary mode overlap, which is a hallmark of frequency-comb measurements.

Although the measurement operators for homodyne measurements are derived here, and most frequency comb measurements today rely on heterodyne, this work provides the necessary foundation for future expansion to a quantum operator view of heterodyne. Moreover, a description of the statistics for heterodyne can always be inferred from the application of repeated homodyne measurements, followed by standard processing (such as a Fourier transform). For the special case of coherent signals, the SNR equation corresponding to the heterodyne measurement SQL can be inferred from the homodyne measurement operators.

This chapter is organized as follows. First, I provide a basic review of quantum optics theory, covering quadrature representations of fields, coherent states, then moving into continuous mode quantum optics.

Then I describe the derivation of the measurement operators, highlighting a temporal mode decomposition technique that allows a convenient description of the measurement operator in two parts.

I then describe several scenarios utilizing these new homodyne operators, identifying that in the coherent signal case, the quantum-limited measurement does not correspond to the SQL typically used in quantum optics measurements. This is due to an excess of signal photons not contributing to the measurement due to mode mismatch, and the measurement operators provide a useful way of understanding the total measurement as a combination of an intensity measurement and a quadrature measurement.

Then I move to experimental predictions of the SQL for frequency comb measurements matching the pure quadrature or coherent state-overlap measurement–matching the standard definition in quantum optics. I review prior work by Jerome Genest and JD Deschenes [21, 22] that utilized a gating technique to move past conventional quantum limits. Lastly, I show efforts to reach the predicted SQL, discussing experimental considerations and limitations in reaching this limit.

4.1 Fundamentals of Quantum Optics

4.1.1 Quantum Harmonic Oscillator and Quadrature Space

Light is governed by Maxwell's equations, which dictate the oscillating wave nature of electromagnetic radiation. Oscillatory systems can be described through the harmonic oscillator, where the energy of the state is parameterized in terms of "kinetic" and "potential" energy. The Hamiltonian for the quantum harmonic oscillator is:

$$\widehat{H} = \frac{\widehat{p}}{2M} + \frac{1}{2}M\Omega^2\widehat{x}^2, \tag{4.1}$$

where $\widehat{p}$ and $\widehat{x}$ are hermitian operators corresponding to measurements of momentum and position, respectively. M is "mass," and Ω is the natural frequency of the oscillator.[2]

The state of the particle or system can then be well described in phase space, where the X axis is the position, and the Y axis is the momentum. This is pictured in Figure 4.2. On the right-hand side of this figure, the particle would move from points A, B, C, D, and back to A, trading kinetic energy for potential energy and back again. This corresponds to the phase space picture on the left-hand side of the figure, where the state traces a circle around the origin. Note that in a classical sense, the position and momentum could be, in principle, exactly defined at the same time.[3]

In the quantum picture, the operators for position and momentum do not commute, which imposes a fundamental limit on the exactness with which position and momentum can be defined at the same time. This can be written as:

$$[\widehat{x}, \widehat{p}] = \widehat{x}\widehat{p} - \widehat{p}\widehat{x} = i\hbar. \tag{4.2}$$

---

[2] The basics of quantum optics are covered in many different texts. I suggest Wolfgang Schleich's *Quantum Optics in Phase Space* [80] as an excellent resource, which I partly follow here.

[3] However, this assertion even breaks down in some classical systems, such as in the time-bandwidth Fourier relationship.

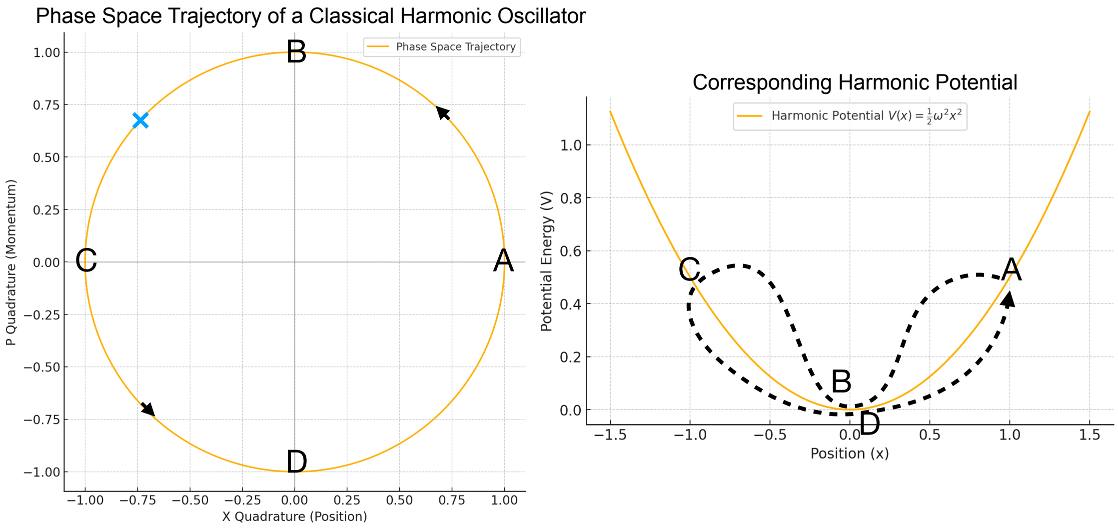

Figure 4.2: Phase space representation of the classical harmonic oscillator **(left)** and the harmonic potential **(right)**.

I also note that the phase space representation is interesting as it depicts Fourier transform pairs on each axis, and thus there is a sense of redundancy to the information displayed in phase space. The same wave function represented in terms of position or momentum is related through a Fourier transform:

$$\psi(x) = (2\pi\hbar)^{-1/2} \int_{\infty}^{\infty} dp \psi(p) e^{ixp/\hbar}. \tag{4.3}$$

4.1.2 Number States

Number states (or Fock states, or energy eigenstates) are perhaps the most natural state to describe given the Hamiltonian above. These are simply states that obey the eigenvalue equation:

$$\hat{H} \left|m\right\rangle = E_m \left|m\right\rangle \tag{4.4}$$

These states can be created from vacuum through the creation operator $\hat{a}^\dagger = \frac{1}{\sqrt{2}}(\hat{x} - i\hat{p})$:

$$\left|n\right\rangle = \frac{1}{\sqrt{n!}} (\hat{a}^\dagger)^n \left|0\right\rangle . \tag{4.5}$$

The number states also obey the following relationships with the creation $a^\dagger$ and annihilation a operators:

$$\hat{a}^\dagger \left|n\right\rangle = \sqrt{n+1} \left|n+1\right\rangle \tag{4.6}$$

and

$$\hat{a} \left|n\right\rangle = \sqrt{n} \left|n-1\right\rangle . \tag{4.7}$$

Number states also form an orthonormal basis in the Hilbert space of states of the quantum harmonic oscillator:[4]

$$\left\langle n\right| \left|m\right\rangle = \delta_{nm}. \tag{4.8}$$

4.1.3 Wigner Function

An exact quantum analogy to the classical phase space is not possible due to the commutation relation of $\hat{x}$ and $\hat{p}$; it is not possible to define a single point corresponding to an exact value of

---

[4] This is not the case for coherent states–which are not normal to each other and over-define the Hilbert space of states.

position and momentum. However, the Wigner function comes close to analogizing the classical phase space picture, and it has some additional properties such as negative values corresponding to the interference of probability amplitudes that prove very valuable for describing non-classical states. The Wigner function is defined as:

$$W(x,p) = \frac{1}{2\pi\hbar}\int_{-\infty}^{\infty} d\xi e^{-\frac{i}{\hbar}p\xi} \left\langle x+\xi/2\right| \hat{\rho} \left|x-\xi/2\right\rangle, \tag{4.9}$$

where $\hat{\rho}$ is the density operator corresponding to the (perhaps mixed) state being described. In words, the Wigner function is the Fourier transform of the shifted position wave functions of some state. This may sound a bit mysterious–and an extended discussion of the Wigner function is beyond the scope of this dissertation–but the marginals of the Wigner distribution are much clearer in their interpretation.

The marginal over momentum p is:

$$\int_{-\infty}^{\infty} dpW(x,p) = \left\langle x\right| \hat{\rho} \left|x\right\rangle = W(x), \tag{4.10}$$

which is simply the probability distribution for the position $W(x)$. Likewise, the marginal over position x is:

$$\int_{-\infty}^{\infty} dxW(x,p) = \left\langle p\right| \hat{\rho} \left|p\right\rangle = W(p), \tag{4.11}$$

which is the probability distribution for the momentum $W(p)$.

4.1.4 Coherent States

Coherent states in quantum optics were first defined by Roy Glauber and E. C. George Sudarshan [23, 81]. These are the states arising from an oscillating charge or dipole, and are equivalent to coherent microwaves emitted through antennas. Perhaps it is surprising that coherent states also describe laser light. In a semi-classical picture, however, the gain medium in an optical resonator can also yield a picture of a classical dipole, as electron clouds move in a synchronized and oscillatory fashion along with the coherent electromagnetic waves reflecting through the resonator.

Another picture of the coherent state is that of a sudden displacement of a harmonic oscillator potential, such that the vacuum Gaussian state is located at, e.g., point A instead of point B/D

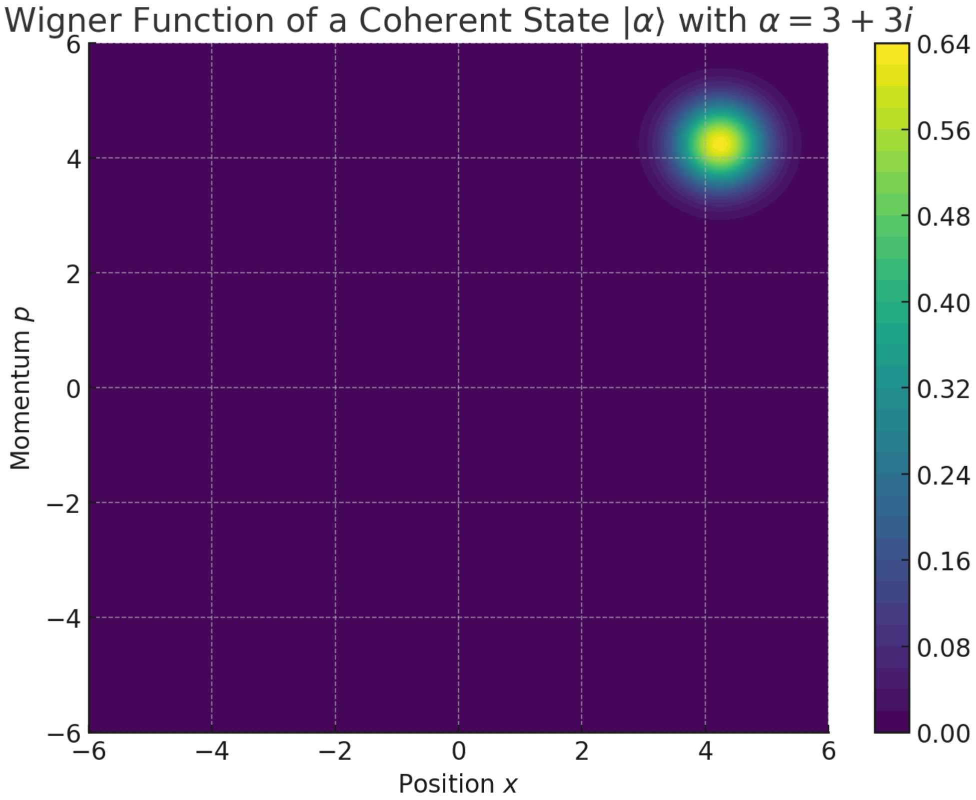

Figure 4.3: Wigner function of a coherent state $|\alpha\rangle$, where the displacement $\alpha = 3 + 3i$. Note that for a bright coherent state of light such as a laser, the mean number of photons is $|\alpha|^2$, and for a 1 µW laser at 1550 nm over 1 µs, this amounts to a mean number of photons of around 8 million, or a $|\alpha|$ of around 3000. Since the width of the Wigner function of a coherent state is always the same, the Wigner function of a coherent state starts to approach the classical definition of phase space defined at a single point.

in figure 4.2. The state then evolves/oscillates because it is not an eigenfunction of the harmonic oscillator potential.

While there are many details about coherent states, here I provide a few significant properties of the coherent state. In terms of number states,

$$|\alpha\rangle = e^{-|\alpha|^2/2} \sum_{n=0}^{\infty} \frac{\alpha^n}{\sqrt{n!}} |n\rangle \, . \tag{4.12}$$

In other words, the coherent state is Poisson distributed in terms of number states–and as we saw in the technical background, at large displacements this yields a Gaussian distribution.

The variance for position and momentum of a coherent state is:

$$\langle\alpha| \, (\Delta x)^2 \, |\alpha\rangle = \langle\alpha| \, (\Delta p)^2 \, |\alpha\rangle = 1/2 \tag{4.13}$$

which is independent of the displacement α.

4.1.5 Positive Operator-Valued Measures

Positive operator-valued measures (POVMs) are a general description of measurements in quantum mechanics, generalizing projective value measurements (that are typically used to describe von Neumann measurements). POVMs are not necessarily orthogonal projectors like PVMs and can therefore describe a wider variety of measurements.

What is a measurement in quantum mechanics? While introductory textbooks claim that it is the projection into some measurement basis of some object or system–in reality, we never directly measure the system that we are interested in. In fact, we couple this object to another system, often termed an ancilla, and then make some kind of measurement on this ancilla. We assume that we know the interaction between the primary system and the ancilla (which can be described by some unitary operator U acting on the joint system of the primary system and the ancilla). Then we ask the following question: What measurement did the ancilla read? Most generally (and frequently) the outcome of this measurement actually corresponds to many possible projective measurements of the primary system. In fact, in full generality, this measurement on the ancilla does not tell us about the final state of the primary system.

POVMs describe this general model of measurement where an ancilla is measured that has interacted with the primary quantum system. The POVM is defined as:

$$E_\alpha = \mathrm{Tr}_A(U^\dagger P_\alpha U \sigma), \tag{4.14}$$

where α is a measurement outcome on the ancilla, denoted as system A, P_α is the sum of projective measurements on the ancilla resulting in α, i.e., $P_\alpha = \sum_j |f_{\alpha j}\rangle \langle f_{\alpha j}|$, and σ is the density matrix of the ancilla, i.e., $\sigma = \sum_k \lambda_k |e_k\rangle \langle e_k|$–where $|e_k\rangle$ are the eigenstates of σ. In fact, the POVM takes into account the state of the ancilla and the possible interactions between the primary system and ancilla that result in some measurement result α, then traces out the ancilla space such that the matrix acts on the space of the primary system. The probability for a measurement outcome α is then:

$$p_\alpha = \mathrm{Tr}(\rho E_\alpha), \tag{4.15}$$

where ρ is the initial state (density matrix) of the primary system. Indeed the POVM gives the *full* probability distribution–whereas many techniques for gleaning probability in quantum optics only give the first and second moments. While the technical background reviewed in this thesis claimed that for most measurements in classical time and frequency metrology Gaussian statistics are all that is needed, exotic quantum states such as cat states and number states (non-Gaussian states) do display statistics that require higher order moments to describe. This generality makes POVMs powerful.

4.1.6 Classical vs. Quantum Optical Homodyne and Heterodyne

Homodyne and heterodyne measurements are cornerstones of both classical and quantum optical experiments. What are the differences between the classical and quantum cases? The differences lie in the common assumptions made about homodyne and heterodyne as well as the emphasis on what the measured quantity is.

In quantum optics, homodyne measurements typically assume that the local oscillator (LO) is much larger than the signal, that the LO and signal are mode-matched, and, as is true in the classical case, that the carrier frequencies are the same between the LO and the signal. As such, measurements are generally made at DC[5] and are considered "phase sensitive," since the relative phase of the LO and the signal can be inferred by the value of the measurement result. In quantum optics experiments, mode-matching is often the ideal case, and close to mode-matching is possible, as the signal can be generated by splitting a portion of the LO and introducing various non-linearities to create non-classical states. Given these conditions, homodyne measurements in quantum optics are understood as measures of an arbitrary quadrature of the electromagnetic field, e.g.,

$$\hat{X}_\theta = \frac{1}{\sqrt{2}}(\hat{a}e^{-i\theta} + \hat{a}^\dagger e^{i\theta}), \tag{4.16}$$

where θ is an angle in phase space.

Heterodyne measurements in quantum optics also generally assume mode-matching and a large LO. In line with the classical situation, the signal and local oscillator have different carrier frequencies. The measurement apparatus is assumed to be able to detect this difference in carrier frequencies, but any information regarding individual "homodyne" measurements composing these data is marginalized when the Fourier transform is taken to analyze the amplitude of the beat between the LO and signal fields. In classical optics, heterodyne can refer to the time trace as well as the Fourier transform, but typically in quantum optics, heterodyne refers to the measurement after the Fourier transform has been taken and is thus considered phase insensitive, since the amplitude of this Fourier component does not depend on the initial phase offset between the signal and LO. Heterodyne also carries a natural interpretation in the language of field quantization. It is considered a simultaneous measurement of two orthogonal quadratures of the field, which simplifies to being the annihilation operator:

$$\hat{X} + i\hat{P} = \frac{1}{2}[(\hat{a} + \hat{a}^\dagger) - i^2(\hat{a} - \hat{a}^\dagger)] = \hat{a}. \tag{4.17}$$

Since it is the quadrature state that is the eigenstate of the homodyne operator (of matching phase), homodyne is considered to be an overlap of the signal with a quadrature eigenstate. Likewise

---

[5] Although sometimes some form of modulation is added or mixed with the DC signal such that low frequency technical noise can be bypassed.

with heterodyne, it is the coherent state that is an eigenstate of the annihilation operator, and heterodyne measurement can be considered overlap with a coherent state.

4.2 Continuous-Mode Quantum Optics and Mode Functions

The above formulations of quantum optics are all built on the assumption of a single mode, which most often means that all states are defined in the same mode–be that frequency, spatial, polarization, temporal, and perhaps others.

Yet in realistic scenarios, mode-matching is often not the case. In most cases we deal with fields of varied spectra and shape, interacting with other fields and apparatuses with their own complex mode function. Here we must employ the additional layer of continuous modes in quantum optics.

Standard mode theory employs boundary conditions of some finite resonator defining the allowed modes of the state. In continuous mode quantum optics, we take the limit to infinity of the resonator length, which produces a continuum of modes.

In other words, in the previous definitions, we assumed that we were referring to a single mode, perhaps a longitudinal mode of an optical resonator. To be more specific, the annihilation and creation operators actually obey the commutation relation:

$$[\hat{a}_i, \hat{a}_j^\dagger] = \delta_{ij}, \tag{4.18}$$

where i and j label orthogonal modes, and for example, the modes of the resonator are spaced by $\Delta\omega = 2\pi c/L$, where L is the resonator length. We seek to take the continuum limit as L approaches infinity and $\Delta\omega$ approaches zero. See Blow *et al.* [82] for a detailed treatment. In this limit,

$$\hat{a}_i \to \sqrt{\Delta\omega}\hat{a}(\omega), \tag{4.19}$$

where the continuous creation and annihilation operators now have units of per square root bandwidth. These continuous operators obey the Dirac delta commutation relations (vs. Kronecker delta):

$$[\hat{a}(\omega), \hat{a}^\dagger(\omega'))] = \delta(\omega - \omega')). \tag{4.20}$$

We have defined the continuous frequency mode annihilation and creation operators, which now, through a Fourier transform, allow us to define the instantaneous annihilation and creation operators in time:

$$\hat{a}^\dagger(t) = \frac{1}{2\pi}\int d\omega \hat{a}^\dagger(\omega)e^{i\omega t}. \tag{4.21}$$

These obey the commutation relation:

$$[\hat{a}(t), \hat{a}^\dagger(t'))] = \delta(t-t'). \tag{4.22}$$

From these instantaneous creation operators, we can now define the arbitrary mode of a field. We define the mode creation operator $\hat{A}^\dagger(\xi)$ in some temporal mode $\xi(t)$, also known as the field envelope,

$$\hat{A}^\dagger(\xi) = \int_0^T dt\, \xi(t)\hat{a}^\dagger(t)\,, \tag{4.23}$$

where $\hat{a}^\dagger(t)$ is the creation operator that creates a photon at time t. These mode operators carry the usual commutation relations $[\hat{A}(\xi), \hat{A}^\dagger(\xi)] = 1$ unlike the instantaneous creation operators which have units of sec$^{-1/2}$. This is the mode function that tells you the complex envelope of the electric field, which allows full definition of any field.[6]

4.3 Past Quantum Optics Treatments of Homodyne

Homodyne measurements [83] are fundamental in both quantum optics and precision metrology, allowing manipulation [84, 85] and characterization [86, 87, 88] of quantum states.

Now that we have covered some of the basic building blocks of continuous-mode quantum optics, we review past treatments of homodyne detection from a quantum optics perspective. In a single mode, homodyne is understood as a measurement of a quadrature of the electromagnetic field [89, 90, 91, 92], e.g.,

$$|x\rangle\langle x|\,. \tag{4.24}$$

---

[6] This is as long as $\omega_0 \gg \Delta\omega$, or that the bandwidth is small compared to the carrier frequency. It is a very interesting question what arises beyond this slowly varying envelope approximation! And one that perhaps we are close to experimentally probing with coherent single cycle laser pulses.

Many multimode homodyne formulations assume that the signal and local oscillator (LO) share the same temporal mode [93, 94, 95, 82, 96, 78] resulting in qualitatively similar quantum descriptions and limits as in the single mode case. In experiment, this is often done by deriving the signal and local oscillator from the same laser source, thus aiding in matching of the underlying carrier frequency as well as the general shape of the pulses (though differential dispersion and nonlinearity of course play a role in mode-mismatch).

The temporal mode mismatch between the signal and LO has been understood as an effective loss [97, 86, 87, 98, 99], meaning that the information or signal gained from the measurement is simply attenuated by the level of mode mismatch. However, these works operate in a regime where the LO strength dominates the signal strength, which is often not realistic. In other words, these works do not consider the effects of finite-strength LOs, high signal strength, and a high mode mismatch evident in many experiments [21, 22, 100]. As will be shown later, these experiments observe additional shot noise due to mode mismatch, which is unexplained by effective loss alone.

4.4 The Situation in Optical Frequency Comb Metrology

Over the past two decades, optical frequency combs [47] have emerged as a powerful tool for characterization and dissemination of the most precise clocks [73, 74, 46], precision spectroscopy [17, 75] and broad bandwidth frequency synthesis [76, 77, 78]. In these measurements, the frequency comb LOs have very high peak power but relatively small average power; as a result, the finite-strength LO effects are important, particularly when the signal has a similar average power to the LO. This is the case in dual-comb spectroscopy as well as in the heterodyne between a frequency comb and a CW laser, which is used to either lock the frequency comb or measure the frequency of the CW laser against the frequency comb reference.

As comb-based measurements near putative shot-noise quantum limits [101, 21, 74, 102], a quantum measurement description that addresses temporal mode mismatch and finite field strengths is crucial to determine the fundamental limits of precision. A complete quantum theory also forms the foundation of frequency comb metrology with non-classical light [103, 104, 105, 106].

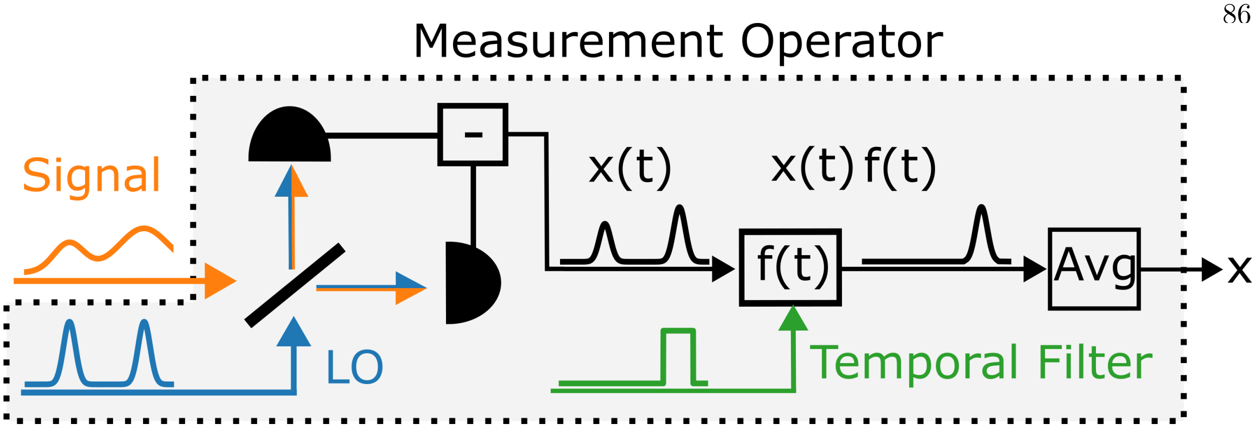

Figure 4.4: Temporally mismatched homodyne measurement with signal processing. The signal and local oscillator (LO) have different temporal modes, resulting in a mismatch. The detectors produce a photocurrent proportional to the intensity of the field and the instantaneous difference is denoted by $x(t) \propto I_1(t) - I_2(t)$. We compute the measurement operators for this setup and consider filtering the photocurrent. This filtering removes the additional shot noise due to mode mismatch. We describe the set of filters that do not affect the measured quadrature and achieve SNRs considerably larger than the unfiltered SNR.

We expect this to be important for comb-based measurements aiming to exceed the standard quantum limit [107, 108, 109, 110, 111].

4.5 Positive Operator Valued Measure-based Quantum Optics Theory

Now we show a quantum description of temporally mismatched homodyne measurement. A conceptual overview of this description is shown in Fig. 4.4. Specifically, we derive the measurement operators, that is, the positive operator-valued measures (POVMs), which enable the calculation of measurement statistics for any signal state and coherent LO both with arbitrary time dependence.[7]

As an overview of the following sections, next, in Sec. 4.5.1 we use continuous mode quantum optics and the Gram-Schmidt procedure to decompose the mode of an incoming signal into the mode of the LO and an orthogonal mode. This temporal mode decomposition is used to derive measurement operators for modal homodyne in Sec. 4.5.2, which is our main result. The measure-

---

[7] POVMs are a generalization to projective measurements akin to the density operator vs. state wavefunction. POVMs describe all measurement statistics.

ment operator consists of two parts: a quadrature measurement (corresponding to the LO mode) and an intensity-like measurement (corresponding to the orthogonal mode). We then illustrate our formalism in Sec. 4.6 with several examples. Specifically we use our analysis to develop a new quantum limit for comb-based measurement and provide quantum theoretic grounds for experimental results demonstrating better-than-shot noise-limited performance by Deschênes and Genest [21] via temporal filtering. We also present measurement statistics for an example non-classical signal that–to our knowledge–cannot be described by existing analyses. Finally, in Sec. 4.6.4 we conclude with a discussion of the implications of our results for heterodyne, which is the standard measurement with frequency combs.

4.5.1 Continuous Modes and Gram-Schmidt

In a balanced homodyne measurement, the signal and local oscillator (LO) are combined on a beamsplitter and both output ports are detected. The resulting photocurrents are then subtracted and the difference is recorded as the measurement result (see Fig. 4.4). Typically, the LO strength dominates the signal strength and the LO is temporally mode-matched to the signal. Here we do not assume that the signal and LO are mode-matched and allow for arbitrary mode overlap. For this reason, we need to employ continuous mode quantum optics [82]–see Sec. 4.5.1.

To describe time-dependent homodyne measurements, we introduce independent and arbitrary complex temporal modes for the signal and LO, denoted by the mode functions $\xi_{\mathrm{S}}(t)$ and $\xi_{\mathrm{LO}}(t)$. These modes are normalized over the detection interval $(0, T)$, that is, $\int dt' \, |\xi(t')|^2 = 1$. To analyze this measurement we build an orthonormal basis of temporal modes around the LO mode. This is physically motivated because the time dependence of ξ_{LO} is known and controlled in an experiment. Although there are perhaps competing definitions for what the LO is and what the signal is—-typically it is the signal that we seek to measure and the LO that serves as a known reference to measure the signal.

We construct this basis using the standard Gram-Schmidt process, beginning with ξ_{LO} and

ξ_{S}. We label this basis as $\{\xi_{\mathrm{LO}}, \xi_{\perp}, \xi_3, ...\}^8$, and define:

$$\begin{aligned} \xi_{\mathrm{LO}}(t) &= \xi_{\mathrm{LO}} \\ \xi_{\perp}(t) &= \frac{\xi_{\mathrm{S}} - \langle \xi_{\mathrm{LO}}, \xi_{\mathrm{S}} \rangle \xi_{\mathrm{LO}}}{\sqrt{1 - |\langle \xi_{\mathrm{LO}}, \xi_{\mathrm{S}} \rangle|^2}} \end{aligned} \tag{4.25}$$

where $\langle f, g \rangle = \int_0^T dt' f^*(t') g(t')$ is the inner product. For convenience we also define the mode overlap, $\gamma \equiv \langle \xi_{\mathrm{LO}}, \xi_{\mathrm{S}} \rangle$. The measurement can be completely understood in these two modes because the signal can be decomposed into a linear combination of just ξ_{LO} and $\xi_{\perp}$.

To demonstrate how to decompose an example signal we can consider the case where the signal is continuous wave (CW) and the LO is a Gaussian pulse, representing, e.g., a short temporal section of a frequency comb. In the frame rotating at the carrier frequency we have,

$$\xi_{\mathrm{S}} = \frac{e^{i\phi}}{\sqrt{T}}, \quad \text{and} \quad \xi_{\mathrm{LO}} = \left[\frac{e^{-(t-\mu)^2/(2\sigma^2)}}{\sqrt{2\pi\sigma^2}} \right]^{1/2}. \tag{4.26}$$

Fig. 4.5 illustrates these modes with $\mu = T/2$, $\sigma \approx .1T$, and $\phi = 0$. Assuming the LO pulse is fully contained in the detection interval the mode overlap is $\gamma = \left(8\pi\sigma^2 T^{-2}\right)^{1/4} e^{i\phi}$. The mode overlap is maximized when the ratio of the pulse width to the detection interval is maximal. Intuitively this is when the pulse is the most "CW like" on the detection interval. Further the appearance of the phase $e^{i\phi}$ demonstrates that the mode overlap is complex in general.

Using equation Eq. (4.25) we can also calculate the perpendicular mode

$$\xi_{\perp} = \frac{e^{i\phi}}{\sqrt{T - \sigma\sqrt{8\pi}}} \left(1 - 2e^{-(t-\mu)^2/(4\sigma^2)}\right), \tag{4.27}$$

which is pictured in Fig. 4.5(b). This mode represents the piece of the signal that does not interact with the local oscillator. We will see in Sec. 4.5.2 that the perpendicular mode will contribute intensity like noise.

Returning to the general case where the modes ξ_{S} and ξ_{LO} are arbitrary, we define modal coherent states as [82, 56, 98],

$$|\alpha_{\xi_{\mathrm{S}}}\rangle = D(\alpha, \xi_{\mathrm{S}})|0\rangle = \exp\left[\alpha \hat{A}^\dagger(\xi_{\mathrm{S}}) - \alpha^* \hat{A}(\xi_{\mathrm{S}})\right] |0\rangle. \tag{4.28}$$

---

[8] The numbered modes are necessary to complete the temporal mode basis, but will not contribute to the measurement operators. Additionally the above basis is ill-defined if $\xi_{\mathrm{LO}} \propto \xi_{\mathrm{S}}$, but this is the mode-matched limit where theoretical treatments already exist.

It is straightforward to show that $A(\xi_{\rm S}) = \gamma^* A(\xi_{\rm LO}) + \sqrt{1-|\gamma|^2}A(\xi_\perp)$. Using this along with an application of the Baker–Campbell–Hausdorff, and $[\hat{A}(\xi_1), \hat{A}^\dagger(\xi_2)] = \langle \xi_1, \xi_2 \rangle$ and we get the modal decomposition,

$$\begin{aligned} D(\alpha, \xi_{\rm S}) =& D(\gamma\alpha, \xi_{\rm LO}) \otimes D(\sqrt{1-|\gamma|^2}\alpha, \xi_\perp) \\ & \times \exp\left\{ |\alpha|^2 \left(\mathrm{Im}(\gamma^* \sqrt{1-|\gamma|^2} \langle \xi_\perp, \xi_{\rm LO} \rangle \right) \right\}. \end{aligned} \tag{4.29}$$

Since we have defined our mode basis to be orthonormal we know that $\langle \xi_\perp, \xi_{\rm LO} \rangle = 0$ and thus the exponential term is 1. This allows us to decompose a coherent state signal into the LO and $\perp$ modes

$$|\alpha_{\xi_{\rm S}}\rangle = |\gamma\alpha_{\xi_{\rm LO}}\rangle \otimes |\sqrt{1-|\gamma|^2}\alpha_{\xi_\perp}\rangle. \tag{4.30}$$

This will be useful in Sec. 4.6 when we consider the measurement of a coherent signal.

4.5.2 Modal Homodyne Measurements

The photodetectors in homodyne measurements respond to intensity. In the noiseless limit, intensity detection is photon number resolving. Like previous work [92, 112] we use photon number resolving detectors for our analysis, but the noisy detector limit can always be recovered by coarse graining. However, in our analysis, we must consider photodetection in certain temporal modes. That is, we model photodetection as projections onto Fock states in a given mode:

$$|n_\xi\rangle = \frac{\hat{A}^\dagger(\xi)^n}{\sqrt{n!}} |\mathrm{vac}\rangle, \tag{4.31}$$

which are eigenstates of the number operator $\hat{A}^\dagger(\xi)\hat{A}(\xi)$. We use the notation where operators with modes are written with parentheses, $M_{n,m}(\xi)$, and states in modes are denoted with subscripts, $|n_\xi\rangle$.

We assume the detector is unable to differentiate a LO-mode photon from an orthogonal-mode photon. The detector acts as a projector onto a combination of all the possible modes in our basis that could produce a click. For this reason, we construct the n click measurement operator

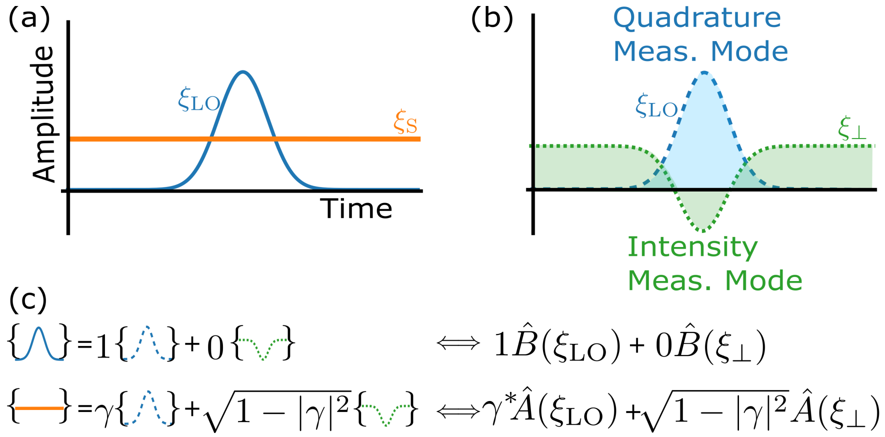

Figure 4.5: (a) The physical CW signal (orange) and Comb pulse LO (blue) modes incident on the beamsplitter. (b) The Gram-Schmidt modes which correspond to quadrature measurement and intensity-like measurement. (c) The signal and LO modes have some overlap, but we can decompose them into the Gram-Schmidt basis. We can write the signal and LO as a linear combination of these basis elements, here γ is the complex-valued mode overlap, $\gamma = \langle \xi_{\rm LO}, \xi_{\rm S} \rangle$. This same decomposition can be used on the operators $\hat{B}(\xi_{\rm LO})$ and $\hat{A}(\xi_{\rm S})$.

by marginalizing over the mode degree of freedom

$$|\mathrm{vac}\rangle\langle n|_D = \sum_{p=0}^{n} |\mathrm{vac}\rangle \left(\langle p_{\xi_{\mathrm{LO}}}| \otimes \langle n - p_{\xi_\perp}|\right) , \tag{4.32}$$

where we assume our detectors absorb photons, hence the projection onto vacuum. Now we follow the analysis of Ref. [112] to arrive at the measurement (Kraus) operator that corresponds to observing n clicks on one detector and m clicks on the other:

$$M_{n,m} = \langle n|_{D1}\langle m|_{D2} U_{\mathrm{BS}}|\psi_{\mathrm{LO}}\rangle . \tag{4.33}$$

We choose the LO to be a coherent state in ξ_{LO}, $|\psi_{\mathrm{LO}}\rangle = |\beta(\xi_{\mathrm{LO}})\rangle \otimes |0_{\xi_\perp}\rangle$. We assume our detectors absorb photons so we have used $\langle n|_{D_1}$ as shorthand for $|\mathrm{vac}\rangle\langle n|_{D_1}$. Here the operator $M_{n,m}$ is not given a mode because it pertains to the total clicks over all modes. At the moment these measurement operators are written in terms of n and m, but ultimately we will express the POVM in terms of the difference and sum photocurrent $x \propto n - m$ and $w \propto n + m$ respectively.

We use the definition in Eq. (4.32) and re-order the tensor product to write the measurement operators in our preferred basis

$$\begin{aligned} M_{n,m} &= \sum_{p,q} \underbrace{\langle p_{\xi_{\mathrm{LO}}}|\langle q_{\xi_{\mathrm{LO}}}|}_{\text{LO modes}} \underbrace{\langle n - p_{\xi_\perp}|\langle m - q_{\xi_\perp}|}_{\perp \text{ modes}} U_{\mathrm{BS}}|\psi_{\mathrm{LO}}\rangle , \\ &= \sum_{p,q} M_{p,q}(\xi_{\mathrm{LO}}) \otimes M_{n-p,m-q}(\xi_\perp) \end{aligned} \tag{4.34}$$

where we assume the beamsplitter behaves uniformly across modes (App. B.1), although this assumption can be relaxed [113]. Equation (4.34) shows a decomposition of the measurement operators into two temporal modes

$$M_{p,q}(\xi_{\mathrm{LO}}) = \langle p_{\xi_{\mathrm{LO}}}|\langle q_{\xi_{\mathrm{LO}}}|U_{\mathrm{BS}}|\beta_{\xi_{\mathrm{LO}}}\rangle \tag{4.35a}$$

$$M_{r,s}(\xi_\perp) = \langle r_{\xi_\perp}|\langle s_{\xi_\perp}|U_{\mathrm{BS}}|\mathrm{vac}\rangle. \tag{4.35b}$$

To obtain our final result for this operator we need to leverage the methods of Refs. [92, 112] which involve four steps. **Step 1.** We need to perform a change of variables on our operators so they are written in terms of the sum and difference variables. For both modes now we change from the n and m variables to sum and scaled difference variables

$$x = \frac{n-m}{\sqrt{2}|\beta|e^{i\theta}} \quad \& \quad w = n+m, \tag{4.36}$$

where θ is the phase of the LO. We do this because we want our operators to describe the observed quantities of the measurement, which is the difference photocurrent. In the large LO limit, we will approximate x as a continuous variable. **Step 2.** We construct the POVM from the measurement operators in Eq. (4.34) as $E = M^\dagger M$ (App. B.2). After a number of approximations we arrive at

$$E_{x,w} = \sum_{w'} \int dx' E_{x',w'}(\xi_{\text{LO}}) \otimes E_{x-x',w-w'}(\xi_\perp)\,, \tag{4.37}$$

where $E_{x,w}(\xi_{\text{LO}})$ and $E_{x,w}(\xi_\perp)$ are the POVMs for the measurement in each mode. The POVM elements are the operators that gives rise to the statistics observed in an experiment. **Step 3.** For the analysis of the LO mode we need to assume the LO is large so that we are in the homodyne limit, this entails assuming that $\langle \hat{n}(\xi_{\text{LO}})\rangle_{\text{S}} \ll \langle \hat{n}(\xi_{\text{LO}})\rangle_{\text{LO}}$, i.e., the LO dominates the signal in the LO mode (App. B.3). Thus the difference variable x is quasi-continuous. **Step 4.** We marginalize over the sum variable as it is not typically observed in experiments. We can now state our main result which is the total POVM for a time-dependent LO

$$E_x = \sum_w E_{x,w} = \int dx' E_{x'}(\xi_{\text{LO}}) \otimes E_{x-x'}(\xi_\perp)\,, \tag{4.38}$$

this is a convolution of a POVM in the LO and perp modes (App. B.4). We absorbed the Jacobian from changing variables into the single mode POVMs so that both the total and single mode POVMs sum to identity. In Eq. (4.38) x on the LHS is the difference photocurrent while x' and $x - x' \equiv v$ on the RHS are the difference variable contributions from the LO and $\perp$ mode respectively, c.f. Eq. (4.34).

A detailed calculation shows the LO mode POVM is a homodyne measurement of a time-dependent quadrature (App. B.2.2)

$$E_{x'}(\xi_{\text{LO}}) = |x'_{\xi_{\text{LO}}}\rangle\langle x'_{\xi_{\text{LO}}}|, \tag{4.39}$$

here $|x'_{\xi_{\rm LO}}\rangle$ is an eigenstate of the modal quadrature operator $\hat{Q}(\xi_{\rm LO}) = (\hat{A}(\xi_{\rm LO}) + \hat{A}^\dagger(\xi_{\rm LO}))/\sqrt{2}$. This quadrature operator is time-dependent in the sense that $\xi_{\rm LO}$ may have different phases at different times, see Fig. 4.6.

In the perpendicular mode, the LO is in vacuum, and the analysis yields a POVM that follows a binomial distribution in n and m. After switching to sum and difference variables we have (App. B.2.1):

$$E_v(\xi_\perp) = \sum_w |w_{\xi_\perp}\rangle\langle w_{\xi_\perp}|\mathrm{Bin}\Big(\frac{|\beta|v}{\sqrt{2}}\Big|w, \frac{1}{2}, 0\Big)\,, \tag{4.40}$$

where $|w_{\xi_\perp}\rangle$ is a Fock state and $\mathrm{Bin}(x\big|n, p, \mu)$ is a binomial distribution characterised by n and p and shifted so that it has mean μ [114]. Here we have used the difference variable v as if it were discrete, but it must be approximated as continuous to be consistent with Eq. (4.38). In Eq. (4.40) the difference variable distribution has mean 0 and variance $w/(2|\beta|^2)$, and this is true regardless of the signal state. Only the variance of the difference variable actually depends on the input state. In other words, this is not a quadrature measurement and instead resembles an intensity measurement, as evidenced by the projector onto Fock states.

We have derived the POVM starting from the slow detector limit. For detectors that can resolve the time dependence of the signal and LO the Kraus operators would change. This time-dependent photo-record must be treated carefully. So long as the additional time dependence is averaged over, the measurement statistics predicted by the POVM presented here would remain correct, meaning our POVM is valid in any detector bandwidth limit (App. B.5).

4.6 Examples

We now illustrate the use of these theoretical tools with three examples. First, we apply our results to coherent signals and explore the limits of filtering. In the first two examples we apply filtering to a signal with known and unknown temporal profiles. These examples explain a remarkable demonstration by [21] of higher SNR than that set by shot noise of the total photocurrent, achieved by filtering the measurement record. Finally, we utilize our measurement operators to

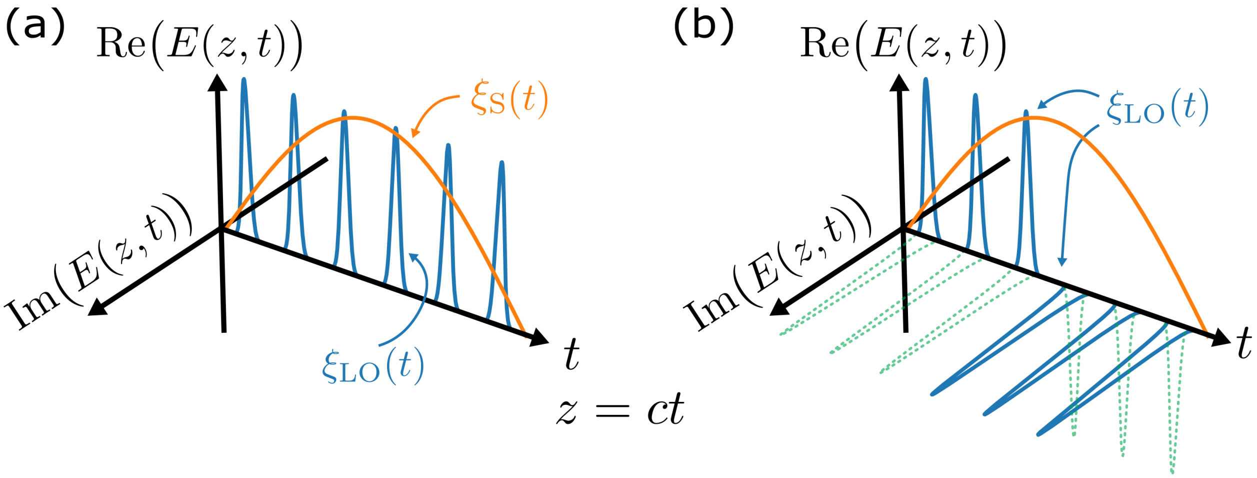

Figure 4.6: The classical mode functions of a time dependant homodyne measurement. Here the mode $\xi_{\mathrm{LO}}(t)$ is that of a comb, while the signal mode ξ_{S} is half a period of a sinusoid. (a) the LO phase is constant over the signal and thus the modal quadrature measurement is consistent with a CW quadrature measurement. (b) the phase of the LO has an abrupt change so the time-dependent quadrature is inconsistent with CW quadrature measurement. Our formalism allows for such time-dependent quadratures. The orthogonal time-dependent quadrature $\hat{P}(\xi_{\mathrm{LO}}) = -i(\hat{A}^{\dagger}(\xi_{\mathrm{LO}}) - \hat{A}(\xi_{\mathrm{LO}}))/\sqrt{2}$ is the dotted line.

analyze the measurement of a single photon which cannot be calculated using semi-classical methods. Moreover, the filtering technique we explore could be of interest to weak field homodyne when there is mismatch between the weak LO and the signal [115, 116, 117].

4.6.1 Coherent State Signal and SNR Bound

We take the signal to be a coherent state $|\psi\rangle_{\mathrm{S}} = |\alpha_{\xi_{\mathrm{S}}}\rangle$ and decompose the signal into the LO mode and the perpendicular ($\perp$) mode as in Eq. (4.30).

We derive the distribution of the total measurement by taking the expectation of the POVM, Eq. (4.38), which is $P(x) = \langle\alpha_{\xi_{\mathrm{S}}}|E_x|\alpha_{\xi_{\mathrm{S}}}\rangle$ (App. B.6). If the detector could differentiate photons in the perpendicular and LO modes, then the joint distribution of clicks in the two modes would be

$$P(x_{\mathrm{LO}}, x_{\perp}) = \mathcal{N}\left(x_{\mathrm{LO}}|\mu_{\mathrm{LO}}, \sigma^2_{\mathrm{LO}}\right)\mathcal{N}\left(x_{\perp}|\mu_{\perp}, \sigma^2_{\perp}\right), \tag{4.41}$$

where $\mathcal{N}$ denotes a normal distribution, $\mu_{\mathrm{LO}} = \sqrt{2}\mathrm{Re}(\alpha\gamma)$, $\sigma^2_{\mathrm{LO}} = 1/2$, $\mu_{\perp} = 0$, and $\sigma^2_{\perp} = |\alpha|^2(1-|\gamma|^2)/2|\beta|^2$. Here we have used the convention that β is real, i.e., the phase of LO is the reference phase. Because the signal is a coherent state, which is uncorrelated in time, the distributions of $x_{\perp}$ and x_{LO} are independent. This means if we marginalize, or filter, over the $\perp$-mode we could obtain an "ideal" homodyne measurement of the signal in the LO mode.

The real detectors cannot differentiate between the two modes so the distributions must be convolved yielding,

$$P(x) = \mathcal{N}\left(\mu = \sqrt{2}\mathrm{Re}(\gamma\alpha), \sigma^2 = \frac{1}{2} + \frac{|\alpha|^2(1-|\gamma|^2)}{2|\beta|^2}\right). \tag{4.42}$$

From this, we find the power signal-to-noise ratio (SNR):

$$\mathrm{SNR} = \frac{|\mu|^2}{\sigma^2} = \frac{4|\beta|^2\mathrm{Re}(\gamma\alpha)^2}{|\beta|^2 + (1-|\gamma|^2)|\alpha|^2}. \tag{4.43}$$

As the signal and LO become mode-matched, i.e., $|\gamma|^2 \to 1$, we recover the expected SNR for ideal homodyne detection: $\mathrm{SNR}_{|\gamma|\to 1} = 4\mathrm{Re}(\gamma\alpha)^2$.

When γ is small and $|\beta|^2 \gg |\gamma\alpha|^2$, i.e., large mode-mismatch, a Taylor expansion yields

$$\mathrm{SNR}^{\mathrm{total}}_{\gamma\to 0} \approx \frac{4|\beta|^2\mathrm{Re}(\gamma\alpha)^2}{|\beta|^2 + |\alpha|^2}. \tag{4.44}$$

Thus $\mathrm{SNR}^{\text{total}}$ has its mean attenuated by the mode-mismatch $\mathrm{Re}(\gamma)$ as predicted by prior theory [97, 86, 87, 99]. Additionally, there are shot noise contributions from both the signal and LO since no assumption allows either noise term to dominate. The above SNR is conventionally accepted as the quantum limit for frequency comb measurements [101].

This conventional SNR limit was first questioned in an experiment by Deschênes and Genest [21], where they applied a filter matched to the LO intensity and achieved a sizeable SNR improvement over Eq. (4.44). We reconsider this technique specifically for the case where we want to measure the time dependent quadrature operator $\hat{Q}(\xi_{\mathrm{LO}})$ and the mode of the signal ξ_{S} is unknown.

The optimal filter of the photocurrent is described by the time-dependent weighting function,

$$f(t) = \begin{cases} 1 & \text{if } \xi_{\mathrm{LO}}(t) \neq 0 \\ 0 & \text{if } \xi_{\mathrm{LO}}(t) = 0 \end{cases}, \tag{4.45}$$

which must be approximated in many cases. This function leaves the LO mode unchanged, so it will preserve the mode of the measured quadrature and leave the mean, unchanged. This filter will reduce the shot noise contribution from the perpendicular mode. The achievable filtered SNR is

$$\mathrm{SNR}^{f(t)} = \frac{4|\beta|^2 \mathrm{Re}(\gamma\alpha)^2}{|\beta|^2 + \eta_f |\alpha|^2}, \tag{4.46}$$

where η_f is the filtering inefficiency given by $\eta_f = \int dt |f(t)|^2 |\xi_\perp(t)|^2$. When $\eta_f = 0$ (perfect filtering) we recover the ideal homodyne SNR and when $\eta_f = 1$ (no filtering) we have the conventional SNR limit; i.e.

$$\underbrace{\frac{4|\beta|^2 \mathrm{Re}(\gamma\alpha)^2}{|\beta|^2 + |\alpha|^2}}_{\text{Conventional}} \leq \underbrace{\frac{4|\beta|^2 \mathrm{Re}(\gamma\alpha)^2}{|\beta|^2 + \eta_f |\alpha|^2}}_{\text{Achievable}} \leq \underbrace{4\mathrm{Re}(\gamma\alpha)^2}_{\text{Ideal}} . \tag{4.47}$$

We plot these limits for parameter values typical in comb experiments in Fig. 4.7 and show a 13 dB improvement from perfect filtering. Note that in this derivation, the "comb" structure of the LO is, by definition, included in the mode ξ_{LO} (see Fig. 4.6), and its impact is described by the overlap with the signal mode ξ_{S}, i.e., the parameter γ.

We caution that the SNR bounds in Eq. (4.47) can be beaten if there is prior information about the shape of the signal mode. However, doing so will cause the measurement to no longer be

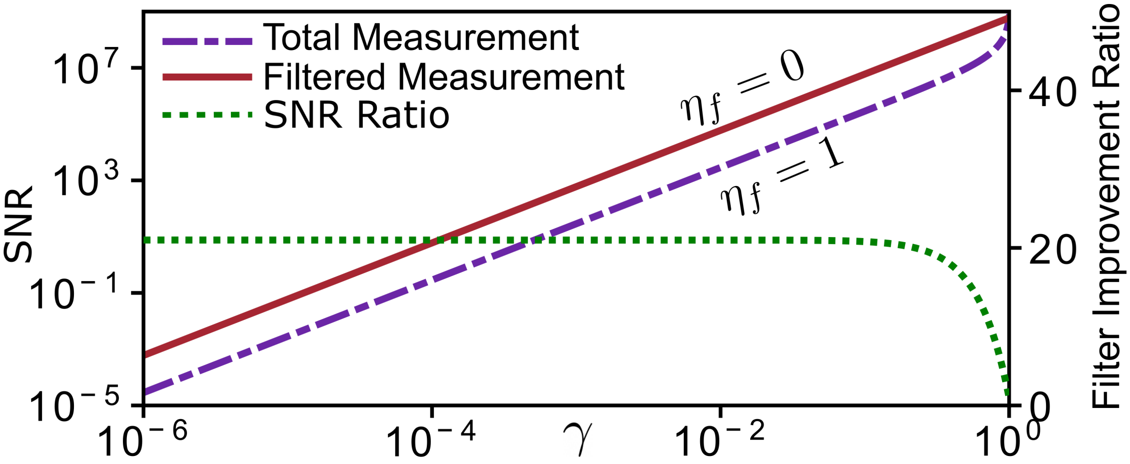

Figure 4.7: SNR vs the mode overlap γ with an experimentally relevant set of parameters. The dashed line is the total measurement SNR containing both LO mode and perpendicular mode clicks ($\eta_f = 1$). The solid line is the SNR after an optimal filter is applied ($\eta_f = 0$). The dotted line is the improvement obtainable using filtering. For this example we take the signal power to be 2 mW, the LO power is 100 μW, and the measurement interval is $\tau = 10$ ns $= 1/f_{rep}$. For a 10 ps pulse and CW signal we would have typical γ of 10^{-2} and η_f of 10^{-3}; here the available SNR gain is ≈ 13 dB.

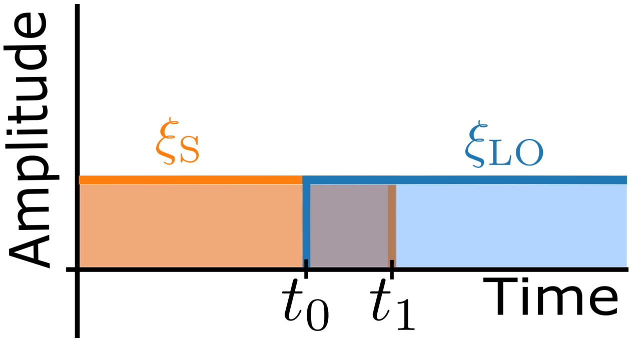

Figure 4.8: We show the modes used to demonstrate filtering performance that exceeds our bounds. Here it is clear that the optimal gate would be the one that only count clicks from the overlapped portion of the measurement and remove all additional shot noise from the LO and signal mode.

of $\hat{Q}(\xi_{\text{LO}})$. For example, if the signal mode is zero while the LO mode is nonzero, that portion of the measurement record only contributes LO shot noise and does not change the mean and could thus be ignored to increase SNR, as explained in Sec. 4.6.2.

4.6.2 A Known Signal Mode Can Violate SNR Bound

Now we consider an example where the SNR bounds we proposed can be violated by changing the effective quadrature being measured. We take the signal and LO modes to both be top hat functions,

$$\xi_{\text{S}} = \begin{cases} \frac{1}{\sqrt{t_1}} & \text{if } t \in (0, t_1) \\ 0 & \text{else} \end{cases} \qquad \xi_{\text{LO}} = \begin{cases} \frac{1}{\sqrt{\tau}} & \text{if } t \in (t_0, T) \\ 0 & \text{else} \end{cases}, \tag{4.48}$$

where $\tau = T - t_0$, see Fig. 4.8. The LO defines the modal measurement. As the signal and LO only overlap on the interval (t_0, t_1) we are predominantly measuring vacuum signal.

As the signal mode function is known we may filter out the measurement of vacuum by only considering detection in the interval (t_0, t_1). This is achieved with the filter

$$f(t) = \begin{cases} 1 & \text{if } t \in (t_0, t_1) \\ 0 & \text{else} \end{cases}. \tag{4.49}$$

This will change the quadrature measured from $\hat{Q}(\xi_{\text{LO}})$ to the top hat "LO mode" in the interval $\hat{Q}(f(t)\xi_{\text{LO}})$.

Redoing the above analysis in this case for a coherent signal $|\alpha_{\xi_\mathrm{S}}\rangle$, the SNR is

$$\mathrm{SNR} = \frac{4\mathrm{Re}(\gamma\alpha\beta^*)^2}{\eta_\mathrm{LO}|\beta|^2 + \eta_\mathrm{S}|\alpha|^2}, \tag{4.50}$$

where $\eta_\mathrm{LO} = (t_1 - t_0)/(T - t_0)$, and $\eta_\mathrm{S} = (t_1 - t_0)/t_1$. In the large LO regime after the filter is applied we get the simplified expression

$$\mathrm{SNR} = \frac{4\mathrm{Re}(\gamma\alpha)^2}{\eta_\mathrm{LO}}, \tag{4.51}$$

where we note that η_LO is between 0 and 1, so this exceeds the bound we propose of $\mathrm{SNR} = 4\mathrm{Re}(\gamma\alpha)^2$ by a factor of η_LO^{-1}. Thus in this example, because we knew ξ_S, we were able to violate the SNR bound at the cost of altering the modal measurement.

4.6.3 Analysing Quantum Light: Single Photon Signal and Weak LO

Now consider the signal to be a single photon state with mode ξ_s. Decomposing this into our basis gives

$$|1_{\xi_s}\rangle = \gamma|1_{\xi_\mathrm{LO}}\rangle|0_{\xi_\perp}\rangle + \sqrt{1-|\gamma|^2}|0_{\xi_\mathrm{LO}}\rangle|1_{\xi_\perp}\rangle\,. \tag{4.52}$$

As the overlap between the signal and LO modes increases the photon is more likely to be found in the LO mode.

To compute the measured quadrature distribution we take the expectation of the POVM in Eq. (4.38) in the state Eq. (4.52) ie.

$$P(x) = \int dx' \langle 1_{\xi_s}|E^\mathrm{LO}_{x'}(\xi_\mathrm{LO}) \otimes E^\perp_{x-x'}(\xi_\perp)|1_{\xi_s}\rangle\,. \tag{4.53}$$

After some manipulation done in App. B.8 we find

$$\begin{aligned} P(x) = \frac{1}{2\sqrt{\pi}}\Big[&4|\gamma|^2x^2e^{-x^2} + (1-|\gamma|^2)\times \\ &(e^{-(x-1/\sqrt{2}|\beta|)^2} + e^{-(x+1/\sqrt{2}|\beta|)^2})\Big]\,. \end{aligned} \tag{4.54}$$

The first term is the quadrature distribution for a single photon which is attained in the mode-matched limit ($\gamma = 1$). For $\gamma = 0$ and $|\beta| \gg 1$ we have the quadrature distribution for vacuum.

For γ between these extremes and large β we have the quadrature distribution for a mixed state of zero and one photons. This is the regime that is characterized by an effective loss and is analyzed in detail in [97]. For small values of β, additional shot noise from the perpendicular mode splits the Gaussian distribution of vacuum into two Gaussians. These features are plotted in figure Fig. 4.9. The Filtered measurement is equivalent to the effective loss results from [97], showcasing the difference the added perpendicular mode noise can make. This feature is not present if mode mismatch is treated as just loss and is highly relevant to applications of homodyne with weak LOs [115, 116, 117].

4.6.4 Summary of POVMs for Arbitrary Mode-Matched Homodyne

In summary, we have found the measurement operators for multimode homodyne detection that are valid for arbitrary time dependence of both the LO and signal. In our construction, the measurement decomposes naturally into two parts: a quadrature measurement in the temporal mode of the LO and an intensity-like measurement on the other modes. We show that perfect filtering of this intensity noise achieves a quadrature noise-limited measurement. In comb-based measurements characterized by large mode-mismatch and strong signals, this establishes a significantly lower quantum limit than conventionally considered. This limit should be sought before pursuing quantum advantage from non-classical states of light. Moreover, because we have developed a fully quantum theory, we can analyze the measurement of any signal state including squeezed states, which are highly relevant to measurements aimed at increased precision. As an example of our fully quantum theory, we analyzed the measurement of a single photon Fock state with a finite strength LO and arbitrary mode overlap. This represents a scenario that existing methods have not been able to fully describe. Our analysis complements related work on POVMs for electro-optic sampling [118]

Many comb-based measurements are based on heterodyne rather than homodyne techniques. Although there are many reasons to prefer homodyne over heterodyne for quantum metrology, the technical limitations of frequency comb measurements make quantum-limited homodyne more

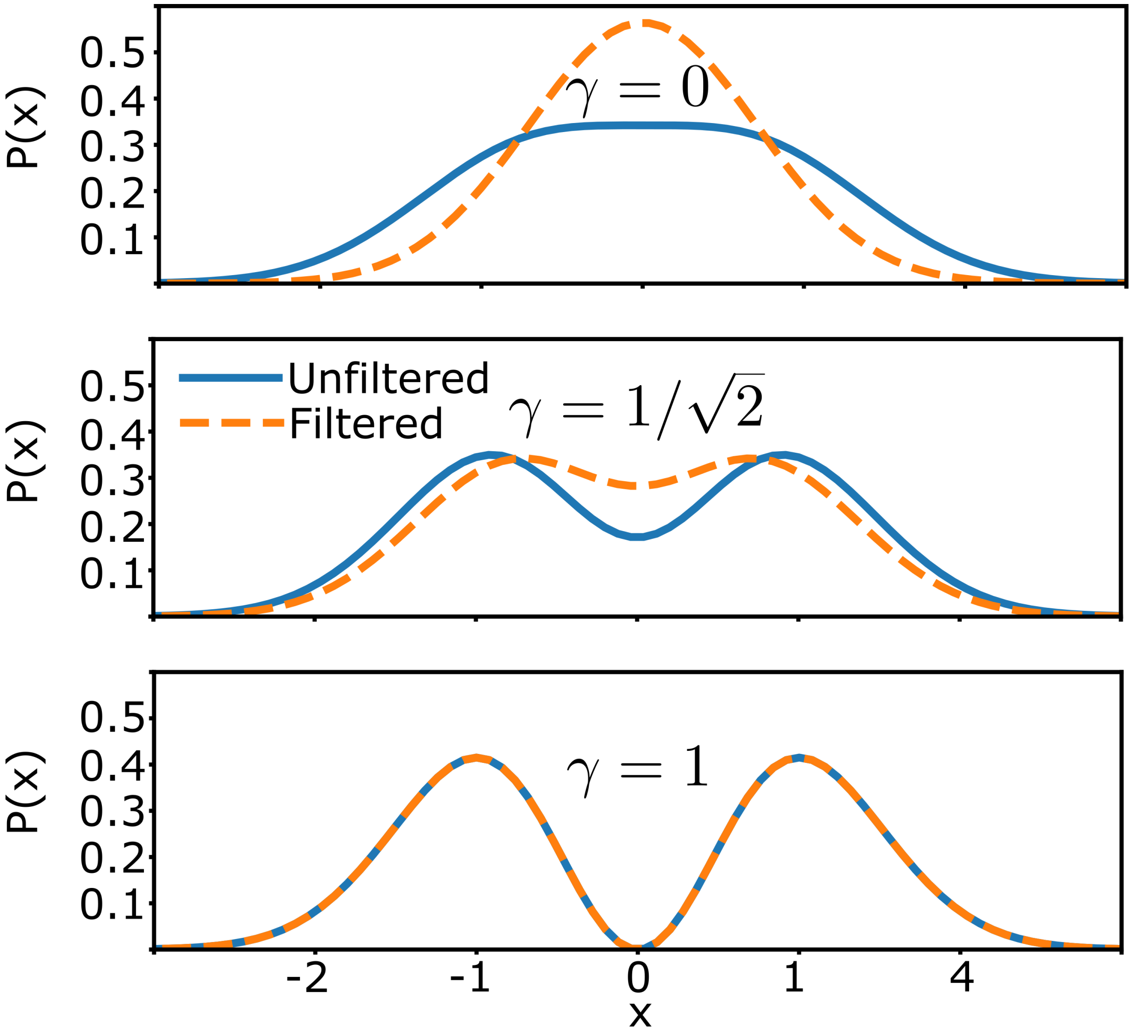

Figure 4.9: Difference variable probability distribution for a single photon signal with varying amounts of mode mismatch. In all figures $\beta = 1$ is used, so that the single photon of shot noise from the signal is not overshadowed. These figures are generated with $\eta_f = 0$. Qualitatively similar results can be observed for larger photon number signal states, but combinatorial expansion complicates the analytical formulations equivalent to Eq. (4.54).

difficult to achieve than heterodyne. We conjecture that the heterodyne SNR is simply half that of homodyne due to sampling of both $\hat{x}$ and $\hat{p}$ quadratures, but a complete analysis of the heterodyne measurement operators is left as future work.

4.7 Comparison of Proposed LO Mode Quadrature Projection Limit vs. Prior Filtering Demonstrations

Here we compare our conjectured heterodyne quantum limit set by quadrature projection noise in the LO mode with filtering demonstrations [21] and [22]. First we assume a Sech squared temporal intensity profile. Omitting complex phase, since here we are only concerned with the absolute mode overlap:

$$|\xi_{\mathrm{S}}| = \frac{1}{\sqrt{T}}, \qquad |\xi_{\mathrm{LO}}| = \frac{1}{\sqrt{2\tau}} \operatorname{sech}\left(\frac{t}{\tau}\right). \tag{4.55}$$

Here τ is the temporal width of the Sech function. The squared mode overlap $|\langle \xi_{\mathrm{S}}, \xi_{\mathrm{LO}} \rangle|^2$ is thus:

$$|\gamma|^2 = \frac{\pi^2 \tau}{2T} \tag{4.56}$$

The fully general heterodyne SNR–which can be derived from a purely moment-based analysis and makes no assumptions about the relative strength of signal and LO–is:

$$\frac{\langle i_S^2 \rangle}{\langle i_N^2 \rangle} = \frac{2(\frac{\eta_q e}{h\nu})^2 \frac{P_{\mathrm{LO}}}{n} P_s}{e\frac{\eta_q e}{h\nu}(P_{\mathrm{LO}} + |\gamma|^2 P_{\mathrm{s}})B}, \tag{4.57}$$

where $\langle i_S^2 \rangle$ is the average signal power, $\langle i_N^2 \rangle$ is the quantum noise solely in the temporal mode of the comb local oscillator, η_q is the quantum efficiency of the detector, e is the fundamental charge, $h\nu$ is the energy per photon, P_{LO} is the total comb power, n is the number of comb teeth, P_{s} is the CW power, and B is the resolution bandwidth. For transform-limited sech pulses $\tau = \frac{0.315}{1.76\Delta\nu}$. Note that this equation is actually equivalent to Eq. (4.47), but we have used n to denote the mode overlap.

In [21], $\nu = 193$ THz, $T = 10$ ns, $\Delta\nu = 32$ GHz, $\eta_q = 0.76$, $P_{\mathrm{LO}} = 6$ nW, $P_{\mathrm{s}} = 2.8$ mW, $n = 320$, and $B = 170$ kHz. Our predicted SQL SNR is 54.5 dB versus the experimentally realized SNR of 36.9 dB. In [20], $\nu = 193$ THz, $T = 10$ ns, $\Delta\nu = 12$ GHz, $\eta_q = 0.7$, $P_{\mathrm{LO}} = 1.74$ μW,

$P_\mathrm{s} = 0.5$ mW, $n = 120$, and $B = 100$ kHz. Our predicted SQL SNR is 78.6 dB versus the experimentally realized SNR of 68.3 dB. Similar SNR figures arise when assuming a Gaussian profile (54.2 dB and 78.5 dB for [21] and [22], respectively).

Similarly, we can calculate η_f for this experiment using some assumptions. Given the 60 ps pulse width we can approximate $f(t)$ by moving 5 standard deviations away from the pulse mean. Since the signal was a CW laser the integral to calculate η_f is simple and we get the following:

$$\eta_f \approx \frac{5\sigma}{T}. \tag{4.58}$$

After correctly converting from pulse width to standard deviations of a Gaussian pulse we get $\eta_f = 1.3 \times 10^{-2}$ for [21]. Along with the other experimental details, this would result in a potential 18.8 dB improvement, slightly less than the 20 dB they achieved. This difference can be explained simply because they did not apply a filter that we consider. Additionally, if we choose to approximate our cutoff after only 3 standard deviations we would have had an improvement of 20.8 dB, which better matches their result.

4.8 Experimental Progress Toward the Comb-Mode Quadrature Estimation Limit

To find a lower “standard quantum limit” of the CW and comb heterodyne measurement, we derived measurement operators for homodyne detection with a comb local oscillator (LO), which determine the statistically and metrologically relevant quantum properties of the measurement. This in turn led to a calculation of the quantum limits of heterodyne detection, since heterodyne detection can be understood as simply consisting of successive homodyne measurements at rotating quadrature angle. Here, we reformulate the result to yield an expression that can be calculated with experimental parameters.

Summarizing the prior theory section, the measurement operators for a homodyne setup with a frequency comb LO is a quadrature measurement in the LO (comb) mode and an intensity-like measurement in the orthogonal part of the signal mode defined through the Gram-Schmidt process

(Fig. 1a). I.e., the comb pulse-overlapped portion of the signal contributes to a quadrature signal, whereas the non-overlapping portion of the signal contributes noise but no quadrature information. Typically both measurements are made thus adding unnecessary noise–though both measurements yield uncertainty that shows up as shot noise.

However, gating shows that intensity-like measurements can be excluded [21, 22]. In fact, if we follow the standard quantum limit established in quantum optics more generally, the SQL would correspond to a measurement of the quadrature variable of the signal only in the comb LO mode. This is the highest SNR measurement we can make given that we do not know the arbitrary mode of the signal–and is perhaps also the highest SNR measurement for a stationary signal, where only the quadrature, or rotating quadrature (heterodyne) information is desired. Thus, we now refer to this limit as the standard quantum limit.

The overlap between the signal and the LO is $\langle \xi_{LO}, \xi_s \rangle = \int \xi^*_{LO}(t)\xi_s(t)dt$, and ξ_{LO} and ξ_s are the square-normalized LO and the signal amplitude modes. Here we consider a hyperbolic secant as the time domain mode for the frequency comb LO and a stationary mode for the CW signal: $\xi_{\mathrm{comb}} = \frac{1}{\sqrt{2\tau}}\mathrm{Sech}(t/\tau)$ and $\xi_{\mathrm{CW}} = \frac{1}{\sqrt{T}}$. The amplitude overlap between these two modes is $\frac{\pi}{\sqrt{2}}\sqrt{\frac{\tau}{T}}$ where τ is the hyperbolic secant width and T is the pulse-to-pulse time interval of the comb (i.e., $1/f_{\mathrm{rep}}$). This sets the SQL SNR as:

$$\frac{\langle i_S^2 \rangle}{\langle i_N^2 \rangle} = \frac{2(\frac{\eta_q e}{h\nu})^2 \frac{P_{\mathrm{comb}}}{n} P_{\mathrm{CW}}}{e\frac{\eta_q e}{h\nu}(P_{comb} + \langle \xi_{\mathrm{comb}}, \xi_{\mathrm{CW}} \rangle^2 P_{\mathrm{CW}})B} = \frac{\frac{\eta_q}{h\nu}\frac{P_{\mathrm{comb}}}{n} P_{\mathrm{CW}}}{(P_{\mathrm{comb}} + \frac{\pi^2 \tau}{2T} P_{\mathrm{CW}})B}, \tag{4.59}$$

where $\langle i_S^2 \rangle$ is the average signal power, $\langle i_N^2 \rangle$ is the quantum noise solely in the temporal mode of the comb, η_q is the quantum efficiency of the detector, e is the fundamental charge, $h\nu$ is the energy per photon, P_{comb} is the total comb power, n is the number of comb teeth, P_{CW} is the CW power, and B is the detection bandwidth. In essence, the signal $\langle i_S^2 \rangle$ is a beat between a single comb tooth and the CW laser, and the noise $\langle i_N^2 \rangle$ is the shot noise solely in the temporal mode of the comb. We note that in the limit of $n = 1$, the comb becomes CW, the overlap integral becomes one, and the SNR reduces to the well-known single-mode heterodyne limit. We can also quantify

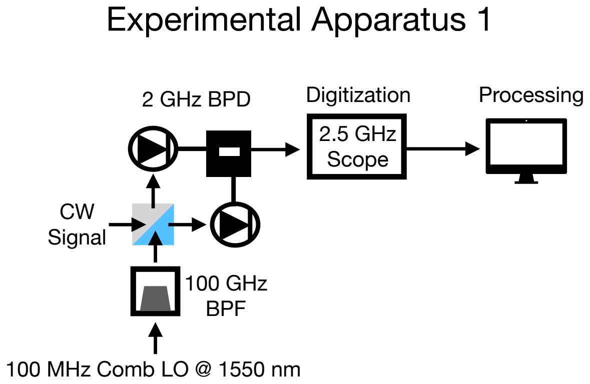

Figure 4.10: Experimental Apparatus 1 for Pure Frequency Comb Coherent State-Overlap Heterodyne Measurement

the improvement of the heterodyne noise limit over the total shot noise $\langle i^2_{N,\mathrm{tot}} \rangle$ limit as:

$$\frac{\langle i^2_{N,\mathrm{tot}} \rangle}{\langle i^2_N \rangle} = \frac{P_{\mathrm{comb}} + P_{\mathrm{CW}}}{P_{\mathrm{comb}} + \frac{\pi^2\tau}{2T} P_{\mathrm{CW}}} \tag{4.60}$$

If the CW power is much greater than the comb power, this ratio simplifies to $\frac{2T}{\pi^2\tau}$. We note that τ may not be limited by the optical pulse width of the comb, but by the detection process, so the maximum improvement ratio given bandwidth-limited detection is approximately $\frac{2T}{\pi^2\tau_D}$, where τ_D is the inverse of the detection bandwidth.

4.8.1 Measurement Version 1: Bandwidth-limited

In our first attempt to approach the SQL, we employ a 2 GHz balanced photodetector, a 100 MHz repetition rate frequency comb filtered to an optical bandwidth of 100 GHz with an avg. power of 6 µW, and a CW laser at 1550 nm and power 1.9 mW–see Fig. 4.10.

Similar to [21], we post-process our time domain measurement by computationally “gating” out temporal regions of the measurement that do not overlap with the comb pulse signal–see Fig. 4.11. We achieve a 7.9 dB improvement in beat note SNR (52.8 dB) versus the total shot noise-limited raw measurement (44.9 dB) at 500 kHz resolution bandwidth. This approaches the expected level of improvement given the detection bandwidth τ_D and the comb rep. rate, i.e., $10\log_{10}[\frac{2T}{\pi^2\tau_D}] = 9.6$ dB, where $\tau_D = .22$ ns and $T = 10$ ns. While we show significant improvement over the total shot noise limit, we fall short of the true SQL SNR of 68 dB by approximately 15 dB. This gap is due to the inability of the detection electronics to fully capture the temporal mode of the comb–i.e., the optical bandwidth is much larger than the electronic bandwidth.

4.8.2 Measurement Version 2: Digitization-limited

In our second attempt at reaching the SQL, we employed a 43 GHz balanced photodetector, a 100 MHz repetition rate frequency comb filtered to an optical bandwidth of 10 GHz with a total power of approximately 20 mW–with approximately 95 percent of the power in the CW signal. We then used a 20 GHz oscilloscope to digitize these data.

The time domain trace of these data can be seen in Fig. 4.13, showing the oscillatory behavior indicative of a linear relative phase evolution between the comb and the CW laser. On the right-hand side of Fig. 4.13, each signal pulse appears to be above and below the 0 V line. This is not because there is phase evolution in the comb pulse, but likely due to length mismatch between the two ports of the balanced detector. I discuss this in greater detail in Sec. 4.8.3.6.

The squared magnitude of the fast Fourier transform of these data (corresponding to the power spectral density) at 50 kHz RBW indicates that we are not shot noise limited in this measurement. Instead, the dynamic range of the oscilloscope (Teledyne-Lecroy LabMaster 10-20Zi-A) limits the measurement, where the effective number of bits (ENOB) is 5.72 leading to a maximum dynamic range (time domain) of 36 dB. In fact, to reach the dynamic range that can encompass the shot noise-limited SNR, an oscilloscope with an ENOB of nearly 16 is required.

The absolute electronic noise floor of the oscilloscope is also near the level of the shot noise out of the fast detector and approximately 10 dB above the thermal noise set by a 50 ohm resistor and measured by a 50 ohm terminated instrument.

This measurement teaches a valuable lesson: we pursued higher bandwidth detection to filter out more of the intensity measurement-related noise that limited us in version 1. We also sought to raise the total shot noise level above the thermal noise floor. This entailed having sizeable optical powers in both the comb and the CW laser. This optical power sets the SNR to be very high,

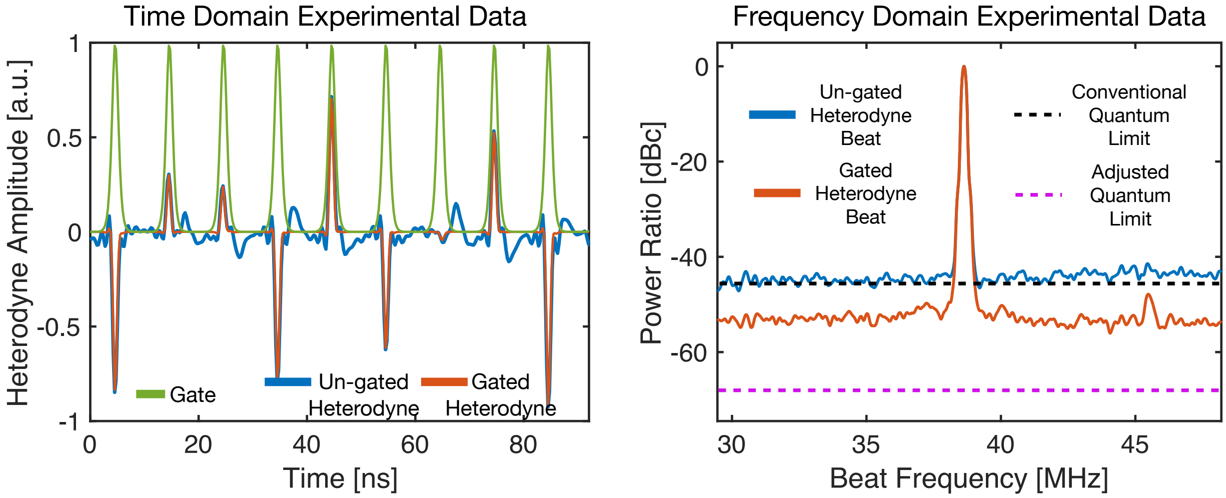

Figure 4.11: **(left)** Time domain trace over nine comb pulses. Green is the gate, blue is the raw signal, and orange is the signal after gating. **(right)** Beat note comparison vs. total shot noise and ”new” SQL. Blue is the raw beat note, orange is the beat note with gating. We show that the raw measurement reaches the conventional quantum limit set by the total shot noise, but is short of the adjusted or pure frequency comb coherent state-overlap heterodyne measurement.

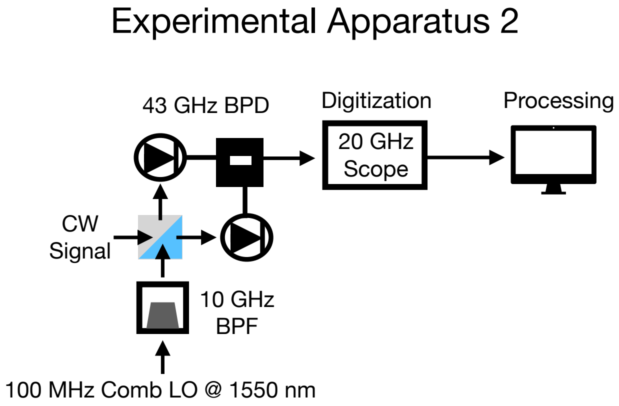

Figure 4.12: Experimental Apparatus 2 for Pure Frequency Comb Coherent State-Overlap Heterodyne Measurement

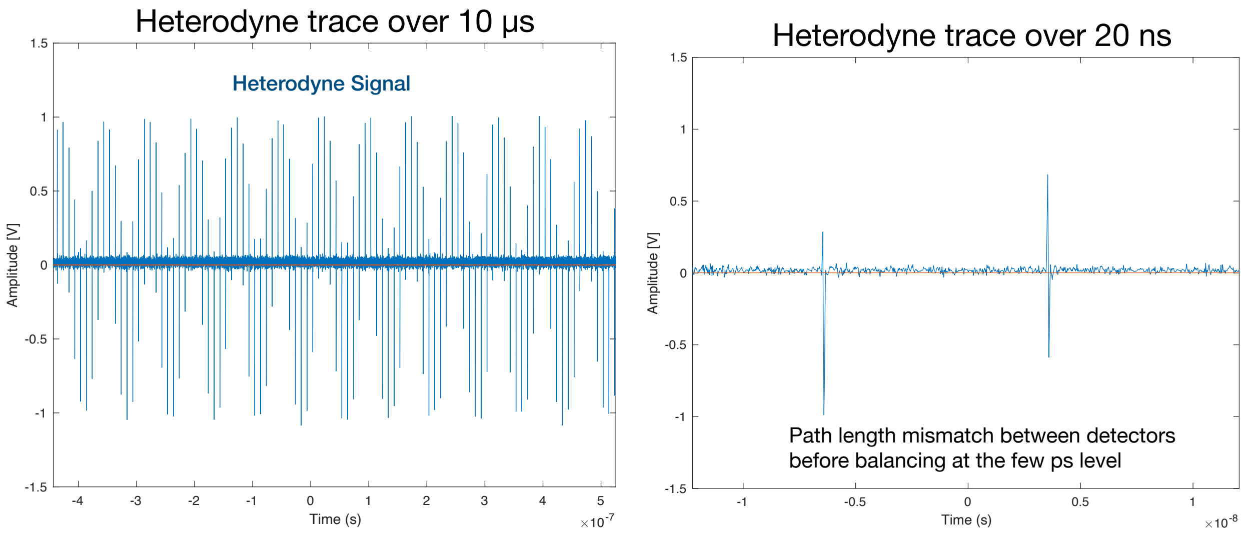

Figure 4.13: **(left)** Trace of heterodyne signal over 10 µs. **(right)** Trace of heterodyne signal over a shorter duration of 20 ns. Note the occurence of both positive and negative amplitudes per pulse, indicating length mismatch in balanced detection at the few ps level.

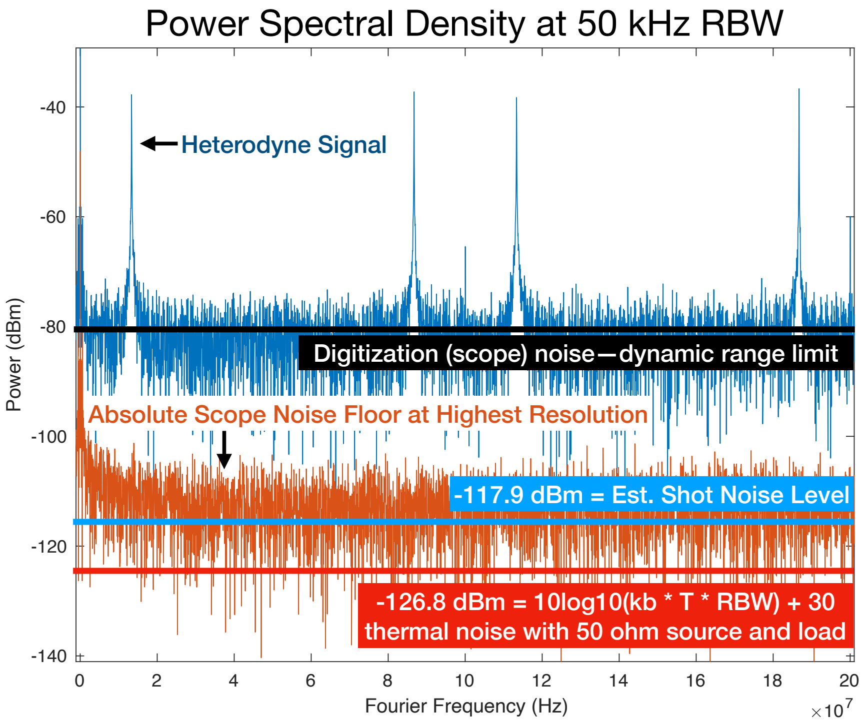

Figure 4.14: Plot of power spectral density for measurement version 2. Note that the heterodyne signal is heavily dynamic range limited. What is more, even the absolute scope noise floor is higher than the *total* shot noise level, indicating that a different approach must be taken to reach the pure frequency comb coherent state-overlap measurement.

especially because the comb power is concentrated in a short section of time, resulting in a high-voltage pulse. Moving to higher detection bandwidths allowed us to resolve the pulse more, which further increased the height of this measured pulse. Furthermore, moving to higher detection bandwidths also lowered the bit depth and ENOB, further lowering our dynamic range. So we entered a regime where we not only increased the dynamic range required to capture our signal, but the available oscilloscopes had an intrinsically lower dynamic range.

4.8.3 How to Make Shot Noise-Limited Measurements

Here I give a run-down of typical things that one needs to consider when making shot noise-limited measurements.

4.8.3.1 Detector Noise

Typically un-amplified detectors are limited by the thermal noise of their equivalent resistance, which is most often 50 ohms. Detectors typically specify a noise equivalent power (NEP) given in units of watts per square root hertz. One can think of this figure as the equivalent optical power needed to match the noise level in a 1 Hz bandwidth of the detector. The denominator is in units of *square root* hertz because we typically represent noise floors in the spectral density of electrical power, which requires a square of the NEP. We show how to use this in the proposed experiment to reach the SQL of frequency comb and CW heterodyne.

4.8.3.2 Amplifier Noise

Amplifiers following the photo detectors are often needed to raise perhaps the signal but most often the noise above the noise floor of measurement equipment such as a radio frequency spectrum analyzer or an oscilloscope. Typically, they specify a noise figure (NF), which most often refers to the reduction in power SNR if the amplifier receives a signal with 50-ohm thermal noise.

Thus, if the noise received by the amplifier is much larger than 50 ohm thermal noise, and the NF is perhaps a few dB (1-3 dB is common for most low-noise amplifiers), the amplifier will not affect the SNR. Since an amplifier amplifies both signal and noise–with amplification of likely greater than 20 dB–it is (generally speaking) only the first amplifier that is critical to have a low noise figure.

4.8.3.3 Instrument Noise and Dynamic Range

Minimum instrument noise is often set by both instrument impedance that leads to a thermal noise floor and an amplifier with a non-zero noise figure. For oscilloscopes, the bit depth and perhaps more importantly the effective number of bits (ENOB) sets the possible dynamic range. The relationship between ENOB and dynamic range (SNR) is the following, neglecting distortion and in the high SNR limit:

$$\mathrm{ENOB} = \frac{\mathrm{SNR} - 1.76}{6.02} \tag{4.61}$$

Dynamic range limitations can be particularly challenging for multi-heterodyne measurements, such as dual-comb spectroscopy as well the filtering measurements described. This is because the signal arrives all at once in a spike of voltage–necessitating a large range over which the instrument must capture the signal. If possible, an oscilloscope with the option to over-sample the waveform is best. One can take the FFT of this data, low pass filter, reverse FFT, then resample back to Nyquist to effectively gain ENOB and dynamic range.

4.8.3.4 Detector Saturation

Detector saturation can occur with the use of frequency comb pulses due to the high peak power of the pulses. In a photodiode-based detector, a bias voltage sets a field across a p-n junction–and when photons create electron-hole pairs, these particles create a current due to the applied field. There are several possible reasons for detector saturation, including the accumulation of charge carriers as a result of a higher electron-hole pair generation than recombination and collection. Heating of the detector from an inefficient generation of electrons can also lead to reduced carrier mobility. All of these effects lead to a decrease in the sensitivity of the photodetector beginning with a roll-off at high frequencies (i.e., the photodetector loses bandwidth). One convenient way to test for this is to directly shine a comb on a detector and vary the power while observing the harmonics of the repetition rate. As power increases, the higher harmonics will begin to drop off.

4.8.3.5 Amplifier Saturation

Amplifiers typically specify a maximum output power or voltage–as that power is approached, the signal starts to be amplified less and less until it becomes clipped. Often, the supply voltage limits the amplifier output voltage. Photodetectors are very frequently loaded with amplifiers themselves, and careful testing of their saturation limits is important to ensure that the signals are accurately recorded.

4.8.3.6 Balancing and Excess Relative Intensity Noise

Excess relative intensity noise refers to technical sources of intensity noise that ride on the light being measured. This is in contrast to shot noise, which is sometimes also considered relative intensity noise but which has to do with the statistical (Poissonian) properties of the coherent state itself. Oftentimes, this distinction is not made, and when relative intensity noise (RIN) is mentioned, it is the *excess* RIN that is being specified. In a classical picture, one can model excess RIN as simply a part of the field:

$$A(t) = A_0 \cos[\omega t] + N(t), \tag{4.62}$$

where N(t) is some random process resulting in excess RIN. Very often excess RIN comes from amplified spontaneous emission, and it is thus important not to amplify laser light more than is necessary.

Excess RIN scales differently with optical power than shot noise, and this is an important way to distinguish noise sources. Since excess RIN can be considered as part of the light field, it scales the same as the signal. Thus, increasing optical power, while limited by excess RIN, does not help raise the signal-to-noise ratio. In terms of measurement in electrical PSD, excess RIN scales as the square of optical power versus shot noise scaling with optical power. See Fig. 4.15

for an illustration of this scaling. Note that electronic noise does not depend on optical power. One can see that in this situation, one would never be shot noise limited–even though there is a region in the center of the plot where the total noise appears to scale linearly with power. This is an important point, as the combination of electronic noise and excess RIN can make the total noise scaling appear as though it is shot noise. Thus, it is important to try to measure the noise across a wide range of optical powers to characterize the excess RIN. However, saturation can also be an issue, especially with pulsed lasers. In this case, even excess RIN might appear to scale linearly with optical power, as increased power also saturates the detector or amplifier. Thus, the techniques mentioned previously to check for saturation are necessary to verify the origins of the noise.

Although the situation in Fig. 4.15 is actually very common, balanced detection can remove excess RIN in the case of a strong local oscillator (and relatively weak signal). Indeed balanced detection has two benefits: 1) all of the light can be used, since a beamsplitter is required anyway to overlap optical modes, and 2) in the strong LO limit, excess RIN can be canceled. As seen in the past results, balancing is not always trivial, especially when detecting signals at higher electrical bands. This is because the length matching and (and overall temporal response matching) becomes more stringent. Balanced detectors specify a common mode rejection ratio (CMRR), which specifies the maximum level of excess RIN suppression (given that one is able to perfectly control beamsplitter ratios and path lengths after splitting).

4.8.4 Proposed Measurement Version 3: Quadrature Estimation Limit at Low Powers

How do we reach the SNR set by the SQL? In the two previous measurements, we sought to reach the shot noise limit first before gating/filtering. Yet, this is not necessary to reach the predicted SQL set by the quadrature/coherent state-overlap measurement in the comb LO mode. Ultimately, we want to make a measurement that is limited by the shot noise of the optical frequency comb. So long as after filtering the noise is dominated by the shot noise of the frequency comb, we

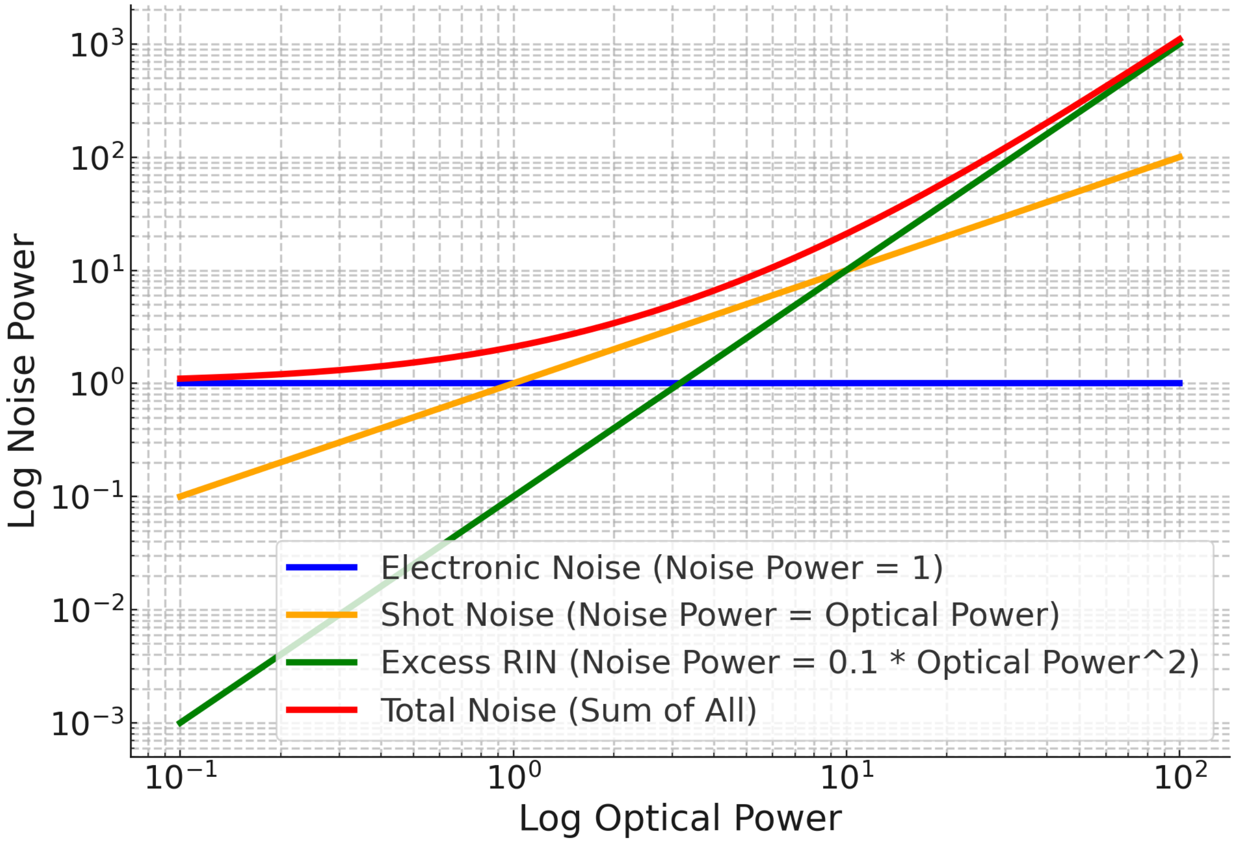

Figure 4.15: A view of noise scaling and how to differentiate noise sources. Electronic noise does not scale with optical power, and shot noise and excess RIN scale with optical power and the square of optical power, respectively. More discussion is included in the main text.

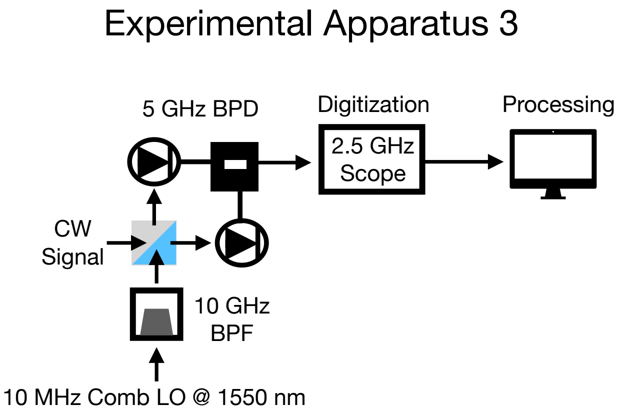

Figure 4.16: Proposed Experimental Apparatus 3 for Pure Frequency Comb Coherent State-Overlap Heterodyne Measurement

can approach the SQL.

In other words, there is a scenario where the non-pulse sections of the measurement are limited by detector and/or electronic noise, but the pulse sections are limited by the comb shot noise. However, in total, the noise is still dominated by electronic noise. Thus, a gating technique that can remove this electronic noise can assist in reaching the SQL.

If we relax the requirement that we reach a shot noise-limited measurement before filtering, we can also lower the optical power, which means that the required dynamic range of the digitization equipment is lessened. We must just make sure that the frequency comb has enough power so that the shot noise in and around the pulse envelope, or within the detector transfer function temporal width, is greater than the technical noise.

To this end, here is a proposal for the next generation of this measurement. We begin by considering a Thorlabs BDX3BA balanced InGaAs detector, with a 3 dB cutoff at 5 GHz, a responsivity of 0.9 A/W, and a noise floor set by 50 ohm resistance. We will amplify the output of the balanced detector with a 1.4 dB NF low-noise amplifier with 11 dBm P1dB (25 dBm IP3) and a bandwidth from 10 MHz to 3 GHz. We will also use a 10 MHz repetition rate comb (which grants for lower overall power usage since the average power can be lowered while maintaining pulse power) optically filtered to a bandwidth of 10 GHz. We digitize the data on a 2.5 GHz oscilloscope.

First, we need to calculate what power the comb needs to have in order to bring shot noise above technical noise. To calculate the technical noise floor assumed set by the thermal noise and the noise figure of 1.4 dB, we have:

$$N_{\text{tech}} = N_{\text{tech}} + 1.4 = 10\log_{10}\left(\frac{k_b T R}{R} \times 10^3\right) + 1.4 = -174 + 1.4 = -172.6 \text{ [dBm/Hz]} \tag{4.63}$$

Assuming that we want the shot noise to be over 10 dB above the technical noise, and recalling that the shot noise mean square current is $2q \times Re \times P\Delta f$, we seek the power at which:

$$10\log_{10}\left(2q \times Re \times P \times R \times 10^3\right) = -172.6 + 10 \approx -160 \text{ [dBm/Hz]}. \tag{4.64}$$

At $P = 7$ mW, the shot noise would measure approximately -160 dBm/Hz.

The oscilloscope bandwidth sets the narrowest span of time over which we can gate the pulses, which is conservatively 1/2.5 GHz or 400 ps. Thus we only need this 7 mW spread over 400 ps. What does this mean in terms of average power and peak optical power of the comb? Given that we are using a 10 MHz repetition rate laser, with 7 mW spread over 400 ps, we can recalculate given that each pulse contains $7 \times 10^{-3} \times 400 \times 10^{-12}$ J = 2.8 pJ of energy. The average power is then merely $2.8 \times 10^{-12} \times 10 \times 10^6$ W = 28 µW.

In order to find the peak power we must first calculate the pulse width given a 10 GHz filter and approximately Gaussian envelope. This is calculated using the time bandwidth product of 0.44 for a Gaussian pulse: FWHM = 0.44/10 GHz = 44 ps. The peak power is thus 2.8 pJ/44 ps = 64 mW.

Now assume a 1 µW CW laser–what is the peak signal over these 44 ps? In dBm, it is:

$$10\log_{10}\left(4Re^2 P_{\text{comb}} P_{\text{CW}} R \times 10^3\right) = -19.8 \text{ dBm}. \tag{4.65}$$

Indeed, we must make sure that when we amplify the peak signal does not exceed the amplifier max of typically 10 dBm, which limits the amount that we can amplify.

Next, what is the peak SNR (dynamic range) that our 2.5 GHz oscilloscope will need to capture? The power SNR is approximately twice the number of signal photons captured.[9] The

---

[9] While one usually specifies SNR at a certain resolution bandwidth–the physical meaning of the resolution

number of signal photons in this window is defined by the oscilloscope bandwidth of 2.5 GHz, where the signal energy is 1 uW/2.5 GHz = 4×10^{-16} J. The number of signal photons captured is $\eta \times 4 \times 10^{-16}$ J$/h\nu \approx 2250$, where η is calculated to be 0.74, h is the Planck constant, and ν is 200 THz. Thus, the power SNR is 4500, and the voltage SNR is the square root of this quantity: 67 (or 18 dB), which is easily covered by the dynamic range of most digitizers.

Since we are now in the standard quantum limit where the noise is limited by the comb local oscillator, the full heterodyne power SNR is the standard equation:

$$\mathrm{SNR} = \frac{\eta|\gamma|^2 P_{\mathrm{CW}}}{hv\Delta f}, \tag{4.66}$$

where

$$|\gamma|^2 = \frac{\pi^2\tau}{2T} = \frac{\pi^2(44\mathrm{ps})}{2(100\mathrm{ns})} \approx .002. \tag{4.67}$$

At a resolution bandwidth of 100 kHz, the power SNR is 120,000 or 50.86 dB.

---

bandwidth is as approximately the inverse of the time over which the signal is captured. In this sense, this defines a total number of signal photons captured, and each point plotted has a resolution bandwidth set by the scope bandwidth.

Chapter 5

Conclusion

The optical frequency comb provides coherent connection and control across the electromagnetic spectrum, from optical to radio, encompassing more than fifteen orders of magnitude of frequency. In providing this coherent link, it has revolutionized timekeeping and a host of other applications that require coherent electromagnetic fields.

If the history of coherent control of radio fields is any indicator, there are powerful connections to be made between coherent fields and non-coherent fields, such as thermal and quantum states of electromagnetic radiation. A longer history of radio control has yielded the field of radio astronomy, which has produced discoveries like the cosmic microwave background and powerful tools like the Event Horizon Telescope. Facility in electronics and fabrication now allows for the exploration of new physics in microwave quantum states, such as in circuit quantum electrodynamics–or used as a computational primitive in quantum computation.

Just as linking coherent optical and radio fields has been tremendously fruitful, as has linking coherent radio techniques with the measurement of thermal and quantum radio fields, I believe that there are opportunities that await further connection between the full coherent control of the electromagnetic spectrum (frequency comb) and the measurement of thermal and quantum light. In this thesis, I have worked toward this connection by defining fundamental limits in the use of the optical frequency comb for the measurement of thermal and quantum fields. This pursuit has also refined a metrological understanding of the measurement of coherent fields with frequency combs.

I explored the measurement and correlation of thermal fields through a technique called dual-comb correlation spectroscopy. This process reveals the spectrum of thermal light at high resolution and across broad bandwidths. New theoretical work uncovered previously unknown fundamental limits on sensitivity when measuring realistically weak thermal light. Experimental investigation verified this scaling. I also demonstrated spectroscopy with this technique at the equivalent power spectral density of our Sun, realizing a greater than 1000x sensitivity increase over past demonstrations of this technique. These insights pave the way for the expansion of this technique to the comb-based spatial correlation of thermal fields. This advancement would allow for extended baseline synthetic aperture hyperspectral imaging throughout the optical spectrum, facilitating novel and profound observations of the universe.

The use of frequency combs for the measurement of quantum light was also investigated. Optical frequency comb measurements break typical quantum optics assumptions, such as large and mode-matched local oscillators, and necessitated new quantum measurement operators. Such measurement operators were derived, which not only describe homodyne measurements on any quantum state of light with a frequency comb local oscillator, but also indicate that the shot noise limit generally reached in comb-based measurements of coherent light (such as in continuous-wave laser heterodyne and dual-comb spectroscopy) does not correspond to the quadrature or coherent state-overlap description standard in quantum optics. Efforts to experimentally reach this “standard” quantum limit demonstrated a significant improvement in the signal-to-noise ratio over the conventional comb-based shot noise limit, paving the way for lower-power portable optical clocks and quantum-enhanced frequency-comb metrology. Just as optical frequency combs have provided a coherent link between radio and optical coherent fields, perhaps they may play a role in coherence-preserving transduction of quantum states between the optical and radio domains. These efforts to define quantum measurement with optical frequency combs may provide part of the foundation for this effort.

Bibliography

[1] James. Vincent. Beyond measure: the hidden history of measurement from cubits to quantum constants. W.W. Norton and Company, 2023.

[2] David S. Landes. Revolution in Time: Clocks and the Making of the Modern World. Belknap Press, Cambridge, MA, 1st edition, 2000.

[3] R. Lange, N. Huntemann, J. M. Rahm, C. Sanner, H. Shao, B. Lipphardt, Chr Tamm, S. Weyers, and E. Peik. Improved Limits for Violations of Local Position Invariance from Atomic Clock Comparisons. Physical Review Letters, 126(1):011102, 2021.

[4] Andrew D. Ludlow, Martin M. Boyd, Jun Ye, E. Peik, and P. O. Schmidt. Optical atomic clocks. Reviews of Modern Physics, 87(2):637, 2015.

[5] Albert A Michelson and E W Morley. On the relative motion of the Earth and the luminiferous ether. American Journal of Science, s3-34(203):333–345, 1887.

[6] LIGO Scientific Collaboration and Virgo Collaboration. Observation of gravitational waves from a binary black hole merger. Physical Review Letters, 116(6):061102, 2016.

[7] United States Naval Observatory. Global positioning system overview. cnmoc.usff.navy.mil/Our-Commands/United-States-Naval-Observatory/Precise-Time-Department/Global-Positioning-System/Global-Positioning-System-Overview/.

[8] James Clerk Maxwell. VIII. A dynamical theory of the electromagnetic field. Philosophical Transactions of the Royal Society of London, 155:459–512, 1865.

[9] J. P. Gordon, H J Zeiger, and C. H. Townes. The maser-new type of microwave amplifier, frequency standard, and spectrometer. Physical Review, 99(4):1264–1274, 1955.

[10] John L Hall. Defining and measuring optical frequencies: the optical clock opportunity–and more. The Nobel Foundation, 2005.

[11] J. Tiedau, M. V. Okhapkin, K. Zhang, J. Thielking, G. Zitzer, E. Peik, F. Schaden, T. Pronebner, I. Morawetz, L. Toscani De Col, F. Schneider, A. Leitner, M. Pressler, G. A. Kazakov, K. Beeks, T. Sikorsky, and T. Schumm. Laser Excitation of the Th-229 Nucleus. Physical Review Letters, 132(18):182501, 2024.

[12] Atsushi Yamaguchi, Yudai Shigekawa, Hiromitsu Haba, Hidetoshi Kikunaga, Kenji Shirasaki, Michiharu Wada, and Hidetoshi Katori. Laser spectroscopy of triply charged 229Th isomer for a nuclear clock. Nature, 629(8010):62–66, 2024.

[13] Chuankun Zhang, Tian Ooi, Jacob S. Higgins, Jack F. Doyle, Lars von der Wense, Kjeld Beeks, Adrian Leitner, Georgy Kazakov, Peng Li, Peter G. Thirolf, Thorsten Schumm, and Jun Ye. Dawn of a nuclear clock: frequency ratio of the ^{229m}th isomeric transition and the ^{87}sr atomic clock. arXiv 2406.18719 [atom-ph, 2024.

[14] Takuma Nakamura, Josue Davila-Rodriguez, Holly Leopardi, Jeff A. Sherman, Tara M. Fortier, Xiaojun Xie, Joe C. Campbell, William F. McGrew, Xiaogang Zhang, Youssef S. Hassan, Daniele Nicolodi, Kyle Beloy, Andrew D. Ludlow, Scott A. Diddams, and Franklyn Quinlan. Coherent optical clock down-conversion for microwave frequencies with 10—18 instability. Science, 368(6493):889–892, 2020.

[15] K. Predehl, G. Grosche, S. M.F. Raupach, S. Droste, O. Terra, J. Alnis, Th Legero, T. W. Hänsch, Th Udem, R. Holzwarth, and H. Schnatz. A 920-kilometer optical fiber link for frequency metrology at the 19th decimal place. Science, 336(6080):441–444, 2012.

[16] Emily D. Caldwell, Jean Daniel Deschenes, Jennifer Ellis, William C. Swann, Benjamin K. Stuhl, Hugo Bergeron, Nathan R. Newbury, and Laura C. Sinclair. Quantum-limited optical time transfer for future geosynchronous links. Nature, 618(7966):721–726, 2023.

[17] Ian Coddington, Nathan Newbury, and William Swann. Dual-comb spectroscopy. Optica, 3(4):414, 2016.

[18] Steven T. Cundiff and Andrew M. Weiner. Optical arbitrary waveform generation. Nature Photonics, 4(11):760–766, 2010.

[19] F. R. Giorgetta, I. Coddington, E. Baumann, W. C. Swann, and N. R. Newbury. Dual Frequency Comb Sampling of a Quasi-Thermal Incoherent Light Source. Conference on Lasers and Electro-optics, CTuS3, 2010.

[20] Sylvain Boudreau and Jérôme Genest. Referenced passive spectroscopy using dual frequency combs. Optics Express, 20(7):7375, 2012.

[21] Jean-Daniel Deschênes and Jérôme Genest. Heterodyne beats between a continuous-wave laser and a frequency comb beyond the shot-noise limit of a single comb mode. Physical Review A, 87:023802, 2013.

[22] Jean-Daniel Deschênes and Jérôme Genest. Chirped pulse heterodyne for optimal beat note detection between a frequency comb and a continuous wave laser. Optics Express, 23(7):9295–9312, 2015.

[23] Roy J. Glauber. Coherent and incoherent states of the radiation field. Physical Review, 131(6):2766–2788, 1963.

[24] E. T. Jaynes. Probability Theory: The Logic of Science. Cambridge University Press, 2003.

[25] Leonard Mandel and Emil Wolf. Optical Coherence and Quantum Optics. Cambridge University Press, 1995.

[26] Grant Sanderson. But what is the central limit theorem?, 2023. Youtube.

[27] J. B. Johnson. Thermal agitation of electricity in conductors. Physical Review, 32(1):97–109, 1928.

[28] H. Nyquist. Thermal agitation of electric charge in conductors. Physical Review, 32(1):110–113, 1928.

[29] Herbert B. Callen and Theodore A. Welton. Irreversibility and generalized noise. Phys. Rev., 83:34–40, Jul 1951.

[30] Hermann A. Haus. Waves and Fields in Optoelectronics. Prentice-Hall, Englewood Cliffs, NJ, 1984.

[31] Robert H. Kingston. Detection of Optical and Infrared Radiation. Springer-Verlag Berlin Heidelberg, Berlin, Heidelberg, 1978.

[32] T. H. Maiman. Stimulated optical radiation in Ruby. Nature, 187(4736):493–494, 1960.

[33] Isaac Newton. Opticks: or, A treatise of the reflections, refractions, inflexions and colours of light: also two treatises of the species and magnitude of curvilinear figures. Printed for Sam. Smith and Benj. Walford, London, 1704.

[34] Joseph Fraunhofer. Bestimmung des Brechungs- und des Farbenzerstreungs-Vermögens verschiedener Glasarten, in Bezug auf die Vervollkommnung achromatischer Fernröhre. Annalen der Physik, 56(7):264–313, 1817.

[35] G. Lemaître. Un Univers homogène de masse constante et de rayon croissant rendant compte de la vitesse radiale des nébuleuses extra-galactiques. Annales de la Société Scientifique de Bruxelles, 47:49–59, 1927.

[36] M. Schmidt. 3C 273: A star-like object with large red-shift. Nature, 197(4872):1040, 1963.

[37] Jesse L. Greenstein and Thomas A. Matthews. Red-Shift of the Unusual Radio Source: 3C 48. Nature 1963 197:4872, 197(4872):1041–1042, 1963.

[38] Michel Mayor and Didier Queloz. A jupiter-mass companion to a solar-type star. Nature, 378(6555):355–359, 1995.

[39] Woodruff Turner Sullivan. Classics in Radio Astronomy. Springer Netherlands, 1982.

[40] M. Ryle. Radio telescopes of large resolving power. Reviews of Modern Physics, 47(3):557–566, 1975.

[41] The Event Horizon Telescope Collaboration. First M87 Event Horizon Telescope Results. I. The Shadow of the Supermassive Black Hole. The Astrophysical Journal Letters, 875(1):L1, 2019.

[42] A. A. Michelson, F. G. Pease, A. A. Michelson, and F. G. Pease. Measurement of the Diameter of α Orionis with the Interferometer. The Astrophysical Journal, 53:249–259, 1921.

[43] John D. Monnier. Optical interferometry in astronomy. Reports on Progress in Physics, 66(5):789–857, 2003.

[44] Gerard T. van Belle, James H. Clark, Henrique R. Schmitt, David Noble, Anders M. Jorgensen, David Mozurkewich, J. Thomas Armstrong, Ellyn K. Baines, Merrick DeWitt, Ty Martinez, Sergio R. Restaino, Jordan Stone, Thomas Coleman, Ben Hardesty, Wyatt E. Clark, Khristian Jones, Bradley Kingsley, Erin Maier, Solvay Blomquist, Nicholas Green,

and Peter Kurtz. The Navy Precision Optical Interferometer: large-aperture observations and infrastructure improvements. In SPIE, volume 12183, page 3. SPIE-Intl Soc Optical Eng, 2022.

[45] W. Zhang, J. M. Robinson, L. Sonderhouse, E. Oelker, C. Benko, J. L. Hall, T. Legero, D. G. Matei, F. Riehle, U. Sterr, and J. Ye. Ultrastable Silicon Cavity in a Continuously Operating Closed-Cycle Cryostat at 4 K. Physical Review Letters, 119(24):243601, 2017.

[46] Qi Shen, Jian Yu Guan, Ji Gang Ren, Ting Zeng, Lei Hou, Min Li, Yuan Cao, Jin Jian Han, Meng Zhe Lian, Yan Wei Chen, Xin Xin Peng, Shao Mao Wang, Dan Yang Zhu, Xi Ping Shi, Zheng Guo Wang, Ye Li, Wei Yue Liu, Ge Sheng Pan, Yong Wang, Zhao Hui Li, Jin Cai Wu, Yan Yan Zhang, Fa Xi Chen, Chao Yang Lu, Sheng Kai Liao, Juan Yin, Jian Jun Jia, Cheng Zhi Peng, Hai Feng Jiang, Qiang Zhang, and Jian Wei Pan. Free-space dissemination of time and frequency with 10^{-19} instability over 113 km. Nature, 610(7933):661–666, 2022.

[47] Scott A. Diddams, Kerry Vahala, and Thomas Udem. Optical frequency combs: Coherently uniting the electromagnetic spectrum. Science, 369(6501), 2020.

[48] Gerard T. van Belle, Aden B. Meinel, and Marjorie Pettit Meinel. The scaling relationship between telescope cost and aperture size for very large telescopes. In Ground-based Telescopes, volume 5489, page 563. SPIE, 2004.

[49] Isobel Hook and Opticon ELT Science Working Group. Science with Extremely Large Telescopes. The Messenger, 121:2–10, 2005.

[50] Michael J. Ireland and John D. Monnier. A dispersed heterodyne design for the planet formation imager. SPIE, 9146:914612, 2014.

[51] D. T. Andreasen, S. G. Sousa, E. Delgado Mena, N. C. Santos, M. Tsantaki, B. Rojas-Ayala, and V. Neves. Near-infrared spectroscopy of the Sun and HD20010: Compiling a new line list in the near-infrared. Astronomy and Astrophysics, 585:A143, 2016.

[52] A. H. Gabriel, B. C. Fawcett, and Carole Jordan. Classification of iron lines in the spectrum of the sun and zeta in the range 167 Å to 220 Å [3]. Nature, 206(4982):390–392, 1965.

[53] Jonas Zmuidzinas. Thermal noise and correlations in photon detection. Applied Optics, 42(25):4989, 2003.

[54] Paul J. Brewer, Jin Seog Kim, Sangil Lee, Oksana A. Tarasova, Joële Viallon, Edgar Flores, Robert I. Wielgosz, Takuya Shimosaka, Sergey Assonov, Colin E. Allison, Adriaan M.H. Van Der Veen, Brad Hall, Andrew M. Crotwell, George C. Rhoderick, Joseph T. Hodges, Joachim Mohn, Christoph Zellweger, Heiko Moossen, Volker Ebert, and David W.T. Griffith. Advances in reference materials and measurement techniques for greenhouse gas atmospheric observations. Metrologia, 56(3):034006, 2019.

[55] Lin Chang, Songtao Liu, and John E. Bowers. Integrated optical frequency comb technologies. Nature Photonics, 16(2):95–108, 2022.

[56] Rodney Loudon. The Quantum Theory of Light. OUP Oxford, third edition, 2000.

[57] Peter R. Griffiths and James A. de Haseth. Fourier Transform Infrared Spectrometry. John Wiley & Sons, second edition, 2007.

[58] N. A. Olsson. Lightwave Systems With Optical Amplifiers. Journal of Lightwave Technology, 7(7):1071–1082, 1989.

[59] Amnon Yariv. Signal-to-noise considerations in fiber links with periodic or distributed optical amplification. Optics Letters, 15(19):1064, 1990.

[60] Jonathan Crass, Andrew Bechter, Eric Bechter, Charles Beichman, Cullen Blake, David Coutts, Tobias Feger, Sam Halverson, Robert J. Harris, Nemanja Jovanovic, Peter Plavchan, Christian Schwab, Gautam Vasisht, James K Wallace, and Ji Wang. The need for single-mode fiber-fed spectrographs, 2019. arXiv:1901.07567 [astro-ph.IM].

[61] Joe P. Ninan, Suvrath Mahadevan, Gudmundur Stefansson, Chad Bender, Arpita Roy, Kyle F. Kaplan, Connor Fredrick, Andrew J. Metcalf, Andrew Monson, Ryan Terrien, Lawrence W. Ramsey, and Scott A. Diddams. Impact of crosshatch patterns in H2RGs on high-precision radial velocity measurements: exploration of measurement and mitigation paths with the Habitable-Zone Planet Finder. Journal of Astronomical Telescopes, Instruments, and Systems, 5(04):1, 2019.

[62] Pooja Sekhar, Molly Kate Kreider, Connor Fredrick, Joe P. Ninan, Suvrath Mahadevan, and Scott A. Diddams. Tunable 30 GHz laser frequency comb for astronomical spectrograph characterization and calibration. in prep., 2024.

[63] Connor Fredrick, Freja Olsen, Ryan Terrien, Suvrath Mahadevan, Franklyn Quinlan, and Scott A. Diddams. Thermal-light heterodyne spectroscopy with frequency comb calibration. Optica, 9(2):221, 2022.

[64] B. Klein, S. Hochgürtel, I. Krämer, A. Bell, K. Meyer, and R. Güsten. High-resolution wide-band fast Fourier transform spectrometers. Astronomy and Astrophysics, 542:L3, 2012.

[65] F. Bouchy, F. Pepe, and D. Queloz. Fundamental photon noise limit to radial velocity measurements. Astronomy and Astrophysics, 374(2):733–739, 2001.

[66] Philippe Guay, Mathieu Walsh, Alex Tourigny-Plante, and Jérôme Genest. Linear dual-comb interferometry at high power levels. Optics Express, 31(3):4393, 2023.

[67] Abijith S. Kowligy, Henry Timmers, Alexander J. Lind, Ugaitz Elu, Flavio C. Cruz, Peter G. Schunemann, Jens Biegert, and Scott A. Diddams. Infrared electric field sampled frequency comb spectroscopy. Science Advances, 5(6), 2019.

[68] Ileana Cristina Benea-Chelmus, Francesca Fabiana Settembrini, Giacomo Scalari, and Jérôme Faist. Electric field correlation measurements on the electromagnetic vacuum state. Nature, 568(7751):202–206, 2019.

[69] C. Riek, P. Sulzer, M. Seeger, A. S. Moskalenko, G. Burkard, D. V. Seletskiy, and A. Leitenstorfer. Subcycle quantum electrodynamics. Nature, 541(7637):376–379, 2017.

[70] A. Richard Thompson, James M. Moran, and George W. Swenson. Interferometry and Synthesis in Radio Astronomy. Astronomy and Astrophysics Library. Springer International Publishing, Cham, 2017.

[71] G. B. Taylor, C. L. Carilli, and R. A. Perley, editors. Synthesis Imaging in Radio Astronomy II, volume 180 of Astronomical Society of the Pacific Conference Series, January 1999.

[72] Stefan Kraus, John D. Monnier, Michael J. Ireland, Gaspard Duchêne, Catherine Espaillat, Sebastian Hönig, Attila Juhasz, Chris Mordasini, Johan Olofsson, Claudia Paladini, Keivan Stassun, Neal Turner, Gautam Vasisht, Tim J. Harries, Matthew R. Bate, Jean-François Gonzalez, Alexis Matter, Zhaohuan Zhu, Olja Panic, Zsolt Regaly, Alessandro Morbidelli, Farzana Meru, Sebastian Wolf, John Ilee, Jean-Philippe Berger, Ming Zhao, Quentin Kral, Andreas Morlok, Amy Bonsor, David Ciardi, Stephen R. Kane, Kaitlin Kratter, Greg Laughlin, Joshua Pepper, Sean Raymond, Lucas Labadie, Richard P. Nelson, Gerd Weigelt, Theo ten Brummelaar, Arnaud Pierens, Rene Oudmaijer, Wilhelm Kley, Benjamin Pope, Eric L. N. Jensen, Amelia Bayo, Michael Smith, Tabetha Boyajian, Luis Henry Quiroga-Nuñez, Rafael Millan-Gabet, Andrea Chiavassa, Alexandre Gallenne, Mark Reynolds, Willem-Jan de Wit, Markus Wittkowski, Florentin Millour, Poshak Gandhi, Cristina Ramos Almeida, Almudena Alonso Herrero, Chris Packham, Makoto Kishimoto, Konrad R. W. Tristram, Jörg-Uwe Pott, Jean Surdej, David Buscher, Chris Haniff, Sylvestre Lacour, Romain Petrov, Steve Ridgway, Peter Tuthill, Gerard van Belle, Phil Armitage, Clement Baruteau, Myriam Benisty, Bertram Bitsch, Sijme-Jan Paardekooper, Christophe Pinte, Frederic Masset, and Giovanni Rosotti. Planet Formation Imager (PFI): science vision and key requirements. In Optical and Infrared Interferometry and Imaging V, volume 9907, page 99071K. SPIE, 2016.

[73] Kyle Beloy, Martha I. Bodine, Tobias Bothwell, Samuel M. Brewer, Sarah L. Bromley, Jwo Sy Chen, Jean Daniel Deschênes, Scott A. Diddams, Robert J. Fasano, Tara M. Fortier, Youssef S. Hassan, David B. Hume, Dhruv Kedar, Colin J. Kennedy, Isaac Khader, Amanda Koepke, David R. Leibrandt, Holly Leopardi, Andrew D. Ludlow, William F. McGrew, William R. Milner, Nathan R. Newbury, Daniele Nicolodi, Eric Oelker, Thomas E. Parker, John M. Robinson, Stefania Romisch, Stefan A. Schäffer, Jeffrey A. Sherman, Laura C. Sinclair, Lindsay Sonderhouse, William C. Swann, Jian Yao, Jun Ye, and Xiaogang Zhang. Frequency ratio measurements at 18-digit accuracy using an optical clock network. Nature, 591(7851):564–569, 2021.

[74] Emily D. Caldwell, Laura C. Sinclair, Nathan R. Newbury, and Jean Daniel Deschenes. The time-programmable frequency comb and its use in quantum-limited ranging. Nature, 610(7933):667–673, 2022.

[75] Nathalie Picqué and Theodor W. Hänsch. Frequency comb spectroscopy. Nature Photonics, 13(3):146–157, 2019.

[76] Yuan Yao, Yanyi Jiang, Hongfu Yu, Zhiyi Bi, and Longsheng Ma. Optical frequency divider with division uncertainty at the 10^{-21} level. National Science Review, 3(4):463–469, 09 2016.

[77] Xiaopeng Xie, Romain Bouchand, Daniele Nicolodi, Michele Giunta, Wolfgang Hänsel, Matthias Lezius, Abhay Joshi, Shubhashish Datta, Christophe Alexandre, Michel Lours, Pierre-Alain Tremblin, Giorgio Santarelli, Ronald Holzwarth, and Yann Le Coq. Photonic microwave signals with zeptosecond-level absolute timing noise. Nature Photonics, 11(1):44–47, 2017.

[78] Kouji Nakamura. Quantum noise and vacuum fluctuations in balanced homodyne detections through ideal multi-mode detectors. Progress of Theoretical and Experimental Physics, 2021(10):103A01, 09 2021.

[79] Dahyeon Lee, Takuma Nakamura, Andrew J. Metcalf, Nathan E. Flowers-Jacobs, Anna E. Fox, Paul D. Dresselhaus, and Franklyn Quinlan. Sub-GHz resolution line-by-line pulse shaper for driving superconducting circuits. APL Photonics, 8(8), 2023.

[80] Wolfgang P. Schleich. Quantum Optics in Phase Space. Wiley, 2001.

[81] E. C.G. Sudarshan. Equivalence of semiclassical and quantum mechanical descriptions of statistical light beams. Physical Review Letters, 10(7):277–279, 1963.

[82] K. J. Blow, Rodney Loudon, Simon J. D. Phoenix, and T. J. Shepherd. Continuum fields in quantum optics. Physical Review A, 42:4102–4114, 1990.

[83] R. Kumar, E. Barrios, A. MacRae, E. Cairns, E. H. Huntington, and A. I. Lvovsky. Versatile wideband balanced detector for quantum optical homodyne tomography. Optics Communications, 285(24):5259–5267, 2012.

[84] T. Gerrits, S. Glancy, and S. W. Nam. A balanced homodyne detector and local oscillator shaping for measuring optical Schrödinger cat states. Advanced Photon Counting Techniques V, 8033:80330X, 2011.

[85] Maria Fuwa, Shuntaro Takeda, Marcin Zwierz, Howard M. Wiseman, and Akira Furusawa. Experimental proof of nonlocal wavefunction collapse for a single particle using homodyne measurements. Nature Communications, 6(1):1–6, 2015.

[86] C Polycarpou, K N Cassemiro, G Venturi, A Zavatta, and M Bellini. Adaptive detection of arbitrarily shaped ultrashort quantum light states. Physical Review Letters, 109(5), 2012.

[87] Zhongzhong Qin, Adarsh S. Prasad, Travis Brannan, Andrew MacRae, A. Lezama, and A. I. Lvovsky. Complete temporal characterization of a single photon. Light: Science and Applications, 4(6):e298–e298, 2015.

[88] Samuele Grandi, Alessandro Zavatta, Marco Bellini, and Matteo G A Paris. Experimental quantum tomography of a homodyne detector. New Journal of Physics, 19(5):053015, 2017.

[89] N.G. Walker. Quantum theory of multiport optical homodyning. Journal of Modern Optics, 34(1):15–60, 1987.

[90] Samuel L. Braunstein. Homodyne statistics. Physical Review A, 42:474–481, 1990.

[91] Konrad Banaszek and Krzysztof Wódkiewicz. Operational theory of homodyne detection. Physical Review A, 55:3117–3123, 1997.

[92] Tomáš Tyc and Barry C Sanders. Operational formulation of homodyne detection. Journal of Physics A: Mathematical and General, 37(29):7341–7357, 2004.

[93] Carl W. Helstrom. Detectability of Coherent Optical Signals in a Heterodyne Receiver. Journal of the Optical Society of America, 57(3):353, 1967.

[94] J. Shapiro. Quantum noise and excess noise in optical homodyne and heterodyne receivers. IEEE Journal of Quantum Electronics, 21(3):237–250, 1985.

[95] M.J. Collett, R. Loudon, and C.W. Gardiner. Quantum theory of optical homodyne and heterodyne detection. Journal of Modern Optics, 34(6-7):881–902, 1987.

[96] Ryan S Bennink and Robert W Boyd. Improved measurement of multimode squeezed light via an eigenmode approach. Physical Review A, 66(5):5, 2002.

[97] F. Grosshans and P. Grangier. Effective quantum efficiency in the pulsed homodyne detection of a n-photon state. European Physical Journal D, 14(1):119–125, 2001.

[98] Z.J. Ou. Quantum Optics For Experimentalists. World Scientific Publishing Company, 2017.

[99] Ziyang Chen, Xiangyu Wang, Song Yu, Zhengyu Li, and Hong Guo. Continuous-mode quantum key distribution with digital signal processing. npj Quantum Information, 9(1):28, 2023.

[100] M. Walsh, P. Guay, and J. Genest. Unlocking a lower shot noise limit in dual-comb interferometry. APL Photonics, 8(7), July 2023.

[101] J. Reichert, R. Holzwarth, Th Udem, and T. W. Hänsch. Measuring the frequency of light with mode-locked lasers. Optics Communications, 172(1):59–68, 1999.

[102] F. Quinlan, T. M. Fortier, H. Jiang, A. Hati, C. Nelson, Y. Fu, J. C. Campbell, and S. A. Diddams. Exploiting shot noise correlations in the photodetection of ultrashort optical pulse trains. Nature Photonics, 7(4):290–293, 2013.

[103] Olivier Pinel, Pu Jian, Renné Medeiros de Araújo, Jinxia Feng, Benoît Chalopin, Claude Fabre, and Nicolas Treps. Generation and characterization of multimode quantum frequency combs. Physical Review Letters, 108:083601, 2012.

[104] Michael Kues, Christian Reimer, Joseph M. Lukens, William J. Munro, Andrew M. Weiner, David J. Moss, and Roberto Morandotti. Quantum optical microcombs. Nature Photonics, 13(3):170–179, 2019.

[105] N. Fabre, G. Maltese, F. Appas, S. Felicetti, A. Ketterer, A. Keller, T. Coudreau, F. Baboux, M. I. Amanti, S. Ducci, and P. Milman. Generation of a time-frequency grid state with integrated biphoton frequency combs. Physical Review A, 102:012607, 2020.

[106] G. Maltese, M. I. Amanti, F. Appas, G. Sinnl, A. Lemaître, P. Milman, F. Baboux, and S. Ducci. Generation and symmetry control of quantum frequency combs. npj Quantum Information, 6(1):13, 2020.

[107] Zijiao Yang, Mandana Jahanbozorgi, Dongin Jeong, Shuman Sun, Olivier Pfister, Hansuek Lee, and Xu Yi. A squeezed quantum microcomb on a chip. Nature Communications, 12(1):4781, 2021.

[108] Y. Cai, J. Roslund, V. Thiel, C. Fabre, and N. Treps. Quantum enhanced measurement of an optical frequency comb. npj Quantum Information, 7(1):82, 2021.

[109] Alexandre Belsley. Quantum-enhanced absorption spectroscopy with bright squeezed frequency combs. Physical Review Letters, 130:133602, 2023.

[110] Melissa A. Guidry, Daniil M. Lukin, Ki Youl Yang, and Jelena Vučković. Multimode squeezing in soliton crystal microcombs. Optica, 10(6):694–701, 2023.

[111] Haowei Shi, Zaijun Chen, Scott E. Fraser, Mengjie Yu, Zheshen Zhang, and Quntao Zhuang. Entanglement-enhanced dual-comb spectroscopy. arXiv:2304.01516 [quant-ph], 2023.

[112] Joshua Combes and Austin P. Lund. Homodyne measurement with a Schrödinger cat state as a local oscillator. Physical Review A, 106(6):063706, 2022.

[113] Arik Avagyan. Quantum state characterization using measurement configurations inspired by homodyne detection. arXiv:2305.19397 [quant-ph], 2023.

[114] Chang Hyuck Oh. A maximum likelihood estimation method for a mixture of shifted binomial distributions. Korean Journal of Data Information Science, 25(1):255–261, 2014.

[115] Werner Vogel. Homodyne correlation measurements with weak local oscillators. Physical Review A, 51:4160–4171, 1995.

[116] G. S. Thekkadath, D. S. Phillips, J. F. F. Bulmer, W. R. Clements, A. Eckstein, B. A. Bell, J. Lugani, T. A. W. Wolterink, A. Lita, S. W. Nam, T. Gerrits, C. G. Wade, and I. A. Walmsley. Tuning between photon-number and quadrature measurements with weak-field homodyne detection. Physical Review A, 101:031801, 2020.

[117] Stefano Olivares, Alessia Allevi, and Maria Bondani. On the role of the local oscillator intensity in optical homodyne-like tomography. Physics Letters A, 384(17):126354, 2020.

[118] Emanuel Hubenschmid, Thiago L. M. Guedes, and Guido Burkard. Complete positive operator-valued measure description of multichannel quantum electro-optic sampling with monochromatic field modes. Physical Review A, 106:043713, 2022.

[119] David W. Allan. Should the classical variance be used as a basic measure in standards metrology? IEEE Transactions on Instrumentation and Measurement, IM-36(2):646–654, 1987.

[120] Enrico Rubiola and Francois Vernotte. The Companion of Enrico's Chart for Phase Noise and Two-Sample Variances. IEEE Transactions on Microwave Theory and Techniques, 71(7):2996–3025, 2023.

[121] Franklyn Quinlan. The Photodetection of Ultrashort Optical Pulse Trains for Low Noise Microwave Signal Generation. Laser and Photonics Reviews, 17(12):2200773, 2023.

[122] D. G. Matei, T. Legero, S. Häfner, C. Grebing, R. Weyrich, W. Zhang, L. Sonderhouse, J. M. Robinson, J. Ye, F. Riehle, and U. Sterr. 1.5 μ m Lasers with Sub-10 mHz Linewidth. Physical Review Letters, 118(26):263202, 2017.

[123] Eugene Tsao, Yijun Xie, Mingming Nie, and Shu-Wei Huang. Monostable dissipative Kerr solitons. Optics Letters, 47(1):122, 2022.

[124] P. Del'Haye, A. Schliesser, O. Arcizet, T. Wilken, R. Holzwarth, and T. J. Kippenberg. Optical frequency comb generation from a monolithic microresonator. Nature, 450(7173):1214–1217, 2007.

[125] Pablo Marin-Palomo, Juned N. Kemal, Maxim Karpov, Arne Kordts, Joerg Pfeifle, Martin H.P. Pfeiffer, Philipp Trocha, Stefan Wolf, Victor Brasch, Miles H. Anderson, Ralf Rosenberger, Kovendhan Vijayan, Wolfgang Freude, Tobias J. Kippenberg, and Christian Koos. Microresonator-based solitons for massively parallel coherent optical communications. Nature, 546(7657):274–279, 2017.

[126] Bill Corcoran, Mengxi Tan, Xingyuan Xu, Andreas Boes, Jiayang Wu, Thach G. Nguyen, Sai T. Chu, Brent E. Little, Roberto Morandotti, Arnan Mitchell, and David J. Moss. Ultra-dense optical data transmission over standard fibre with a single chip source. Nature Communications, 11(1):1–7, 2020.

[127] Myoung Gyun Suh, Xu Yi, Yu Hung Lai, S. Leifer, Ivan S. Grudinin, G. Vasisht, Emily C. Martin, Michael P. Fitzgerald, G. Doppmann, J. Wang, D. Mawet, Scott B. Papp, Scott A. Diddams, C. Beichman, and Kerry Vahala. Searching for exoplanets using a microresonator astrocomb. Nature Photonics, 13(1):25–30, 2019.

[128] Ewelina Obrzud, Monica Rainer, Avet Harutyunyan, Miles H. Anderson, Junqiu Liu, Michael Geiselmann, Bruno Chazelas, Stefan Kundermann, Steve Lecomte, Massimo Cecconi, Adriano Ghedina, Emilio Molinari, Francesco Pepe, François Wildi, François Bouchy, Tobias J. Kippenberg, and Tobias Herr. A microphotonic astrocomb. Nature Photonics, 13(1):31–35, 2019.

[129] P. Trocha, M. Karpov, D. Ganin, M. H.P. Pfeiffer, A. Kordts, S. Wolf, J. Krockenberger, P. Marin-Palomo, C. Weimann, S. Randel, W. Freude, T. J. Kippenberg, and C. Koos. Ultrafast optical ranging using microresonator soliton frequency combs. Science, 359(6378):887–891, 2018.

[130] Myoung Gyun Suh, Qi Fan Yang, Ki Youl Yang, Xu Yi, and Kerry J. Vahala. Microresonator soliton dual-comb spectroscopy. Science, 354(6312), 2016.

[131] Shu Wei Huang, Jinghui Yang, Mingbin Yu, Bart H. McGuyer, Dim Lee Kwong, Tanya Zelevinsky, and Chee Wei Wong. A broadband chip-scale optical frequency synthesizer at 2.7 × 10-16 relative uncertainty. Science Advances, 2(4):e1501489, 2016.

[132] Erwan Lucas, Pierre Brochard, Romain Bouchand, Stéphane Schilt, Thomas Südmeyer, and Tobias J. Kippenberg. Ultralow-noise photonic microwave synthesis using a soliton microcomb-based transfer oscillator. Nature Communications, 11(1):1–8, 2020.

[133] Kunpeng Jia, Xiaohan Wang, Dohyeon Kwon, Jiarong Wang, Eugene Tsao, Huaying Liu, Xin Ni, Jian Guo, Mufan Yang, Xiaoshun Jiang, Jungwon Kim, Shi-ning Zhu, Zhenda Xie, and Shu-Wei Huang. Photonic Flywheel in a Monolithic Fiber Resonator. Physical Review Letters, 125(14):143902, 2020.

[134] Tobias J. Kippenberg, Alexander L. Gaeta, Michal Lipson, and Michael L. Gorodetsky. Dissipative Kerr solitons in optical microresonators. Science, 361:6402, 2018.

[135] Qing Li, Travis C. Briles, Daron A. Westly, Tara E. Drake, Jordan R. Stone, B. Robert Ilic, Scott A. Diddams, Scott B. Papp, and Kartik Srinivasan. Stably accessing octave-spanning microresonator frequency combs in the soliton regime. Optica, 4(2):193, 2017.

[136] Alexander W. Bruch, Xianwen Liu, Zheng Gong, Joshua B. Surya, Ming Li, Chang Ling Zou, and Hong X. Tang. Pockels soliton microcomb. Nature Photonics, 15(1):21–27, 2021.

[137] Xiaoxiao Xue, Xiaoping Zheng, and Bingkun Zhou. Soliton regulation in microcavities induced by fundamental–second-harmonic mode coupling. Photonics Research, 6(10):948, 2018.

[138] Chengying Bao, Yi Xuan, Daniel E. Leaird, Stefan Wabnitz, Minghao Qi, and Andrew M. Weiner. Spatial mode-interaction induced single soliton generation in microresonators. Optica, 4(9):1011, 2017.

[139] H. Guo, M. Karpov, E. Lucas, A. Kordts, M. H.P. Pfeiffer, V. Brasch, G. Lihachev, V. E. Lobanov, M. L. Gorodetsky, and T. J. Kippenberg. Universal dynamics and deterministic switching of dissipative Kerr solitons in optical microresonators. Nature Physics, 13(1):94–102, 2017.

[140] Mingming Nie, Yijun Xie, and Shu Wei Huang. Deterministic generation of parametrically driven dissipative Kerr soliton. Nanophotonics, 10(6):1691–1699, 2021.

[141] Scott B. Papp, Pascal Del'Haye, and Scott A. Diddams. Parametric seeding of a microresonator optical frequency comb. Optics Express, 21(15):17615, 2013.

[142] Pascal Del'Haye, Katja Beha, Scott B. Papp, and Scott A. Diddams. Self-injection locking and phase-locked states in microresonator-based optical frequency combs. Physical Review Letters, 112(4):1–6, 2014.

[143] Thibault Wildi, Victor Brasch, Junqiu Liu, Tobias J. Kippenberg, and Tobias Herr. Thermally stable access to microresonator solitons via slow pump modulation. Optics Letters, 44(18):4447, 2019.

[144] Victor Brasch, Michael Geiselmann, Martin H. P. Pfeiffer, and Tobias J. Kippenberg. Bringing short-lived dissipative Kerr soliton states in microresonators into a steady state. Optics Express, 24(25):29312, 2016.

[145] Xu Yi, Qi-Fan Yang, Ki Youl Yang, and Kerry Vahala. Active capture and stabilization of temporal solitons in microresonators. Optics Letters, 41(9):2037, 2016.

[146] Heng Zhou, Yong Geng, Wenwen Cui, Shu-Wei Huang, Qiang Zhou, Kun Qiu, and Chee Wei Wong. Soliton bursts and deterministic dissipative Kerr soliton generation in auxiliary-assisted microcavities. Light: Science & Applications, 8(1):50, 2019.

[147] Yang He, Qi-Fan Yang, Jingwei Ling, Rui Luo, Hanxiao Liang, Mingxiao Li, Boqiang Shen, Heming Wang, Kerry Vahala, and Qiang Lin. Self-starting bi-chromatic LiNbO 3 soliton microcomb . Optica, 6(9):1138, 2019.

[148] Boqiang Shen, Lin Chang, Junqiu Liu, Heming Wang, Qi-Fan Yang, Chao Xiang, Rui Ning Wang, Jijun He, Tianyi Liu, Weiqiang Xie, Joel Guo, David Kinghorn, Lue Wu, Qing-Xin Ji, Tobias J. Kippenberg, Kerry Vahala, and John E. Bowers. Integrated turnkey soliton microcombs. Nature, 582(7812):365–369, 2020.

[149] R Desalvo, D J Hagan, G Stegeman, and E W Van Stryland. Self-focusing and self-defocusing by cascaded second-order effects in KTP. Optics Letters, 17(1):28–30, 1992.

[150] Stéphane Coen, Hamish G. Randle, Thibaut Sylvestre, and Miro Erkintalo. Modeling of octave-spanning Kerr frequency combs using a generalized mean-field Lugiato–Lefever model. Optics Letters, 38(1):37, 2013.

[151] Tal Carmon, Lan Yang, and Kerry J Vahala. Dynamical thermal behavior and thermal self-stability of microcavities. Optics Express, 12(20):4742–4750, 2004.

[152] Zheng Gong, Xianwen Liu, Yuntao Xu, Mingrui Xu, Joshua B. Surya, Juanjuan Lu, Alexander Bruch, Changling Zou, and Hong X. Tang. Soliton microcomb generation at 2 μm in z-cut lithium niobate microring resonators. Optics Letters, 44(12):3182, 2019.

[153] Lute Maleki, Vladimir S. Ilchenko, Anatoliy A. Savchenkov, and Andrey B. Matsko. Crystalline whispering gallery mode resonators in optics and photonics. Practical Applications of Microresonators in Optics and Photonics, pages 133–209, 2009.

[154] Stéphane Coen and Miro Erkintalo. Universal scaling laws of Kerr frequency combs. Optics Letters, 38(11):1790, 2013.

[155] Changjing Bao, Lin Zhang, Andrey Matsko, Yan Yan, Zhe Zhao, Guodong Xie, Anuradha M. Agarwal, Lionel C. Kimerling, Jurgen Michel, Lute Maleki, and Alan E. Willner. Nonlinear conversion efficiency in Kerr frequency comb generation. Optics Letters, 39(21):6126, 2014.

[156] L. A. Lugiato and R. Lefever. Spatial dissipative structures in passive optical systems. Physical Review Letters, 58(21):2209–2211, 1987.

[157] Jie Wang, Bowen Zhu, Zhenzhong Hao, Fang Bo, Xiaolei Wang, Feng Gao, Yigang Li, Guoquan Zhang, and Jingjun Xu. Thermo-optic effects in on-chip lithium niobate microdisk resonators. Optics Express, 24(19):21869, 2016.

[158] Luigi Moretti, Mario Iodice, Francesco G. Della Corte, and Ivo Rendina. Temperature dependence of the thermo-optic coefficient of lithium niobate, from 300 to 515 K in the visible and infrared regions. Journal of Applied Physics, 98(3):036101, 2005.

[159] Morten Bache and Roland Schiek. Review of measurements of Kerr nonlinearities in lithium niobate: the role of the delayed Raman response, 2012. arXiv:1211.1721 [physics.optics].

[160] Xiaoxiao Xue, Minghao Qi, and Andrew M. Weiner. Normal-dispersion microresonator Kerr frequency combs. Nanophotonics, 5(2):244–262, 2016.

[161] M. Haelterman, S. Trillo, and S. Wabnitz. Dissipative modulation instability in a nonlinear dispersive ring cavity. Optics Communications, 91(5-6):401–407, 1992.

[162] Cyril Godey, Irina V. Balakireva, Aurélien Coillet, and Yanne K. Chembo. Stability analysis of the spatiotemporal Lugiato-Lefever model for Kerr optical frequency combs in the anomalous and normal dispersion regimes. Physical Review A, 89(6):063814, 2014.

[163] Boris Desiatov, Amirhassan Shams-Ansari, Mian Zhang, Cheng Wang, and Marko Lončar. Ultra-low-loss integrated visible photonics using thin-film lithium niobate. Optica, 6(3):380, 2019.

[164] M. Leidinger, S. Fieberg, N. Waasem, F. Kühnemann, K. Buse, and I. Breunig. Comparative study on three highly sensitive absorption measurement techniques characterizing lithium niobate over its entire transparent spectral range. Optics Express, 23(17):21690, 2015.

[165] Andrey B. Matsko, Anatoliy A. Savchenkov, Dmitry Strekalov, Vladimir S. Ilchenko, and Lute Maleki. Optical properties of photorefractive whispering gallery mode resonators. In 2006 Conference on Lasers and Electro-Optics and 2006 Quantum Electronics and Laser Science Conference, pages 1–2, 2006.

Appendix A

Frequency Domain Derivation of Signal-to-Noise Ratio of Dual-Comb Correlation Spectroscopy of Thermal Light

Here, a more detailed derivation of SNR in the frequency domain is described.

A.1 Photodetection

We begin by looking at the heterodyne beat photocurrent between a comb tooth and the thermal light right before the electronic mixer. We represent it over a bandwidth $2B_f$ in terms of uncorrelated cosines. This follows techniques in Appendix 3.5.3.1.

$$i_{\text{het, single tooth}} = \frac{\eta e}{h\nu}\sqrt{4S_{det}\delta\nu P_t}\sum_{k=-B_f/\delta\nu}^{B_f/\delta\nu}\sqrt{2}\cos(2\pi k\delta\nu t + \Phi_k - \Theta). \tag{A.1}$$

S_{det} is the power spectral density of the thermal light coming into each balanced detector. B_f is the bandwidth of the RF low-pass filters we place after balanced detection. Note that this is an equivalent representation of the mean square value white noise of Equation 3.5.3.2.

Next we represent the current arising from heterodynes of all comb teeth. We choose to have $N+1$ comb teeth. In other words, we have $N+1$ sums from the full comb interfering with the thermal light. This choice allows us to sum from $n=0$ to $n=N$. Thus our full expression before the electronic mixer is:

$$i_{\text{het}} = \frac{\eta e}{h\nu}\sum_{n=0}^{n=N}\sqrt{4S_{det}\delta\nu P_t}\sum_{k=-B_f/\delta\nu}^{B_f/\delta\nu}\sqrt{2}\cos(2\pi k\delta\nu t + \Phi_{k,n} - \Theta_n). \tag{A.2}$$

We index the random phase ($\Phi_{k,n}$) by the comb number so that all cosine terms have random relative phases with respect to each other. We also index the comb tooth phase Θ_n by the comb tooth number since we are including many comb teeth now. We note that these teeth are spaced by f_r in the frequency domain, where f_r is the repetition rate. We assume that the total comb power is distributed evenly among all teeth (rectangular spectral profile).

Next, we consider the other comb and thermal signal. This is similar to the equation above:

$$i'_{\text{het}} = \frac{\eta e}{h\nu} \sum_{m=0}^{m=N} \sqrt{4S_{det}\delta\nu P'_t} \sum_{j=-B_f/\delta\nu}^{B_f/\delta\nu} \sqrt{2}\cos(2\pi j\delta\nu t + \Phi'_{j,m} - \Theta'_m). \tag{A.3}$$

We note two differences between this equation and the last equation. The second comb has a power per tooth of P'_t, and the phases in the cosine argument are not the same, denoted by the prime notation. However, $\Phi_{k,n}$ and $\Phi'_{j,m}$ have a special relationship when $n = m$; they are derived from the same quasi-thermal light. We thus have the relation:

$$\Phi_{k,n} = \Phi'_{j',n} \tag{A.4}$$

when $j' = k + \frac{n\Delta f_r}{\delta\nu}$. $\Delta f_r = f_r - f'_r$, where f'_r is the repetition rate of the second comb and is assumed to be smaller than f_r.

At this point we should also take note of the shot noise of the first comb after balanced detection:

$$i_{SN,RMS} = \sqrt{2ei_{LO}B_f} = \sqrt{2e\frac{\eta e}{h\nu}(N+1)P_tB_f}. \tag{A.5}$$

Note that the total comb power is $(N+1)P_t$, i.e., the number of comb teeth multiplied by the power per tooth. In order to evaluate how the shot noise propagates through the electronics, we represent the shot noise current as a sum of cosines with uncorrelated phases.

$$\begin{aligned} i_{SN} &= \sqrt{\frac{2e\frac{\eta e}{h\nu}(N+1)P_tB_f}{2B_f(N+1)/\delta\nu}} \sum_{n=0}^{N} \sum_{k=-B_f/\delta\nu}^{B_f/\delta\nu} \sqrt{2}\cos(2\pi k\delta\nu t + \phi_{k,n}) \\ &= \sqrt{2e\frac{\eta e}{h\nu}P_t\delta\nu} \sum_{n=0}^{N} \sum_{k=-B_f/\delta\nu}^{B_f/\delta\nu} \sqrt{2}\cos(2\pi k\delta\nu t + \phi_{k,n}). \end{aligned} \tag{A.6}$$

Note that quadrature summation of the RMS values of the cosines takes i_{SN} back to $i_{SN,RMS}$. Similarly, the RMS shot noise of the second comb is:

$$i_{SN,RMS} = \sqrt{2ei'_{LO}B_f} = \sqrt{2e\frac{\eta e}{h\nu}(N+1)P'_tB_f}. \tag{A.7}$$

And the shot noise photocurrent of the second comb can be written as:

$$i'_{SN} = \sqrt{2e\frac{\eta e}{h\nu}P'_t\delta\nu}\sum_{m=0}^{N}\sum_{k=-B_f/\delta\nu}^{B_f/\delta\nu}\sqrt{2}\cos(2\pi j\delta\nu t+\phi'_{j,m}). \tag{A.8}$$

We may also have excess relative intensity noise (RIN) due to balancing that is not perfect. We can represent the RMS intensity noise current of the first comb as:

$$i_{RIN,RMS} = \sqrt{(N+1)B_fS_{IN}}. \tag{A.9}$$

S_{IN} is the power spectral density of the intensity noise photocurrent per comb tooth, in units of amps squared per root hertz. Likewise, for the other comb, the RMS intensity noise current is:

$$i'_{RIN,RMS} = \sqrt{(N+1)B_fS'_{IN}}. \tag{A.10}$$

It is most convenient for us to treat all the noise from the photodetectors at once, so we combine the shot noise and the intensity noise into a total photodetected noise term $i_{PDN,RMS}$ for the first comb:

$$i_{PDN,RMS} = \sqrt{i^2_{SN,RMS}+i^2_{RIN,RMS}} = \sqrt{\sqrt{2e\frac{\eta e}{h\nu}(N+1)P_tB_f}^{\,2} + \sqrt{(N+1)B_fS_{RIN}}^{\,2}} \tag{A.11}$$

As before, we define this total photodetected noise in terms of a sum over cosines:

$$\begin{aligned} i_{PDN} &= i_{PDN,RMS}\sqrt{\frac{\delta\nu}{2(N+1)B_f}}\sqrt{2}\sum_{n=0}^{N}\sum_{k=-B_f/\delta\nu}^{B_f/\delta\nu}\cos(2\pi k\delta\nu t+\phi'_{k,n}) \\ &= i_{PDN,RMS}\sqrt{\frac{\delta\nu}{(N+1)B_f}}\sum_{n=0}^{N}\sum_{k=-B_f/\delta\nu}^{B_f/\delta\nu}\cos(2\pi k\delta\nu t+\phi'_{k,n}). \end{aligned} \tag{A.12}$$

We define the total photodetected noise for the second comb similarly, such that:

$$i'_{PDN,RMS} = \sqrt{i'^2_{SN,RMS}+i'^2_{IN,RMS}} = \sqrt{\sqrt{2e\frac{\eta e}{h\nu}(N+1)P'_tB_f}^{\,2} + \sqrt{(N+1)B_fS'_{RIN}}^{\,2}}, \tag{A.13}$$

and:

$$i'_{PDN} = i'_{PDN,RMS}\sqrt{\frac{\delta\nu}{(N+1)B_f}}\sum_{m=0}^{N}\sum_{j=-B_f/\delta\nu}^{B_f/\delta\nu}\cos(2\pi j\delta\nu t+\phi'_{j,m}). \tag{A.14}$$

Thus, the total current of the first comb heterodyne signal before mixing is:

$$i_{\text{tot}} = i_{\text{het}} + i_{PDN}, \tag{A.15}$$

and the second is:

$$i'_{\text{tot}} = i'_{\text{het}} + i'_{PDN}. \tag{A.16}$$

If limited by light noise, these are the currents that result from the two detectors. Next we move to the mixing stage.

A.2 Mixing of Heterodyne Signal with Heterodyne Signal

Mixing the two heterodyne signals results in:

$$i_{\text{mix}} = i_{\text{tot}} \times i'_{\text{tot}} = (i_{\text{het}} + i_{PDN}) \times (i'_{\text{het}} + i'_{PDN}) = i_{\text{het}} i'_{\text{het}} + i_{\text{het}} i'_{PDN} + i_{PDN} i'_{\text{het}} + i_{PDN} i'_{PDN}. \tag{A.17}$$

We will see that the first term that is the product of the two heterodyne currents contributes to both noise and signal, while the three other terms contribute to noise. First we examine the thermal heterodyne product term.

$$\begin{aligned} i_{\text{het}} i'_{\text{het}} = \frac{\eta e}{h\nu} \sum_{n=0}^{n=N} \sqrt{4 S_{det} \delta\nu P_t} \sum_{k=-B_f/\delta\nu}^{B_f/\delta\nu} \sqrt{2} \cos(2\pi k \delta\nu t + \Phi_{k,n} - \Theta_n) \\ \times \frac{\eta e}{h\nu} \sum_{m=0}^{m=N} \sqrt{4 S_{det} \delta\nu P'_t} \sum_{j=-B_f/\delta\nu}^{B_f/\delta\nu} \sqrt{2} \cos(2\pi j \delta\nu t + \Phi'_{j,m} - \Theta'_m) \end{aligned} \tag{A.18}$$

Simplifying, we have:

$$\begin{aligned} i_{\text{het}} i'_{\text{het}} &= (\frac{\eta e}{h\nu})^2 8 (S_{det} \delta\nu) \sqrt{P_t P'_t} \\ &\times \sum_{n=0}^{n=N} \sum_{m=0}^{m=N} \sum_{k=-B_f/\delta\nu}^{B_f/\delta\nu} \sum_{j=-B_f/\delta\nu}^{B_f/\delta\nu} \cos(2\pi k \delta\nu t + \Phi_{k,n} - \Theta_n) \cos(2\pi j \delta\nu t + \Phi'_{j,m} - \Theta'_m) \end{aligned} \tag{A.19}$$

At this point, we note that the quasi-thermal light is uncorrelated across its spectrum. Thus, when $n \neq m$, $\Phi_{k,n}$ and $\Phi'_{j,m}$ are uncorrelated regardless of k and j. However, when $n = m$, $\Phi_{k,n}$ and $\Phi'_{j,m}$ are correlated (i.e., the same) under the condition that $j = k + \frac{n\Delta f_r}{\delta\nu}$. We then split the above heterodyne product into two terms: when $n \neq m$ and when $n = m$.

$$\begin{aligned}
i_{\text{het}} i'_{\text{het}} &= (\frac{\eta e}{h\nu})^2 8(S_{det}\delta\nu)\sqrt{P_t P'_t} \\
&\times \Big(\sum_{n=0}^{n=N} \sum_{m=0,m\neq n}^{m=N} \sum_{k=-B_f/\delta\nu}^{B_f/\delta\nu} \sum_{j=-B_f/\delta\nu}^{B_f/\delta\nu} \cos(2\pi k\delta\nu t + \Phi_{k,n} - \Theta_n)\cos(2\pi j\delta\nu t + \Phi'_{j,m} - \Theta'_m) \\
&\quad + \sum_{n=0,n=m}^{n=N} \sum_{k=-B_f/\delta\nu}^{B_f/\delta\nu} \sum_{j=-B_f/\delta\nu}^{B_f/\delta\nu} \cos(2\pi k\delta\nu t + \Phi_{k,n} - \Theta_n)\cos(2\pi j\delta\nu t + \Phi'_{j,m} - \Theta'_m) \Big)
\end{aligned} \tag{A.20}$$

We must further break down the $n = m$ product into those without correlated phases and those with correlated phases (i.e., split the sum):

$$\begin{aligned}
i_{\text{het}} i'_{\text{het}} &= (\frac{\eta e}{h\nu})^2 8(S_{det}\delta\nu)\sqrt{P_t P'_t} \\
&\times \Big(\sum_{n=0}^{n=N} \sum_{m=0,m\neq n}^{m=N} \sum_{k=-B_f/\delta\nu}^{B_f/\delta\nu} \sum_{j=-B_f/\delta\nu}^{B_f/\delta\nu} \cos(2\pi k\delta\nu t + \Phi_{k,n} - \Theta_n)\cos(2\pi j\delta\nu t + \Phi'_{j,m} - \Theta'_m) \\
&+ \sum_{n=0,n=m}^{n=N} \sum_{k=-B_f/\delta\nu}^{B_f/\delta\nu} \sum_{j=-B_f/\delta\nu, j\neq k+\frac{n\Delta f_r}{\delta\nu}}^{B_f/\delta\nu} \cos(2\pi k\delta\nu t + \Phi_{k,n} - \Theta_n)\cos(2\pi j\delta\nu t + \Phi'_{j,m} - \Theta'_m) \\
&\quad + \sum_{n=0,n=m}^{n=N} \sum_{j=-B_f/\delta\nu, j=k+\frac{n\Delta f_r}{\delta\nu}}^{B_f/\delta\nu} \cos(2\pi k\delta\nu t + \Phi_{k,n} - \Theta_n)\cos(2\pi j\delta\nu t + \Phi'_{j,m} - \Theta'_m) \Big)
\end{aligned} \tag{A.21}$$

However, even here in the last term there exist products that do not contain correlated phases. These uncorrelated product terms are the ones residing at the outer edges of the bandwidth B_f. To fully capture this, we must split the last term into three more terms: one term from the middle section and two terms from the edge of the bandwidth to $n\Delta f_r$ inside.

$$\begin{aligned}
i_{\text{het}} i'_{\text{het}} &= (\frac{\eta e}{h\nu})^2 8(S_{det}\delta\nu)\sqrt{P_t P'_t} \\
&\times \Bigg(\sum_{n=0}^{n=N} \sum_{m=0,m\neq n}^{m=N} \sum_{k=-B_f/\delta\nu}^{B_f/\delta\nu} \sum_{j=-B_f/\delta\nu}^{B_f/\delta\nu} \cos(2\pi k\delta\nu t + \Phi_{k,n} - \Theta_n)\cos(2\pi j\delta\nu t + \Phi'_{j,m} - \Theta'_m) \\
&+ \sum_{n=0,n=m}^{n=N} \sum_{k=-B_f/\delta\nu}^{B_f/\delta\nu} \sum_{j=-B_f/\delta\nu, j\neq k+\frac{n\Delta f_r}{\delta\nu}}^{B_f/\delta\nu} \cos(2\pi k\delta\nu t + \Phi_{k,n} - \Theta_n)\cos(2\pi j\delta\nu t + \Phi'_{j,m} - \Theta'_m) \\
&+ \sum_{n=0,n=m}^{n=N} \sum_{j=-B_f/\delta\nu, j=k+\frac{n\Delta f_r}{\delta\nu}}^{-B_f/\delta\nu+\frac{n\Delta f_r}{\delta\nu}} \cos(2\pi k\delta\nu t + \Phi_{k,n} - \Theta_n)\cos(2\pi j\delta\nu t + \Phi'_{j,m} - \Theta'_m) \\
&+ \sum_{n=0,n=m}^{n=N} \sum_{j=B_f/\delta\nu-\frac{n\Delta f_r}{\delta\nu}, j=k+\frac{n\Delta f_r}{\delta\nu}}^{B_f/\delta\nu} \cos(2\pi k\delta\nu t + \Phi_{k,n} - \Theta_n)\cos(2\pi j\delta\nu t + \Phi'_{j,m} - \Theta'_m) \\
&+ \sum_{n=0,n=m}^{n=N} \sum_{j=-B_f/\delta\nu+\frac{n\Delta f_r}{\delta\nu}, j=k+\frac{n\Delta f_r}{\delta\nu}}^{B_f/\delta\nu-\frac{n\Delta f_r}{\delta\nu}} \cos(2\pi k\delta\nu t + \Phi_{k,n} - \Theta_n)\cos(2\pi j\delta\nu t + \Phi'_{j,m} - \Theta'_m)\Bigg)
\end{aligned} \tag{A.22}$$

Next, we simplify the cosine products, identical for each sum.

$$\begin{aligned}
&\cos(2\pi k\delta\nu + \Phi_{k,n} - \Theta_n)\cos(2\pi j\delta\nu + \Phi'_{j,m} - \Theta'_m) \\
&= \frac{\cos(2\pi(k+j)\delta\nu t + \Phi_{k,n} - \Theta_n + \Phi'_{j,m} - \Theta'_m)}{2} + \frac{\cos(2\pi(k-j)\delta\nu t + \Phi_{k,n} - \Theta_n - \Phi'_{j,m} + \Theta'_m)}{2}
\end{aligned} \tag{A.23}$$

We substitute the cosine products into the mixed heterodyne signal equation:

$$
\begin{aligned}
& i_{\text{het}} i'_{\text{het}} = (\frac{\eta e}{h\nu})^2 8(S_{det}\delta\nu)\sqrt{P_t P'_t} \\
& \times \Bigg(\sum_{n=0}^{n=N} \sum_{m=0, m\neq n}^{m=N} \sum_{k=-B_f/\delta\nu}^{B_f/\delta\nu} \sum_{j=-B_f/\delta\nu}^{B_f/\delta\nu} \\
& \frac{\cos(2\pi(k+j)\delta\nu t + \Phi_{k,n} - \Theta_n + \Phi'_{j,m} - \Theta'_m)}{2} + \frac{\cos(2\pi(k-j)\delta\nu t + \Phi_{k,n} - \Theta_n - \Phi'_{j,m} + \Theta'_m)}{2} \\
& + \sum_{n=0, n=m}^{n=N} \sum_{k=-B_f/\delta\nu}^{B_f/\delta\nu} \sum_{j=-B_f/\delta\nu, j\neq k+\frac{n\Delta f_r}{\delta\nu}}^{B_f/\delta\nu} \\
& \frac{\cos(2\pi(k+j)\delta\nu t + \Phi_{k,n} - \Theta_n + \Phi'_{j,m} - \Theta'_m)}{2} + \frac{\cos(2\pi(k-j)\delta\nu t + \Phi_{k,n} - \Theta_n - \Phi'_{j,m} + \Theta'_m)}{2} \\
& + \sum_{n=0, n=m}^{n=N} \sum_{j=-B_f/\delta\nu, j=k+\frac{n\Delta f_r}{\delta\nu}}^{-B_f/\delta\nu+\frac{n\Delta f_r}{\delta\nu}} \\
& \frac{\cos(2\pi(k+j)\delta\nu t + \Phi_{k,n} - \Theta_n + \Phi'_{j,m} - \Theta'_m)}{2} + \frac{\cos(2\pi(k-j)\delta\nu t + \Phi_{k,n} - \Theta_n - \Phi'_{j,m} + \Theta'_m)}{2} \\
& + \sum_{n=0, n=m}^{n=N} \sum_{j=B_f/\delta\nu-\frac{n\Delta f_r}{\delta\nu}, j=k+\frac{n\Delta f_r}{\delta\nu}}^{B_f/\delta\nu} \\
& \frac{\cos(2\pi(k+j)\delta\nu t + \Phi_{k,n} - \Theta_n + \Phi'_{j,m} - \Theta'_m)}{2} + \frac{\cos(2\pi(k-j)\delta\nu t + \Phi_{k,n} - \Theta_n - \Phi'_{j,m} + \Theta'_m)}{2} \\
& + \sum_{n=0, n=m}^{n=N} \sum_{j=-B_f/\delta\nu+\frac{n\Delta f_r}{\delta\nu}, j=k+\frac{n\Delta f_r}{\delta\nu}}^{B_f/\delta\nu-\frac{n\Delta f_r}{\delta\nu}} \\
& \frac{\cos(2\pi(k+j)\delta\nu t + \Phi_{k,n} - \Theta_n + \Phi'_{j,m} - \Theta'_m)}{2} + \frac{\cos(2\pi(k-j)\delta\nu t + \Phi_{k,n} - \Theta_n - \Phi'_{j,m} + \Theta'_m)}{2} \Bigg)
\end{aligned}
\tag{A.24}
$$

These correspond to the currents directly after the mixer. After the mixer, we now consider a low-pass filter $B_{f,m}$ to block the high frequency noise. In the simplest case, we choose a filter where $B_{f,m} = B_f$. After the mixer, the mixed heterodyne signals are the following, where only the sum terms only cover $|k+j| < B_{f,m}/\delta\nu$, and the difference terms only cover $|k-j| < B_{f,m}/\delta\nu$ due to the low pass filter bandwidth of $B_{f,m}$:

$$
\begin{aligned}
i_{\text{het}} i'_{\text{het}} &= (\frac{\eta e}{h\nu})^2 8(S_{det}\delta\nu)\sqrt{P_t P'_t} \\
&\times \Bigg(\sum_{n=0}^{n=N} \sum_{m=0,m\neq n}^{m=N} \sum_{k=-B_f/\delta\nu}^{B_f/\delta\nu} \sum_{j=-B_f/\delta\nu,|k+j|<B_{f,m}/\delta\nu}^{B_f/\delta\nu} \frac{\cos(2\pi(k+j)\delta\nu t+\Phi_{k,n}-\Theta_n+\Phi'_{j,m}-\Theta'_m)}{2} \\
&+ \sum_{n=0}^{n=N} \sum_{m=0,m\neq n}^{m=N} \sum_{k=-B_f/\delta\nu}^{B_f/\delta\nu} \sum_{j=-B_f/\delta\nu,|k-j|<B_{f,m}/\delta\nu}^{B_f/\delta\nu} \frac{\cos(2\pi(k-j)\delta\nu t+\Phi_{k,n}-\Theta_n-\Phi'_{j,m}+\Theta'_m)}{2} \\
&+ \sum_{n=0,n=m}^{n=N} \sum_{k=-B_f/\delta\nu}^{B_f/\delta\nu} \sum_{j=-B_f/\delta\nu,j\neq k+\frac{n\Delta f_r}{\delta\nu},|k+j|<B_{f,m}/\delta\nu}^{B_f/\delta\nu} \frac{\cos(2\pi(k+j)\delta\nu t+\Phi_{k,n}-\Theta_n+\Phi'_{j,m}-\Theta'_m)}{2} \\
&+ \sum_{n=0,n=m}^{n=N} \sum_{k=-B_f/\delta\nu}^{B_f/\delta\nu} \sum_{j=-B_f/\delta\nu,j\neq k+\frac{n\Delta f_r}{\delta\nu},|k-j|<B_{f,m}/\delta\nu}^{B_f/\delta\nu} \frac{\cos(2\pi(k-j)\delta\nu t+\Phi_{k,n}-\Theta_n-\Phi'_{j,m}+\Theta'_m)}{2} \\
&+ \sum_{n=0,n=m}^{n=N} \sum_{j=-B_f/\delta\nu,j=k+\frac{n\Delta f_r}{\delta\nu},|k+j|<B_{f,m}/\delta\nu}^{-B_f/\delta\nu+\frac{n\Delta f_r}{\delta\nu}} \frac{\cos(2\pi(k+j)\delta\nu t+\Phi_{k,n}-\Theta_n+\Phi'_{j,m}-\Theta'_m)}{2} \\
&+ \sum_{n=0,n=m}^{n=N} \sum_{j=-B_f/\delta\nu,j=k+\frac{n\Delta f_r}{\delta\nu},|k-j|<B_{f,m}/\delta\nu}^{-B_f/\delta\nu+\frac{n\Delta f_r}{\delta\nu}} \frac{\cos(2\pi(k-j)\delta\nu t+\Phi_{k,n}-\Theta_n-\Phi'_{j,m}+\Theta'_m)}{2} \\
&+ \sum_{n=0,n=m}^{n=N} \sum_{j=B_f/\delta\nu-\frac{n\Delta f_r}{\delta\nu},j=k+\frac{n\Delta f_r}{\delta\nu},|k+j|<B_{f,m}/\delta\nu}^{B_f/\delta\nu} \frac{\cos(2\pi(k+j)\delta\nu t+\Phi_{k,n}-\Theta_n+\Phi'_{j,m}-\Theta'_m)}{2} \\
&+ \sum_{n=0,n=m}^{n=N} \sum_{j=B_f/\delta\nu-\frac{n\Delta f_r}{\delta\nu},j=k+\frac{n\Delta f_r}{\delta\nu},|k-j|<B_{f,m}/\delta\nu}^{B_f/\delta\nu} \frac{\cos(2\pi(k-j)\delta\nu t+\Phi_{k,n}-\Theta_n-\Phi'_{j,m}+\Theta'_m)}{2} \\
&+ \sum_{n=0,n=m}^{n=N} \sum_{j=-B_f/\delta\nu+\frac{n\Delta f_r}{\delta\nu},j=k+\frac{n\Delta f_r}{\delta\nu},|k+j|<B_{f,m}/\delta\nu}^{B_f/\delta\nu-\frac{n\Delta f_r}{\delta\nu}} \frac{\cos(2\pi(k+j)\delta\nu t+\Phi_{k,n}-\Theta_n+\Phi'_{j,m}-\Theta'_m)}{2} \\
&+ \sum_{n=0,n=m}^{n=N} \sum_{j=-B_f/\delta\nu+\frac{n\Delta f_r}{\delta\nu},j=k+\frac{n\Delta f_r}{\delta\nu},|k-j|<B_{f,m}/\delta\nu}^{B_f/\delta\nu-\frac{n\Delta f_r}{\delta\nu}} \frac{\cos(2\pi(k-j)\delta\nu t+\Phi_{k,n}-\Theta_n-\Phi'_{j,m}+\Theta'_m)}{2} \Bigg)
\end{aligned}
\tag{A.25}
$$

At this point, we will go through and describe each term again:

- The first term contains sum frequency terms from non-same bins (i.e., no spectral overlap of the quasi-thermal light).

- The second term contains the difference frequency terms of non-same bins.
- The third term contains sum frequency terms of matching bins, but between intermediate frequencies that are not correlated.
- The fourth term contains difference frequency terms of matching bins, but between intermediate frequencies that are not correlated.
- The fifth and seventh terms contain sum frequency terms of matching bins that are not correlated due to the offset of the two teeth from separate combs–these sums correspond to the lower and upper non-overlapped optical regions.
- Likewise, the sixth and eighth terms contain difference frequency terms of matching bins that are not correlated due to the offset of the two teeth from separate combs–again, these sums correspond to the lower and upper non-overlapped optical regions.
- The ninth (second to last) term contains sum frequency terms between correlated heterodyne terms–however, there is no cancellation of phase due to sum frequency addition, so these terms are, like all those preceding it, uncorrelated.
- The tenth and final term contains difference frequency terms between correlated heterodyne terms; **this contains our signal.**

We separate this tenth term, our mixed heterodyne signal, into two parts, the noise and the signal, where $i_{\text{het}} i'_{\text{het}} = N_{\text{het}} + A_{\text{het}}$ such that:

$$A_{\text{het}} = (\frac{\eta e}{h\nu})^2 8(S_{det}\delta\nu)\sqrt{P_t P'_t}$$

$$\sum_{n=0,n=m}^{n=N} \sum_{j=-B_f/\delta\nu+\frac{n\Delta f_r}{\delta\nu},j=k+\frac{n\Delta f_r}{\delta\nu},|k-j|<B_{f,m}/\delta\nu}^{B_f/\delta\nu-\frac{n\Delta f_r}{\delta\nu}} \frac{\cos(2\pi(k-j)\delta\nu t+\Phi_{k,n}-\Theta_n-\Phi'_{j,m}+\Theta'_m)}{2} \tag{A.26}$$

Because we examine interferograms in this method, we will look at the peak value of the signal in the time domain. The maximal value occurs when we assume that both Θ_n and Θ'_m are linear across the optical frequencies spanned by N comb teeth. This linearity ensures constructive addition at the center of the resulting interferogram. Note that we also consider the low pass filter of $B_{f,m} = B_f$, which filters out 3/4 of the heterodyne tones. This is because the frequencies of this mixed term follow a triangular distribution centered at 0 with a width of $4B_f$; filtering at $\pm B_f$ cuts out 1/4 of these tones. The phases $\Phi_{k,n}$ and $\Phi'_{j,m}$ cancel at the indicated indices. We also sum over the N comb teeth, resulting in $N+1$ bins. Thus our peak signal is:

$$A_{\text{het,peak}} = (\frac{\eta e}{h\nu})^2 8(S_{det}\delta\nu)\sqrt{P_t P_t'} \times (N+1) \times \frac{3}{4}\frac{2B_f}{\delta\nu}\frac{1}{2} \tag{A.27}$$

Simplifying,

$$A_{\text{het,peak}} = 8 \times \frac{3}{4}(\frac{\eta e}{h\nu})^2 S_{det}\sqrt{P_t P_t'} \times (N+1) \times B_f \tag{A.28}$$

Next, we take the RMS of the heterodyne noise terms, i.e., all but the last term in Eqn. A.2 as follows.

$$\begin{aligned}
N_{\text{het,rms}} = {} & (\frac{\eta e}{h\nu})^2 8(S_{det}\delta\nu)\sqrt{P_t P_t'} \\
& \times \Bigg((\sqrt{N(N+1)}\sqrt{\frac{3}{4}\frac{2B_f}{\delta\nu}\frac{3}{4}\frac{2B_f}{\delta\nu}}\frac{1}{2\sqrt{2}})^2 + (\sqrt{N(N+1)}\sqrt{\frac{3}{4}\frac{2B_f}{\delta\nu}\frac{3}{4}\frac{2B_f}{\delta\nu}}\frac{1}{2\sqrt{2}})^2 \\
& + (\sqrt{N+1}\sqrt{\frac{3}{4}\frac{2B_f}{\delta\nu}\frac{3}{4}(\frac{2B_f}{\delta\nu}-1)}\frac{1}{2\sqrt{2}})^2 + (\sqrt{N+1}\sqrt{\frac{3}{4}\frac{2B_f}{\delta\nu}\frac{3}{4}(\frac{2B_f}{\delta\nu}-1)}\frac{1}{2\sqrt{2}})^2 \\
& + (\sqrt{N+1}\sqrt{\frac{3}{4}\frac{(2B_f-\frac{n\Delta f_r}{\delta\nu})}{\delta\nu}}\frac{1}{2\sqrt{2}})^2 + (\sqrt{N+1}\sqrt{\frac{3}{4}\frac{(2B_f-\frac{n\Delta f_r}{\delta\nu})}{\delta\nu}}\frac{1}{2\sqrt{2}})^2 \\
& + (\sqrt{N+1}\sqrt{\frac{3}{4}\frac{(\frac{n\Delta f_r}{\delta\nu})}{\delta\nu}}\frac{1}{2\sqrt{2}})^2 + (\sqrt{N+1}\sqrt{\frac{3}{4}\frac{(\frac{n\Delta f_r}{\delta\nu})}{\delta\nu}}\frac{1}{2\sqrt{2}})^2 + (\sqrt{N+1}\sqrt{\frac{3}{4}\frac{2B_f}{\delta\nu}}\frac{1}{2\sqrt{2}})^2\Bigg)^{\frac{1}{2}}
\end{aligned} \tag{A.29}$$

Interestingly, these terms all follow a nested structure. We could simplify further and find that the nesting in fact makes the terms whole, but here we make size arguments to simplify. The first two terms are much larger than the following two terms by a factor of N, and the following two terms are a factor $\frac{B_f}{\delta\nu}$ much larger than the terms that follow those. We assume that $\frac{B_f}{\delta\nu} \gg 1$, thus for the first four terms we have:

$$N_{\text{het},RMS} = (\frac{\eta e}{h\nu})^2 8(S_{det}\delta\nu)\sqrt{P_t P_t'}\frac{1}{2\sqrt{2}} \\ \times\left(N(N+1)\frac{3}{4}\frac{2B_f}{\delta\nu}\frac{3}{4}\frac{2B_f}{\delta\nu}+N(N+1)\frac{3}{4}\frac{2B_f}{\delta\nu}\frac{3}{4}\frac{2B_f}{\delta\nu}+(N+1)\frac{3}{4}\frac{2B_f}{\delta\nu}\frac{3}{4}\frac{2B_f}{\delta\nu}+(N+1)\frac{3}{4}\frac{2B_f}{\delta\nu}\frac{3}{4}\frac{2B_f}{\delta\nu}\right)^{\frac{1}{2}} \tag{A.30}$$

We can further combine terms:

$$N_{\text{het},RMS} = (\frac{\eta e}{h\nu})^2 8(S_{det}\delta\nu)\sqrt{P_t P_t'}\frac{1}{2\sqrt{2}} \times \frac{3\sqrt{2}}{4}\left((N+1)^2\frac{2B_f}{\delta\nu}\frac{2B_f}{\delta\nu}\right)^{\frac{1}{2}} \tag{A.31}$$

Taking the square root and simplifying, we have:

$$N_{\text{het},RMS} = 8 \times \frac{3}{4}(\frac{\eta e}{h\nu})^2 S_{det}\sqrt{P_t P_t'} \times (N+1) \times B_f \tag{A.32}$$

A.3 Mixing of Heterodyne Noise and Photodetected Noise

Now, we examine another source of noise: the mixing of the photocurrents from the optical heterodyne and the photodetected noise.

$$N_{PDN,\text{het}} = \frac{\eta e}{h\nu}\sum_{n=0}^{n=N}\sqrt{4S_{det}\delta\nu P_t}\sum_{k=-B_f/\delta\nu}^{B_f/\delta\nu}\cos(2\pi k\delta\nu t + \Phi_{k,n} - \Theta_n) \\ \times i'_{PDN,RMS}\sqrt{\frac{\delta\nu}{(N+1)B_f}}\sum_{m=0}^{N}\sum_{j=-B_f/\delta\nu}^{B_f/\delta\nu}\cos(2\pi j\delta\nu t + \phi'_{j,m}). \tag{A.33}$$

We simplify and combine terms:

$$N_{PDN,\text{het}} = \frac{\eta e}{h\nu}\sqrt{4S_{det}\delta\nu P_t}\, i'_{PDN,RMS}\sqrt{\frac{\delta\nu}{(N+1)B_f}} \\ \times\sum_{n=0}^{n=N}\sum_{k=-B_f/\delta\nu}^{B_f/\delta\nu}\sum_{m=0}^{N}\sum_{j=-B_f/\delta\nu}^{B_f/\delta\nu}\cos(2\pi k\delta\nu t + \Phi_{k,n} - \Theta_n)\cos(2\pi j\delta\nu t + \phi'_{j,m}) \tag{A.34}$$

Like our treatment of the mixed optical heterodyne signals, we separate the cosine product into sum and difference components. This noise also passes through the same $B_{f,m}$ bandpass filter after the mixer, thus constraining the number of included sum frequency components.

$$\begin{aligned} N_{PDN,\text{het}} = {} & \frac{\eta e}{h\nu}\sqrt{4S_{det}\delta\nu P_t}\, i'_{PDN,RMS}\sqrt{\frac{\delta\nu}{(N+1)B_f}} \\ & \times \left(\sum_{n=0}^{n=N} \sum_{k=-B_f/\delta\nu}^{B_f/\delta\nu} \sum_{m=0}^{N} \sum_{j=-B_f/\delta\nu}^{B_f/\delta\nu} \cos(2\pi k\delta\nu t + \Phi_{k,n} - \Theta_n - (2\pi j\delta\nu t + \phi'_{j,m})) \right. \\ & \left. + \sum_{n=0}^{n=N} \sum_{k=-B_f/\delta\nu}^{B_f/\delta\nu} \sum_{m=0}^{N} \sum_{j=-B_f/\delta\nu, |j+k|<B_{f,m}/\delta\nu}^{B_f/\delta\nu} \cos(2\pi k\delta\nu t + \Phi_{k,n} - \Theta_n + 2\pi j\delta\nu t + \phi'_{j,m}) \right). \end{aligned} \tag{A.35}$$

Again, choosing $B_{f,m} = B_f$, the number of terms is multiplied by 3/4. Taking the RMS of the cosines and summing in quadrature, we have:

$$\begin{aligned} N_{PDN,\text{het},RMS} = {} & \frac{\eta e}{h\nu}\sqrt{4S_{det}\delta\nu P_t}\, i'_{PDN,RMS}\sqrt{\frac{\delta\nu}{(N+1)B_f}} \\ & \times \sqrt{\left(\frac{3}{4}\sqrt{(N+1)^2\left(\frac{2B_f}{\delta\nu}\right)^2}\frac{1}{\sqrt{2}}\right)^2 + \left(\frac{3}{4}\sqrt{(N+1)^2\left(\frac{2B_f}{\delta\nu}\right)^2}\frac{1}{\sqrt{2}}\right)^2}. \end{aligned} \tag{A.36}$$

Simplifying the square root:

$$\begin{aligned} N_{PDN,\text{het},RMS} = {} & \frac{\eta e}{h\nu}\sqrt{4S_{det}\delta\nu P_t}\, i'_{PDN,RMS}\sqrt{\frac{\delta\nu}{(N+1)B_f}} \\ & \times \frac{1}{\sqrt{2}}\sqrt{\left(\frac{3}{4}\right)^2(N+1)^2\left(\frac{2B_f}{\delta\nu}\right)^2 + \left(\frac{3}{4}\right)^2(N+1)^2\left(\frac{2B_f}{\delta\nu}\right)^2}. \end{aligned} \tag{A.37}$$

Further simplifying:

$$\begin{aligned} N_{PDN,\text{het},RMS} = {} & \frac{\eta e}{h\nu}\sqrt{4S_{det}\delta\nu P_t}\, i'_{PDN,RMS}\sqrt{\frac{\delta\nu}{(N+1)B_f}} \\ & \times \frac{\sqrt{2}}{\sqrt{2}}\frac{3}{4}\sqrt{(N+1)^2\left(\frac{2B_f}{\delta\nu}\right)^2}. \end{aligned} \tag{A.38}$$

Simplifying the square root again:

$$N_{PDN,\text{het},RMS} = \frac{\eta e}{h\nu}\sqrt{4S_{det}\delta\nu P_t}\, i'_{PDN,RMS}\sqrt{\frac{\delta\nu}{(N+1)B_f}} \times \frac{3}{4}(N+1)\frac{2B_f}{\delta\nu}. \tag{A.39}$$

Simplifying:

$$N_{PDN,\text{het},RMS} = 2 \times \frac{3}{4}\frac{\eta e}{h\nu}\sqrt{4S_{det}P_t}i'_{PDN,RMS}\sqrt{(N+1)B_f}. \tag{A.40}$$

By the same argument, the noise from the other sum is:

$$N'_{PDN,\text{het},RMS} = 2 \times \frac{3}{4}\frac{\eta e}{h\nu}\sqrt{4S_{det}P'_t}i_{PDN,RMS}\sqrt{(N+1)B_f}. \tag{A.41}$$

A.4 Mixing of Photodetected Noise and Photodetected Noise

Next, we look to the last noise term, when the photodetected noise from one comb mixes with the photodetected noise from the other comb.

$$\begin{aligned} N_{PDN,PDN} = {} & i_{PDN,RMS}\sqrt{\frac{\delta\nu}{(N+1)B_f}}\sum_{n=0}^{N}\sum_{k=-B_f/\delta\nu}^{B_f/\delta\nu}\cos(2\pi k\delta\nu t + \phi_{k,n}) \\ & \times i'_{PDN,RMS}\sqrt{\frac{\delta\nu}{(N+1)B_f}}\sum_{m=0}^{N}\sum_{j=-B_f/\delta\nu}^{B_f/\delta\nu}\cos(2\pi j\delta\nu t + \phi'_{j,m}). \end{aligned} \tag{A.42}$$

Rearranging:

$$\begin{aligned} N_{PDN,PDN} = {} & i_{PDN,RMS}i'_{PDN,RMS}\frac{\delta\nu}{(N+1)B_f} \\ & \sum_{n=0}^{N}\sum_{k=-B_f/\delta\nu}^{B_f/\delta\nu}\cos(2\pi k\delta\nu t + \phi_{k,n})\sum_{m=0}^{N}\sum_{j=-B_f/\delta\nu}^{B_f/\delta\nu}\cos(2\pi j\delta\nu t + \phi'_{j,m}). \end{aligned} \tag{A.43}$$

Rearranging the summations:

$$\begin{aligned} N_{PDN,PDN} = {} & i_{PDN,RMS}i'_{PDN,RMS}\frac{\delta\nu}{(N+1)B_f} \\ & \sum_{n=0}^{N}\sum_{m=0}^{N}\sum_{k=-B_f/\delta\nu}^{B_f/\delta\nu}\sum_{j=-B_f/\delta\nu}^{B_f/\delta\nu}\cos(2\pi k\delta\nu t + \phi_{k,n})\cos(2\pi j\delta\nu t + \phi'_{j,m}). \end{aligned} \tag{A.44}$$

Next, we split this photocurrent into sum and difference terms, accounting for the low-pass filter after the mixer with bandwidth $B_{f,m}$:

$$\begin{aligned} N_{PDN,PDN} = i_{PDN,RMS} i'_{PDN,RMS} \frac{\delta\nu}{(N+1)B_f} \\ \Bigg(\sum_{n=0}^{N} \sum_{m=0}^{N} \sum_{k=-B_f/\delta\nu}^{B_f/\delta\nu} \sum_{j=-B_f/\delta\nu}^{B_f/\delta\nu} \cos(2\pi k\delta\nu t + \phi_{k,n} + 2\pi j\delta\nu t + \phi'_{j,m}) \\ + \sum_{n=0}^{N} \sum_{m=0}^{N} \sum_{k=-B_f/\delta\nu}^{B_f/\delta\nu} \sum_{j=-B_f/\delta\nu, |j+k|<B_{f,m}/\delta\nu}^{B_f/\delta\nu} \cos(2\pi k\delta\nu t + \phi_{k,n} - (2\pi j\delta\nu t + \phi'_{j,m})) \Bigg) \end{aligned} \tag{A.45}$$

Assuming that $B_{f,m} = B_f$, there are 3/4 the terms. We now take the root-mean-square and sum in quadrature.

$$\begin{aligned} N_{PDN,PDN,RMS} = i_{PDN,RMS} i'_{PDN,RMS} \frac{\delta\nu}{(N+1)B_f} \\ \sqrt{\left(\frac{3}{4}\sqrt{(N+1)^2(2Bf/\delta\nu)^2}\frac{1}{\sqrt{2}}\right)^2 + \left(\frac{3}{4}\sqrt{(N+1)^2(2Bf/\delta\nu)^2}\frac{1}{\sqrt{2}}\right)^2} \end{aligned} \tag{A.46}$$

Simplifying:

$$\begin{aligned} N_{PDN,PDN,RMS} = i_{PDN,RMS} i'_{PDN,RMS} \frac{\delta\nu}{(N+1)B_f} \\ \frac{1}{\sqrt{2}}\sqrt{\left(\frac{3}{4}\right)^2 (N+1)^2(2Bf/\delta\nu)^2 + \left(\frac{3}{4}\right)^2 (N+1)^2(2Bf/\delta\nu)^2} \end{aligned} \tag{A.47}$$

Further simplifying:

$$N_{PDN,PDN,RMS} = i_{PDN,RMS} i'_{PDN,RMS} \frac{\delta\nu}{(N+1)B_f} \frac{\sqrt{2}}{\sqrt{2}} \frac{3}{4} \sqrt{(N+1)^2(2Bf/\delta\nu)^2} \tag{A.48}$$

Evaluating the square root:

$$N_{PDN,PDN,RMS} = i_{PDN,RMS} i'_{PDN,RMS} \frac{\delta\nu}{(N+1)B_f} \frac{3}{4} (N+1)(2Bf/\delta\nu) \tag{A.49}$$

Further simplifying:

$$N_{PDN,PDN,RMS} = 2 \times \frac{3}{4} i_{PDN,RMS} i'_{PDN,RMS} \tag{A.50}$$

A.5 Total Noise

Next, we consider all the noise together. The total noise is:

$$N_{\mathrm{tot}} = \sqrt{N^2_{\mathrm{het},RMS} + (N_{PDN,\mathrm{het},RMS})^2 + (N'_{PDN,het,RMS})^2 + N^2_{PDN,PDN,RMS}} \tag{A.51}$$

Plugging in these terms, we have:

$$\begin{aligned} N^2_{\mathrm{tot}} = &\left(8 \times \frac{3}{4}(\frac{\eta e}{h\nu})^2 S_{det}\sqrt{P_t P'_t} \times (N+1) \times B_f\right)^2 + \left(2 \times \frac{3}{4}\frac{\eta e}{h\nu}\sqrt{4S_{det}P_t}\, i'_{PDN,RMS}\sqrt{(N+1)B_f}\right)^2 \\ &+ \left(2 \times \frac{3}{4}\frac{\eta e}{h\nu}\sqrt{4S_{det}P'_t}\, i_{PDN,RMS}\sqrt{(N+1)B_f}\right)^2 + \left(2 \times \frac{3}{4} i_{PDN,RMS}\, i'_{PDN,RMS}\right)^2 \end{aligned} \tag{A.52}$$

To simplify, we assume that the photodetected noise on both combs is the same. We also assume that the comb power is the same $P_t = P'_t$.

$$\begin{aligned} N^2_{\mathrm{tot}} = \left(2 \times \frac{3}{4}\right)^2 \Bigg[&\left((\frac{\eta e}{h\nu})^2 4S_{det}P_t \times (N+1) \times B_f\right)^2 + \left(\frac{\eta e}{h\nu}\sqrt{4S_{det}P_t}\, i_{PDN,RMS}\sqrt{(N+1)B_f}\right)^2 \\ &+ \left(\frac{\eta e}{h\nu}\sqrt{4S_{det}P_t}\, i_{PDN,RMS}\sqrt{(N+1)B_f}\right)^2 + \left(i_{PDN,RMS}\, i_{PDN,RMS}\right)^2 \Bigg] \end{aligned} \tag{A.53}$$

We recognize that this is a squared sum:

$$N^2_{\mathrm{tot}} = \left(2 \times \frac{3}{4}\right)^2 \left[(\frac{\eta e}{h\nu})^2 4S_{det}P_t \times (N+1) \times B_f + i^2_{PDN,RMS}\right]^2 \tag{A.54}$$

Expanding out the noise current term in terms of the noise power spectral density, we have:

$$N_{\mathrm{tot}} = \left(2 \times \frac{3}{4}\right) \left[(\frac{\eta e}{h\nu})^2 4S_{det}P_t \times (N+1) \times B_f + (N+1)B_f S_{IN}\right] \tag{A.55}$$

If this is at the shot noise limit, then the total noise is:

$$N_{\mathrm{tot},SNL} = \left(2 \times \frac{3}{4}\right) \left[(\frac{\eta e}{h\nu})^2 4S_{det}(N+1)P_t B_f + 2\frac{\eta e^2}{h\nu}(N+1)P_t B_f\right] \tag{A.56}$$

A.6 Calculating SNR at Shot Noise and Technical Limits

Recall that the signal is:

$$A_{\text{het, peak}} = 8 \times \frac{3}{4}(\frac{\eta e}{h\nu})^2 S_{det}\sqrt{P_t P'_t} \times (N+1) \times B_f \tag{A.57}$$

We'll now make a change of variables of $S_{tot} = 2S_{det}$, referring now to the total thermal PSD being measured over both balanced detectors. We'll also assume the same comb power, i.e., $P_t = P_t'$. Thus:

$$A_{\text{het, peak}} = \frac{3}{4}(\frac{\eta e}{h\nu})^2 4S_{tot}P_t \times (N+1) \times B_f. \tag{A.58}$$

The SNL noise can be written as:

$$N_{\text{tot},SNL} = \frac{3}{4}\left[(\frac{\eta e}{h\nu})^2 4S_{tot}(N+1)P_tB_f + 4\frac{\eta e^2}{h\nu}(N+1)P_tB_f\right]. \tag{A.59}$$

The SNL SNR is:

$$\text{SNR}_{SNL} = \frac{A_{\text{het, peak}}}{N_{\text{tot},SNL}} = \frac{\frac{3}{4}(\frac{\eta e}{h\nu})^2 4S_{tot}P_t \times (N+1) \times B_f}{\frac{3}{4}\left[(\frac{\eta e}{h\nu})^2 4S_{tot}(N+1)P_tB_f + 4\frac{\eta e^2}{h\nu}(N+1)P_tB_f\right]}. \tag{A.60}$$

Simplifying,

$$\text{SNR}_{SNL} = \frac{\frac{\eta}{h\nu}S_{tot}}{\left[\frac{\eta}{h\nu}S_{tot} + 1\right]} = \frac{\eta\langle n\rangle}{\eta\langle n\rangle + 1}. \tag{A.61}$$

Note that one could also go through this process with RIN following the formalism in the last section. In the main text we simply parameterize the RIN as part of the total noise, which is a multiple of the shot noise, hence the equation:

$$\text{SNR}_{\text{Tech}} = \frac{\eta\langle n\rangle}{\eta\langle n\rangle + \chi}. \tag{A.62}$$

Where χ is the multiple of the total noise including technical noise (such as RIN) over just the shot noise.

Appendix B

Notes on the POVMs for Arbitrary Continuous Mode Homodyne with Coherent Local Oscillators

B.1 Mode Decomposition of Beamsplitter

We show the the beamsplitter acts the same for every mode, under the assumption that the transmission and reflection coefficients of the beamsplitter are constants over the relevant frequencies of the signal and LO mode. From our assumption we have the the action of the beamsplitter in every mode is described by the following input output relations,

$$U_{\mathrm{BS}}^{\dagger}(\xi)\hat{A}(\xi)U_{\mathrm{BS}}(\xi) = \frac{\hat{A}(\xi)+\hat{B}(\xi)}{\sqrt{2}} \tag{B.1a}$$

$$U_{\mathrm{BS}}^{\dagger}(\xi)\hat{B}(\xi)U_{\mathrm{BS}}(\xi) = \frac{\hat{A}(\xi)-\hat{B}(\xi)}{\sqrt{2}}\,. \tag{B.1b}$$

We want to show that this implies a tensor product structure to the beamsplitter unitary, i.e we can split the unitary into a beamsplitter for each mode independently. We can demonstrate this by considering decomposing a single mode into a combination of modes and seeing how the unitary must act. Consider a annihilation operator in some mode $\hat{A}(\xi)$. Further allow ξ to be decomposed as $\xi = c_1\xi_1 + c_2\xi_2 + \ldots$. When we conjugate $\hat{A}(\xi)$ by the beamsplitter we have,

$$U_{\mathrm{BS}}^{\dagger}\hat{A}(\xi)U_{\mathrm{BS}} = U_{\mathrm{BS}}^{\dagger}\left(\sum_n c_n\hat{A}(\xi_n)\right)U_{\mathrm{BS}}\,. \tag{B.2}$$

but from Eq. (B.1) we know this must produce a sum of operators in the ξ mode.

$$U_{\mathrm{BS}}^{\dagger}\left(\sum_n c_n\hat{A}(\xi_n)\right)U_{\mathrm{BS}} = \frac{1}{\sqrt{2}}\sum_n c_n(\hat{A}(\xi_n)+\hat{B}(\xi_n))\,. \tag{B.3}$$

In order for this to hold we need the following to be true,

$$U_{\mathrm{BS}}^{\dagger}\hat{A}(\xi_n)U_{\mathrm{BS}} = \frac{\hat{A}(\xi_n)+\hat{B}(\xi_n)}{\sqrt{2}}. \tag{B.4}$$

This equation allows us to write $U_{\mathrm{BS}}(\xi)$ by its action on every mode. Meaning we can decompose the beamsplitter unitary into modes as

$$U_{\mathrm{BS}} = U_{\mathrm{BS}}(\xi_1)\otimes U_{\mathrm{BS}}(\xi_2)\otimes \ldots, \tag{B.5}$$

as desired.

B.2 Deriving the Single Mode POVMs from Kraus Operators

B.2.1 Perpendicular Mode

First we address the perpendicular mode, which is significantly easier. We start with equation Eq. (4.35b)

$$M_{r,s}(\xi_\perp) = \langle r_{\xi_\perp}|\langle s_{\xi_\perp}|U_{\mathrm{BS}}|\mathrm{vac}\rangle\,, \tag{B.6}$$

which represents r and s clicks in the perpendicular mode. Using the definition of photon number states from Eq. (4.31) to expand the bras into operators acting of vacuum

$$M_{r,s}(\xi_\perp) = \langle\mathrm{vac}|\langle\mathrm{vac}|\frac{\hat{A}^r\hat{B}^s}{\sqrt{r!s!}}U_{\mathrm{BS}}|\mathrm{vac}\rangle. \tag{B.7}$$

We have omitted the mode label since every operator in this equation acts on the perpendicular mode. We now insert identity, i.e. $U_{\mathrm{BS}}^{\dagger}U_{\mathrm{BS}} = I$, after every operator so we can apply the input-output relations of the beamsplitter, $U_{\mathrm{BS}}^{\dagger}\hat{A}U_{\mathrm{BS}} = (\hat{A}+\hat{B})/\sqrt{2}$ and $U_{\mathrm{BS}}^{\dagger}\hat{B}U_{\mathrm{BS}} = (\hat{A}-\hat{B})/\sqrt{2}$. Doing this and applying the remaining beamsplitter unitary to the vacuum modes on the left we get the following equation

$$M_{r,s}(\xi_\perp) = \langle\mathrm{vac}|\langle\mathrm{vac}|\frac{\left(\hat{A}+\hat{B}\right)^r\left(\hat{A}-\hat{B}\right)^s}{\sqrt{r!s!}2^{(r+s)/2}}|\mathrm{vac}\rangle \tag{B.8}$$

where the $\hat{B}$ operator acts on the Hilbert space of the LO, which in this case is in vacuum. We can apply this vacuum state effectively replacing each $\hat{B}$ operator with a 0 and get,

$$\begin{aligned} M_{r,s}(\xi_\perp) &= \langle \text{vac}| \frac{\hat{A}^{r+s}}{\sqrt{r!s!}2^{(r+s)/2}} \\ &= \langle r+s| \frac{\sqrt{(r+s)!}}{\sqrt{r!s!}2^{(r+s)/2}} \\ &= \langle r+s| \frac{1}{2^{(r+s)/2}} \sqrt{\binom{r+s}{r}} \end{aligned}$$

Now we move to the POVMs $E_{r,s} = M^\dagger_{r,s} M_{r,s}$

$$E_{r,s} = \frac{|r+s\rangle\langle r+s|}{2^{(r+s)}} \binom{r+s}{r}, \tag{B.9}$$

and change to sum and difference variables as follows,

$$E_{x,w} = \frac{|w\rangle\langle w|}{2^w} \binom{w}{\frac{\tilde{x}}{2} + \frac{w}{2}}. \tag{B.10}$$

This is a shifted binomial distribution in x with mean 0 in the difference variable and variance w. While we could further approximate this distribution in the limit where w is large we choose not to for two reasons. Firstly, we want the mode-matched limit $\gamma = 1$ to appear naturally from our results and in that limit w in the perpendicular mode goes to zero. Second, the binomial distribution has some nice properties particularly when coupled with the Poisson distribution of a coherent input state that make the marginalization integrals analytically solvable. For these reasons we will scale the difference variable, but leave it discrete at the POVM level. Depending on the input state the difference variable can be made continuous in a variety of ways, most commonly by approximating the binomial distribution as normal. The resulting marginalization over w will be difficult under this approximation but can easliy be solved numerically. After appropriately scaling variables we get the following POVM:

$$E_{x,w} dx = dx |w\rangle\langle w| \text{Bin}\Big(\frac{|\beta| x}{\sqrt{2}}\Big| w, \frac{1}{2}, 0\Big) \tag{B.11}$$

where $\text{Bin}(x|n, p, \mu)$ is a binomial distribution characterized by n and p and shifted so that it has mean μ

$$\text{Bin}(x|n, p, \mu) = \binom{n}{x + \frac{n}{2} - \mu} p^{n/2 + x - \mu}(1-p)^{n/2 - x + \mu}. \tag{B.12}$$

B.2.2 LO Mode

The calculation in the LO mode is more involved, but has been described in detail in [112]. We start with Eq. (4.35a),

$$M_{p,q}(\xi_{\mathrm{LO}}) = \langle p_{\xi_{\mathrm{LO}}}|\langle q_{\xi_{\mathrm{LO}}}|U_{\mathrm{BS}}|\beta_{\xi_{\mathrm{LO}}}\rangle\,. \tag{B.13}$$

We apply the same steps as before up to Eq. (B.8), the only difference being the state of the LO is no longer vacuum. Doing this yields

$$M_{p,q} = \langle \mathrm{vac}|\langle \mathrm{vac}|\frac{\left(\hat{A}+\hat{B}\right)^p\left(\hat{A}-\hat{B}\right)^q}{\sqrt{p!q!}2^{(p+q)/2}}|\beta\rangle\,, \tag{B.14}$$

where the mode designations are omitted because every operator and state is in the LO mode. After acting operators on the LO coherent state we arrive at

$$M_{p,q} = \langle \mathrm{vac}|\frac{\left(\hat{A}+\beta\right)^p\left(\hat{A}-\beta\right)^q}{\sqrt{p!q!}2^{(p+q)/2}}e^{-|\beta|^2/2}. \tag{B.15}$$

Now this operator acts only on the signal Hilbert space.

From here we apply a series of algebraic manipulations to arrange the operator into a form where we can apply the large local oscillator assumption. When we do this we will assume without loss of generality that $p \geq q$, but the calculation goes much the same with the opposite assumption. After manipulation we get

$$\begin{aligned} M_{p,q} = \langle \mathrm{vac}|(-1)^q\left(1+\frac{\hat{A}}{\beta}\right)^{p-q}\left(1-\frac{\hat{A}^2}{\beta^2}\right)^q \times \\ \frac{e^{-|\beta|^2/4}}{\sqrt{p!}}\left(\frac{\beta}{\sqrt{2}}\right)^p\frac{e^{-|\beta|^2/4}}{\sqrt{q!}}\left(\frac{\beta}{\sqrt{2}}\right)^q \end{aligned} \tag{B.16}$$

We have arranged these terms so that we see the appearance of two Poisson distributions in p and q as well as two terms that can be expanded in the large β limit into exponentials. From here we again move partially to the sum and difference variables of Eq. (4.36) and also replace m with its mean $|\beta|^2/2$. Applying the large LO limit allows us to approximate these Poisson distributions as normal as well. Doing this will move us from discrete variables p and q to continuous variables p'

and q'. Applying all of these leads us to

$$\begin{aligned} M_{p',q'} \approx & \langle\text{vac}|(-1)^{q'} e^{\sqrt{2}e^{-i\theta}x\hat{A}} e^{-e^{-2i\theta}\hat{A}^2/2} \times \\ & \left(\frac{e^{-(p'-|\beta|^2/2)^2/(2|\beta|^2)}}{(\pi|\beta|^2)^{1/4}}\right)\left(\frac{e^{-(q'-|\beta|^2/2)^2/(2|\beta|^2)}}{(\pi|\beta|^2)^{1/4}}\right) \end{aligned} \tag{B.17}$$

where $e^{i\theta}$ is the phase of β. Here we recognize the form of a quadrature eigenstate and we combine the two normal distributions to get the much simpler form,

$$M_{p',q'} = \langle x_\theta| \frac{(-1)^q e^{i\theta(p'+q')}}{|\beta|(\pi)^{1/4}} e^{-(p'+q'-|\beta|^2)^2/(4|\beta|^2)} \tag{B.18}$$

Now we see that p' and q' only appear in terms of the sum and difference variable so we can completely move to those variables, including the Jacobian terms we get

$$M_{x,w}\sqrt{dxdw} = \langle x_\theta|e^{iw\theta}(-1)^{q'} \frac{e^{-(w-|\beta|^2)^2/(4|\beta|^2)}}{(2\pi)^{1/4}\sqrt{|\beta|}}\sqrt{dxdw} \tag{B.19}$$

Now we move to the POVMs where the phase terms will cancel yielding a very simple form

$$dxdwE_{x,w} = \frac{e^{-(w-|\beta|^2)^2/(2|\beta|^2)}}{\sqrt{(2\pi)|\beta|^2}}|x_\theta\rangle\langle x_\theta|dxdw \tag{B.20}$$

where we can see that after marginalizing over w we would get

$$E_x = |x_\theta\rangle\langle x_\theta| \tag{B.21}$$

as expected.

B.3 Photon Number Considerations

When discussing the large-LO limit we can break the signal photons into the two modes and compare the number of signal photons that fall into the LO mode to the total number of photons from the LO. There is a subtlety here because we effectively saying that $\langle\psi_{\text{S}}|\hat{n}(\xi_{\text{S}})|\psi_{\text{S}}\rangle = \langle\psi_{\xi_{\text{LO}}}|\hat{n}(\xi_{\text{LO}})|\psi_{\xi_{\text{LO}}}\rangle + \langle\psi_{\xi_\perp}|\hat{n}(\xi_\perp)|\psi_{\xi_\perp}\rangle$, which is surprisingly nontrivial, because as an operator equation $\hat{n}(\xi_{\text{S}}) \neq \hat{n}(\xi_{\text{LO}}) + \hat{n}(\xi_\perp)$. We know that the first equation must be true because it says that the total number of photons in the signal is equal to the number of photons from the signal in the

LO mode plus the number of photons from the signal in the perpendicular mode. Since the signal mode is described by a linear superposition of just those two modes we know that no photons could fall in any other mode in our decomposition.

We can also provide evidence that it is true by taking an example of a coherent state signal. We use the decomposition of Eq. (4.30) before taking the expectation value,

$$\begin{aligned}\langle\alpha_{\xi_\mathrm{S}}|\hat{n}(\xi_s)|\alpha_{\xi_\mathrm{S}}\rangle =&\langle\gamma\alpha_{\xi_\mathrm{LO}}|\hat{n}(\xi_\mathrm{LO})|\gamma\alpha_{\xi_\mathrm{LO}}\rangle+\\ &\langle\sqrt{1-|\gamma|^2}\alpha_{\xi_\perp}|\hat{n}(\xi_\perp)|\sqrt{1-|\gamma|^2}\alpha_{\xi_\perp}\rangle\end{aligned} \tag{B.22}$$

and

$$|\alpha|^2 = |\gamma|^2|\alpha|^2 + (1-|\gamma|^2)|\alpha|^2. \tag{B.23}$$

A proof of this fact for any signal state is more subtle, but it begins by introducing an auxiliary mode with no photons in it so that we can treat the change of mode basis thoroughly. This is always allowed since we are extending our single mode basis to include other modes which have no weight.

We write the signal as $|\pi_\mathrm{S}\rangle = |\psi_{\xi_\mathrm{S}}\rangle \otimes |0(\xi_\mathrm{aux})\rangle$. We can now decompose our mode operators in the normal way where $\hat{A}(\xi_\mathrm{S}) \to \gamma\hat{A}(\xi_\mathrm{LO}) + \sqrt{1-|\gamma|^2}\hat{A}(\xi_\mathrm{S})$, only now we add in the auxiliary mode so we can write the change of basis as the action of a unitary,

$$\begin{bmatrix} A(\xi_\mathrm{S}) \\ A(\xi_\mathrm{aux}) \end{bmatrix} = \begin{bmatrix} \gamma & \sqrt{1-|\gamma|^2} \\ \sqrt{1-|\gamma|^2} & -\gamma^* \end{bmatrix} \begin{bmatrix} A(\xi_\mathrm{LO}) \\ A(\xi_\perp) \end{bmatrix} \tag{B.24}$$

where we have filled in the bottom row by requiring the matrix to be unitary. Now we can calculate $\hat{A}^\dagger(\xi_\mathrm{S})\hat{A}(\xi_\mathrm{S})$ and see that there are terms present that depend on both modes,

$$\begin{aligned}\hat{A}^\dagger(\xi_\mathrm{S})\hat{A}(\xi_\mathrm{S}) = &|\gamma|^2\hat{A}^\dagger(\xi_\mathrm{LO})\hat{A}(\xi_\mathrm{LO}) + (1-|\gamma|^2)\hat{A}^\dagger(\xi_\perp)\hat{A}(\xi_\perp)\\ &+\gamma\sqrt{1-|\gamma|^2}\hat{A}^\dagger(\xi_\mathrm{LO})\hat{A}(\xi_\perp) + \gamma^*\sqrt{1-|\gamma|^2}\hat{A}^\dagger(\xi_\perp)\hat{A}(\xi_\mathrm{LO}).\end{aligned}$$

Similarly we carry out the same calculation for the auxiliary mode

$$\begin{aligned}\hat{A}^\dagger(\xi_\mathrm{aux})r\hat{A}(\xi_\mathrm{aux}) = &|\gamma|^2\hat{A}^\dagger(\xi_\perp)\hat{A}(\xi_\perp) + (1-|\gamma|^2)\hat{A}^\dagger(\xi_\mathrm{LO})\hat{A}(\xi_\mathrm{LO})\\ &-\gamma\sqrt{1-|\gamma|^2}\hat{A}^\dagger(\xi_\mathrm{LO})\hat{A}(\xi_\perp) - \gamma^*\sqrt{1-|\gamma|^2}\hat{A}^\dagger(\xi_\perp)\hat{A}(\xi_\mathrm{LO}).\end{aligned}$$

We now take expectations of the auxiliary mode $\langle \hat{A}^\dagger(\xi_{\text{aux}})\hat{A}(\xi_{\text{aux}})\rangle = 0$ and we get the following condition,

$$\begin{aligned}&\langle |\gamma|^2 \hat{A}^\dagger(\xi_\perp)\hat{A}(\xi_\perp) + (1-|\gamma|^2)\hat{A}^\dagger(\xi_{\text{LO}})\hat{A}(\xi_{\text{LO}})\rangle \\ &= \langle \gamma\sqrt{1-|\gamma|^2}\hat{A}^\dagger(\xi_{\text{LO}})\hat{A}(\xi_\perp) + \gamma^*\sqrt{1-|\gamma|^2}\hat{A}^\dagger(\xi_\perp)\hat{A}(\xi_{\text{LO}})\rangle.\end{aligned} \tag{B.25}$$

Now take expectation in the signal mode,

$$\begin{aligned}\langle \hat{A}^\dagger(\xi_{\text{S}})\hat{A}(\xi_{\text{S}})\rangle &= \langle |\gamma|^2 \hat{A}^\dagger(\xi_{\text{LO}})\hat{A}(\xi_{\text{LO}}) + (1-|\gamma|^2)\hat{A}^\dagger(\xi_\perp)\hat{A}(\xi_\perp)\rangle \\ &\quad + \langle \gamma\sqrt{1-|\gamma|^2}\hat{A}^\dagger(\xi_{\text{LO}})\hat{A}(\xi_\perp) + \gamma^*\sqrt{1-|\gamma|^2}\hat{A}^\dagger(\xi_\perp)\hat{A}(\xi_{\text{LO}})\rangle.\end{aligned} \tag{B.26}$$

Finally just plug in the condition we derived above to get

$$\langle \hat{A}^\dagger(\xi_{\text{S}})\hat{A}(\xi_{\text{S}})\rangle = \langle \hat{A}^\dagger(\xi_\perp)\hat{A}(\xi_\perp)\rangle + \langle \hat{A}^\dagger(\xi_{\text{LO}})\hat{A}(\xi_{\text{LO}})\rangle, \tag{B.27}$$

as desired.

B.4 Combination Rule for POVM

Starting from the total Kraus operator in n and m variables Eq. (4.34),

$$M_{n,m} = \sum_{p,q} M_{p,q}(\xi_{\text{LO}}) \otimes M_{n-p,m-q}(\xi_\perp)\,. \tag{B.28}$$

We can rewrite the order of this sum in terms of discrete sum and difference variables,

$$M_{n,m} = \sum_{p+q=0}^{n+m} \sum_{p-q=x_{\text{min}}}^{x_{\text{max}}} M_{p,q}(\xi_{\text{LO}}) \otimes M_{n-p,m-q}(\xi_\perp), \tag{B.29}$$

where $x_{\text{min}} = \max(-w,-n,-m)$ and $x_{\text{max}} = -x_{\text{min}}$. This sum can be approximated quite well in the limit where the difference variable is much less than the sum variable, i.e. $x \ll w$, which is almost always the case for quadrature detection,

$$M_{n,m} = \sum_{p+q=0}^{n+m} \sum_{p-q=-p+q}^{p+q} M_{p,q}(\xi_{\text{LO}}) \otimes M_{n-p,m-q}(\xi_\perp)\,. \tag{B.30}$$

Now move to the sum and difference variables, $x = (p-q)/\sqrt{2}|\beta|$, $w = p+q$. Since we have scaled the difference variable so that it is small, we can approximate the sum over it as an integral. Applying all this in the large LO limit gives

$$M_{x,w} = \sum_{w'} \int_{-\infty}^{\infty} \frac{|\beta| dx'}{\sqrt{2}} M_{x',w'}(\xi_{\text{LO}}) \otimes M_{x-x',w-w'}(\xi_\perp)\,. \tag{B.31}$$

This demonstrates that the total Kraus operator is a convolution of the two constituent Kraus operators. We now need to determine how this convolution changes when we move to the POVMs. This can be done by direct computation but the necessary orthogonality relations are more clear before we move to the sum and difference variables so we will start again from Eq. (4.34)

$$\begin{aligned} E_{n,m} = M^\dagger_{n,m} M_{n,m} &= \sum_{p,q} M^\dagger_{p,q}(\xi_{\mathrm{LO}}) M^\dagger_{n-p,m-q}(\xi_\perp) \sum_{p',q'} M^\dagger_{p',q'}(\xi_{\mathrm{LO}}) M^\dagger_{n-p',m-q'}(\xi_\perp)\,. \\ &= \sum_{p,q} \sum_{p',q'} M^\dagger_{p,q}(\xi_{\mathrm{LO}})(\xi_\perp) M_{p',q'}(\xi_{\mathrm{LO}}) M^\dagger_{n-p,m-q} M_{n-p',m-q'}(\xi_\perp)\,. \end{aligned} \tag{B.32}$$

Now we need to remember the form of the single mode Kraus operators using Eq. (4.38),

$$\begin{aligned} M^\dagger_{p,q}(\xi_{\mathrm{LO}})(\xi_\perp) M_{p',q'}(\xi_{\mathrm{LO}}) &= \langle\beta|U^\dagger_{\mathrm{BS}}|p\rangle|q\rangle\langle p|\langle q||q'\rangle|p'\rangle\langle q'|\langle p'|U_{\mathrm{BS}}|\beta\rangle \\ &= \langle\beta|U^\dagger_{\mathrm{BS}}|p\rangle|q\rangle\langle q|\langle p|U_{\mathrm{BS}}|\beta\rangle\delta_{p,p'}\delta_{q,q'}, \end{aligned} \tag{B.33}$$

where we have applied the orthogonality of Fock states. A similar identity holds for the perpendicular mode. Applying this to the POVM reduces the four sums to a sum over just two variables so we get

$$\begin{aligned} E_{n,m} &= \sum_{p,q} M^\dagger_{p,q}(\xi_{\mathrm{LO}}) M_{p,q}(\xi_{\mathrm{LO}}) M^\dagger_{n-p,m-q} M_{n-p,m-q}(\xi_\perp) \\ &= \sum_{p,q} E_{p,q}(\xi_{\mathrm{LO}}) E_{n-p,m-q}(\xi_\perp)\,. \end{aligned} \tag{B.34}$$

From here we notice that this matches the form of what we started with in Eq. (B.28) so we can assert the combination rule for the POVMs in terms of the sum and difference variable is

$$E_{x,w} = \sum_{w'} \int_{-\infty}^{\infty} \frac{|\beta| dx'}{\sqrt{2}} E_{x',w'}(\xi_{\mathrm{LO}}) \otimes E_{x-x',w-w'}(\xi_\perp)\,. \tag{B.35}$$

B.5 Time-Dependent Photo Record

If we now assume that our detector does produce timing information then we can still get the same answer but our measurement operators must change. We still want to average the time-dependent photo-record which will be accomplished by coarse-graining over time. First we must make some assumptions about our detector. We will model the detector time dependence by saying each detection even is contained in a time bin $(t_i, t_i + \Delta t)$. We will also assume that Δt is small with respect to the total detection time T.

With these assumptions, we can write a corrected form of our detector.

$$\begin{aligned} |n\rangle_D(t_i) &= |0\rangle \otimes ... |0\rangle \otimes |n\rangle \otimes |0\rangle \otimes ... |0\rangle \\ &\equiv |n_i\rangle \end{aligned} \tag{B.36}$$

This represents getting n clicks in the i^{th} time bucket. With these, we can write the most general measurement operator for our apparatus as

$$M_{n,m}(t_i, t_j) = \langle n_i|\langle m_j|U_{\text{BS}}. \tag{B.37}$$

which corresponds to n clicks on one detector in the i^{th} and m clicks in the other in the j^{th} bucket. Up to this point, our measurement operators are fully time-dependent and indeed this analysis could be continued without coarse-graining, but the resulting theory is difficult to parse analytically and seems more suited for numerics. For this reason, we will consider the case of the averaged photo current which requires coarse-graining over time.

Once we have the measurement operators we can assemble the POVMs. The fully time-dependent POVMs would be

$$E_{n,m}(t_i, t_j) = M^\dagger_{n,m}(t_i, t_j) M_{n,m}(t_i, t_j) \tag{B.38}$$

and the naively coarse-grained POVMs should be

$$\begin{aligned} E_{n,m} &= \sum_{i,j} M^\dagger_{n,m}(t_i, t_j) M_{n,m}(t_i, t_j) \\ &= \sum_{i,j} U^\dagger_{\text{BS}} |n_i\rangle|m_j\rangle\langle n_i|\langle m_j|U_{\text{BS}} \end{aligned} \tag{B.39}$$

but this only accounts for the cases were all n and m clicks were in a single time bin. It should also be possible to get say $n/2$ clicks in the first bin and $n/2$ in the second bin for a total of n clicks. So we need to add in these terms.

$$E_{n,m} = \sum_{n_i}^{n} \sum_{m_j}^{m} U^\dagger_{\text{BS}} |n_i\rangle|m_j\rangle\langle n_i|\langle m_j|U_{\text{BS}} \tag{B.40}$$

where $\sum_{n_i}^{n}$ indicates a sum over all possible values of $n_1, n_2, ...$ such that $\sum_i n_i = n$. An illustrative special case is when there are only two detection windows, (t_1, t_2) and we get:

$$E_{n,m} = \sum_p \sum_q U_{\mathrm{BS}}^{\dagger} \left(|p\rangle_1 \otimes |n-p\rangle_2\right) \left(|q\rangle_1 \otimes |m-q\rangle_2\right) \left(\langle p|_1 \otimes \langle n-p|_2\right) \left(\langle q|_1 \otimes \langle m-q|_2\right) U_{\mathrm{BS}} \tag{B.41}$$

Now we note that POVMs are basis independent i.e the measurement statistics are the same regardless of any change of bases we make on the POVMs. So we can conjugate our POVM by some unitary U so that we move to the Gram-Schmidt basis defined in Eq. (4.25). This is where we will assume that $\Delta t \ll T$ so that our bin basis spans the same set of functions as our Gram-Schmidt basis. Now we have

$$V^{\dagger} E_{n,m} V = \sum_p \sum_q U_{\mathrm{BS}}^{\dagger} \left(|p_{\xi_{\mathrm{LO}}}\rangle \otimes |n - p_{\xi_{\perp}}\rangle\right) \left(|q_{\xi_{\mathrm{LO}}}\rangle \otimes |m - q_{\xi_{\perp}}\rangle\right) \tag{B.42}$$

$$\left(\langle p_{\xi_{\mathrm{LO}}}| \otimes \langle n - p_{\xi_{\perp}}|\right) \left(\langle q_{\xi_{\mathrm{LO}}}| \otimes \langle m - q_{\xi_{\perp}}|\right) U_{\mathrm{BS}} \,, \tag{B.43}$$

where V denotes a change of basis from the numbered modes to the Gram-Schmidt basis. The final expression is equivalent to what we had before. Note that here we are able to limit ourselves to the special case of just two modes because we are omitting the trivial modes that complete our basis, but carry 0 photons.

B.6 Coherent State Difference Variable Distribution Calculations

Using the total POVM from Eq. (4.38) we can derive the distribution of the total measurement by taking the expectation of the POVM in the signal state,

$$\begin{aligned} P(x) &= \langle \alpha_{\xi_{\mathrm{S}}} | E_x | \alpha_{\xi_{\mathrm{S}}} \rangle \\ &= \int dx' \langle \gamma\alpha | E_{x'}(\xi_{\mathrm{LO}}) | \gamma\alpha \rangle \times \\ &\qquad \langle \sqrt{1-|\gamma|^2}\alpha | E_{x-x'}(\xi_{\perp}) | \sqrt{1-|\gamma|^2}\alpha \rangle \,. \end{aligned}$$

This distribution can naturally be decomposed into two parts, and then combined by a convolution.

First, let's consider the component in the local oscillator mode. The probability distribution is given by $P(x) = \langle \gamma\alpha_{\xi_{\mathrm{LO}}} | E^{\beta}_{x,\xi_{\mathrm{LO}}} | \gamma\alpha_{\xi_{\mathrm{LO}}}\rangle$ i.e.

$$\begin{aligned} P(x) = |\langle x|\gamma\alpha\rangle|^2 &= \frac{e^{-x^2}}{\sqrt{\pi}} |\langle 0| e^{\sqrt{2}x\hat{a}} e^{-\hat{a}^2/2} |\gamma\alpha\rangle|^2 \\ &= \frac{e^{-x^2}}{\sqrt{\pi}} |e^{-|\gamma\alpha|^2/2} e^{\sqrt{2}\gamma\alpha} e^{-\gamma^2\alpha^2/2}|^2 \\ &= e^{-|\gamma\alpha|^2} \frac{e^{-x^2}}{\sqrt{\pi}} e^{2\sqrt{2}\mathrm{Re}(\gamma\alpha)} e^{-\mathrm{Re}(\gamma^2\alpha^2)}\,. \end{aligned} \tag{B.44}$$

Here we should recall our convention that α is real and that the phase is completely contained in the modes and thus in γ. We can introduce shorthand $\gamma = \gamma_R + i\gamma_I$.

Now we can complete the square to obtain a Gaussian distribution in x that is not mean 0

$$-(x^2 - 2\sqrt{2}x\alpha\gamma_R) = -(x - \sqrt{2}\alpha\gamma_R)^2 + 2\alpha^2\gamma_R^2. \tag{B.45}$$

With this we can rewrite the distribution

$$P(x) = \frac{e^{-(x-\sqrt{2}\alpha\gamma_R)^2}}{\sqrt{\pi}} \exp\big[-\alpha^2(|\gamma|^2 + \gamma_R^2 - \gamma_I^2 - 2\gamma_R^2)\big] \tag{B.46}$$

where we have used the fact that $\mathrm{Re}(\gamma^2) = \gamma_R^2 - \gamma_I^2$. It can be shown in a couple lines of algebra that $|\gamma|^2 + \gamma_R^2 - \gamma_I^2 - 2\gamma_R^2 = 0$ and so we end up with just a normal distribution in x.

$$P(x) = \frac{e^{-(x-\sqrt{2}\alpha\gamma_R)^2}}{\sqrt{\pi}} \tag{B.47}$$

For the perpendicular mode we start with Eq. (4.35)

$$P(x,w)_\perp = \langle \sqrt{1-|\gamma|^2}\alpha | \sum_w |w_{\xi_\perp}\rangle\langle w_{\xi_\perp}| \mathrm{Bin}\Big(\frac{|\beta|x}{\sqrt{2}}\Big| w, \frac{1}{2}, 0\Big) | \sqrt{1-|\gamma|^2}\alpha\rangle \tag{B.48}$$

where we can apply the explicit formula for the shifted binomial distribution. At this point both x and w are discrete so we will need to move to continuous variables after we simplify the expression. After taking expectation in the coherent state we have,

$$P(x,w)_\perp = \frac{w!}{\big(\frac{|\beta|x}{\sqrt{2}} + \frac{w}{2}\big)!\,\big(\frac{w}{2} - \frac{|\beta|x}{\sqrt{2}}\big)!} \frac{1}{2^w} \frac{((1-|\gamma|^2)|\alpha|^2)^w e^{-(1-|\gamma|^2)|\alpha|^2}}{w!} \tag{B.49}$$

which is the product of the shifted binomial and the Poisson distribution. We can simplify this into the product of two Poisson distributions as

$$P(x,w)_\perp = \left(\frac{(1-|\gamma|^2)|\alpha|^2}{2}\right)^{w/2-|\beta|x/\sqrt{2}} \frac{e^{-(1-|\gamma|^2)|\alpha|^2/2}}{\left(\frac{w}{2}-\frac{|\beta|x}{\sqrt{2}}\right)!} \left(\frac{(1-|\gamma|^2)|\alpha|^2}{2}\right)^{w/2+|\beta|x/\sqrt{2}} \frac{e^{-(1-|\gamma|^2)|\alpha|^2/2}}{\left(\frac{w}{2}+\frac{|\beta|x}{\sqrt{2}}\right)!} . \tag{B.50}$$

No we move to continuous variables by approximating both Poisson distributions as normal, this is valid so long as $(1-|\gamma|^2)|\alpha|^2$ is large enough for the central limit theorem to apply. Doing this an applying some algebraic simplification yields,

$$P(x,w)_\perp dxdw = \frac{|\beta|dxdw}{\sqrt{2}\pi(1-|\gamma|^2)|\alpha|^2} \exp\left[-\frac{|\beta|^2x^2}{(1-|\gamma|^2)|\alpha|^2}\right] \exp\left[-\frac{(w-(1-|\gamma|^2)|\alpha|^2)^2}{2(1-|\gamma|^2)|\alpha|^2}\right] , \tag{B.51}$$

which we can marginalize over w to get the difference variable distribution

$$\begin{aligned} P(x)_\perp &= \frac{|\beta|}{\sqrt{\pi(1-|\gamma|^2)|\alpha|^2}} \exp\left[-\frac{|\beta|^2x^2}{(1-|\gamma|^2)|\alpha|^2}\right] \\ &= \mathcal{N}\left(x, \mu=0, \sigma^2 = \frac{|\alpha|^2(1-|\gamma|^2)}{2|\beta|^2}\right) . \end{aligned} \tag{B.52}$$

B.7 Filtering Theory

In single mode homodyne we know that the measurement reduces to a measurement of a quadrature defined by the phase of the LO. As long as the LO is large enough for the LO shot noise to dominate the signal shot noise we can reduce the effective quadrature noise to that of vacuum fluctuations. For the multimode case we show in Eq. (4.37), that the measurement is a quadrature measurement convolved with additional intensity noise from the measurement of the mismatched portion of the signal. The goal of filtering in this context is to reduce the intensity like noise present in our time-averaged outcome, while not affecting the quadrature measurement at all.

We will first imagine that we have very fast detectors that collect photons in a very small time bin $d\tau$ for each data point. Over the entire detection interval, T we will assume we have many data points i.e $d\tau \ll T$. We will consider the filtering operation as applying some time-dependent set of weights $f(t)$ to the photocurrent, and then averaging over the filtered data. This means that any outcome of our measurement x is given by

$$x = \int_0^T f(t)x(t)dt, \tag{B.53}$$

where we can easily replace this integral with a sum if the detector window $d\tau$ is not infinitesimal.

In order to ensure that the operator being measured is $\hat{Q}(\xi_{\mathrm{LO}})$ any filter we apply must be constant over the LO mode. If this is not the case then the measurement will have reduced sensitivity to the portions of the LO mode when $f(t)$ is small. The extreme example of this is when $f(t) = 0$ on some interval (t_0, t_1), clearly since these data points are completely removed from the final measurement outcome our measurement has no sensitivity to the part of the LO mode. So we conclude that the filter must leave the LO mode unchanged so the measurement is maintained , i.e $f(t)\xi_{\mathrm{LO}}(t) \propto \xi_{\mathrm{LO}}(t)$

The set of all possible filters $f(t)$ under these restrictions becomes

$$f(t) = \begin{cases} c & \text{if } \xi_{\mathrm{LO}}(t) \neq 0 \\ \\ g(t) & \text{if } \xi_{\mathrm{LO}}(t) = 0 \end{cases}. \tag{B.54}$$

where c is some constant. Without loss of generality we will assume that $c = 1$ because any other choice of constant would merely scale the value of all outcomes, leaving the SNR unchanged. The problem is now to find $g(t)$ so that we have the minimum perpendicular mode noise in our measurement.

At this point we should note that in many cases $\xi_{\mathrm{LO}}(t)$ is never zero. While ultimately this means that there is no filter that will leave the LO mode unchanged, it may still be desirable to find an approximate filter which greatly increases SNR at the cost of a small change in the measurement. For example if the LO is a Gaussian pulse then 5 standard deviations away from the mean might be sufficient to approximate $\xi_{\mathrm{LO}}(t) \approx 0$. If we want to ensure that some small fraction p of the total LO mode photons are excluded by our gate then we have the condition

$$|\xi_{\mathrm{LO}}(t)|^2 < \frac{p}{d\tau}. \tag{B.55}$$

Lets now consider the case where the signal is a coherent state $|\alpha_{\xi_\mathrm{S}}\rangle$. Here semiclassical analysis tells us how the mean and variance will change under the proposed filter,

$$\begin{aligned} \mu &\to 2\mathrm{Re}(\alpha\beta^*)\mathrm{Re}(\int_0^T f(t)\xi^*_{\mathrm{LO}}(t)\xi_s(t)dt) \\ \sigma^2 &\to |\beta|^2\int_0^T |f(t)|^2|\xi_{\mathrm{LO}}(t)|^2dt + |\alpha|^2\int_0^T |f(t)|^2|\xi_\mathrm{S}(t)|^2dt. \end{aligned} \tag{B.56}$$

Now we apply the fact that $f(t)\xi_{\mathrm{LO}}(t) = \xi_{\mathrm{LO}}(t)$ and the convention that β is real to get the simplified mean

$$\mu = 2|\beta|\mathrm{Re}(\gamma\alpha), \tag{B.57}$$

and the variance

$$\begin{aligned} \sigma^2 &= |\beta|^2 + |\alpha|^2\int_0^T |f(t)|^2|\xi_\mathrm{S}(t)|^2 \\ &= |\beta|^2 + |\alpha|^2\int_0^T |f(t)|^2|\gamma\xi_{\mathrm{LO}} + \sqrt{1-|\gamma|^2}\xi_\perp|^2. \end{aligned} \tag{B.58}$$

We can expand the second term (the one proportional to $|\alpha|^2$ to $\int_0^T |f(t)|^2[|\gamma\xi_{\mathrm{LO}}|^2 + (1-|\gamma|^2)|\xi_\perp|^2 + \gamma\sqrt{1-|\gamma|^2}(\xi^*_{\mathrm{LO}}\xi_\perp + \xi_{\mathrm{LO}}\xi^*_\perp)]$ which eventually gives

$$\sigma^2 = |\beta|^2 + |\alpha|^2\left[|\gamma|^2 + (1-|\gamma|^2)\int_0^T |f(t)|^2|\xi_\perp|^2\right], \tag{B.59}$$

where we have again used that fact that $f\xi_{\mathrm{LO}} = \xi_{\mathrm{LO}}$ and that $\langle\xi_{\mathrm{LO}}, \xi_\perp\rangle = 0$. Finally we can apply the assumption that $|\beta|^2 \gg |\gamma\alpha|^2$ to get

$$\mathrm{SNR} = \frac{\mu^2}{\sigma^2} = \frac{4|\beta|^2\mathrm{Re}(\gamma\alpha)}{|\beta|^2 + \eta_f|\alpha|^2} \tag{B.60}$$

where $\eta_f = \int_0^T |f(t)|^2|\xi_\perp|^2$

B.8 Single Photon Distribution

We start the calculation from the input state in Eq. (4.52),

$$|\psi\rangle_s = \gamma|1_{\xi_{\mathrm{LO}}}\rangle|0_{\xi_\perp}\rangle + \sqrt{1-|\gamma|^2}|0_{\xi_{\mathrm{LO}}}\rangle|1_{\xi_\perp}\rangle. \tag{B.61}$$

Taking expectation of the POVM would produce four terms because the input state is written as two terms.

$$\begin{aligned} P(x) &= dx \int dx' \langle \psi_s | E^{\mathrm{LO}}_{x'}(\xi_{\mathrm{LO}}) \otimes E^{\perp}_{x-x'}(\xi_{\perp}) | \psi_s \rangle \,, \\ &= \int dx' \left(\gamma^* \langle 1 | \langle 0 | + \sqrt{1-|\gamma|^2} \langle 0 | \langle 1 | \right) E^{\mathrm{LO}}_{x'} \otimes E^{\perp}_{x-x'} | \left(\gamma |1\rangle |0\rangle + \sqrt{1-|\gamma|^2} |0\rangle |1\rangle \right) , \end{aligned} \tag{B.62}$$

where we have simplified the mode labels for conciseness. Now we just note that $\langle m_{\xi_\perp} | E^{\perp} | n_{\xi_\perp} \rangle \propto \delta_{m,n}$ because it is a projection onto Fock states, and so only two terms survive,

$$\begin{aligned} P(x) &= \int dx' |\gamma|^2 \langle 1 | E^{\mathrm{LO}}_{x'} | 1 \rangle \langle 0 | E^{\perp}_{x-x'} | 0 \rangle + (1-|\gamma|^2) \langle 0 | E^{\mathrm{LO}}_{x'} | 0 \rangle \langle 1 | E^{\perp}_{x-x'} | 1 \rangle \\ &= \int dx' \frac{|\gamma|^2}{2\sqrt{\pi}} e^{-x'^2} H_1^2(x') \mathrm{Bin}\Big(\frac{|\beta|(x-x')}{\sqrt{2}} \Big| 0, \frac{1}{2}, 0 \Big) + \frac{(1-|\gamma|^2)}{\sqrt{\pi}} e^{-x'^2} \mathrm{Bin}\Big(\frac{|\beta|(x-x')}{\sqrt{2}} \Big| 1, \frac{1}{2}, 0 \Big) \end{aligned} \tag{B.63}$$

Now we are in a regime of very weak signal where we can not approximate these binomial distributions as normal, instead we will mimic the discrete distribution by restricting the distribution of $(x-x')$ to only discrete values. In this case that can best be done by approximating the binomial as a sum of delta functions,

$$\begin{aligned} P(x) &= \int dx' \frac{|\gamma|^2}{2\sqrt{\pi}} e^{-x'^2} H_1^2(x') \delta(x-x') \\ &\quad + \frac{(1-|\gamma|^2)}{\sqrt{\pi}} e^{-x'^2} \left(\frac{1}{2} \delta \left(x - x' - \frac{1}{\sqrt{2}|\beta|} \right) + \frac{1}{2} \delta \left(x - x' + \frac{1}{\sqrt{2}|\beta|} \right) \right) \\ &= \frac{|\gamma|^2}{2\sqrt{\pi}} e^{-x^2} H_1^2(x) + \frac{(1-|\gamma|^2)}{2\sqrt{\pi}} \left(e^{-(x-1/\sqrt{2}|\beta|)^2} + e^{-(x+1/\sqrt{2}|\beta|)^2} \right) \\ &= \frac{1}{2\sqrt{\pi}} \left[4|\gamma|^2 e^{-x^2} x^2 + (1-|\gamma|^2) \left(e^{-(x-1/\sqrt{2}|\beta|)^2} + e^{-(x+1/\sqrt{2}|\beta|)^2} \right) \right] . \end{aligned} \tag{B.64}$$

This matches with the results in Eq. (4.54)

Appendix C

Instability and Allan Variance

In the technical background, I covered the basics of statistical distributions and how one characterizes typical Gaussian distributions by the ratio of mean squared and variance, or SNR. I have also shown what SNR one would expect in ideal homodyne and heterodyne measurements.

It is important to understand how this impacts measurements of frequency instability–a critical measurement in precision spectroscopy and timekeeping.

The standard method to characterize time and frequency instability is the Allan variance [119, 120], which was formulated to avoid issues with the standard variance diverging over long time scales due to correlated noise (1/f). Consider the classical variance of:

$$\sigma_f^2 = \langle (\bar{f} - f_n)^2 \rangle, \tag{C.1}$$

where $\bar{f}$ is the average frequency measured. If the process being measured contains correlations in time the noise is no longer white and has a frequency dependence of $f^{-\alpha}$, where $\alpha = 1$, 2,..., such as flicker noise ($\alpha = 1$). This translates to a change of $\bar{f}$ depending on the timescale over which it is defined and a lack of convergence of σ_f^2. In order to characterize the instability of processes with temporal correlations, the Allen variance was adopted, formulated as:

$$\sigma_y^2(\tau) = \frac{1}{2} \langle (\bar{y}_{n+1} - \bar{y}_n)^2 \rangle, \tag{C.2}$$

where

$$\bar{y}_i = \frac{x(i\tau + \tau) - x(i\tau)}{\tau}, \tag{C.3}$$

$i = 1, 2, \ldots$, $x(t)$ is the reading of the clock under test, and t is the time on a reference clock. Thus, $\bar{y}_n$ is the nth fractional frequency (or time) average over τ. Note that the Allan deviation follows the standard relationship with variance: ADEV $= \sigma_y(\tau)$.

The Allan variance yields a measure of how the frequency stability changes as the averaging period changes. As a consequence, the Allan variance is used not only to characterize instability but also to differentiate between different noise types (see [120]).

The role of quantum noise in measurement uncertainty is central to this thesis work. While ironically the Allan variance is most useful for non-white noise, here I show how shot noise impacts fractional instability or the Allan variance.

The Allan variance can be reconstructed from the phase-noise power spectral density. Shot noise results in white phase noise, and for shot noise derived from slowly (i.e., CW) modulated lasers[1] , the single sideband phase noise (see [121]) in a 1 Hz bandwidth is:

$$\mathcal{L}(f) = \frac{2q}{I_{\text{avg}}}. \tag{C.4}$$

The Allan variance (see [120]) is:

$$\sigma_y^2(\tau) = \frac{3f_H}{4\pi^2} \frac{4q}{\nu_0^2 I_{\text{avg}} \tau^2}, \tag{C.5}$$

where f_H is the high frequency RF cutoff, ν_0 is the optical frequency of the carrier, and $I_{\text{avg}} = q\eta P_{\text{opt}}/hv_0$ is the average current. At 1 second, $f_H = 100$ MHz, $\nu_0 = 200$ THz, $\eta = 2/3$, $P_{\text{opt}} = 1$ µW, the Allan deviation σ_y (fractional instability) is 1.2×10^{-17}, a figure close to that set by the technical noise of the best optical oscillators today [122].

---

[1] Phase noise is actually lower for signals derived from the direct detection of pulses, arising from the uneven distribution of amplitude and phase noise due to the cyclostationary nature of the signal [102].

Appendix D

Monostable Dissipative Kerr Solitons

In this chapter, I detail work [123] done before joining Scott Diddams' group. This work seeks to address the intrinsic difficulty for reliable Kerr comb generation, due to both the Kerr nonlinearity and higher temperatures shifting the cavity resonance in the same direction. Intriguingly, a synthetic Kerr nonlinearity with the opposite sign (opposite resonance shift) yields an apparently robust means to reliably access the single soliton state.

As the use of periodically poled chi-2 active materials with engineered dispersion increases, this may be an interesting area to explore. Of particular interest to me in this work was that the interaction of fast (Kerr) and slow (thermal) processes seemed to change the convexity of the problem, moving from a situation where many local minima could be found corresponding to a different number of solitons to a convex solution of a single soliton. Perhaps the nature of optics is amenable to such investigations, since optical nonlinearities occur at timescales incredibly fast compared to electronic control scales (GHz), and thermal scales (MHz-KHz), and this separation could yield unforeseen capabilities for control.

D.1 Introduction

The optical frequency comb has revolutionized timekeeping and optical frequency metrology, providing a simple and powerful means of coherently linking radio frequency electronics with optical frequency atomic transitions [47]. Whereas these original frequency combs are formed in tabletop optical cavities, since then, frequency combs have also been found to form in continuous-wave (CW) pumped, high quality factor (Q) nonlinear microresonators [124], a finding that has established the basis for a new kind of frequency comb. These so-called Kerr microcombs rely on a double balance of nonlinearity and dispersion, and (nonlinear) gain and (linear) loss to stably host dissipative Kerr solitons (DKS), the time-domain waveform of this frequency comb. Unique from traditional table-top frequency combs due to high GHz-to-THz repetition rates and low µm-to-mm sizes, Kerr microcombs open new applications for frequency combs, such as highly multiplexed coherent optical communication [125, 126], astrocombs [127, 128], ranging [129], dual-comb spectroscopy [130], integrated frequency synthesizers [131, 132], and optical flywheels [133], all with the hope of chip integration [134].

Despite compelling advantages and promising applications, a significant barrier to the widespread use of Kerr microcombs is unreliable access of the single DKS, which is the preferred time-domain waveform for a smooth frequency comb spectrum. Broadly, efforts to render single DKS generation reliable lie in two categories: deterministic access and self-starting behavior.

The first and primary effort is to engineer the deterministic access of the single DKS. This entails breaking the degeneracy or multistability of the single DKS and multiple DKS, i.e., guaranteeing single soliton generation as opposed to multiple soliton generation. This multistability breaking is necessary because the soliton number is effectively stochastic due to the modulation instability-seeded chaotic generation behavior [135]. Past approaches to isolate the single DKS have relied on delicate mode interactions or cascaded quadratic processes [136, 137, 138, 139, 140]. To make matters worse, typical thermal effects inhibit access to the single DKS through adiabatic pump modulation altogether. Because DKSs exist on the thermally unstable, red-detuned side of the cavity resonance, the relatively low-average power single soliton state is ordinarily thermally inaccessible when adiabatically detuning the pump laser across the resonance–the conventional means of accessing DKS states. At the cost of complexity, several methods have been developed to overcome this thermal issue including pump power modulation [141, 142, 143], abrupt power kicking [144, 145], and auxiliary laser assisted pumping [146]. However, these techniques do not break DKS multistability and address deterministic access. The second and more recent effort toward "turn-key" Kerr microcombs is to engineer self-starting behavior of solitons [147, 148]. These experiments seek to simplify the complicated, path dependent pump modulation schemes that generate solitons, so that successful DKS generation merely requires a CW pump laser at a static power and detuning. While these separate efforts represent significant steps towards scalable and robust Kerr microcombs, until now, deterministic access and self-starting behavior have not been satisfied simultaneously.

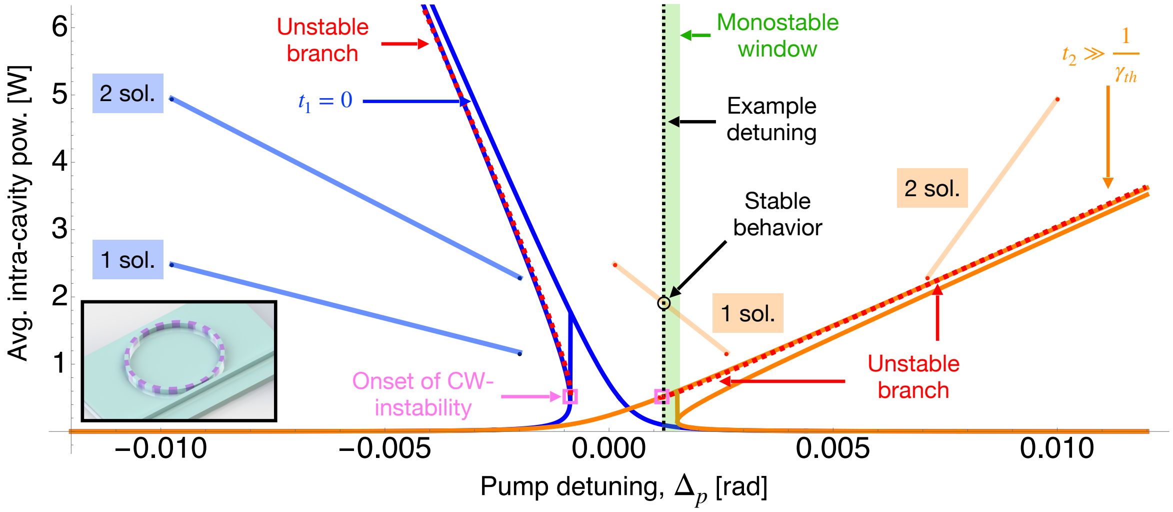

Figure D.1: Cavity resonance profile, illustrating the MS-DKS existence window shaded in green. The initial Kerr-only resonance profile and DKS states (lines marked 1 or 2 sol.) are plotted in blue, while the steady-state counterparts are plotted in orange. The unstable branches are marked by red dashed lines, and the instability onsets are marked by pink squares.

In this paper, we theoretically and numerically establish a means by which *both* deterministic access and self-starting of the single DKS are granted for the first time. We do this by exploiting the opposing interactions of a slow thermal response, and a fast, *negative*, Kerr nonlinearity. More specifically, under the conditions of thermal effects, normal dispersion, and a negative Kerr nonlinearity from the cascaded quadratic process [149], we graphically (Fig. D.1) find a regime in which multistability is broken and deterministic single DKS access is guaranteed, and the underlying CW-only solution is unstable. Here, the single DKS is the only stable behavior. We term this novel operating regime monostable-DKS (MS-DKS). We discuss design principles to access the MS-DKS state in periodically poled lithium niobate (PPLN) microresonators. We numerically demonstrate MS-DKS by solving the Lugiato-Lefever equation [150] alongside a cavity thermal dynamics equation [151]. We observe cycling through behaviors such as chaos, soliton states, and CW-only that settles into stable single soliton behavior, indicating self-starting and deterministic operation. Finally, we demonstrate the resilience of MS-DKS by rapidly perturbing the pump detuning and observing the reemergence of the single DKS.

D.2 MS-DKS Criteria

The three essential criteria that define MS-DKS are 1) to break the multistability of solitons, 2) to open up a monostable window, and 3) to position the single soliton existence range within the monostable window. Here, we define these criteria graphically, describing an example case.

In [135], Li *et al.* introduced a graphical method of determining soliton stability in order to predict whether the single soliton is adiabatically accessible in the presence of thermal effects. We build on this model in Fig. D.1, plotting the analytically determined average power of the CW-only solution and DKS solutions as a function of pump detuning. To visualize the dynamics of cavity behavior, we plot the initial resonance profile affected only by the instantaneous Kerr nonlinearity (blue, t_1) and the steady-state resonance profile that also takes into account the delayed thermal response (orange, t_2). Details about the resonance profile construction, additional examples, and the cavity thermal dynamics are given in the Supplement Sections 1, 2, and 3.

To satisfy the first aforementioned criterion for MS-DKS, breaking multistability, the fast Kerr-induced resonance shift must *oppose* the slow thermally-induced resonance shift. Such a condition has not been satisfied in conventional Kerr combs until now. In our proposed PPLN platform (Supplement Sections 3 and 4), the necessary negative Kerr nonlinearity is achieved from the cascaded quadratic process [149]. DKS existence is guaranteed by normal dispersion waveguide design and the negative Kerr nonlinearity. We see in Fig. D.1 that the opposing Kerr and thermal effects separate the single- and two-soliton existence ranges in the steady-state resonance profile (t_2), breaking multistability.

While opposing Kerr and thermal effects break the multistability between the single- and multi-soliton states, a stable CW-only solution can still co-exist at the same pump detuning. To satisfy the second criterion, opening up a monostable window, there must be a pump detuning range where stable CW-only solutions are forbidden. It is well known that the Kerr nonlinearity leads to an unstable branch of the cavity resonance profile (red dotted lines in Fig. D.1), and thus the design goal here is to ensure that the unstable branch extends over a portion of the stable branch at steady state (green shaded area in Fig. D.1 called the monostable window). This is made possible by the opposing fast Kerr and slow thermal effects, but the exact monostable window characteristics are determined by a variety of parameters as described later in Fig. D.2.

To satisfy the third criterion, placing the single soliton existence range within the monostable window, the single DKS average power must be higher than the onset power of the CW instability (pink squares in Fig. D.1). This arrangement allows the t_1 single soliton existence region to thermally shift into a t_2 position within the monostable window.

D.3 Design Principles

The most direct way to separate the single soliton from the double (and higher number) soliton existence regions is through a large thermal effect. However, discussed shortly, the strength of the thermal shift and the strength of the effective Kerr nonlinearity are co-constrained, and the thermal shift is not the most readily adjustable parameter because the effective Kerr nonlinearity must be generated though stringent cascaded $\chi^{(2)}$ processes (see Supplement Section 4). Instead, it is better to decrease the max detuning of the soliton state (Eq. S7), minimizing the soliton existence range, and thus lowering the thermal shift needed to separate the one and two soliton existence ranges. The simplest way to lower the maximum detuning is by lowering the pump power (as long as one is above threshold). Notably, this does not influence soliton characteristics. We also consider that there is an additional relationship between thermal shifts and the effective Kerr nonlinearity because changes in temperature affect the phase-matching conditions at the heart of the cascaded-quadratic nonlinearity; we discuss this in Supplement Section 5 and find that the

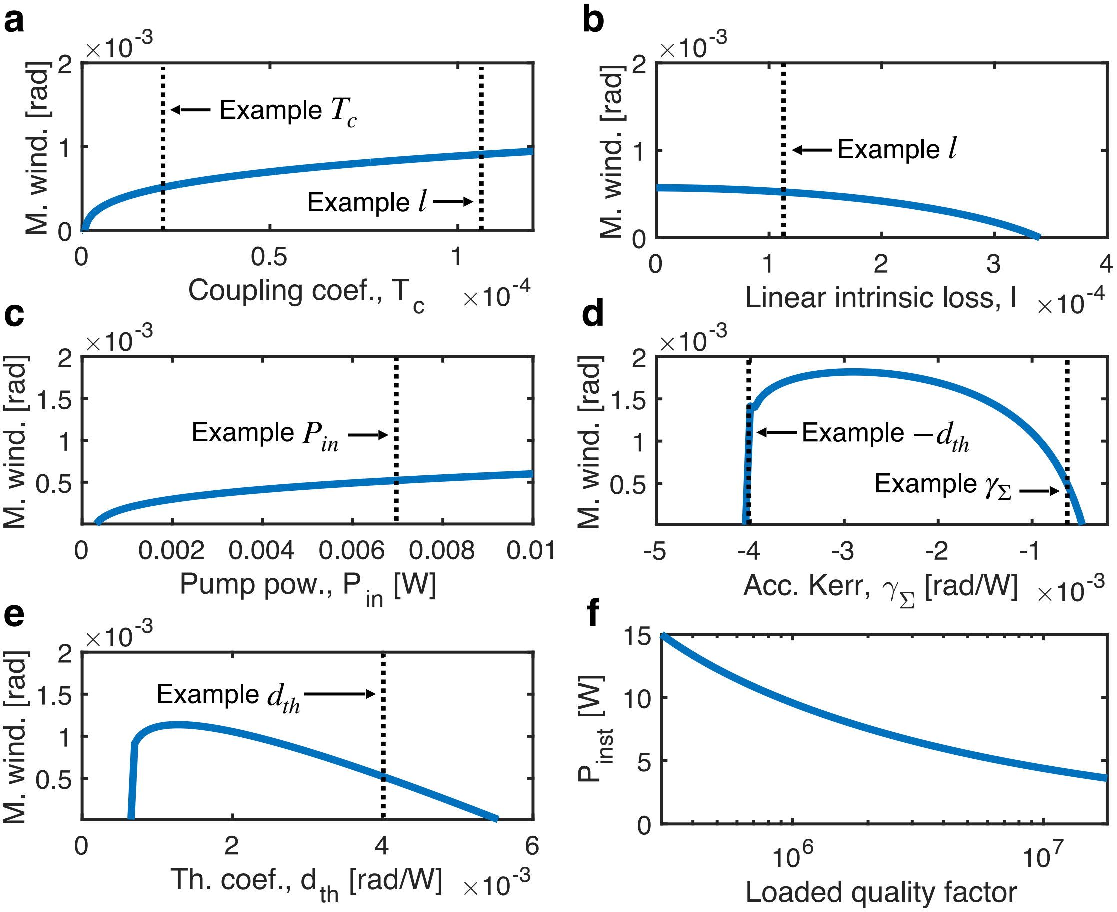

Figure D.2: Monostable window (M. wind.) analysis. (a) M. wind. vs. coupling coefficient, T_c. (b) M. wind. vs. intrinsic loss, l. (c) M. wind. vs. pump power, P_{in}. (d) M. wind. vs. accumulated Kerr nonlinearity, γ_Σ. Strength of the thermal shift coefficient, d_{th}, shown as well. (e) M. wind. vs. thermal shift coefficient, d_{th}. (f) P_{inst} vs. loaded quality factor when critically coupled.

effect is negligible.

We investigate the effects of various resonator parameters on the width of the monostable window (Fig. D.2), varying one parameter individually from the example MS-DKS case (see Supplement Section 2). We find the monostable window by determining the minimum intra-cavity power at which CW-instability occurs, where the unstable central branch of the CW-solution meets the stable underlying branch. Once the location of this point is found, as shown by the pink squares in Fig. D.1, the monostable window can be calculated as detailed in Supplement Section 7.

In Fig. D.2a, we see that increasing the coupling coefficient, T_c, increases the monostable window. However, increasing sources of dissipation comes at a trade-off between increasing the monostable window and placing the single soliton inside the window discussed in the next subsection. l, the linear absorption loss, is shown for comparison. In Fig. D.2b, as we increase l, the monostable window decreases until vanishing. In Fig. D.2c, we find that the monostable window increases with pump power. However, as mentioned, increasing pump power comes with the trade-off of decreasing the separation between the single soliton and double soliton existence ranges. In Fig. D.2d, we vary the accumulated Kerr nonlinearity $\gamma_\Sigma = \gamma L$, where γ is the effective nonlinear coefficient, and L is the resonator circumference. When $|\gamma_\Sigma|$ is greater than $|d_{th}|$, the effective thermal shift parameter, monostability cannot occur. While it may appear that increasing $|\gamma_\Sigma|$ closer to d_{th} would be beneficial in increasing the monostable window, much like increasing the pump power, increasing $|\gamma_\Sigma|$ counter-productively increases overlap between the single soliton and two soliton states. In practice, we find that MS-DKS operation is ideal when d_{th} is several times $|\gamma\Sigma|$. In Fig. D.2e we vary the effective thermal shift parameter, d_{th}. At lower strengths, the monostable window briefly increases with d_{th}. After, the monostable window shrinks and eventually closes.

In order to position the single soliton in the monostable window, the average power of the single soliton must be greater than the power at which CW-instability begins. To achieve this inequality, one must increase DKS average power and/or decrease the CW-instability threshold. Increasing the DKS average power can be accomplished by increasing second order dispersion, which is governed by the device design. Lowering the Kerr inflection point can be accomplished by decreasing resonator losses–i.e. increasing loaded Q as shown in Fig. D.2f.

Given resonator parameters (based on Z-cut LN) listed in Supplement Section 2, notably limited by a GVD of 400 fs^2/mm, we believe that quality factors of 30 million or higher are required to enter the regime of MS-DKS. Increasing the GVD of the cavity would, however, lower this requirement. We note that, presently, LN microresonators have not yet reached the material limit of LN which would push the quality factor well past 30 million (see Supplement Section 8).

D.4 Numerical Demonstration and Dynamics

We generate numerical simulations by solving the Lugiato-Lefever equation [150] simultaneously with a thermal rate equation through a split-step Fourier method (see Supplement Section 9). In Fig. D.3, at $t = 0$ the pump is switched on and the pump detuning is held constant, as displayed in the central panel of Fig. D.3. We observe that the pump shifts the cavity resonance and thus the effective detuning, which drives the cavity through a cycle of chaos and CW-only behavior (seen in upper and lower panels depicting heat map temporal evolution, and average-intracavity power evolution, respectively). Eventually, the cavity generates a single soliton, after which the cavity enters steady-state (longer and shorter-term views are in Supplement Section 10). A stable single soliton was always realized over hundreds of separate iterations beginning from randomized quantum noise.

We note that in the first chaotic cycle shown, a single soliton is not generated and the cavity reenters CW-only behavior, before resuming the chaotic behavior that precedes the single soliton. This cyclical behavior is a product of the instability of CW-only behavior which can be understood through Fig. D.1. If a single soliton is not generated and the CW-only solution is accessed instead, the cavity undergoes repeating cycles in which the instantaneous profile shifts over to the long-term profile, reseeding soliton behavior until the single soliton is accessed.

Reliable Kerr comb operation requires resiliency against perturbation. In Fig. D.4 we set the pump parameters to operate in the MS-DKS regime, observing the formation of the single soliton. After this formation, a sharp detuning step of 50 mrad lasting 3.3 ms destroys the soliton. But

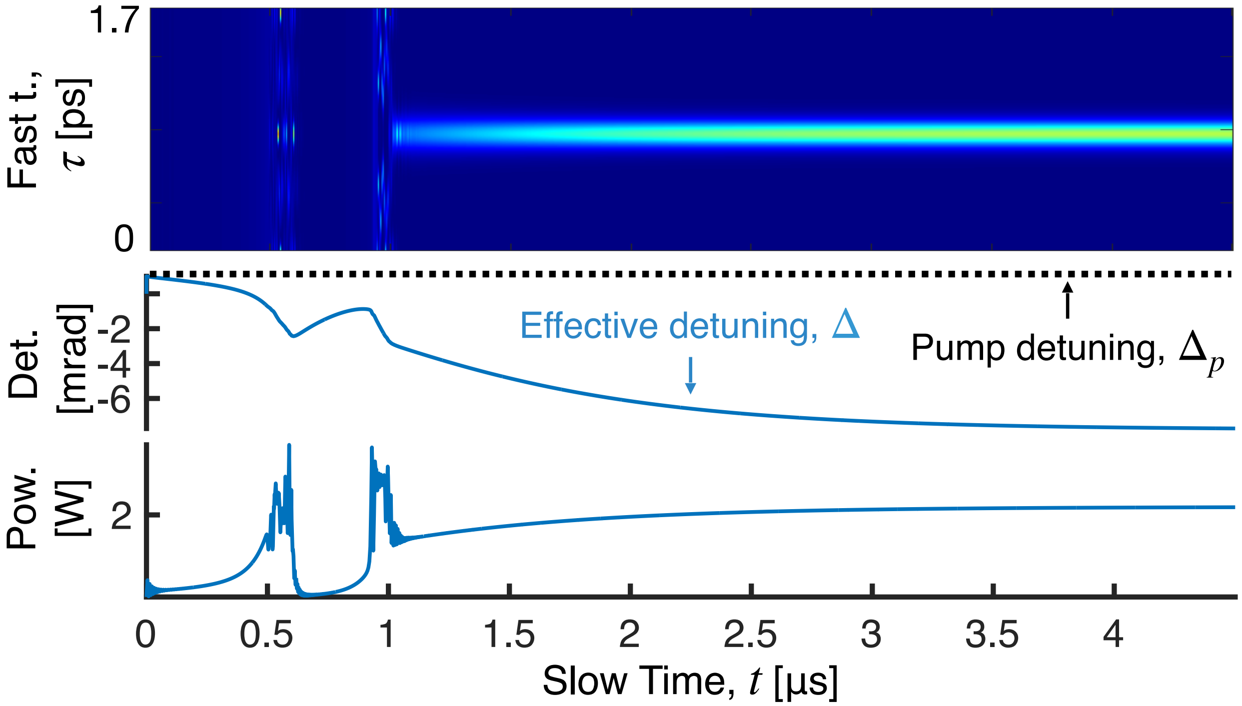

Figure D.3: (a) Top panel: heat map of MS-DKS formation. Middle panel: pump detuning (dotted line) and effective detuning (blue line). Lower panel: avg. intra-cavity power dynamics.

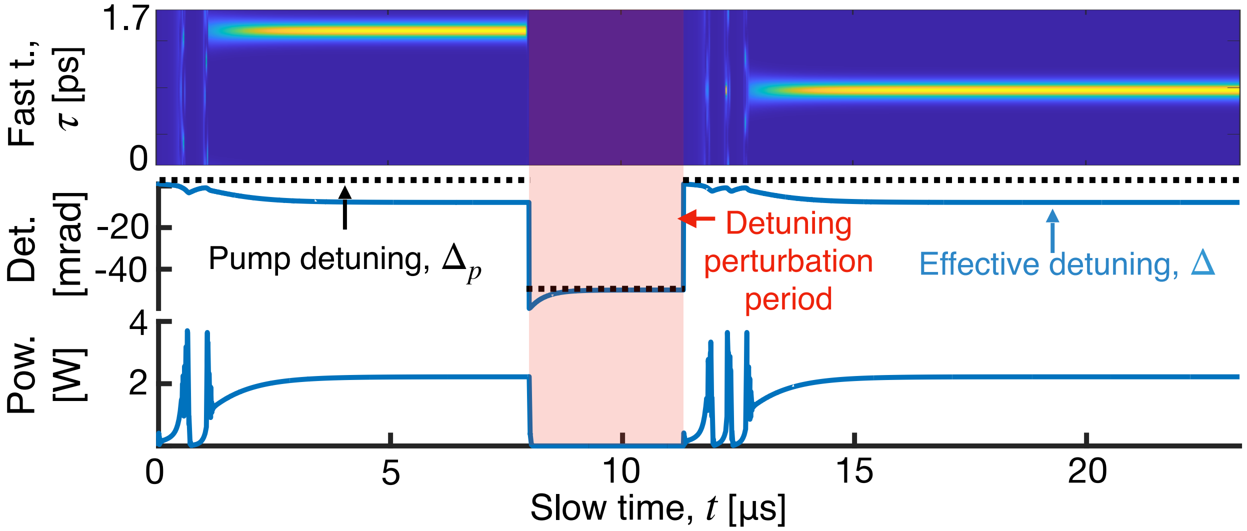

Figure D.4: Perturbation dynamics for MS-DKS.

after the detuning has returned to within the MS-DKS regime, the single soliton is formed again (non-MS example in Supplement Section 10a for comparison).

D.5 Conclusion

In closing, we propose a new operating regime for DKS where multistability is broken, and the underlying CW solution is rendered unstable through the competing effects of a Kerr nonlinearity and a counteracting, slow, power-dependent resonance shift such as a thermal shift. Hence, in MS-DKS, the single soliton is self-starting and deterministic with a CW pump. We provide a graphical means of finding and analyzing this behavior through instantaneous and long-term resonance profiles. We give guidelines for how to access MS-DKS behavior beyond simply a negative Kerr nonlinearity and positive dispersion. This includes a high quality factor, relatively low pump powers, and a thermal effect several times stronger than the Kerr shift.

We emphasize that this regime *in general* is made possible through the interaction of a fast Kerr nonlinearity and a *much slower, counteracting*, average power-dependent shift. This is similar to recent experiments where the interaction of a Kerr effect and a slow photorefractive effect in lithium niobate grants bi-directional switching and deterministic access [147, 152]. One difference is that thermal effects are average power-dependent, whereas the photorefractive effect is intensity-dependent like the Kerr nonlinearity. Fundamentally, this difference leads to less coupling between the thermal shift and the Kerr shift, which widens the parameter space to access the MS-DKS regime.

The MS-DKS mechanism points to fundamentally enhanced reliability of Kerr microcombs [148]. This mechanism may also aid in the reliable generation of other interesting behaviors such as soliton breathers and soliton crystals. Our analysis suggests fruitful opportunities in exploring nonlinear optical behavior subject to counteracting shifts at very different timescales [147].

D.6 Analytic Resonance Profile Construction

A simple and effective way to view soliton stability is by analyzing the resonance profile. We construct an analytical model of the resonance profile by directly solving for the CW behavior under a Kerr shift and a thermal shift, while also plotting the analytically well-approximated soliton stability zones. This analytic graphical model allows for the rapid analysis of soliton and CW stability, as well as the direct incorporation of the thermal trajectory of the cavity. Moreover, due to the orders of magnitude difference in timescales between the Kerr effect and thermal shift, the ability to examine the Kerr-only resonance profile and the Kerr and thermally-shifted resonance profiles allows us to effectively examine instantaneous and long term (in)stability. It should be noted that this graphical model ignores non-CW and non-soliton behavior such as chaos and Turing patterns, which are not directly relevant to soliton stability.

First, we begin with the unshifted resonance profile, $P_{CW}[\Delta_p]$ [153]:

$$P_{CW}[\Delta_p] = P_{in} \times R_c[\Delta_p] \tag{D.1}$$

where

$$R_c[\Delta] = \frac{\left|\sqrt{T_c}\right|^2}{\left|1 - e^{-i\Delta} e^{-l} \sqrt{1 - T_c}\right|^2} \tag{D.2}$$

$\Delta_p = t_R(\omega_0 - \omega_p)$ is the pump detuning from the unshifted (cold) cavity resonance, t_R is the round trip time, ω_0 is the cold cavity resonance frequency, and ω_p is the pump frequency. P_{in} is the pump power, R_c is the cavity optical response, Δ is the effective detuning from the shifted cavity resonance, T_c is the fractional coupling loss per round trip, and l is the fractional linear propagation loss per round trip.

We calculate the instantaneous, Kerr-only-shifted resonance profile by solving for the average intra-cavity power as a function of pump detuning in the presence of a Kerr-shift:

$$P_{CW,K}[\Delta_p] = P_{in} \times R_c\left[\Delta_p - \gamma L P_{CW}[\Delta_p]\right] \tag{D.3}$$

γ is the effective Kerr coefficient i.e. $\gamma = (2\pi n_2)/(\lambda A_{eff})$, n_2 is the Kerr nonlinear coefficient, λ is the pump wavelength, A_{eff} is the effective modal area, and L is the resonator circumference.

We find the long-term, Kerr and thermally-shifted resonance profile similarly, but also incorporating the thermal shift:

$$P_{CW,KT}[\Delta_p] = P_{in} \times R_c[\Delta_p - \gamma L P_{CW}[\Delta_p] - d_{th} P_{CW}[\Delta_p]] \tag{D.4}$$

Here, the thermal effect is incorporated through the parameter d_{th}, which relates the average intracavity power to a shift of the resonance. This parameter is described further in the discussion of Eq. D.8.

The nth order dissipative Kerr soliton (DKS) contribution to average intra-cavity power is [154, 155]:

$$P_{DKS}[\Delta, n] = \frac{n\int_{-t_R/2}^{t_R/2}\left(\sqrt{\frac{2|\Delta|l}{|\gamma|L}}Sech\left(\tau\sqrt{\frac{2|\Delta|l}{|\beta_2|L}}\right)\right)^2 d\tau}{t_R} + P_{CW}[\Delta] \tag{D.5}$$

where β_2 is the group velocity dispersion, and n is the soliton order (number). The instantaneous i.e. Kerr-only maximum stable detuning for solitons away from the cavity resonance is [155]:

$$\Delta_{edge} = \frac{\pi^2 \gamma T_c L P_{in}}{8 l^3} \tag{D.6}$$

The long term, Kerr and thermally-shifted, maximum stable detuning for solitons away from the cavity resonance is therefore:

$$\Delta_{edge,T}[n] = \frac{\pi^2 \gamma T_c L P_{in}}{8 l^3} + d_{th} P_{DKS}[\Delta_{edge}, n] \tag{D.7}$$

With these expressions, we then analytically construct resonance profiles granting graphical exploration of resonator parameter space, as shown in the main text and in the following section.

D.7 Resonance Profile Examples

First, we describe conventional DKS, which form in the presence of a positive Kerr nonlinearity and anomalous dispersion, in Fig. D.1a. Depicted in blue is the resonance profile associated with the Kerr effect only, which is the instantaneous response of the resonator. The dashed profile corresponds to the intermediate response of the resonator, before the resonator has reached full thermal equilibrium. The orange profile corresponds to the long-term cavity response, when both Kerr and thermal effects are considered, i.e. at times much greater than the inverse of the thermal relaxation rate γ_{th}. We emphasize that both the Kerr shift of the resonance and the thermal shift of the resonance occur in the same direction. Typically, solitons are formed by scanning from blue (left) to red (right) through resonance. This formation protocol allows the cavity behavior to pass through chaos, which is necessary to seed the soliton waveform. Chaos occurs near the apex of the resonance profile, where there is large intra-cavity power. In the adiabatic limit (denoted by the orange tilted profile and orange soliton stability regions), thermal shifts are typically strong enough that the single soliton is no longer a stable structure at this maximum detuning, as shown by the dashed black line labeled "example detuning 1." The stable behaviors at this detuning are circled, and in this case correspond to the CW-only solution, or three DKS solution. This dilemma necessitates additional techniques to access the single soliton, as mentioned in the introduction. Furthermore, on the blue (left) side of the soliton existence range, demarcated by "example detuning 2," while the single DKS is stable and multiple DKS are not, the higher power CW, Turing, or chaotic behavior is also stable, and typically the single DKS is dominated by such behavior in this regime.

In the general case of a negative Kerr nonlinearity and normal dispersion (Fig. D.1b), the soliton existence range flips to the *blue* side of the cavity resonance. A red-shifting thermal effect shifts the soliton stability regions, breaking multistability (degeneracy) on the blue (left) side of the cavity resonance as depicted in Fig. D.1b with the translucent blue lines indicating the instantaneous DKS existence range and orange lines indicating the long-term DKS existence range. As can be seen by the dotted vertical line labeled ”example detuning,” there exists a detuning range in which only the low power CW-only solution and the single soliton solution are stable, indicated by black circles. This breaking of multistability with higher number solitons and other higher power behavior is a direct consequence of the opposing shifts of the negative Kerr effect and the thermal effect and leads to the ability to deterministically access the single soliton, i.e., eliminating the possibility of accidentally accessing other soliton numbers.

Another key feature described by the resonance profile of Fig. D.1b is the dynamics due to the relatively slow thermal effect. For example, turning the pump laser on at the example detuning initially produces optical cavity behavior obeying the blue, instantaneous Kerr-only profile. As the cavity transitions into thermal equilibrium, the resonance profile tilts to the right, moving through the intermediate dotted profile and eventually settling into the long-term orange profile. This transient behavior has the effect of detuning the pump laser through chaos, which seeds soliton behavior. This process is shown in Fig. D.6. We note that a jump in power (turning on the pump laser as in Fig. D.6) is not the only way to excite this beneficial transient behavior; discrete steps in detuning can also trigger this same process. In Fig. D.1b, we also mark the branch of the resonance profile that is subject to CW-instability with a dashed red line, and the onset of this instability with pink squares. While not relevant to the case pictured in Fig. D.1b, the onset of CW-instability is crucial for the following monostable case, which we describe next.

Below, we list the parameters used for the resonance profiles in Fig. D.5 and in the main text, as well as corresponding simulations. These are the intrinsic loss l, the coupling loss T_c, the resonator length L, the intrinsic quality factor Q_{int}, pump power P_{in}, pump wavelength λ_p, group velocity dispersion β_2, accumulated Kerr nonlinearity $\gamma_\Sigma = \int_{x=0}^{x=L} \gamma dx = \gamma L$, thermal shift coefficient d_{th}, and the ratio of the accumulated Kerr nonlinearity to the thermal shift, $\frac{\gamma_\Sigma}{d_{th}}$.

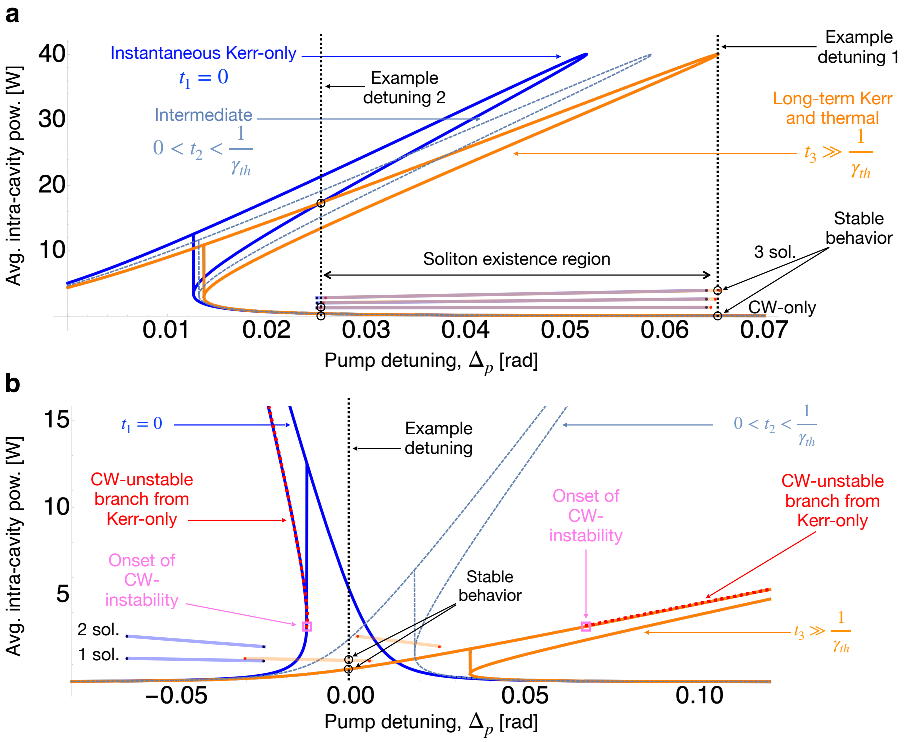

Figure D.5: (a) Example resonance profile of conventional Kerr comb. Note that the single soliton stability region (shown on the lower right hand side) cannot be accessed through continuous detuning through resonance. (b) Resonance profile of general negative Kerr, normal dispersion, and thermal red-shift case. The soliton stability region is flipped to the blue (left) side of the resonance because of the negative Kerr effect and normal dispersion. Due to the opposition of the negative Kerr effect and the thermal effect, there exists a detuning region over which only the single soliton and the low power CW-only solution are stable, such as at the example detuning.

Type	l	T_c	L [mm]	Q_{int} [$\times 10^6$]	P_{in} [W]
Conventional	0.0025	0.0025	0.5	1.7	0.1
General proposed	0.0025	0.0025	0.5	2.6	0.1
MS-DKS	.000113	.0000226	0.22	26.5	.007

Type	λ_p [µm]	β_2 [fs^2/mm]	γ_Σ [rad/W]	d_{th} [rad/W]	$\frac{\gamma_\Sigma}{d_{th}}$
Conventional	1.6	-130	.0013	.00033	0.48
General proposed	1.6	130	$-.0013$	.025	-0.05
MS-DKS	1	400	$-.00064$	.004	-0.11

D.8 Additional Examples of Dynamics

We describe the dynamics of the general negative Kerr nonlinearity and anomalous dispersion case with the resonance profile of Fig. D.5b and dynamics shown in Fig. D.6. In Fig. D.6a, at $t = 0$ we turn the pump laser on at a fixed detuning, marked by the black dashed line in the central panel. In the bottom panel, we observe an initial spike in intra-cavity power, followed by a stable power at longer t. In the central panel, we find that this power spike is linked with the effective detuning shifting to larger negative detuning (as the resonance shifts red), shown by the blue line. In the upper panel, we monitor the heat map of the intensity evolution of the cavity. We see that indeed a single soliton is stably accessed. In Fig. D.6b we take a detailed view of the formation dynamics of the single soliton, where the time window is demarcated by the dashed red box. We observe that the effective detuning shift corresponds to a transition from CW-only behavior, through chaos, into the single soliton state. This behavior is in direct agreement with the resonance profile picture of Fig. D.5b; upon turning the pump laser on, the cavity behavior is CW-only and exists on the instantaneous, blue resonance profile. As the cavity equilibrates, it is driven through intermediate resonance profiles, exemplified by the dashed profile (t_2) which passes the cavity through the chaotic regime. Finally, the long-term, orange resonance profile is accessed, at which (at this detuning) the single soliton is stable.

Notably, both the CW-only solution and the single soliton solution are stable, so over the

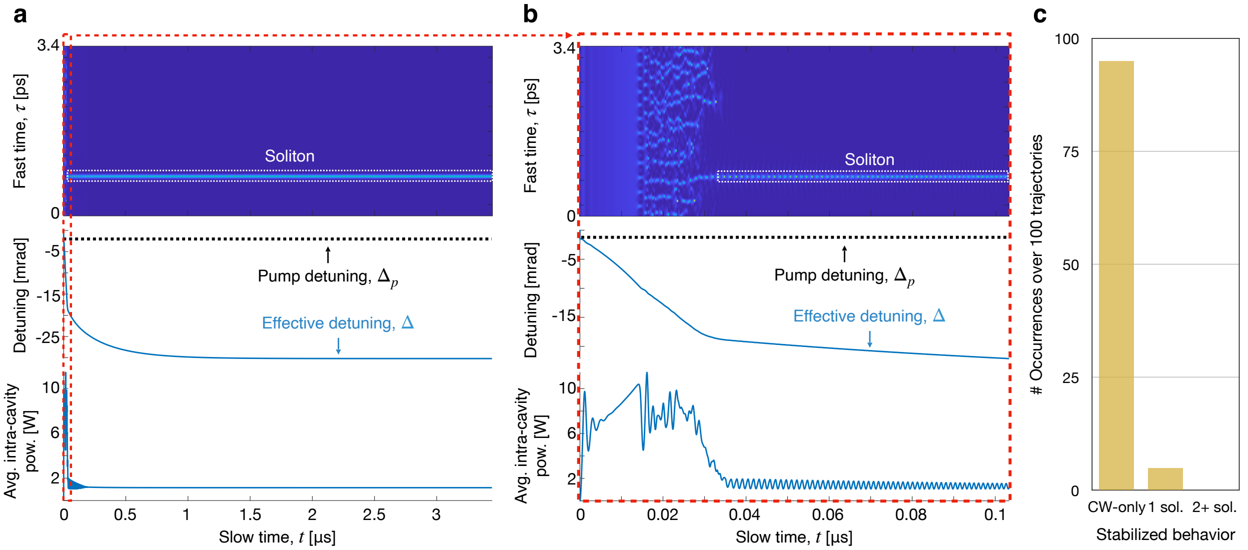

Figure D.6: (a) Top panel: heat map of soliton formation for general proposed case of Fig. D.5b. At $t = 0$ the pump is turned on and then held constant in power and detuning. Middle panel: pump detuning protocol (dotted line) and effective detuning (blue line). Lower panel: intra-cavity power dynamics. (b) Close-up view of initial dynamics. Top panel: heat map of soliton formation. The time interval is indicated by the dashed red lines. Middle panel: pump detuning protocol and effective detuning. Lower panel: initial average intra-cavity power dynamics. (c) Histogram of stabilized behavior over 100 trajectories, of which (a) and (b) display one example. Note that only CW-only behavior or single soliton behavior are accessed.

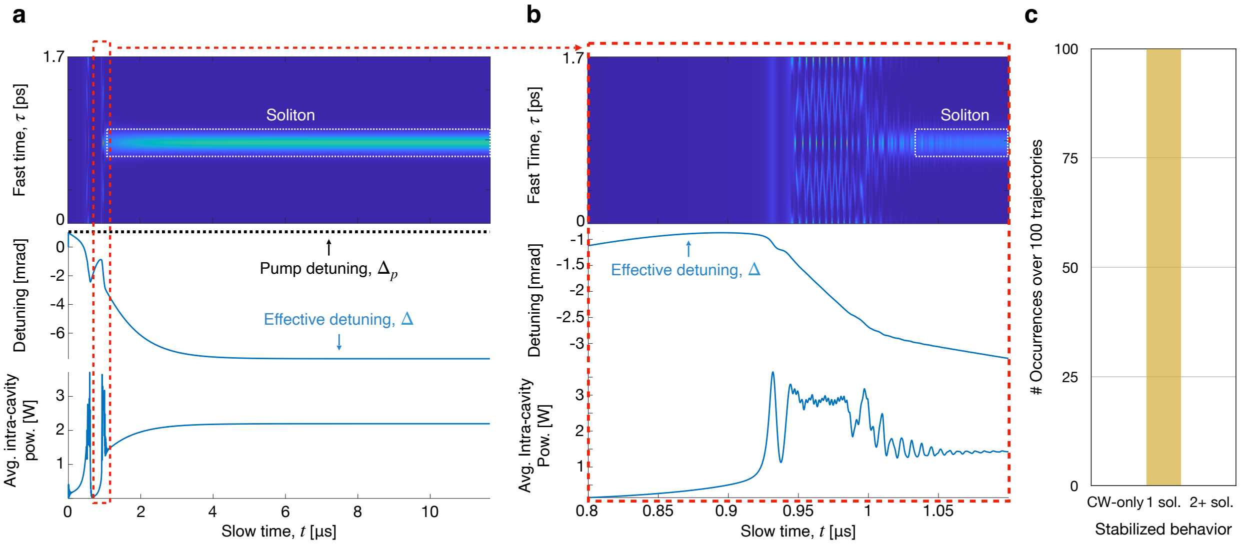

Figure D.7: (a) Top panel: heat map of soliton formation for MS-DKS proposed case of Fig. D.5c. Middle panel: pump detuning protocol (dotted line) and effective detuning (blue line). The pump detuning is held constant for MS-DKS, while the effective detuning cycles until the cavity reaches the single soliton state. Lower panel: average intra-cavity power dynamics. Successive power spikes indicate cycling through chaos and CW-only behavior. (b) Close-up view of cycling and soliton entry dynamics, as indicated by the dashed red boxes. Top panel: detailed view of cycling and soliton entrance dynamics. Middle panel: the effective detuning drifts and has a time delay associated with increased intra-cavity power, while the pump detuning is held constant. Lower panel: power dynamics show spiky chaotic behavior as well as breathing behavior before entering stable soliton state. If no soliton is excited, as in the first cycle, the cavity enters low power CW-only behavior, but eventually cycles back into chaos (the second cycle depicted in b). Upon entering a breathing soliton state, the cavity resonance continues to shift until the stable soliton is accessed. (c) Histogram of stabilized behavior over 100 trajectories, of which (a) and (b) display one example. For the MS-DKS case, only the single soliton is accessed.

course of many trajectories, the cavity frequently reenters the CW-only solution as shown by the histogram in Fig. D.6c which displays the statistics of final cavity behavior after 100 trajectories, initialized from random quantum noise.

D.9 Derivation of the Thermal Differential Equation

In our treatment of thermal dynamics, we show how cavity parameters such as thermal conductivity K_c, specific heat C_p, thermal expansion ϵ, thermo-refractive effect $\frac{\delta n}{\delta T}$, and linear absorption κ_{lin} define the dynamic resonance shift, described by the simple rate equation in the main text:

$$\frac{d\Delta_{th}}{dt} = -\gamma_{th}\left(\Delta_{th} - d_{th}P_{avg}\right) \tag{D.8}$$

Δ_{th} is the detuning shift [rad] due to thermo-optics effects, t is time, γ_{th} is the thermal decay rate, d_{th} is a constant that relates the average intra-cavity power to a shift in detuning, and P_{avg} is the average intra-cavity power.

We derive Eq. D.8 beginning with results from Carmon *et al.* [151]:

$$\dot{\Delta T}(t) = -\frac{K_c}{C_p}\left(\Delta T(t) - \frac{\dot{q_{in}}}{K_c}\right) \tag{D.9}$$

$$\lambda_r(\Delta T) - \lambda_0 = \lambda_0 a \Delta T \tag{D.10}$$

$$a \approx \epsilon + \frac{\frac{dn}{dT}}{n_0} \tag{D.11}$$

where $\Delta T(t)$ is the change in temperature, K_c is the thermal conductance, C_p is the specific heat, $\dot{q_{in}}$ is the absorbed intra-cavity power, λ_r is the hot cavity resonance wavelength, λ_0 is the cold cavity resonance wavelength, and a is a constant that combines both a thermal expansion coefficient ϵ and thermo-refractive effect $\frac{\delta n}{\delta T}$. Translating this change in resonance wavelength to a change in detuning, defined as:

$$\Delta_{th} = t_R \times \delta_{th} = t_R\left(\omega_0 - \omega_{0,th}\right) \tag{D.12}$$

where $\delta_{th} = \omega_0 - \omega_{0,th}$, we then rearrange the left-hand side of (D.10) such that

$$\lambda_r(\Delta T) - \lambda_0 = 2\pi c\left(\frac{1}{\omega_{0,th}} - \frac{1}{\omega_0}\right) = 2\pi c\frac{\omega_0 - \omega_{0,th}}{\omega_{0,th}\omega_0} = 2\pi c\frac{\delta_{th}}{(\omega_0 - \delta_{th})\omega_0} \tag{D.13}$$

where $\delta_{th} = \omega_0 - \omega_{0,th}$, ω_0 is the cold cavity resonance frequency and $\omega_{0,th}$ is the thermally shifted resonance frequency. In general, thermal shifts are on the order of megahertz, whereas the carrier frequency is on the order of hundreds of terahertz, hence $\delta_{th} \ll \omega_0$, and thus the δ_{th} term in the denominator of (D.13) can be neglected. We then extract the linear relation between ΔT and Δ_{th}:

$$2\pi c \frac{\delta_{th}}{a\lambda_0\omega_0^2} = \frac{\Delta_{th}}{t_R a\omega_0} = \Delta T \tag{D.14}$$

Substituting (D.14) into (D.9) yields:

$$\frac{1}{t_R a\omega_0}\frac{d\Delta_{th}}{dt} = -\frac{K_c}{C_p}\left(\frac{1}{t_R a\omega_0}\Delta_{th} - \frac{\dot{q_{in}}}{K_c}\right) \tag{D.15}$$

We then define the absorbed power as the product of linear absorption and the average intracavity power $\dot{q_{in}} = \kappa_{lin} \times P_{avg}$, where $P_{avg} = \frac{\int_{-t_R/2}^{t_R/2} |A|^2 dt}{t_R}$ and $\kappa_{lin} = Q/Q_{abs}$ i.e. the ratio of the total Q to the Q due only to absorption. Thus (D.15) becomes:

$$\frac{d\Delta_{th}}{dt} = -\frac{K_c}{C_p}\left(\Delta_{th} - \frac{t_R a\omega_0\kappa_{lin}}{K_c} \times P_{avg}\right) \tag{D.16}$$

where t_R is the cavity round trip time. Defining $d_{th} = \frac{t_R a\omega_0\kappa_{lin}}{K_c}$ and $\gamma_{th} = \frac{K_c}{C_p}$, we then substitute into (D.16) to form the simplified thermal differential equation (D.8).

Importantly, the effective detuning Δ (which is input into the Lugiato-Lefever equation) is then defined as:

$$\Delta_{\mathit{eff}} = \Delta_c - \Delta_{th} = t_R\left((\omega_0 - \omega_p) - (\omega_0 - \omega_{0,th})\right) = t_R\left(\omega_{0,th} - \omega_p\right) \tag{D.17}$$

D.10 Simulation Details

We generate numerical simulations by solving the Lugiato-Lefever equation (LLE) (D.18) [156, 150] simultaneously with a thermal rate equation (D.8) through a split-step Fourier method, updating both the thermal effect and the LLE once per round-trip.

$$t_R\frac{dA}{dt} = \left[-(T_c + l)/2 - i\Delta_{\mathit{eff}} - iL\frac{\beta_2}{2}\frac{\delta^2}{\delta\tau^2} + i\gamma L\,|A|^2\right]A + \sqrt{T_c}A_{in} \tag{D.18}$$

A is the intra-cavity field, in units of $\sqrt{\mathrm{W}}$. t is slow time, τ is fast time, and A_{in} is the pump field.

D.11 Estimating the Thermal Shift Coefficient in LN

As a best estimate for the d_{th} parameter of a PPLN microring resonator, we draw on parameters from [157, 158] as well as a parameter sheet from NanoLN. We find that $C_p = 0.15\,\text{cal/gK}$, $\epsilon = 1.44\times10^{-5}\,\text{K}$, $\frac{dn}{dT}/n_0 = 1.9\times10^{-5}\,\text{K}$, $a = 3.31\times10^{-5}\,\text{K}$, $t_R = 1.7\,\text{ps}$, and $\kappa_{lin} = 5\times10^{-3}$. From Wang *et al.* [157], we extract the device dependent thermal conductance, choosing the thermal conductance from the substrate to the environment, as their geometry is a microdisk rather than a ring resonator, $K_c = 5.9\times10^{-3}\,\text{J/sK}$. This results in $d_{th} \approx 0.09\,\text{rad/W}$. While this is larger than the example MS-DKS d_{th} value, implementation of external temperature control, cladding, and co-design of the effective nonlinear refractive index n_2 can be adjusted to engineer this parameter.

The parameter γ_{th} does not need to itself be engineered, because it does not change the overall mechanism of MS-DKS so long as its timescale (typically sub-MHz) is far removed from the Kerr timescale (PHz).

D.12 Device design for effective Kerr nonlinearity

Typically, the Kerr effect in microresonators is limited by the intrinsic, third-order, material nonlinearity $n_{2,Kerr}$, and has positive sign. We can, however, break this limitation, generating very strong, as well as negative Kerr nonlinearities. We can do so by employing a cascaded second-order (quadratic) nonlinear (CQN) process, which results in an intensity dependent change in refractive index, i.e. a virtual Kerr effect denoted as $n_{2,CQN}$ [149]. Specifically, we can exploit a phase mismatch between the fundamental frequency and its second harmonic to generate $n_{2,CQN}$, where the coupled equations are:

$$\frac{\delta}{\delta z}A_{FF} = -j\frac{\omega_0 d_{\mathit{eff}}}{n_{FF}c}A_{FF}^{*}A_{SH}e^{-j\Delta kz} \tag{D.19}$$

$$\frac{\delta}{\delta z}A_{SH} = -j\frac{\omega_0 d_{\mathit{eff}}}{n_{SH}c}A_{FF}^{2}e^{j\Delta kz} \tag{D.20}$$

where ω_0 is the fundamental carrier frequency, d_{eff} is the effective second-order nonlinear coefficient, n is the index of refraction, c is the speed of light, n_{FF} is the effective refractive index at the fundamental frequency, n_{SH} is the effective refractive index at the second harmonic, A_{FF} is the fundamental field, A_{SH} is the second harmonic field, and Δk is the total phase-mismatch. In the small conversion efficiency limit (where $|\Delta k| \gg \frac{\omega_0 d_{\mathit{eff}} |E_0|}{c\sqrt{n_{SH} n_{FF}}}$, and E_0 is the field strength in V/m), these coupled equations lead to an effective nonlinear refractive index:

$$n_{2,CQN} = -\frac{4\pi d_{\mathit{eff}}^2}{\lambda_{FF} \epsilon_0 c n_{SH} n_{FF}^2 \Delta k}, \tag{D.21}$$

where λ_{FF} is the fundamental wavelength.

We can then calculate the device parameters for the example MS-DKS. We set the modal cross-section to $A_{eff} = 0.1\,\mu\mathrm{m}^2$, the desired effective Kerr coefficient $\gamma = -2.9$, and operate at a fundamental wavelength $\lambda_{FF} = 1.05\,\mu\mathrm{m}$. The resonator length $L = 0.22\,\mathrm{mm}$, group velocity $GV = 7564\,\mathrm{ps/m}$, vacuum permittivity $\epsilon_0 = 8.854\,\mathrm{pF/m}$, speed of light $c = 0.3\,\mathrm{m/ns}$, $n_{SH} = 2.2605$, $n_{FF} = 2.1676$, $d_{eff} = 33\,\mathrm{pm/V}$, and an intrinsic Kerr nonlinearity $n_2 = 8.33 \times 10^{-19}\,\mathrm{m}^2/\mathrm{W}$ [159]. Index and dispersion data calculated in COMSOL.

We subtract the intrinsic Kerr nonlinearity from the desired total effective Kerr nonlinearity, finding:

$$n_{2,CQN} = n_{2,tot} - n_{2,int} = -5.7 \times 10^{-18}\,\mathrm{m}^2/\mathrm{W} \tag{D.22}$$

We simply rearrange (D.21) to find the desired phase-mismatch:

$$\Delta k = \frac{-4\pi d_{\mathit{eff}}^2}{n_{2,CQN} \lambda_{FF} \epsilon_0 c n_{SH} n_{FF}^2} = 80\,521\,\mathrm{m} \tag{D.23}$$

We can then calculate the poling period as,

$$\Gamma = \frac{2\pi}{\Delta k_{int} - \Delta k} = 6.09\,\mu\mathrm{m} \tag{D.24}$$

where Δk_{int} is the intrinsic phase-mismatch. Furthermore, we calculate the efficiency parameter with a maximal intra-cavity field E_0 corresponding to 20 W average intra-cavity power:

$$\frac{\omega_0 d_{\mathit{eff}} |E_0|}{c\sqrt{n_{SH} n_{FF}}} = 3444\,\mathrm{m} \tag{D.25}$$

which is indeed much smaller than Δk and thus confirms operation with small conversion efficiency.

D.13 CW-Instability and Monostable Calculation

In order to find the monostable window, we first find the points at which the CW-only solution becomes unstable. To do so, we first analyze the gain dispersion for the typical damped, driven nonlinear Schrödinger equation [160, 161, 156]:

$$g = -1 + \sqrt{4Y\left(\Delta_n - \eta\Omega^2\right) - \left(\Delta_n - \eta\Omega^2\right)^2 - 3Y^2} \tag{D.26}$$

where g is the gain parameter, $Y = \frac{|A|^2|\gamma|L}{\alpha_{tot}}$ and is the normalized stationary intracavity power, $\Delta_n = \Delta/\alpha_{tot}$ is the normalized detuning, α_{tot} is the total round trip loss including intrinsic and external coupling, η is the sign of the dispersion, Ω is the modulation frequency difference from the carrier, and the plane wave Ansatz has the form $e^{gt\pm i\Omega\tau}$. In the case of pure CW instability, we examine only the DC perturbation, i.e. $\Omega = 0$. The gain is then described as:

$$g = -1 + \sqrt{4Y\Delta_n - \Delta_n^2 - 3Y^2} \tag{D.27}$$

We then confine our analysis to the set of non-oscillating and stable solutions, setting $g = 0$. Solving for the stationary intracavity power Y, we find that:

$$Y = \frac{2\Delta_n \pm \sqrt{\Delta_n^2 - 3}}{3} \tag{D.28}$$

This is, in fact, the same condition for the two inflection points between the three CW-only solutions of the Lugiato-Lefever equation [156, 162]. Indeed, the instability points occur at these inflection points, which can also be confirmed by virtue of the real part of g being negative for the overlying and underlying CW-only solutions, but positive (unstable) for the central solution.

Thus, we calculate the monostable window by finding the power at which the inflection point occurs on the Kerr-only curve, then mark this point on the Kerr and thermal curve as illustrated in the resonance profiles of Fig. 2 in the main text.

D.14 Linear Absorption Loss in LN

There has been substantial progress recently in increasing the quality factor of LN microring resonators. For example, Desiatov *et al.* fabricated resonators with intrinsic quality factors up to 11 million [163]. However, this quality factor is still far less than the material absorption limit, and loss in LN resonators is likely still dominated by scattering. As a point of reference, in bulk, undoped, congruent LN, absorption loss at 1 µm has been demonstrated to be as low as 6.8×10^{-4} cm [164]. A resonator of the same dimensions and operating wavelength as the proposed MS-DKS design would, if limited by this linear absorption loss, have an intrinsic quality factor of $\sim$ 200 million. Additional studies on the limit of the intrinsic quality factor in LN indicate a quality factor of 380 million for stoichiometric LN and a quality factor of 200 million for congruent LN at 1550 nm [165]. Therefore, we believe that the requirement for MS-DKS of a Q beyond 30 million may well be in reach as LN microfabrication capabilities are improved.